# Deformation at Oceanic Plate Boundaries: Insights from Geophysical Observations

Maleen Wijeratna Kidiwela

A dissertation

submitted in partial fulfillment of the

requirements for the degree of

Doctor of Philosophy

University of Washington

2026

Reading Committee:

William S.D. Wilcock, Chair

Marine A. Denolle

Harold Tobin

Program Authorized to Offer Degree:

School of Oceanography

University of Washington

## Abstract

Deformation at Oceanic Plate Boundaries: Insights from Geophysical Observations

Maleen Wijeratna Kidiwela

Chair of the Supervisory Committee:
William S. D. Wilcock
School of Oceanography

Studies of deformation along submarine plate boundaries are constrained by the difficulties associated with conducting seismic and geodetic measurements on the seafloor. This dissertation advances three geophysical methods (tomography, geodesy, and ambient noise interferometry) to investigate how deformation is accommodated within strain cycles across the principal tectonic systems of the Wilson Cycle: rifting, seafloor spreading, and subduction.

At Orca Volcano in the Bransfield Basin, a new tomographic workflow incorporating secondary arrivals through a magma chamber. The tomographic models revealed a transition in rifting style controlled by variations in mantle hydration linked to a tear in the subducting Phoenix slab. At Axial Seamount on the Juan de Fuca Ridge, three years of horizontal acoustic ranging across the caldera demonstrated that inter-eruptive extension is primarily accommodated by volumetric inflation from two pressure sources at different depths, providing new constraints on magma storage geometry and the localization of eruptions. In the Cascadia subduction zone, a decade of ambient noise interferometry with novel denoising methods uncovered distinct regional variations in shallow megathrust dynamics, including evidence for slow slip on protothrusts and fluid migration.

Across these three settings, two themes emerged: fluids exert a first-order control on crustal deformation at every stage of the plate tectonic cycle, and slab tears on different depths along the subducting plate influence crustal deformation in distinct ways. Together, these studies demonstrate the value of diverse geophysical methods for resolving deformation processes that remain largely hidden beneath the oceans.

## Table of Contents

Acknowledgements ..... 7

**Chapter 1: Introduction and Organization of the Dissertation ..... 9**

**Chapter 2: Late-Stage Rift Evolution at Back Arc Basins: Insights from a Tomography Experiment at Orca Volcano, Bransfield Basin ..... 14**

**2.0 Abstract ..... 14**

**2.1 Introduction ..... 15**

**2.2 Background ..... 17**

**2.3 Experimental Geometry and Data ..... 24**

**2.4 Methods ..... 30**

**2.5 Results ..... 37**

**2.6 Discussion ..... 49**

**2.7 Conclusions ..... 65**

**2.8 Acknowledgements ..... 66**

**Chapter 3: Insights into the Inflation of Axial Seamount from Horizontal Seafloor Geodesy ..... 67**

**3.0 Abstract ..... 67**

**3.1 Introduction ..... 68**

**3.2 Data ..... 74**

**3.3 Methods ..... 75**

**3.4 Results ..... 82**

**3.5 Discussion ..... 83**

**3.6 Conclusions ..... 87**

**3.7 Acknowledgements ..... 87**

**Chapter 4: Active Protothrusts and Fluid Highways: Seismic Noise Reveals Hidden Subduction Dynamics in Cascadia ..... 89**

**4.0 Abstract ..... 89**

**4.1 Introduction ..... 89**

**4.2 Materials and methods ..... 93**

**4.3 Results ..... 101**

**4.4 Discussion ..... 107**

**4.5 Acknowledgement ..... 113**

**Chapter 5 Conclusions ..... 114**

**Chapter 6 Future Work ..... 115**

References…..... 116

Appendix A: Supplementary Materials for Chapter 2 ..... 167

Appendix B: Supplementary Materials for Chapter 3 ..... 190

Appendix C: Supplementary Materials for Chapter 4 ..... 209

**Acknowledgements**

This dissertation is the culmination of many years of meticulous work, difficult conversations, and, above all, a deep desire to understand the planet we call home. To those who have shared their love of the scientific process and their commitment to protecting lives from the forces of nature, thank you for inspiring me every single day.

It would be impossible to name everyone who has shaped this work. I am grateful to my committee, my friends, Wilcock lab group, my cohort, and my colleagues across the School of Oceanography, Arthur Nowell, and the Denolle Lab, whose kindness and support carried me through even the most uncertain days. Above all, I thank my advisor, William Wilcock, whose guidance challenged me to become a better scientist and whose patience taught me lessons I will carry for the rest of my career. During the isolating years of the pandemic, when so much felt still, his steadfast commitment gave me the resolve to keep going.

To my friends and family, whose love through this long and winding journey kept me grounded: I could not have done any of this without you. To Tony Dimauro, my high school physics teacher who inspired me to become a geophysicist; to Candace Eldridge, who supported me through community college; and to Adam Skarke, who made me curious about geophysical processes beneath the ocean, thank you all for helping me fulfill my dream of becoming a scientist.

*As a child, I wandered through the natural world with wide eyes and endless questions, each answer only opening the door to something deeper. It was Arthur C. Clarke's Richter 10 that first set my imagination ablaze, planting a dream that has never left me: to one day build a digital twin of our planet, a living replica capable of recreating the full symphony of Earth's processes. But it was the Indian Ocean tsunami of 2004 that transformed that dream from fantasy into purpose. I watched the ocean, something I had known my whole life as a source of beauty and wonder, become an unrecognizable force of destruction, reshaping coastlines and communities in minutes. The earth had spoken, and we had not understood it in time. That failure haunted me, and it fueled in me a need not just to marvel at our planet but to listen to it, to learn its language well enough that we might one day hear what it is trying to tell us before it is too late. I have not yet reached that horizon, but this dissertation is a step along the path, a small stone laid toward something far greater than itself.*

## Chapter 1: Introduction and Organization of the Dissertation

Knowledge of plate boundary deformation is fundamental to understanding tectonic processes. Plate tectonics, as the key mechanism shaping Earth's surface, involves a limited number of rigid plates moving relative to one another, generating convergent, divergent, and translational movement concentrated at plate boundaries. This process recycles Earth's lithosphere and manifests as the Wilson Cycle, wherein continental extension leads to the breakup of landmasses and the formation of rift zones that eventually evolve into ocean basins, and ultimately the closure of ocean basins through subduction and continental collision (Wilson et al., 2019). Over timescales of decades to centuries, accumulated strain at boundaries can release through large magnitude earthquakes (Satake & Atwater, 2007). Plate boundary deformation reflects the evolution of this cycle through spatial and temporal patterns of tectonic stress accumulation and release over millions of years. In addition to rapid strain release in earthquakes and slow interseismic strain accumulation, deformation may also be accommodated by transient magmatic processes such as dike intrusion, volcanic inflation, and deflation, particularly in extensional and volcanic plate boundary settings. Therefore, the ability to measure both rapid strain release in earthquakes and slow strain accumulation is essential for understanding plate boundary deformation and tectonic processes.

In terrestrial settings, we now have tools to measure spatiotemporal accumulation and release of strain. Seismic networks have long been able to detect strain release during earthquakes and volcanic eruptions (McNutt, 2002; Romanowicz et al., 1993). However, seismicity alone can only resolve a portion of the strain field and detecting inter-seismic deformation and aseismic slip is not possible with seismic data because these styles of deformation do not generate

seismic waves (Avouac, 2015; Kanamori, 1977). Geodetic measurements of areal strain, either from Ground Positioning Systems (GPS) and Synthetic Aperture Radar (SAR) observations have been a revolution of the late 20th century that gave rise to space-based geodetic techniques that can resolve the full strain field (Bürgmann & Thatcher, 2013; Thatcher, 2009). Together, these technologies enable precise measurements of ground deformation, capturing both gradual strain accumulation and aseismic movements, thus providing a more complete picture of tectonic processes.

In contrast, observations of deformation in the ocean are more challenging. While seismic observations are limited by spatial coverage, these have been partially overcome through advances in ocean-bottom seismometers (OBS), improving our understanding of subduction zones (e.g., Morton et al., 2018; Obana & Kodaira, 2009), mid-ocean ridges (Tolstoy et al., 2008; Weekly et al., 2014), and submarine volcanoes (Maya Tolstoy et al., 2002; Wilcock et al., 2016). Geodesy is more challenging in the oceans because traditional satellite-based geodetic techniques are ineffective underwater due to their dependence on radio waves (Bürgmann & Chadwell, 2014). This limitation necessitates the development of alternative geodetic methods for submarine settings such as pressure geodesy (Fredrickson et al., 2019; Nooner & Chadwick, 2016), GNSS-acoustic positioning (Gagnon et al., 2005; Sun et al., 2014; Yokota et al., 2016), and direct-path acoustic ranging (McGuire & Collins, 2013; Petersen et al., 2019). However, the challenges of sustaining long-term deployments results in sparse and intermittent geodetic observations (Petersen et al., 2019). Moreover, complex oceanographic phenomena can introduce  may obscure subtle deformation signals. For example, ocean circulation affects pressure changes recorded by ocean-bottom pressure sensors (Dobashi & Inazu, 2021), while sound speed heterogeneities from

hydrothermal activity and water mass mixing impact acoustic ranging (Chadwell & Sweeney, 2010; Hannemann et al., 2017). All these seafloor geodetic techniques require further refinement. Due to the lack of direct observations, deformation patterns for strain cycles at submarine plate boundaries are often indirectly inferred using methods such as tomography and ambient noise interferometry. Tomographic studies reveal the cumulative effects of tectonic deformation through seismic velocity observations (Arnulf et al., 2018a; Li et al., 2021; Zhao & Hua, 2021). Ambient noise interferometry offers a powerful means to infer spatiotemporal variations in seismic velocity structure. It has been used to detect deformation in submarine settings resulting from various events, such as earthquakes (Ikeda & Tsuji, 2018; Taira et al., 2015), slow slip events (Tonegawa et al., 2022a; Uemura et al., 2018; W. Wang et al., 2022), and volcanic inflation (Lee et al., 2024).

A central question to be addressed in this thesis is: How is deformation accommodated within strain cycles at submarine plate boundaries. This dissertation presents three studies, each employing distinct geophysical methods to investigate the principal tectonic systems involved in the Wilson cycle: rifting, seafloor spreading, and subduction.

In chapter 2, I developed a three-dimensional tomographic model of Orca Volcano using active source tomography data and OBS deployments from the BRAnsfield VOlcanoes SEISmology (BRAVOSEIS) project (Almendros et al., 2020). In addition to the traditional P-wave tomography from Pg arrivals, we utilized secondary arrivals to improve imaging of the magma chamber. The resultant model, encompassing the magma chamber, volcanic edifice, and adjacent rift zones, provided a means to investigate how magmatism and distinct rifting styles influence deformation processes in continental rift systems. A high-quality tomographic image in a critical location within the basin, combined with prior geochemical observations, enabled me to uncover

basin scale processes that would have otherwise gone unnoticed. This work was accepted for publication in the *Journal of Geochemistry, Geophysics, Geosystems* (Kidiwela et al., 2026a).

In chapter 3, I analyzed three years of horizontal acoustic ranging observations across the caldera of Axial Seamount on the Juan de Fuca Ridge, to constrain the partitioning of strain between distributed volumetric inflation and slip on caldera ring fault. Axial Seamount is a hotspot volcano that has been monitored through three eruptive cycles with extensive vertical geodetic observations documenting repeated inflation and deflation, yet models based on vertical motions alone cannot constrain how the deformation is partitioned between fault slip and volumetric inflation (Hefner et al., 2020; Nooner & Chadwick, 2016; S. R. Slead et al., 2024). To constrain the horizontal deformation field, three seafloor transponders were deployed in the western, central-northern, and eastern caldera, together with a fourth cabled transponder in the central caldera.. Despite the failure of the cabled transponder, I was able to combine the three available baselines across the caldera with vertical geodetic data, were sufficient to constrain a non-unique set of inflation-source models consistent with the observed uplift and extension. This work is being prepared for submission to *Geophysical Research Letters.*

In chapter 4, I used a decade of continuous ambient seismic data from two cabled seafloor observatories on the Cascadia Subduction Zone to identify distinct regional variations in subduction dynamics through seismic velocity variability. I investigated whether there is evidence for interseismic strain release in the shallow portion of the plate. Geodetic models derived from onshore data (Li et al., 2018a; Schmalzle et al., 2014; Yousefi et al., 2020) and preliminary offshore geodetic data (DeSanto et al., 2022) suggest that the shallow plate interface in Cascadia is locked from the coast to the trench along most of the margin. However, the lack of studies seeking to observe shallow seismicity and shallow slow slip, precludes a complete understanding of the

locking state at these depths (Kelin Wang & Tréhu, 2016). Our results uncover complex interactions between strain accumulation, fault slip, and fluid migration within a shallow subduction zone. This work is published in *Science Advances* (Kidiwela, et al., 2026b).

## Chapter 2: Late-Stage Rift Evolution at Back Arc Basins: Insights from a Tomography Experiment at Orca Volcano, Bransfield Basin

**Maleen Kidiwela[1], William S. D. Wilcock[1], Dax C. Soule[2,3], Javier Almendros[4]**

[1] School of Oceanography, University of Washington, Seattle, WA, United States

[2] School of Earth and Environmental Sciences, City University of New York - Queens College, New York, NY, United States

[3] City University of New York Graduate Center, New York, NY, United States

[4] University of Granada, Granada, Spain

### 2.0 Abstract

Back-arc basins provide insights into the processes governing the evolution of continental rifting to seafloor spreading. The Bransfield basin hosts a back arc rift that is hypothesized to be in the late stages of this transition. Orca volcano is a submarine volcano that lies on the most evolved portion of the rift. It coincides with a transition in rifting style from a clearly delineated magmatic rift to the southwest to a wide and deeper faulted graben with thicker sediment to the northeast. We conducted an active-source tomography experiment to image the three-dimensional isotropic and anisotropic P-wave velocity structure of the upper crust of Orca Volcano. We developed a method to incorporate secondary arrivals to improve the imaging of the volcano's magma chamber. The magma chamber extends from ~1 km beneath the seafloor to 3-4 km depth with a maximum melt fraction of 16-41% and a melt volume of 0.8-2.3 $km^3$.The southwest rift of Orca volcano is characterized by a narrow zone of low velocities that connects to the magma chamber and by strong rift parallel anisotropy at shallow depths. Its structure has similarities to a slow spreading ridge consistent with a rift that is transitioning to seafloor spreading. Extension to the northeast of Orca is more distributed and not clearly linked to the volcano. We infer that the change

in extensional style results from a more hydrated and weaker mantle to the northeast that may be caused by a tear in the Phoenix slab and a consequent change in slab depth.

## 2.1 Introduction

Continental rifting plays a fundamental role in plate tectonics because it can lead to the formation of new ocean basins. While significant progress has been made in understanding rift evolution, the scarcity of locations where the transition from rifting to seafloor spreading can currently be observed impedes our understanding of these processes. Many key questions remain about the processes governing the transition from continental rifting to seafloor spreading and why only some rifts evolve to this stage (Brune et al., 2023; Liao & Gerya, 2015; Ruppel, 1995). In particular, our knowledge of the timescales of magmatism and faulting during rift evolution, as well as the mechanisms initiating mid-ocean ridge development, is still limited (Brune et al., 2023; Ebinger et al., 2013; Pagli et al., 2015).

One of the key processes controlling the evolution of rifts is the level of magmatism. In magma rich settings, initial deformation is coupled from the upper-crust to the mantle through narrow shear zones in the lower-crust, leading to relatively rapid crustal thinning and mantle uplift and the localization of extension (Cochran, 2005; Ebinger & Casey, 2001; Huismans & Beaumont, 2011; Sutherland, 2006; Watanabe et al., 2010). On-axis volcanism creates focused spreading sites that can rapidly grow and coalesce into a continuous spreading axis (Cochran, 2005; El Khrepy et al., 2021). Conversely, in magma-poor rifts, extension is accommodated through the coupled stretching of crust and lithospheric mantle beneath isolated magmatic zones and decoupled deformation assisted by fluids from deeper asthenospheric melts (Njinju et al., 2019). Where the lower-crust is weak and hydrous, initial deformation is characterized by viscous thinning of the

lower-crust over a broad area, decoupling deformation between the upper-crust and mantle and leading to comparatively slow rates of crustal thinning and mantle uplift. This slow thinning results in the formation of a wide system of horsts and grabens (Buck, 1991; Cameselle et al., 2020; Deng et al., 2020).

The processes result in two distinct types of rifted passive margins: volcanic passive margins (VPM) and non-volcanic passive margins (NVPM) (Geoffroy, 2005; Michael et al., 2003; Wilson et al., 2001). VPMs record intense magmatism and elevated mantle temperatures that can be linked to plume impact, while NVPMs reflect slow extension, delayed magmatism, and a reliance on brittle faults to accommodate strain. Although NVPMs eventually develop magmatism to form new oceanic crust at mid-ocean ridges, the timing and volume of melt emplacement differ significantly from VPMs (Conder, 2022; El Khrepy et al., 2021). Since magma-rich environments tend to localize deformation, they promote simple shear, whereas magma-poor environments involve more complex deformation patterns with components of pure shear (Bosworth & Stockli, 2016; Stockli & Bosworth, 2019; Wernicke, 1985). Importantly, variations between magma-rich and magma-poor conditions can occur over small spatial scales, leading to alternating styles of deformation along a rift system (Frizon de Lamotte et al., 2015; Shillington et al., 2009).

Back-arc basins serve as valuable analogs for breakup of continental crust in mid-plate settings. These basins form by slab rollback in subduction zones, where the subducting plate sinks away from the overriding plate (Dewey, 1980; Molnar & Atwater, 1978; Uyeda & Kanamori, 1979). The stresses from slab rollback are influenced by the steepness of the subducting slab, with steeper slabs tending to result in more extension of the upper plate (Brune et al., 2023). Compared to back-arcs formed by ocean-ocean plate convergence, continental-ocean back-arcs, which

generally have shallow subduction (<45 degrees) of young (<40 My) buoyant oceanic plates, are less likely to transition to seafloor spreading due to inefficient mantle convection and slab rollback (Artemieva, 2023).

Geochemical studies in back-arc magmas show that the subduction signature in their trace elements and the water content grows stronger with arc proximity (Arai & Dunn, 2014; Pearce & Stern, 2006). Many studies of back-arc magmatism have shown the importance of mantle hydration from slab fluids for basin evolution (Arai & Dunn, 2014; Harmon & Blackman, 2010; Hawkins & Melchior, 1985). Martinez et al., (2018) and Sleeper et al., (2021) argue that the increased water content with arc proximity, along with slower spreading rates, promotes a change from focused to distributed seafloor spreading.

In this study, we utilize seismic tomography to constrain the three-dimensional variations in the isotropic and anisotropic velocity structure of the upper-crust beneath Orca Volcano and its environs in the back-arc Bransfield Basin. Orca volcano lies on the Bransfield back-arc continental rift at a site where there is a sharp along-axis change in the morphology of the rift and where it has been hypothesized that the rift is transitioning to seafloor spreading. Our results provide insights into the magmatic structure beneath Orca Volcano and the adjoining rifts. We interpret our results in terms of the transition from continental rifting to seafloor spreading and the impacts of slab geometry on rift morphology and evolution.

**2.2 Background**

Bransfield Basin is a back-arc basin located between the South Shetland Islands and the Antarctic Peninsula (Figure 1). Subduction of the Phoenix plate beneath the Antarctic Peninsula since >200 Ma led to the formation of the South Shetland volcanic arc. From the late Cretaceous

to Cenozoic, the western segments of the now extinct Antarctic-Phoenix Ridge spreading center (Figure 1, inset) were sequentially subducted beneath West Antarctica, effectively welding the oceanic crust to the Antarctic plate (Eagles & Jokat, 2014; Larter & Barker, 1991). At about 4 Ma, the last ridge-trench collision occurred southwest of the Hero fracture zone (Barker, 1982) creating a slab window. At this time, spreading along the Antarctic-Phoenix Ridge to the northeast essentially stopped and subduction beneath the South Shetland Arc progressively slowed enabling the remainder of the Phoenix plate to slowly become part of Antarctica (Barker, 1982; Eagles et al., 2004; Larter & Barker, 1991; Lawver et al., 1996). The estimated present day convergence rate is only 0.25–0.75 cm/yr (Henriet et al., 1992); subduction appears to be ceasing (Lawver et al., 1995) with the slowly subducting young hot slab thermally assimilating at intermediate depths without generating deeper seismicity (Birkenmajer et al., 1990; Robertson Maurice et al., 2003). The decline in convergence rate coincided with the initiation of back-arc extension and the formation of the Bransfield Basin (Larter & Barker, 1991).

The Bransfield Basin is made up of three sub-basins that run southwest-northeast: the Western, Central, and Eastern Bransfield Basins (WBB, CBB and EBB, respectively) (Figure 1). The WBB is the least magmatically active among the three with faulted block structures indicative of early stage extension (Barker & Austin, 1998). The CBB is the most magmatically active based on the number of young volcanic structures (Gràcia et al., 1996) and covers an area of 200 km by 50 km, bounded by morphological steps at Deception and Bridgeman Islands. The EBB is characterized by four deep troughs with small scattered volcanic cones rather than the large, aligned edifices seen in the CBB (Gràcia et al., 1996).

Two mechanisms likely contributed to the formation on the Bransfield Basin. First, the creation of the slab window is believed to have facilitated slab rollback and back-arc extension

(Barker, 1982). Based on the presence of older (21 Ma), denser oceanic crust in the northeast portion of the Phoenix slab (Larter & Barker, 1991), Barker & Austin (1998) proposed that rollback extension propagated from the northeast to southwest. Second, left-lateral transtension associated with reorganization of the triple junction at the Shackleton Fracture Zone–South Scotia Ridge intersection (Figure 1 inset) would have augmented the extension from slab rollback in the northeast (Klepeis & Lawver, 1996; Lawver et al., 1996). Indeed, some researchers have suggested that this may be the sole mechanism for extension so that the Bransfield Basin is a marginal basin without the presence of slab rollback (Fretzdorff et al., 2004; González-Casado et al., 2000). Global Positioning System data are consistent with these models, where the WBB and CBB are extending in the northwest direction at rates of 2.3-3.0 mm/yr and 7.0 mm/yr, respectively, while the EBB basin moves with the Scotia Plate westward at 7.3 mm/yr (Taylor et al., 2008). Thus, the

CBB is opening faster than the WBB while the EBB basin moves with the Scotia Plate westward (Berrocoso et al., 2016; Dietrich et al., 2004; Taylor et al., 2008).

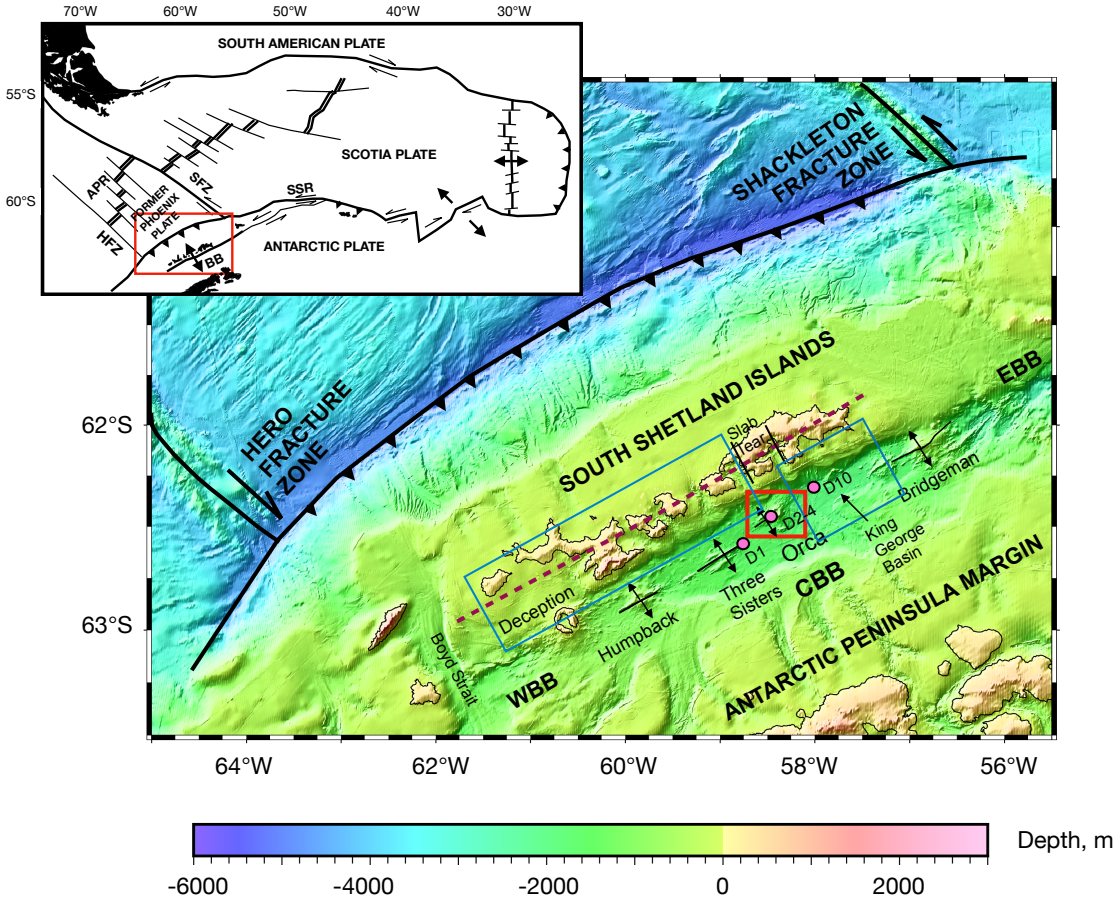


**Figure 1.** Bathymetric map of the Bransfield Basin. The map shows the volcanic features across the Bransfield Basin along the rift zone with spreading centers that are misaligned. WBB: Western Bransfield Basin, EBB: Eastern Bransfield Basin, CBB: Central Bransfield Basin. The red rectangle shows the area of Figure 2a centering on Orca Volcano. The maroon dashed line shows the P-wave receiver function analysis profile of Parera-Portell et al. (2023) with two black lines indicating the slab tear. Blue rectangles are the regions where we infer the slab is at the depths of 61-93 km, the depth of peak dehydration (Wada & Wang, 2009), calculated by extrapolating the

slab depths observed by Parera-Portell et al. (2023) with a slab dip of 30°. Labeled pink circles with a black outline are dredge station locations from R/V Nathan B. Palmer cruise 93-01 (Keller et al., 1994) labeled by the dredge number in the cruise. The inset map shows the Scotia plate region between South America and the Antarctic Peninsula, showing area of the main figure (red box) and the main tectonic units and interactions with features labeled as follows: BB - Bransfield Basin, HFZ - Hero Fracture Zone, APR - Antarctic Phoenix Ridge, SFZ - Shakleton Fracture Zone, SSR - South Scotia Ridge.

However, neither the propagating extension or marginal basin models fully explain crustal thickness observations and geochemical evidence in the CBB. Northeast to southwest propagation would require the thinnest crust and most evolved magmas in the northeast. Seismic measurements along the axis of the basin show that the smallest sediment-corrected crustal thickness of ~10 km is found at Orca Volcano near the middle of the CBB with the crust thickening within the CBB by 5-10 km to the southwest and several kilometers to the northeast (Christeson et al., 2003; Li et al., 2021). Geochemical data from dredges along the rift show no systematic variation that supports northeast to southwest propagation, Instead, lavas with the least evolved compositions closest to mid-ocean ridge basalts (MORBs) are found near Orca and Three Sisters volcanoes (Keller et al., 2002) in the middle of CBB. These observations led Galindo-Zaldívar et al. (2006) to infer that extension is greatest in the middle of the basin with the CBB opening outward.

Recent work has integrated these observations into a more nuanced framework. In line with the idea of incorporating both transtension in the EBB and the rollback of the Phoenix plate (Barker & Austin, 1998; Klepeis & Lawver, 1996; Lawver et al., 1996), Li et al. (2021) proposed that the collision between the Phoenix plate and the Antarctic plate southwest of the Hero Fracture Zone, caused forearc rotation of the South Shetland block, promoting greater extension in the northeast

region of the CBB compared to the southwest. Recent receiver function studies (Parera-Portell et al., 2023) have revealed the existence of a slab tear underneath Orca volcano; the slab is 15 km shallower to the northeast of a ~20 km gap. Parera-Portell et al., (2023) argue that the tear marks a transition between regions with different degrees of extension, with increased slab pull, a deeper Moho beneath the arc, and more symmetrical extension southwest of the tear, leading to the highest rates of extension in the middle of the CBB.

The CBB exhibits pronounced along-axis variations in crustal structure and morphology that reflect the progressive stages of back-arc rifting. The crustal thickness is asymmetric across the CBB, decreasing sharply offshore across the narrow margin of the South Shetland Islands, but only gently over the wider margin off the coast of the Antarctic Peninsula (Christeson et al., 2003). The CBB widens and deepens towards the northeast in morphological steps at Three Sisters and Orca Volcano (Barker et al., 1988; Christeson et al., 2003; Gràcia et al., 1996), with a particularly abrupt change in rift morphology occurring at Orca Volcano where the structure transitions from an axial high to a deeper sedimented plain forming the King George Basin (Figure 1). The volcanic processes in the CBB occur along a neo-volcanic zone aligned perpendicular to the extension direction (Figure 1), herein referred as the "rift", which is delineated by a shallow zone of anomalously high magnetization (Catalán et al., 2013). As a result of the high rate of sediment supply (Prieto et al., 1999), the average basement depth in the neo-volcanic zone is 1.5 km. Despite substantial crustal thinning in the CBB, the basin is not underlain by normal-thickness oceanic crust, leading to the inference that ocean spreading has not yet begun (Barker et al., 2003). However, based on gravity and magnetic data (Catalán et al., 2013) and active (Barker & Austin,

1998) and passive (Li et al., 2021) seismic studies, several authors argue that the CBB is transitioning to oceanic spreading.

Multiple lines of evidence demonstrate that this rift is segmented. These include clear offsets between the neo-volcanic spreading center (Gràcia et al., 1996; Grad et al., 1992) (Figure 1) and associated magnetic and gravity anomalies (Catalán et al., 2013), along-axis changes in depth and morphology of the rift (Gràcia et al., 1996), and seismic velocity (Christeson et al., 2003). These segment boundaries are not correlated with the horst and graben structures in the Antarctic Peninsula margin that predate the basin's formation, but are instead a consequence of rifting (Christeson et al., 2003). The observed seismicity along the Bransfield rift is discontinuous and consistent with a set of offset segments rather than a continuous, linear rift (Almendros et al., 2020; Dziak et al., 2010). The nature of this segmentation becomes increasingly complex in the northeast CBB where the bathymetry deepens along the neo-volcanic zone, without a clear indication of the rift, suggesting the presence of distributed extension rather than focused rifting in this segment (Gràcia et al., 1996).

Orca Volcano is a prominent volcanic feature that coincides with a marked transition in rifting style within the CBB (Almendros et al., 2020; Gràcia et al., 1996; Lawver et al., 1995). Rising about 1 km above the seafloor, it has a 3 km by 4 km caldera that is 300-500 m deep and elongated across the rift (Figure 2a). The bathymetric features around the volcano include two sub-parallel volcanic ridges extending outward from the southwest and west sides of the caldera and four closely spaced ridges extending to the northeast from a breach in the caldera wall on the north side of the volcano. Christeson et al. (2003) observed high upper-crustal velocities, with values as high as 6.0 km/s at ~2 km depth beneath Orca and Three-sisters to the southwest, indicating a narrower zone of volcanically influenced basement than the northeastern portion of the basin. To

the northeast of Orca, the basin is a heavily-faulted, deep graben with thick sediment (Barker & Austin, 1998). Fresh basalts, including fresh glass have been dredged on and near the volcano. The geochemical analyses of samples along the neovolcanic zone shows a general northeastward change from more MORB-like to arc-like with Orca volcano having the least arc-like samples (Keller et al., 2002).

Recent seismic activity demonstrates ongoing active processes at Orca Volcano. Beyond previously documented seismicity (Dziak et al., 2010; Kaminuma, 2001; Robertson Maurice et al., 2003), a swarm of approximately 85,000 earthquakes occurred northeast of the volcano from August - November 2020, indicating a northeast propagating dike that is likely an ongoing volcano-tectonic process associated with rifting (Cesca et al., 2022; Loureiro Olivet et al., 2021).

### 2.3 Experimental Geometry and Data

As part of the Bransfield Volcano Seismology (BRAVOSEIS) project (Almendros et al., 2020), we conducted a tomographic experiment on Orca Volcano and the ridges extending to the west and southwest (Figure 2) using 16 ocean bottom seismometers (OBSs), each equipped with a three-component seismometer and hydrophone. Fifteen instruments were US short-period Ocean Bottom Seismograph Instrument Pool (OBSIP) seismometers, and 1 was a German Instrument Pool for Amphibian Seismology (DEPAS) broadband OBS (Schmidt-Aursch & Haberland, 2017). The network had an instrument spacing of 3-4 km around the volcano with 3 OBS in the caldera area ~1.5 km apart. For the tomography experiment, a total of 2426 air gun shots were fired with a 6-gun 2540-cubic-inch (41.6 l) array. Shots were spaced 200 m apart along shot lines totaling 485 km in length. Most shots were on 21 lines (T1-29) oriented southwest-northeast. Each line was 21 km long and they were spaced 0.5 to 1 km apart with the highest shot density above the

caldera and the southwest ridge (Figure 2b). To generate deeper ray paths from the northeast, tomography shots were also obtained along two curved lines (T31-36) running southeast-northwest.

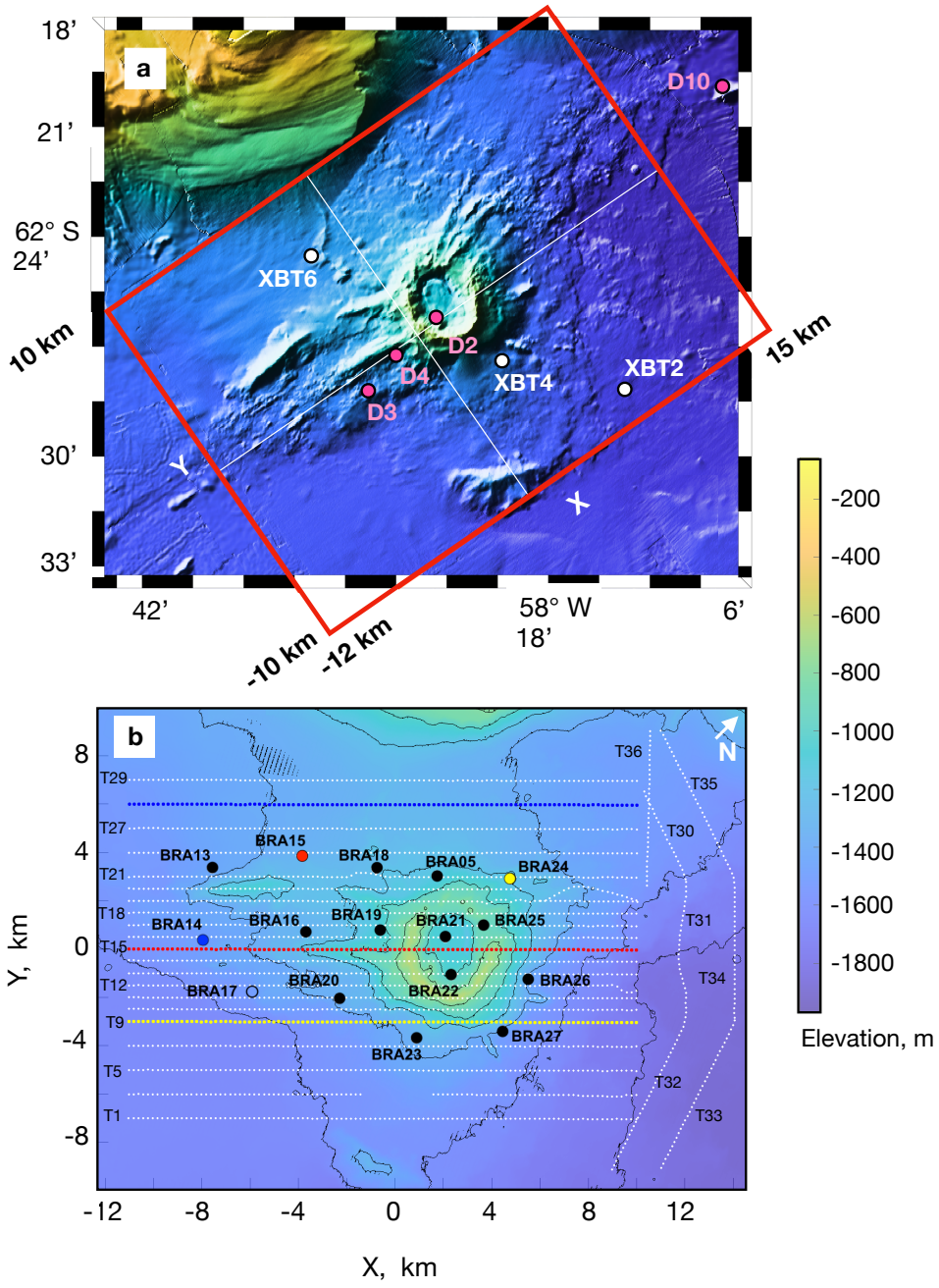

**Figure 2.** (a) Bathymetric map of Orca Volcano illuminated from the northwest. The red box shows the area covered by the tomography model and is labeled with the *x*-*y* coordinates. It has a rotation of 36° counterclockwise relative to geographic coordinates and an origin shown by the intersection of thin white lines at 58.4400°S, 62.4413°W. Expendable Bathythermograph (XBT) locations are marked as white circles and plotted in Figure S1. Labeled pink circles with a black outline are dredge station locations from Keller et al. (1994). (b) Bathymetric map of the area covered by the tomography model showing OBS locations (circles) and tomographic shots (white dots). The open circle shows station BRA17, which was not recovered. Tomographic lines are labeled from T1-T36 (even-numbered lines are missing where the line spacing increases from 0.5 km to 1 km). The blue, red, and yellow symbols delineate the OBSs and shots for the record sections shown in Figures 3a, b, and c, respectively.

Most of the ocean bottom seismometers produced high-quality data despite a few technical issues. Station BRA17 was not recovered (Figure 2b). Of the remaining OBSs, 13 of 15 yielded good-quality data on both the hydrophone and vertical channels. The seismometer on BRA27 did not deploy correctly, and the hydrophone channel on BRA24 was noisy. The OBS locations were determined by inverting 8394 manually picked water wave arrivals for shots within 5 km of each OBS using a water velocity of 1456 m/s (Creager & Dorman, 1982). More details are provided in Supporting Information Text S1,Table S1 and Figure S1.

Most of the data show clear crustal Pg arrivals (Figure 3a). In map view the intersection of straight paths between shot and receiver for records with attenuated Pg are consistent with the shadow zone from a shallow magma body centered beneath the caldera (Figure S2). Within the

shadow zone, there is a secondary delayed arrival (Figure S3), which we term Pmc (P magma chamber), that is emergent and often has a low amplitude (Figure 3b-c).

Arrival times were picked manually using the vertical and hydrophone channels. For 10 OBSs, we were able to improve the signal to noise for picking by summing these two channels which have similar amplitudes in digital units. For the other 5 OBS we picked on a single channel (the hydrophone for BRA22, BRA25, BRA26 and BRA27 and the vertical channel for BRA24) because the other channel was noisy. After applying a 5-30 Hz $4^{th}$ order minimum-phase Butterworth bandpass filter, we picked all Pg arrivals with an iterative strategy. We first picked the clearest impulsive Pg arrivals at shorter ranges and inverted for a preliminary 3-D velocity model. We used the predicted Pg arrival times for this 3-D model to flatten the record section so that distant arrivals were more visible and picked additional times using consistent criteria and conservative uncertainties. We repeated the process several times until all the Pg arrivals visible in the data were picked. The total number of Pg arrival picks is 25567.

The Pmc arrivals, which have a dominant frequency of 12-14 Hz, were picked after applying a $4^{th}$ order minimum-phase Butterworth 10-20 Hz bandpass filter. Comparisons with the 5-30 Hz bandpass filter used for Pg arrivals showed that this filter did not change the times of picks but improved the signal to noise. To aid in phase identification, the Pmc arrivals were picked on record sections that were flattened with the predicted Pg arrivals times from our final Pg isotropic model. For most records, the onset of the $1^{st}$ and $2^{nd}$ cycles was difficult to identify except at shorter ranges because of low signal-to-noise ratio (Figure S4), so our approach was to pick the start of the $3^{rd}$ cycle on all records and to pick the $1^{st}$ and $2^{nd}$ cycles when clearly visible. We determined mean offsets of $76 \pm 5$ ms for the 125 Pmc arrivals picked on the $1^{st}$ and $2^{nd}$ cycles and $75 \pm 8$ ms for 581 Pmc arrivals with picks on the $2^{nd}$ and $3^{rd}$ cycles (Figure S4). These mean offsets

were then used to correct the earliest Pmc pick on each record to the onset time. From our preliminary 3-D Pg-Pmc inversion, we found that a small proportion of Pmc picks had large residuals consistent with our misidentifying their cycle and after inspecting the record sections, we

adjusted the picks accordingly. A total of 4439 Pmc arrivals were obtained for the 11 stations with this phase.

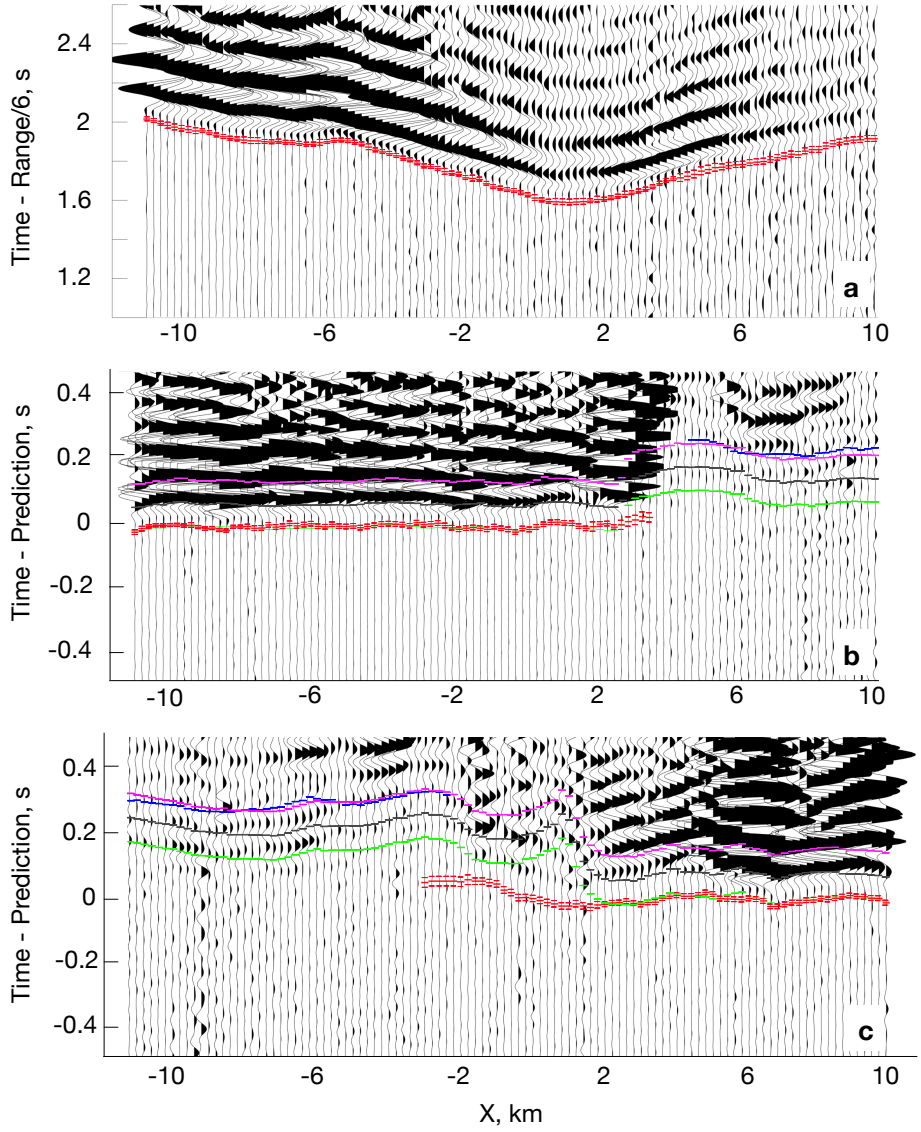


**Figure 3.** Example record sections showing (a) Line T28 on station BRA14 (blue symbols in Figure 2) plotted with a reduction velocity of 6 km/s (b) Line T15 on BRA15 (red symbols on Figure 2) relative to the predicted Pg arrival and (c) Line T9 on BRA24 relative to the predicted Pg arrivals (along yellow symbols on Figure 2). The record sections are filtered with a 4$^{th}$ order

minimum-phase Butterworth 10-20 Hz bandpass filter. They show picked Pg (red) with assigned uncertainties (thin red line) and Pmc on the start of the 3rd cycle (blue) and predictions for the Pg-Pmc isotropic model presented in section 5.2 for Pg (green) and Pmc for the onset (green) and the start of the 2nd (black), and 3rd cycles (magenta).

Pick uncertainties were estimated visually, with larger uncertainties assigned to waveforms with significant trace-to-trace variability or low signal-to-noise ratios. About 43%, 31% and 26% of Pg picks were assigned uncertainties of 10, 15 and 18 ms, respectively. Pmc arrivals are harder to pick, and we assigned uncertainties of 15 ms to the 3% of Pmc arrivals that are visible on the first cycle, 20 ms to the 11% of Pmc arrivals visible on the 2nd cycle, and 25-30 ms to remaining Pmc arrivals that are only visible on the 3rd cycle.

### 2.4 Method

We used a three-dimensional tomographic technique to invert travel times for isotropic slowness and seismic anisotropy (Dunn et al., 2005; Toomey et al., 1994) that forward models ray paths using a shortest path (in time) algorithm based on graph theory (Moser, 1991). We created three tomography models, isotropic models from inversions of only Pg picks and from both Pg and Pmc picks, and a third anisotropic model from only Pg picks.

#### 2.4.1 Forward Problem

The model volume measures 27 km x 20 km x 10 km and is rotated 36° counterclockwise relative to geographic coordinates so that the X-axis parallels the southwest ridge and the shot line orientation (Figure 2). The origin is centered on the southwest flank of the caldera (Figure 2a). For the forward problem, slowness nodes are spaced 200 m apart on a cubic grid. To parameterize the anisotropic medium, we followed the approach of Dunn et al. (2005).

Pg arrivals were forward modeled directly from the shortest paths obtained from graph theory (Moser, 1991). Seafloor topography was incorporated by vertically shearing nodes to follow the seafloor (Toomey et al., 1994). When seismic waves encounter a sizeable low-velocity body, the wavefront scatters around the body and heals in its wake leading to delayed first arrivals with lower amplitudes (Paulatto et al., 2022). However, because the first arriving energy does not propagate through the body, travel time tomography using just these arrivals will underpredict the amplitude of the low velocity body. This limitation can be addressed by considering secondary arrivals that pass through the body. At Newberry volcano, Beachly et al. (2012) used finite difference waveform modeling to show that decreased first arrival amplitudes and a secondary arrival required a sizeable magma chamber that was poorly resolved by Pg travel time tomography. Here we incorporate secondary magma chamber (Pmc) arrivals into the travel time tomography by forcing the paths for these arrivals to pass through a preassigned magma chamber volume. This is an extension of the approach used to model secondary arrivals that diffract below the magma lens at the East Pacific Rise (Dunn et al., 2000).

The shortest path method requires modification for secondary arrivals. At the East Pacific Rise, Dunn et al., (2000) modeled arrivals that passed below an axial magma lens by introducing a volume of high slowness above it to block faster paths in this region. We employed a similar approach but with a 3-D blocking geometry by forcing the paths for these arrivals to pass through a preassigned magma chamber volume. We considered a range of magma chamber sizes parameterized by an elliptical conical frustum overlying an elliptical cylinder (Figure 4). Pg rays are forward modeled by assigning high slownesses to the magma chamber so that rays travel around it. Pmc rays are forward modeled by including an 0.6 km (3 nodes) thick blocking curtain of high slowness above and to both sides of the magma chamber volume, extending perpendicular

to a horizontal line connecting the station to the center of the caldera. This approach requires a different slowness model for each station but is easily accommodated for the shortest path method since it computes all the travel times for each station separately in a procedure that is commonly parallelized. We use a line integration to get the slowness along each ray segment rather than endpoint averaging to prevent ray segments from crossing over the blocking regions.

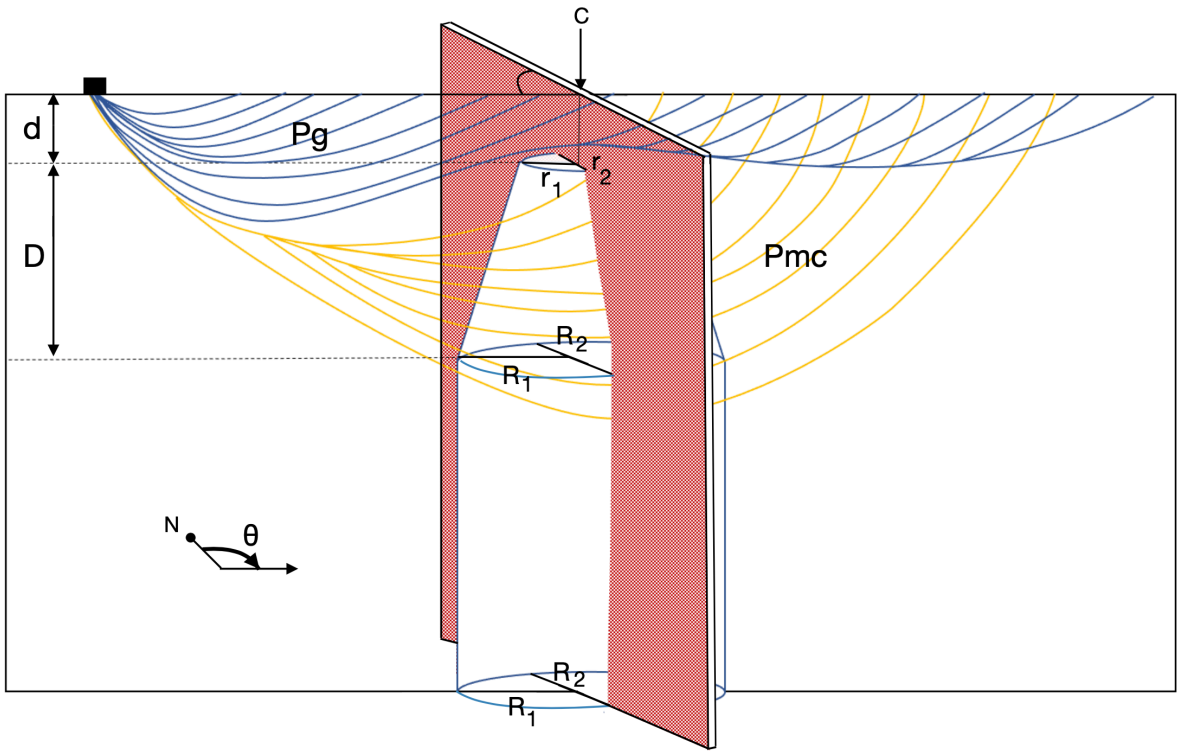


**Figure 4.** Cartoon illustrating the method used to model Pg (blue) and Pmc (yellow) ray paths in the magma chamber volume for the joint inversion of Pg and Pmc arrivals. The magma chamber is represented by an elliptical conical frustum on top of an elliptical cylinder with the geometry defined by an azimuth measured clockwise from north, of the major axis $q$, the depths to the top, $d$, and the base, $D$, of the frustum, and dimensions $R_1$, $R_2$, $r_1$, $r_2$, where subscripts 1 and 2 denotes the major and minor axes of the ellipse, respectively. Pg arrivals are forward modeled after setting the slowness within the magma chamber high so that shortest paths in time do not pass through it.

Pmc arrivals are forced through the magma chamber (Figure S3) by adding a 0.6 km thick blocking curtain of high slowness outside the magma chamber volume (brown shading) oriented perpendicular to the horizontal line connecting the station being modeled to the center of the blocking region (labeled C in Figure 2a) which lies near the center of the caldera (X = 2 km, Y = 0 km). Preferred values for the magma chamber geometry were determined to be $\theta$ = 36°, $R_1$ = 3 km, $R_2$ = 2.5 km, $r_1$ = 0.6 km, $r_2$ = 0.5 km, $d$ = 1 km, $D$ = 4 km, X = 2 km and Y = 0 km.

### 2.4.2 Inverse Problem

We inverted the travel time data for isotropic slowness and seismic anisotropy (Dunn et al., 2005; Toomey et al., 1994) using a cubic 0.5 km x 0.5 km x 0.5 km perturbation grid, employing both jumping and creeping strategies (Shaw & Orcutt, 1985). The isotropic inversions minimize a functional of the general form:

$$s^2 = \Delta \boldsymbol{t} \boldsymbol{C_d^{-1}} \Delta \boldsymbol{t} + \lambda_p (\Delta \boldsymbol{m_i})' \boldsymbol{C_m^{-1}} (\Delta \boldsymbol{m_i}) + \lambda_V (\Delta \boldsymbol{m_i})' \boldsymbol{C_V^{-1}} (\Delta \boldsymbol{m_i}) + \lambda_H (\Delta \boldsymbol{m_i})' \boldsymbol{C_H^{-1}} (\Delta \boldsymbol{m_i}) \qquad (1)$$

In the first term, the vector of differences between observed and predicted travel times, $\Delta \boldsymbol{t}$ is minimized with respect to $\boldsymbol{C_d}$, a diagonal matrix of the arrival-time variances. The second term damps changes to the model, $\Delta \boldsymbol{m}$ based on the diagonal matrix of the a priori model variance, $\boldsymbol{C_m}$ with a weight $l_p$. The third and fourth terms apply vertical and horizontal Gaussian smoothing to the model changes through matrices $\boldsymbol{C_V}$ and $\boldsymbol{C_H}$ with weights $l_V$ and $l_H$. The inversion incorporates separate damping and smoothing weights for isotropic and anisotropic model parameters, with the notation $l_{Ap}$, $l_{AV}$ and $l_{AH}$ for anisotropic weights.

When utilizing a creeping strategy, $\boldsymbol{Dm_i}$ stores the perturbation of the current iteration, $i$. In a jumping strategy, $\boldsymbol{Dm_i}$ is replaced by a vector of cumulative perturbation to the isotropic slowness and anisotropic model parameters from previous iterations. Consequently, using a

jumping strategy perturbs the model relative to the starting model, while the creeping strategy perturbs the model relative to the previous iteration (Shaw & Orcutt, 1985).

Following Weekly et al. (2014) and Heath et al. (2019) we adopted a multi-stage inversion approach. First, we inverted our data for a one-dimensional velocity model (Figure 5) using a starting model that was extracted from Line 2 of the regional refraction experiment of Christeson et al. (2003). Second, using this starting 1-D velocity model and employing a jumping strategy, we inverted the data for a three-dimensional isotropic model with $l_p = 1$, $l_V = 200$, $l_H = 300$, the same parameters used by Weekly et al. (2014). We obtained a smoothed approximation to the long wavelength isotropic structure by applying a three-dimensional Gaussian filter with standard deviations of 1.6 km, 1 km, and 0.2 km in the X, Y, and Z directions, respectively. A long wavelength starting model is useful in heterogeneous regions to prevent smoothing from working against longer wavelength features when exploring a range of smoothing weights to fit short wavelength features (Weekly et al., 2014). The larger smoothing length scale in the X than the Y direction accounts for the elongation of features parallel to the rift.

This long wavelength model was used as the starting model for the third inversion step for Pg isotropic, Pg-Pmc isotropic and Pg anisotropic models. For the Pg isotropic model, we employed a jumping strategy and explored a variety of smoothing and damping weights to generate trade-off L-curves (VanderBeek & Faccenda, 2021) in which the data residual norm after 4 iterations was plotted against the model norm to determine the optimal smoothing and damping weights (see Supporting Information Text S2 and Figure S5).

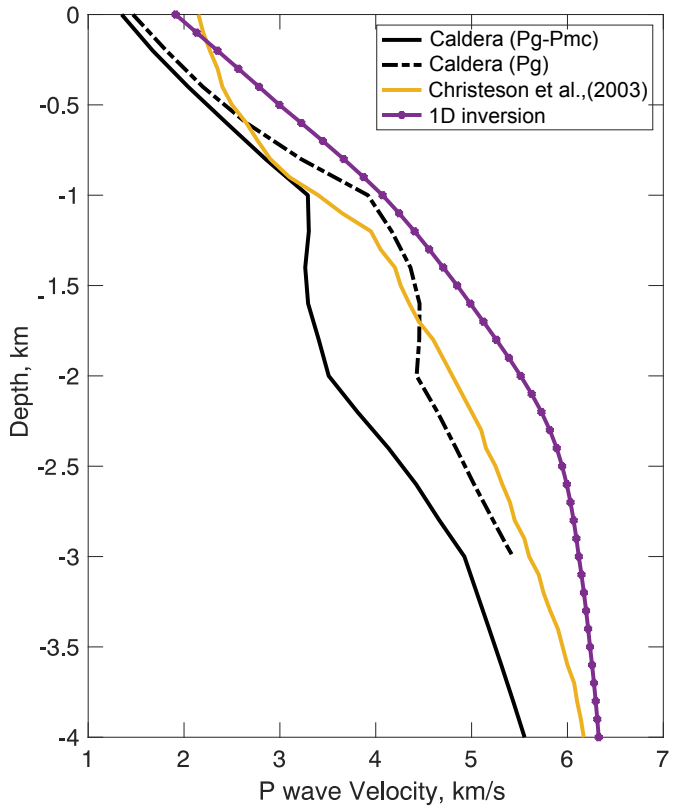


**Figure 5.** One-dimensional velocity profiles for a model for our study area that was extracted from line 2 of the regional refraction experiment of Christeson et al., (2003) (yellow), an inversion of the Pg data for 1-D structure (purple), and 1-D models for the caldera obtained from our 3-D Pg isotropic (solid black line) and Pg-Pmc isotropic (black dashed line) inversions by averaging within the region shown by a purple box in Figure 6f.

For the Pg-Pmc isotropic model, we adopted a creeping strategy to allow steep slowness gradients at the edges of the magma chamber volume and used the optimized smoothing and damping weights from the Pg isotropic inversion. By systematically adjusting the dimensions of

the magma chamber volume, the inversion process identifies the model with the best fit to Pg and Pmc arrival times (Supporting Information Text S3 and Figure S6).

Following Dunn et al. (2005), horizontal anisotropic slowness was parameterized on the slowness grid as:

$$U(r) = \frac{U_{iso}(r)}{1+A(r)\cos[2\theta(r)]+B(r)\sin[2\theta(r)]} \quad (2)$$

where $U_{iso}$ is the isotropic slowness, $r$ is the position, $\theta$ is the raypath azimuth, and $A$ and $B$ are scale terms that control the magnitude and azimuthal orientation of the fast direction of anisotropy, which are given by $2(A^2 + B^2)^{0.5}$ and $\text{atan}(B/A)/2$, respectively. This parameterization allows an explicit inversion for three-dimensional variations in both the orientation and percentage of seismic anisotropy. We inverted for both 1-D and 3-D anisotropic models each with 3-D isotropic structure using the long wavelength isotropic starting model with a jumping strategy. We explored the parameter space for the optimal smoothing and damping weights using trade-off L curves while keeping the same optimal isotropic parameters from the Pg isotropic model (see Supporting Information Text S2 and Figure S5).

## 2.5 Results

### 2.5.1 Pg Isotropic Structure

After six iterations, the isotropic Pg inversion had a residual of 14.7 ms and a $c^2$ value of 1.13. residual variance, which we define in as

$$\chi^2 = \frac{1}{N}\sum_{i=1}^{N}\left(\frac{dt_i}{\sigma_i}\right)^2 \quad (3)$$

where $N$ is the number of observations, $dt$, travel time residual and uncertainty $s$). Checkerboard tests (Figure S7, S8) indicate that 2 km x 2 km x 1 km features are resolved down to 3 km depth within the network. Outside the network but within the shooting grid to the northeast, the resolution decreases, and features are more smeared. The model lacks vertical resolution in the corners due to the absence of crossing rays.

Figure 6a-d shows depth sections of velocity anomalies for the Pg isotropic model, and Figure 7a-e shows vertical cross-sections. Absolute velocity cross sections are shown in Figure S9a-e. The figures are masked when the derivative weight sum (DWS) is <100, since the checkerboard tests show the model is poorly resolved in these regions (Figure S7, S8). The structure is very heterogeneous above 1 km depth (Figure 6a). There are low velocities in the corners of the model where the vertical resolution is poor (Figures S7, S8), consistent with a significant sediment thickness. On and immediately around the volcano, the near surface velocity variations are presumably indicative of changes in porosity rather than lithology. Positive velocity anomalies reaching ≥0.5 km/s, with ~3.8 km/s absolute velocities in regions to the south, east and northwest of the volcano (Figure 6a) can be attributed to massive lava flows (Yang et al., 2024). The caldera flanks and the ridges extending to southwest, west, and north of the caldera are relatively heterogeneous with low-velocity anomalies down to -0.3 km/s, suggesting the presence

of high porosity extrusives. High-velocity anomalies of +0.3 km/s wrap around the caldera rim, indicating that low-porosity intrusive rocks extend close to the seafloor. In contrast, low-velocity anomalies down to -0.7 km/s are observed within the caldera floor suggesting that rocks are highly fractured and/or hydrothermally altered (Carlson, 2014) from the seafloor down to the magma chamber interface seen in reflection profiles at 0.6 km depth (Soule et al., 2025). Laboratory experiments show alteration can lead to a velocity decrease in basalts of 0.5–1.5 km/s (Carlson, 2014).

Low velocities are also observed at larger depths beneath the caldera. The most negative velocity anomaly is -1.23 km/s at 2.2 km depth (Figure 6c), indicative of the magma chamber beneath Orca volcano. Although the southwest and west ridges have similar bathymetry (Figure 2a, 6e) and shallow velocity structures, only the southwest ridge is manifested at depth. It is characterized by a region of low velocities that extends to the base of the resolved model at ~3.5 km (Figure 7d-e), with the most negative anomaly of -1.05 km/s at 3 km depth. The width of the low-velocity zone increases from ~1 km at 1 km depth to 2-3 km at 3 km depth (Figure 6b-d). At 3 km depth, it extends to near the southwestern edge of the resolved model at x=-8 km (Figure 6d). On either side of this low-velocity zone at 1-3 km depth, there are high-velocity anomalies of up to 1 km/s (Figures 6b-d, 7a). These extend over a large wedge-shaped area that reaches the northwest and southeast edges of the model near Orca Volcano. We infer that the southwest ridge marks an active rift that is underlain by hot and possibly partially molten rock with cold intrusive rocks to either side.

At 1-2 km depth, there is a band of low velocities with an anomaly of -0.5 km/s that wraps around the northeast side of Orca Volcano (x = 6 km) (Figure 6b-c and 7c). Connecting to this region, the northern ridges are underlain by a low-velocity zone with anomalies down to -0.6 km/s

that extend to the base of the model (Figure 6c and 7b). This sector is significantly wider than the low velocity zone that underlies the southwest ridge. The low velocities under the northern ridges to the northeast of the caldera appear to merge with the low-velocity body beneath the caldera at depths ≥ 2 km (Figure 6d and 7d). East of the volcano at the edge of the model (x > 7 km), we observe a higher velocity anomaly of +0.3 km/s at 1-3 km depth (Figure 6b-d).

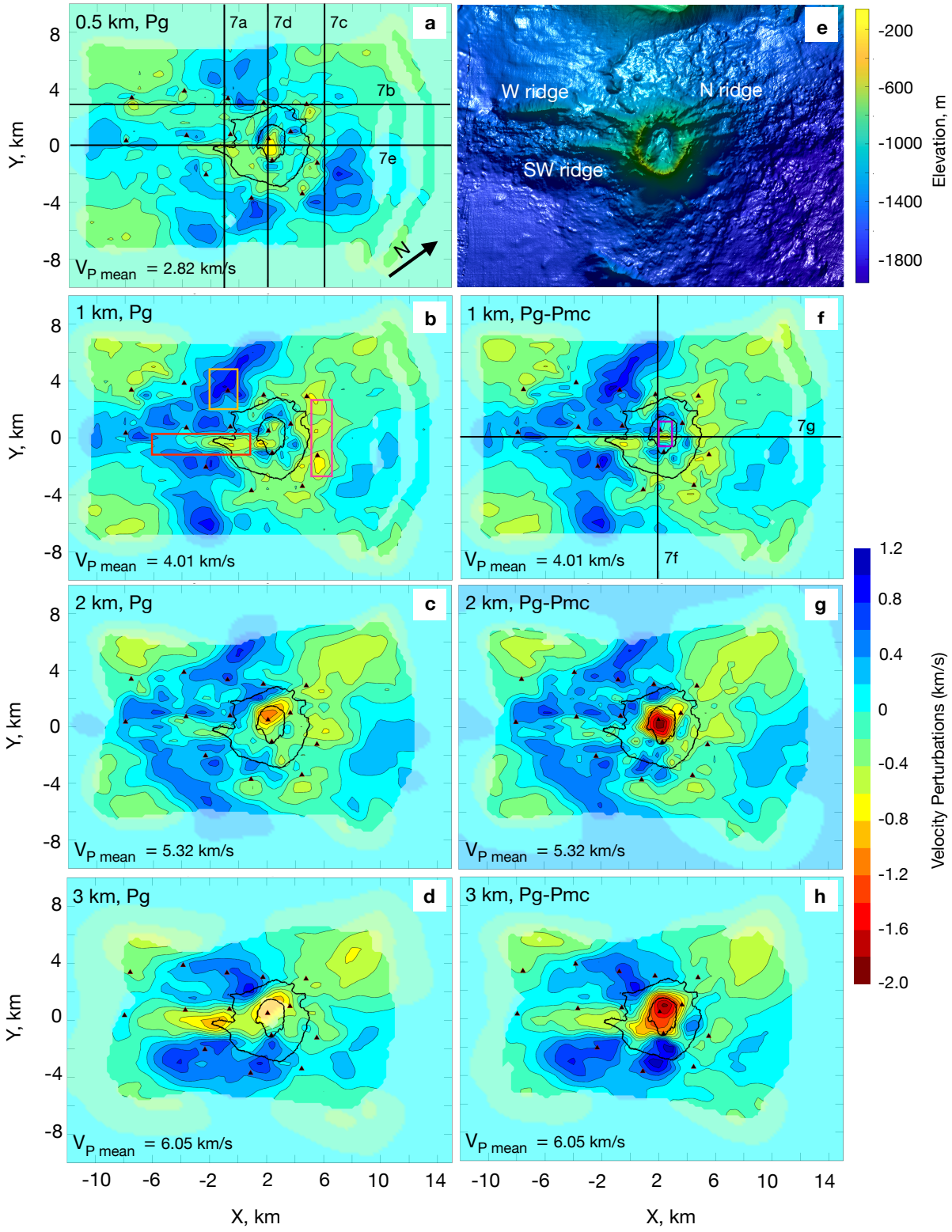
0.5 km, Pg
7a
7d
7c
7b
7e
a
$V_{P\ mean}$ = 2.82 km/s
N
e
W ridge
N ridge
SW ridge
-200
-600
-1000
-1400
-1800
Elevation, m
1 km, Pg
b
$V_{P\ mean}$ = 4.01 km/s
1 km, Pg-Pmc
f
7g
$V_{P\ mean}$ = 4.01 km/s
7f
2 km, Pg
c
$V_{P\ mean}$ = 5.32 km/s
2 km, Pg-Pmc
g
$V_{P\ mean}$ = 5.32 km/s
3 km, Pg
d
$V_{P\ mean}$ = 6.05 km/s
3 km, Pg-Pmc
h
$V_{P\ mean}$ = 6.05 km/s
1.2
0.8
0.4
0
-0.4
-0.8
-1.2
-1.6
-2.0
Velocity Perturbations (km/s)
Y, km
8
4
0
-4
-8
-10
-6
-2
2
6
10
14
X, km

**Figure 6.** Depth sections of velocity anomalies for the Pg isotropic tomography model at (a) 0.5 km, (b) 1 km, (c) 2 km, and (d) 3 km depth beneath the seafloor. Velocity anomalies are relative to the mean velocity at each depth in the Pg isotropic inversion. Coloring is muted in regions with the derivative weight sum (DWS) less than 100. The volcano and its caldera are shown by 2 contours at 1000 m depth. Stations are shown as black triangles. (e) Bathymetry of Orca Volcano for the model region. (f-h) As for (b-d) except for the Pg-Pmc isotropic tomography model. The purple box on (f) shows regions in which velocities were averaged horizontally to produce caldera velocity profiles shown in Figures 5 and 11a. Red, tan and pink boxes of (b) correspond to southwest rift, off-axis, northeast velocity zone averaged for velocity profiles in Figures 11 and 12. Labeled lines on (a) and (f) show the location of vertical cross sections in Figure 7. On (f) the intersection of the profiles coincides with the center of the magma chamber volume (i.e., *C* in Figure 4)

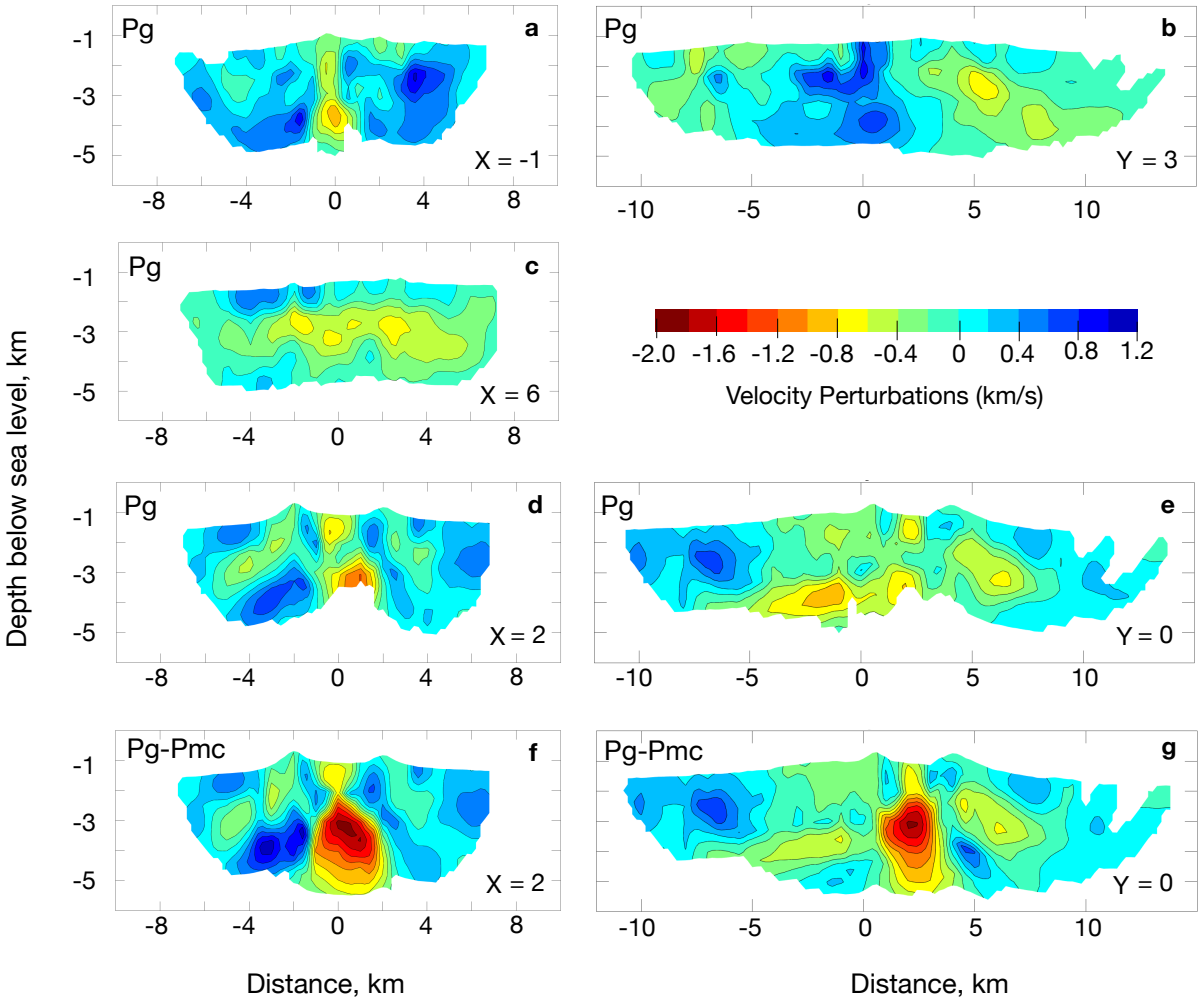


**Figure 7.** Vertical cross-sections of velocity anomalies for the Pg isotropic tomography model at (a) $X$ = -1 km, (b) $Y$ = 3 km, (c) $X$ = 6 km, and (d) $X$ = 2 km (e) $Y$ = 0 km and for the Pg-Pmc isotropic tomography model at (f) $X$ = 2 km, and (g) $Y$ = 0 km plotted as depth below the sea surface. The velocity perturbations are cropped for DWS < 100. Perturbations are plotted with respect to the mean velocity at each depth in the Pg isotropic inversion. The locations of these cross-sections are shown in Figures 6a and 6f. The models are masked to show regions with a DWS ≥100. Absolute velocity for these cross sections are plotted in Figure S9.

### 2.5.2 Pg-Pmc Isotropic Structure

For the Pg-Pmc isotropic inversion, we explored a range of parameter values for the magma chamber volume used to guide rays (Figure 4) and the preferred values that minimize residuals are $\theta = 36°$, $R_1 = 3$ km, $R_2 = 2.5$ km, $r_1 = 0.6$ km, $r_2 = 0.5$ km, $d = 1$ km, $D = 4$ km, X = 2 km and Y = 0 km (Supporting Information Text S3 and Figure S6). The top of the magma chamber is located at 1 km depth which blocks rays traveling deeper than 0.8 km and is thus consistent with the presence of magma chamber reflectors seen at 0.6 – 1.0 km depth in multichannel seismic data collected as part of the BRAVOSEIS experiment (Soule et al., 2025). The top of the cylindrical region is at 4 km, the maximum depth of Pg rays. The conical frustrum is slightly elongated roughly parallel to the rift. The root mean square (RMS) travel time residuals for Pg and Pmc arrivals are 14.5 ms and 14.6 ms, respectively, equivalent to $c^2$ values of 1.10 for Pg and 0.65 for Pmc arrivals. Since the onset of the Pg arrivals is clearly identifiable with less uncertainty than Pmc (Figure 3), this suggests that the uncertainties for both phases are overestimated but that the Pg arrivals are not fit to their uncertainty, presumably because they are influenced by fine-scale structure that is not fully resolved in the inversions. Reducing the uncertainties of Pmc arrivals in the inversion so that they are more strongly weighted and their final $c^2$ value is close to unity has no significant effect on the model.

Figure 6f-h shows depth sections of velocity anomalies for the Pg-Pmc isotropic model, and Figure 7f-g shows vertical cross-sections. In comparison with the Pg-only inversion, the magma chamber volume has a much larger negative velocity anomaly and is imaged over a larger region that extends to greater depth (Figure 7f-g versus Figure 7d-e, Figure S9f-g versus Figure S9d-e). The vertical velocity profile averaged over the caldera is lower at all depths in the Pg-Pmc

isotropic inversion than the Pg isotropic inversion (Figure 5). Above the magma chamber, the difference is only 0.1-0.3 km/s, but within the magma chamber volume, it reaches 1.0 km/s. In the Pg-Pmc inversion, the negative anomaly reaches -1.95 km/s at 2.6 km depth, corresponding to an absolute velocity of 3.97 km/s.

The creeping strategy employed in the Pg-Pmc inversion was adopted to enable the solution to obtain a sharp velocity contrast between the magma chamber volume and surrounding regions (Figure 7f-g). We tested an alternative inversion with jumping. This led to a significant increase in residuals to 18.0 ms for Pg arrivals and 19.7 ms for Pmc, confirming the importance of using a creeping strategy in the Pg-Pmc inversion. The creeping strategy also allowed the inversion to generate larger velocity contrasts away from the magma chamber volume (for example, compare the high-velocity anomalies between Figures 6d and 6h and between Figures 7d and 7f).

Synthetic inversions with uniform velocity anomaly of -2.0 km/s within the assumed magma chamber volume illustrate the advantage of incorporating the secondary Pmc arrivals (Figure S10). The recovery of low velocities and the depth at which they are imaged are greatly improved. The Pg-Pmc synthetic inversion suggest that the observed decrease in the maximum anomaly below 3-4 km depth in the real inversion (Figure 7f-g) is well resolved because it is not seen in synthetic inversion where the magma chamber extends to the base of the model (Figure S10). We infer that the magma chamber beneath the caldera extends to a maximum depth of ~4 km.

### 2.5.3 Pg Anisotropic Structure

The travel time residuals for the Pg isotropic inversion show a clear cos(2θ) azimuthal variation, which requires faster propagation along ray paths oriented northeast-southwest (Figure

8). The amplitude of the cosine(2θ) dependence is higher at shallow depths, decreasing from 4 ms/km peak-to-peak for rays turning above 0.75 km to 0.5 ms/km for rays turning below 2.5 depth.

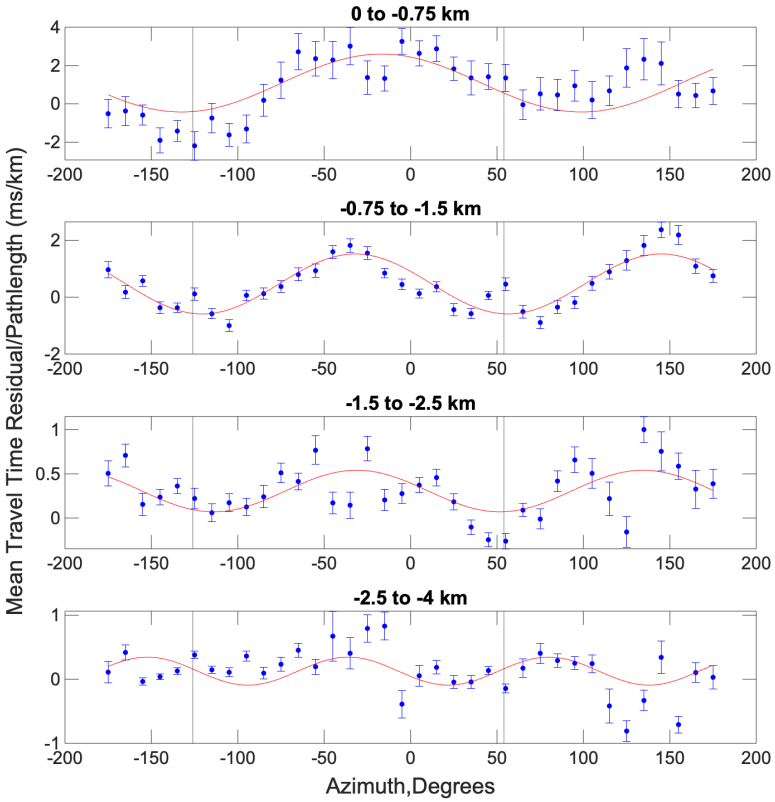


**Figure 8.** Mean travel time residuals and their standard error averaged in 10° azimuth bins plotted against azimuth for rays turning at depths between (a) 0–0.75 km, (b) 0.75–1.5 km, (c) 1.5–2.5 km, and (d) 2.5-4 km. Azimuths are plotted as degrees clockwise from north with black vertical lines showing the azimuth of the southwest ridge of Orca volcano. Solid red lines show cosine curves of the form $A\cos(2q + B) + C$, where $A$, $B$, and $C$ are constants that have been fit to the observations using a least squares approach.

A 1-D anisotropic Pg inversion shows that the percent anisotropy decreases from 5.2 % at 0.4 km to 1.5 % at 4 km (Figure 9). This change in anisotropy with depth matches the variations of the mean travel time residuals with azimuth and depth (Figure 8). It is consistent with the anisotropy resulting from cracks aligned with the rift axis, with the high anisotropy at depths of less than 1 km resulting from the low overburden pressure.

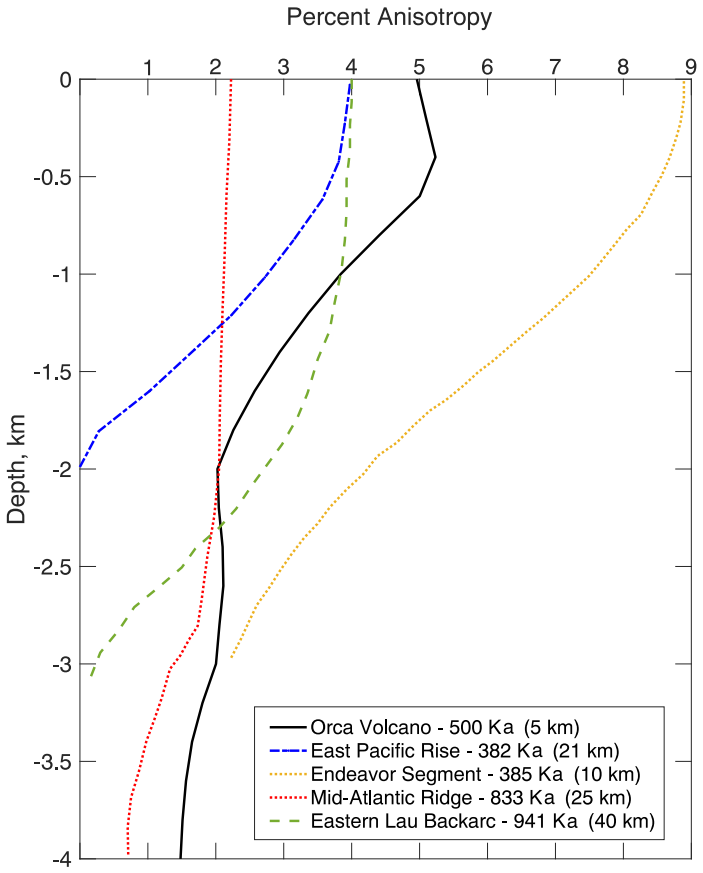


**Figure 9.** Vertical profiles of the percent anisotropy comparing a 1-D inversion at Orca Volcano with the East Pacific Rise at 9°30'N (Dunn & Toomey, 2001), the Endeavor segment of the Juan

de Fuca Ridge (Weekly et al., 2014), the Mid Atlantic Ridge at 35°N (Dunn et al., 2005) and the Eastern Lau Spreading Center (Dunn et al., 2013).

The 3-D anisotropic Pg inversion has a residual of 14.0 ms and a $c^2$ value of 1.01. Checkerboard tests suggest that the inversion can resolve both the magnitude and orientation of anisotropic features within the network (-7 km < $x$ < 8 km and -5 km < $y$ < 5 km) measuring 5 x 5 km horizontally (Figures S11, S12) but does not have good vertical resolution on this scale.

At 0.5 km depth, the highest anisotropy of up to 8.5 % is observed to the southwest of Orca volcano, approximately coincident with the southwest ridge with the fast axis paralleling this feature (Figure 10). This is consistent with the interpretation of this low velocity feature as an active rift with high densities of ridge-parallel fractures due to ongoing extension. Within the caldera, the magnitude of the anisotropy drops to a maximum of ~5 %. Synthetic inversion suggests that this reduction in the magnitude of anisotropy is resolved (Figure S1). On the northeast and east flanks, the magnitude of the anisotropy increases to 6.5% with lower values in this region than on the southwest side of the volcano. On the north and northeast flanks, the fast axis of anisotropy is rotated anticlockwise, consistent with an orientation of the cracks that is more northerly. However, the percent anisotropy beneath the four closely spaced ridges to the north of the volcano is low. Given that the model has reasonable resolution in this region (Figures S11, S12), it suggests that active extension is focused to the south of these ridges.

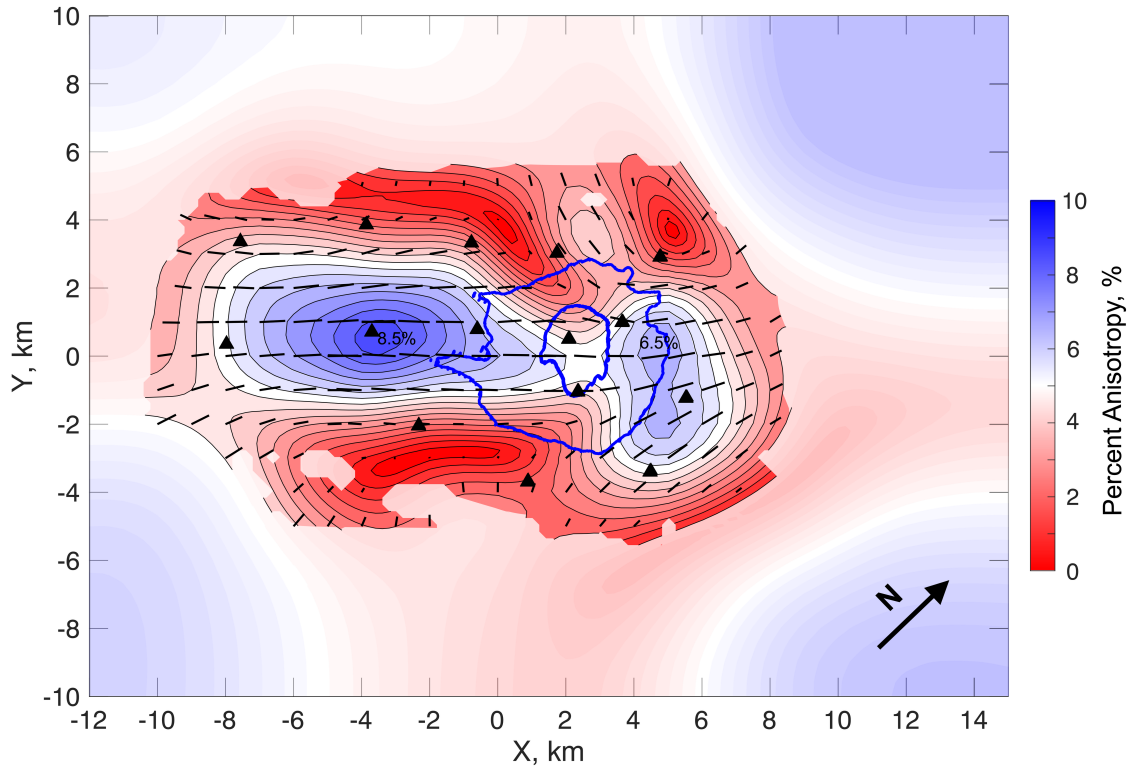


**Figure 10.** Depth section of the 3-D anisotropic structure at 0.5 km depth with the color scale and contours at 0.5% delineating the percent anisotropy and the fast direction shown by ticks scaled to the percent anisotropy. The model is masked to show regions with DWS >500 to indicate regions that are well resolved. Bathymetry contours at 1000 m (blue) show the location of Orca volcano and its caldera. Black triangles show station locations.

## 2.6 Discussion

### 2.6.1 Shallow Structure

The structure of the upper crust within volcanoes is often poorly resolved in terrestrial tomography studies due to poor ray coverage or the large wavelength of surface waves used for imaging (Lesage et al., 2018). In contrast, active-source tomography studies of submarine volcanoes yield higher-resolution images, revealing information about their construction and recent volcanic history (Bushenkova et al., 2019; Castellano et al., 2008; Hooft et al., 2019; Zandomeneghi et al., 2009).

We observe lower velocities in the corners of our models at shallow depths (Figure 6a) that can be attributed to sediment layers that are also inferred from bathymetry (Figure 6e) (García et al., 2009, 2011). These low velocities generally extend to the base of the imaged volume at 2-3 km depth (Figure 6), but in these regions, the models lack vertical resolution because there are no crossing rays. The maximum basement depth in this area is less than 1.5 km, according to Christeson et al., (2003). These sediments are interpreted as turbidites to the north and glaciomarine deposits to the west and south (García et al., 2009, 2011).

We attribute the surficial high-velocity regions to the northeast, south and east of Orca Volcano to low porosity lava flows that extend up to ~5 km from the base of the volcano. There are three dredge stations at Orca Volcano (Keller et al., 1994) (Figure 2a). Station D2 in the caldera has samples with $SiO_2$ contents ranging from 50-60% and averaging 54%, station D4 on flank near the southwest ridge has samples with basaltic andesite compositions ($SiO_2$ of 52-54)%, and station D3 located furthest from the volcano and nearest to a surficial high-velocity region has samples that are transitional from basalt to basaltic andesite (51-52% $SiO_2$) (Keller et al., 2002). This is

consistent with the high velocity surficial features away from the volcano being more basaltic and less viscous. Basaltic lavas from submarine volcanoes can travel long distances because the pressure of the overlying ocean keeps volatiles dissolved in the lava, which prevents viscosity increases associated with volatile exsolution and vesiculation (Gregg & Fornari, 1998; Q. Sun et al., 2019). While basaltic andesites are relatively more viscous compared to basalt lavas, long run-out lava flows are still observed in submarine volcanoes with higher silicic content (~60% $SiO_2$) such as the Central Mariana Back-Arc Spreading Center (Chadwick et al., 2018), the NE Lau Basin (Embley & Rubin, 2018), and the Havre Caldera Volcano (Ikegami et al., 2018).

Low and variable velocities seen on the steep flanks of the volcano are consistent with complex deposits of higher porosity igneous rocks. Many volcanoes, including Deception (Ben-Zvi et al., 2009), Santorini (Hooft et al., 2019) and Stromboli (Castellano et al., 2008), have similar low-velocity flanks that were attributed to pillow lavas, fractured vesicular lavas, volcanoclastic sediments, mass slumps, and incoherent sedimentary deposits. Volcanoes such as Brothers Seamount (Georgatou et al., 2024) and Miyakejima Volcano (Geshi et al., 2022) have volcanoclastic and phreatomagmatic debris on their flanks. These observations are consistent with the presence of similar lower velocity flanks at other volcanoes.

The caldera rim is underlain by a ring of higher-velocity material that in map view is particularly apparent at 1 km depth (Figures 6b, f) but in cross section can be seen reaching to near the seafloor (Figures 7d-g). High-velocity rings beneath caldera rims are observed at many volcanoes including Deception Island (Zandomeneghi et al., 2009), Campi Flegrei (Zollo et al., 2003), Axial Seamount (Arnulf et al., 2018; Baillard et al., 2019), Santorini (Hooft et al., 2019), and Newberry (Heath et al., 2015). They have been attributed to frozen shallow-level intrusions

that formed before caldera formation and remnants from a pre-caldera shield phase (Heath et al., 2015; Hooft et al., 2019; Zandomeneghi et al., 2009).

The caldera floor has the lowest shallow velocities in the model ($V_P$ = 2.1 km/s at 0.5 km depth, Figure 6a), consistent with very high porosities. Similar observations at Santorini (Hooft et al., 2019) and Deception (Zandomeneghi et al., 2009) are interpreted as resulting from a combination of chaotic collapse along reverse faults, phreatomagmatic fracturing, and infilling with tuffs and ignimbrites rather than massive basaltic lava flows. This interpretation is consistent with the variable compositions of the six samples from dredge D2 in the caldera of Orca volcano (50-60% $SiO_2$) which suggest that the caldera interior hosts a fragmented mixture of lavas. Since the caldera of Orca volcano is inferred to be hydrothermally active (Rodrigo et al., 2018), hydrothermal alteration may also contribute to these low velocities.

### 2.6.2 Orca Volcano Magma Chamber

Our approach provides a method to improve the imaging of three-dimensional magma bodies when secondary arrivals can be picked. Pg-based tomography models at numerous volcanoes including Santorini (McVey et al., 2020), Axial Seamount (West et al., 2001), Soufrière Hills (Paulatto et al., 2012), Augustine (Syracuse et al., 2011), Kolumbo (Chrapkiewicz et al., 2022) have shown under-recovery of magma chamber low-velocity anomalies but it is difficult to assess to what degree (Paulatto et al., 2022). Although our assumed magma chamber volume is a simple geometrical shape, the Pmc arrival times fit better than their estimated uncertainties, presumably because the spatial pattern of velocities can adapt within this volume. The volume of the magma chamber in the Pg-Pmc inversion (Figures 6g-h, 7f-g) is much larger than in Pg inversion (Figures 6c-d, 7d-e). Likewise, the maximum negative anomaly is -1.95 km/s compared to only -1.23 km/s in the Pg inversion.

We use the approach described by Paulatto et al., (2019) to estimate the melt content of the magma chamber. The difference between the velocity profile beneath the caldera and a background profile (Figure 11a) is first ascribed to temperature, including anharmonic and anelastic terms (Figure 11b). The velocity anomaly that cannot be explained by temperatures up to the solidus is then attributed to melt using a self-consistent effective medium for two endmember crack aspect ratios of 0.5 and 0.05 (Figure 11c). An explanation of the calculations and the choice of parameters is presented in Supporting Information Text S4 and Table S2

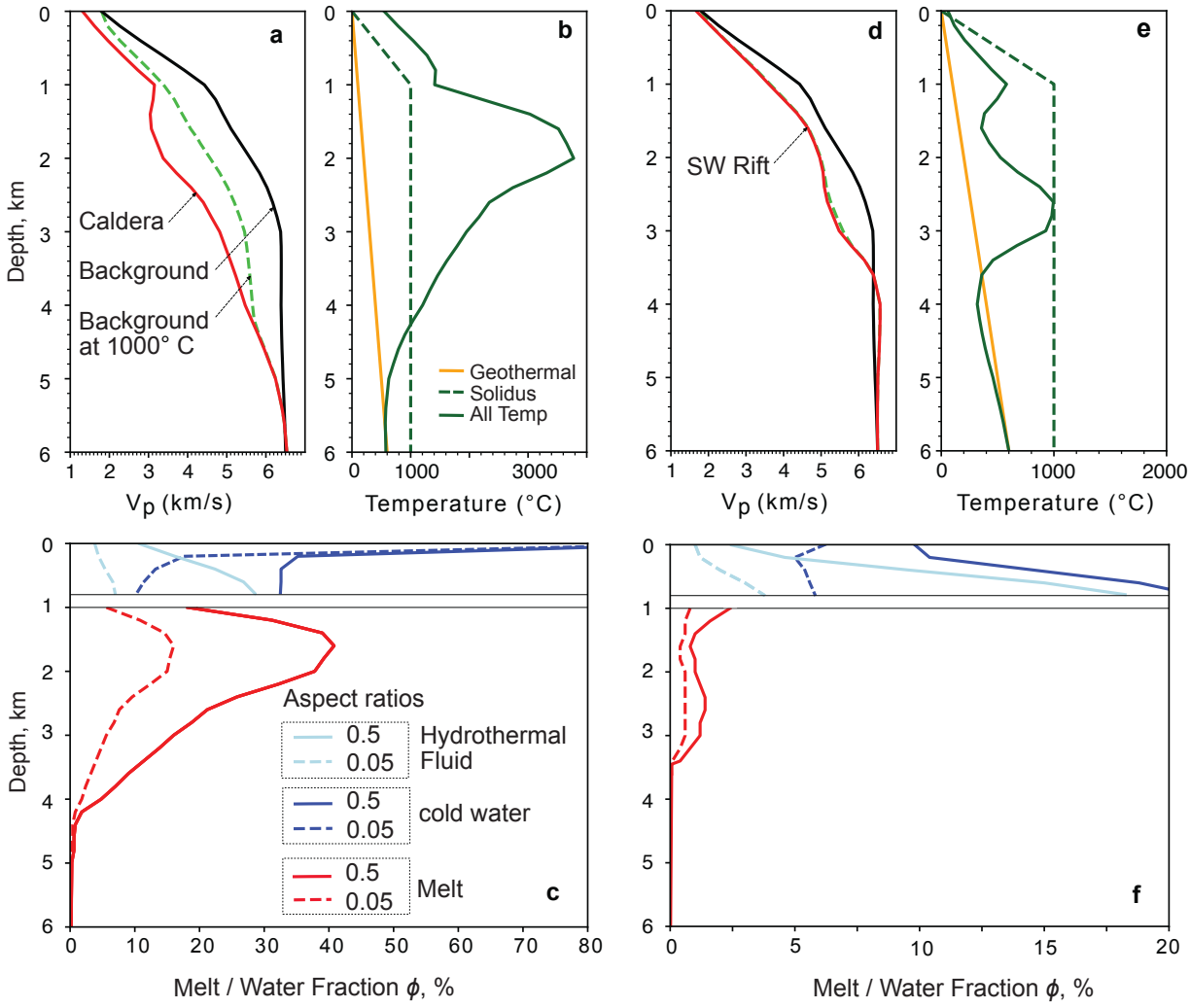

**Figure 11.** Physical property calculations beneath (a-c) the caldera for the Pg -Pmc inversion and (d-f) the southwest rift for the Pg inversion. (a) Background (black) and caldera (red) vertical velocity models obtained by averaging velocities in the regions shown by tan rectangle in Figure 6b and purple box in Figure 6f , respectively. The green dashed line shows the background velocity profile adjusted to 1000°C, the assumed solidus temperature. (b) Temperature profile obtained by assuming the difference between the background and caldera velocity profiles is explained by temperature (green) assuming a geothermal gradient of 100°C / km (orange). The dashed line shows the assumed solidus temperature of 1000°C for the melt calculations. (c) Estimated fluid content for pore aspect ratios of 0.05 (dashed lines) and 0.5 (solid lines) for melt at ≥1 km depth (red) and water at ≤0.8 km depth assuming cold water (dark blue) and hot hydrothermal fluid (light blue). (d-f) As for (a-c), except for a velocity profile below the southwest rift (red box in Figure 6b).

Our Pg-Pmc inversion calculations predict maximum melt concentrations of 16% and 41% beneath the caldera for pore aspect ratios of 0.05 and 0.5, respectively (Figure 11c), compared with only 2% and 6% for the Pg inversion (Figure S13). These large melt percentages for the Pg-Pmc inversion are comparable to estimates at other volcanoes that used methods other than first arrival travel time tomography to improve the recovery of velocity anomalies including 11-33% obtained at Newberry volcano from forward modeling secondary arrivals (Beachly et al., 2012), 26-53% at Kolumbo Volcano from full waveform inversion (Chrapkiewicz et al., 2022), 50% at Katla Volcano from forward modeling travel times with wavefront tracking (Gudmundsson et al., 1994), and 30-60% at Long Valley caldera from combining receiver function analysis with tomography (Seccia et al., 2011). They are also comparable to melt fraction estimates based on comparing travel time tomographic images to inversions of a synthetic magma chamber to account for the under recovery

of velocity anomalies. For example, maximum melt percentages of 38% at Deception Island (Ben-Zvi et al., 2009) and 35% at Soufriere Hills Volcano (Paulatto et al., 2012) were obtained with this approach.

We estimate that the magma chamber beneath Orca Volcano has a volume of 11.5 $km^3$ and contains 0.8-2.3 $km^3$ of melt (Supporting Information Text S4). This melt volume is less than estimated for many other volcanoes, such as Soufriere Hills (13.6 $km^3$) (Paulatto et al., 2012), Newberry (8 $km^3$) (Heath et al., 2015), Santorini (27-43 $km^3$) and Axial Seamount (26-60 $km^3$) (Arnulf et al., 2014a), commensurate with the smaller size of the edifice. However, when normalized to the rate of extension, it is quite large when compared to the shallow crustal melt volumes estimated beneath oceanic spreading centers. Lucky Strike volcano which lies at the center of a 70 km segment of the mid-Atlantic Ridge spreading at 2 cm/yr is estimated to contain < 1 $km^3$ of melt (Escartín et al., 2014). Melt volumes per kilometer of ridge are estimated to be 0.08 $km^3$ (Arnoux et al., 2019) at the Endeavour segment spreading at 5 cm/yr and 0.05-0.21 $km^3$ (Dunn et al., 2000) and 0.75 $km^3$ (Key & Constable, 2002) for the East Pacific Rise near 9°50'N spreading at 10 cm/yr. We infer that Orca volcano stores a relatively large amount of melt for a volcano in an ultra-slow spreading rift, typically associated with low melt supply (Cannat et al., 2019; Minshull et al., 2006; Momoh et al., 2020).

### 2.6.3 Rift Structure

Volcanic ridges extend from Orca volcano to the southwest, west, and north (Figure 6e) and have the characteristics of features formed by dike intrusions. At 0.5 km depth (Figure 6a), they are characterized by low velocities consistent with high porosity pillow lavas (Gini et al., 2021; Searle et al., 2010). Higher velocities surrounding the ridges suggest lower porosity sheet

flows pooling in bathymetric lows. These characteristics resemble the distribution of extrusives observed at slow-spreading ridges (Gini et al., 2021).

Of the two volcanic ridges on the west side of the volcano, only the southwest ridge is underlain by low velocities at depths ≥1 km, with characteristics that show that it is the locus of active rifting. The rift is characterized by a ~1 km wide low velocity zone at 1 km depth (Figure 6b) that with increasing depth extends further to the southwest, clearly connect to Orca Volcano's magma chamber, and widens to 2-3 km (Figures 6c-d, 7a and 7e). The rift is flanked by a laterally extensive region of high-velocity anomalies (Figures 6b-d, 7a) that at 1-2 km depth form a wedge shape that encircles the southwest side and tapers to the southwest and a more rectangular shape at 3 km depth. This velocity structure is similar to that seen in tomography experiments at slow-spreading mid-ocean ridges, such as segments of the Mid-Atlantic Ridge (Arnulf et al., 2014b; Dunn et al., 2005, 2017; Minshull et al., 2003) and the Eastern Lau Spreading Center (Dunn et al., 2013). In these settings, the higher velocities at depth adjacent to the spreading center are interpreted as cooled mafic intrusions whose porosity has been reduced by hydrothermal deposition (Barclay et al., 1998; Dunn et al., 2005; Zhao et al., 2012).

The southwest rift also coincides with a region of strong rift parallel anisotropy in the uppermost crust with amplitudes up to 8.5% at 0.5 km depth, contrasting with amplitudes ~2% a few kilometers away from the rift (Figure 10). A similar pattern is also observed at oceanic spreading centers, namely the Endeavour segment (Weekly et al., 2014), East Pacific Rise at 9°30'N (Dunn & Toomey, 2001), Mid-Atlantic Ridge at 35°N (Dunn et al., 2005), and Eastern Lau Spreading Center (Dunn et al., 2013). High levels of shallow anisotropy on axis are explained by ongoing extensional fracturing at shallow depths where the overburden pressure does not close

cracks, while the decrease in anisotropy off axis is attributed to the infilling of cracks by hydrothermal deposition (e.g., Dunn et al., 2005).

Melt estimates for the southwest rift zone are a few percent (Figure 11d-f) which is consistent with observations from other slow mid-ocean ridges where shallow magma bodies are generally ephemeral (Sinton & Detrick, 1992) and low melt fractions in the upper crust can be attributed to a deep magma reservoir (Canales et al. 2000a, Collins, et al., 2000; Dunn et al., 2005, 2017) or along axis migration (Meier et al., 2022). Extensional diking events in the southwest rift zone of Orca Volcano could be fed from deeper magma bodies underlying the rift but we prefer a model in which they are primarily fed by dikes that propagate laterally from the substantial magma chamber underlying Orca Volcano. This is similar to the pattern of spreading at ultra-slow spreading ridges, where magma budgets are low but focusing leads to melt accumulation under sparsely distributed volcanic centers that inferred to supply neighboring, less prominent rift segments (Meier et al., 2022; Schmid et al., 2017). It also mirrors the geometry of eruptions observed in many settings. In Iceland, magma stored under central volcanoes (e.g., Krafla, Bárðarbunga) repeatedly propagates 30–50 km laterally to feed fissure swarm eruptions, and triggering caldera deflation (Ágústsdóttir et al., 2019; Hollingsworth et al., 2012). At Axial Seamount, the deflation of the summit caldera is accompanied both by eruptions within the caldera and by dikes that propagate 20-50 km along the north and south rifts to feed fissure eruptions (Chadwick et al., 2016; Dziak & Fox, 1999). Dim João de Castro Seamount in the Azores is an example of lateral melt transport from a central edifice via dikes along an ultra-slow spreading rift (Romer et al., 2021). Finally, at Miyakejima volcano off Japan, there is evidence for diking events feeding intrusions up to 30 km from a volcano (Yamaoka et al., 2005).

A comparison of the average vertical velocity structure of the southwest rift with zero-age velocity profiles for ultraslow (Figure 12a) and slow spreading centers (Figure 12b) shows that the velocities in the southwest rift are somewhat lower than mid-ocean ridges, but they are similar to the Valu Fa Ridge (VFR) and Southern Mariana Trench (SMT) back-arc spreading centers (Figure 12b). The VFR has an intermediate spreading rate of 40-63 mm/year and the crust has an andesitic composition (Eason & Dunn, 2015), while the SMT has a slow spreading rate of 30-45 mm/year and is primarily basaltic (Anderson et al., 2017). Given that off-axis velocities for the southwest rift are also on the low end of the range seen at ultraslow and slow spreading ridges in similar ages (1 Ma), (Figure 12c), the lower velocities in the southwest rift may be a consequence of a composition that is basaltic-andesite (Keller et al., 2002) and the enhanced porosities that result from higher volatile concentrations in the back arc spreading centers than mid-ocean ridges. Alternatively, the difference may result because the zero-age upper-crust is entirely solidified at most of the comparative mid-ocean ridge sites.

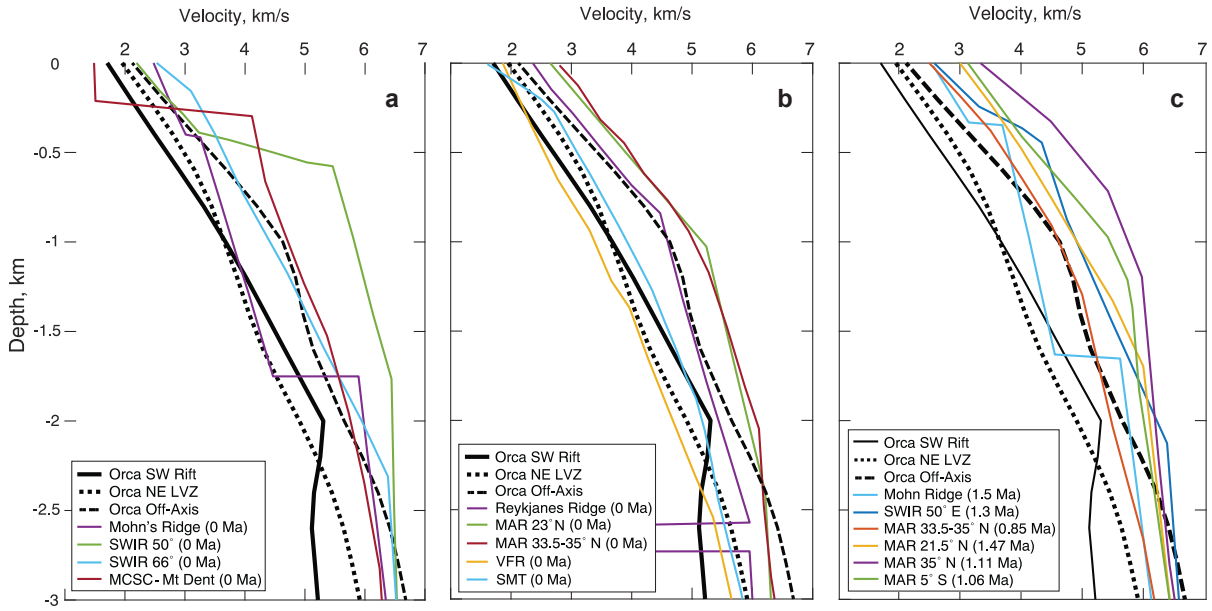

**Figure 12.** Comparisons of 1-D velocity profiles from the southwest rift, northeast low velocity zone (NE LVZ), and off-axis at Orca Volcano (averaged from red, pink, and tan rectangles from Figure 6b, respectively) with other spreading centers. (a) Comparison with on axis profiles at ultra-slow spreading centers from the Mohns Ridge (Klingelhöfer et al., 2000), Southwest Indian Ridge at 50° E (SWIR) (Niu et al., 2015), SWIR at 66° E (Minshull et al., 2006), and Mid Cayman Spreading Center (MCSC) (Harding et al., 2017). (b) Comparison with on axis profiles at slow spreading centers from Reykjanes Ridge (Weir et al., 2001), Mid Atlantic Ridge at 23° N (MAR) (Purdy & Detrick, 1986), and MAR at 33.5 – 35° N (Hooft et al., 2000) and from back arc spreading centers at Valu Fa Ridge (VFR) (Turner et al., 1999) and Southern Mariana Trough (SMT) (Sato et al., 2015). (c) Comparison with off-axis profiles and slow and ultra slow spreading centers from the Mohns Ridge (Klingelhöfer et al., 2000), SWIR at 50° E (Niu et al., 2015), MAR at 33.5 – 35° N (Hooft et al., 2000), MAR at 21.5° N (Dannowski et al., 2011), MAR at 5° S (Planert et al., 2009) and MAR 35° N (Canales et al., 2000a; Detrick, et al., 2000). Crustal ages vary from 0.85 – 1.47 Ma and are listed in the legend.

Our anisotropic models indicate that relatively high rift-parallel anisotropy (3-5%) cuts across the caldera structure although with a lower amplitude than on the southwest rift (Figure 10). Similar rift-parallel anisotropy patterns have been observed in the Aluto caldera in the Main Ethiopian Rift (Nowacki et al., 2018). This suggests that the caldera has been influenced by regional extensional stresses, which would explain the slight elongation of Orca Volcano caldera perpendicular to the rift. Similar elongations are observed in other calderas in extensional environments, such as Newberry (Heath et al., 2015), Fantale (Maestrelli et al., 2021), and Suswa (Bosworth et al., 2000) calderas. A synthetic inversion (Figure S14) suggests that the reduced amplitude of the anisotropy in the caldera compared to the southwest rift zone is well resolved.

This may indicate that the caldera forming event reset the anisotropy and/or reflect the enhanced infilling of cracks from vigorous hydrothermal circulation within the caldera (Rodrigo et al., 2018).

The closely spaced ridges that extend northeastward from the north side of the volcano are underlain at depths of 2-3 km by an elongated low velocity body that is wider than observed below the southwest rift and has smaller anomalies (Figures 6c-d). It is not as clearly connected to the Orca Volcano magma chamber as the southwest rift, but the low velocities in this region (Figure 12, profile labeled Orca NE LVZ) are consistent with a region of elevated temperatures underlying a continuation of the rift. However, the location and strike of this feature is also consistent with the shallow southwestern limit of the deeply sourced dike that was inferred from the August, 2020 swarm of 85,000 earthquakes to the northeast of Orca Volcano (Cesca et al., 2022). Thus, it may not be linked to the Orca volcano magmatic system.

At depths ≤ 2 km, the velocities are on average lower on the northeast side of the volcano (X > 3 km) than on the southwest side (Figure 6b-c) which may be explained by a change in crustal composition. The highest anisotropy is observed to the northeast of the volcano rather than to the north (Figure 10). Indeed, the axis of rifting as defined by the maximum anisotropy appears to step to the southeast on the northeast side of the volcano rather than to the northwest as would be expected from the location of the ridges. Synthetic inversions (Figure S14) suggest that this offset in the anisotropy is well resolved. We infer that the extension is more dispersed on the northeast side of the volcano and not clearly linked to the volcanic ridges and the magmatic system of Orca

### 2.6.4 Transition in rifting style across Orca Volcano

Our inference of a transition in rifting style across Orca volcano coincides with a change in the structure of the basin. Our isotropic model shows a sharp velocity transition northeast of the

volcano with velocities at 1-3 km depth about 0.5 km/s lower to the northeast of X = 4 km (Figures 6b-d). Basin scale P-wave refraction images (Christeson et al., 2003) and ambient noise S-wave images (Li et al., 2021) show a similar transition that extends to just over 5 km depth. This change is associated with a morphologic step in which the basin deepens and broadens to the northeast (Gràcia et al., 1996). Multichannel seismic profiles (Barker & Austin, 1998) show a distinct volcanic basement at the surface to the southwest and a heavily faulted lithosphere to the northeast. The topography formed by volcanic ridges found on the southwestern side of Orca Volcano disappears towards the northeast, where the seafloor deepens, forming a broad, graben-like structure. Reduced-to-pole geomagnetic anomalies show a narrow band of positive anomalies along the southwest rift that change to a broader anomaly across the volcano to the northeast (Almendros et al., 2020; Soule et al., 2025). Several studies have placed a fault at this boundary. These range from a normal fault northeast of the volcano inferred from bathymetry and multichannel seismic profiles (Gràcia et al., 1996; Prieto et al., 1998) to a possible transform fault across Orca volcano from aeromagnetic surveys (González-Ferrán, 1991). However, there is no evidence of a fault crossing the whole basin in this location and the morphological step at Orca volcano does not align with structural boundaries on the Antarctic Peninsula side of the basin, which are interpreted to predate basin formation (Christeson et al., 2003).

Abrupt transitions in spreading style occur in other back arc basins including the Scotia Basin (Livermore et al., 1997), Lau Basin (Dunn & Martinez, 2011), Manus Basin (Taylor & Martinez, 2003), Southern Mariana Trough (Sleeper et al., 2021), and Black Sea (Shillington et al., 2009). Martinez et al., (2018) and Sleeper et al., (2021) have developed a model for how slow spreading rates and a hydrous mantle affect rifting styles in back arc spreading centers. The Southern Mariana Trough (SMT) and Southern Valu Fa Ridge (VFR) exhibit axial highs that

abruptly transition to diffuse spreading zones (DSZs). At typical spreading centers mantle dehydration leads to lithospheric strengthening (Hirth & Kohlstedt, 1996) that focuses deformation and melt delivery to a narrow rift. However, continuous water addition from the subducting slab is hypothesized to weaken the overriding lithosphere and in conjunction with slow spreading rates, promotes a sharp transition to distributed extension and crustal accretion (Martinez et al., 2018). A similar mechanism may explain the transition in rifting styles across Orca volcano.

Dredge samples from the Bransfield Basin reveal a significant change in the mantle source composition across Orca Volcano, which appears to correlate with a change in volatile content. The southwestern end of the CBB exhibits a more MORB-like mantle source, evidenced by lower $K_2O/P_2O_5$, higher K/Rb, and higher Ba/Rb ratios (Keller et al., 2002). In contrast, the northeastern side shows a stronger arc component, indicated by arc-like $^{87}Sr/^{86}Sr$ and $^{143}Nd/^{144}Nd$, high Ba/Rb, and low Ce/Pb (Keller et al., 2002). The increase in fluid-mobile/immobile element ratios (U/Nb, Rb/Nb) from dredge stations D1-4 to D10 (Figure 1, 2a) (Keller et al., 2002) mirrors the transition from MORB-like to arc-like lavas toward the northeast side of Orca Volcano (Fretzdorff et al., 2004). Such elevated U/Nb and Rb/Nb values are a proxy for a larger influx of $H_2O$-rich slab fluids (Wang et al., 2022), implying that the mantle source beneath the volcano becomes progressively hydrous to the northeast. Additional evidence for an increase in volatile content to the northeast are an increase in the vesicularity of dredged basalts (Keller et al., 2002) and lower Ce/Y ratios that suggest a higher degree of melting (Keller et al., 1992; Weaver et al., 1979).

An analysis of P-wave receiver function beneath the South Shetland Islands reveals that there is a slab tear beneath Orca Volcano (Parera-Portell et al., 2023). The slab tear causes the slab depths beneath the islands to decrease from ~75 km to the southwest to ~60 km to the northeast (Figure 13). Subducting slabs dehydrate as hydrous minerals break down, releasing water that

moves upwards into the overlying mantle wedge, facilitating mantle melting and wedge hydration (Wang et al., 2019). The subducting plate in the Bransfield strait is relatively young and warm (14 - 23 Ma). In warm subduction zones, the major crustal dehydration reactions (eclogite transition) occur in depths shallower than 70-80 km (Kirby et al., 1996). Models for subducting plates of similar age, such as the Mexico (13 Ma), Colombia-Ecuador (16 Ma), South Central Chilean (25 Ma), and Kyushu (27 Ma) subduction zones, predict peak crustal dehydration at between 60-90 km depth (van Keken et al., 2011; Wada & Wang, 2009). In some warm slabs, mantle dehydration continues to greater depths at a rate that is dependent on the level of mantle serpentinization but below the peak rate (van Keken et al., 2011). For the warmest subduction zones with the lowest thermal parameters (Cascadia and Mexico), dehydration of both crust and mantle is complete above 100 km depth (van Keken et al., 2011). Given that the former Phoenix plate is now subducting extremely slowly (Henriet et al., 1992; Lawver et al., 1995) , it may be similarly warm, consistent with the absence of intermediate-depth (>60 km) earthquakes in this region (Robertson Maurice et al., 2003). Assuming a slab dip of 30-40° estimated by Parera-Portell et al. (2023) for the slab southwest of the tear, places peak dehydration beneath the South Shetland Islands west of Orca Volcano but beneath the back-arc rift to the northeast (Figure 1, 13). The offset of peak dehydration may be even larger if the slab to the northeast has a shallower dip as the sense of the tear would suggest. Thus, the change in slab depth to either side of the tear can account for the increased mantle hydration beneath the rift zone to the northeast, which promotes the transition to distributed extension (Martinez et al., 2018).

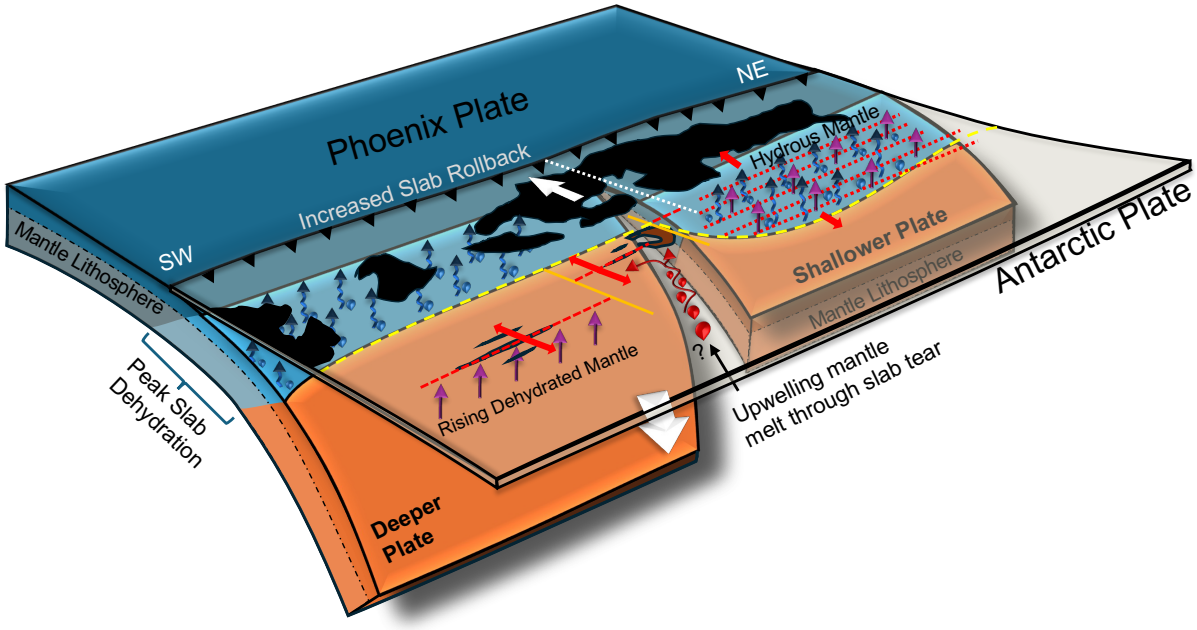


**Figure 13**. Schematic diagram of processes affecting the style of rifting across Orca Volcano. Red dashed and dotted lines indicate the axes of focused and distributed extension, respectively, with thick red double-sided arrows indicating spreading. Yellow solid lines indicate rift offsets. A white dashed line shows the location of inferred transform fault formed by slab tear induced rollback.

Blue and orange slab colors indicate regions of peak slab dehydration and mostly dehydrated slab, respectively. Blue wavy arrows indicate the regions where the dehydration of the slab peaks and releases water to hydrate the overlying mantle. Purple arrows indicate where the mantle upwells to support rifting. Red drops and a wavy red arrow indicate rising dehydrated mantle through the slab tear that preferentially draws this upwelling mantle to the southwest due to increased slab roll back. The yellow dashed line is the maximum extent of the hydrated zone at the surface obtained by extrapolating the slab depths of Parera-Portell et al. (2023) beneath the South Shetland Islands with a slab dip of 30-40° and assuming a maximum slab dehydration depth

of 100 km (van Keken et al., 2011). Distributed extension to the northwest of Orca volcano is result of the rift overlying the region of hydrated mantle.

The slab tear imaged by Parera-Portell et al. (2023) is also marked by a ~20 km gap in Ps arrivals from the top of the subducting slab that may indicate horizontal opening of the tear. Indeed, Parera-Portell et al. (2023) speculate that mantle flow through the tear may lead to crustal underplating in the region. While the observations beneath the South Shetland Islands are not sufficient to determine whether there is a slab gap beneath Orca volcano, this would be consistent with work elsewhere. A slab tear can involve both vertical offset and horizontal motions, because the shallowing and steepening of a slab on either side of a tear induces tensional stresses (Gianni et al., 2019). Mantle flow through slab tears has been observed in other subduction systems even without significant vertical offsets (Lynner et al., 2017).

If a slab gap is present at the tear, it would provide a pathway for depleted upper mantle to upwell from beneath the slab and thus can explain why Orca Volcano has the least arc-like magmas in the basin (Keller et al., 2002). The faster rates of slab roll back to southwest would preferentially draw this upwelling mantle to the southwest (Jacoby, 1973; Strak et al., 2024) explaining the transition in source composition from more MORB-like to more arc like northeast of Orca volcano (Keller et al., 2002). Faster roll back to the southwest would also promote higher rates of extension to the southwest, although extension may also be enhanced to the northeast by the contributions of transtension at the Scotia-Antarctic plate boundary (González-Casado et al., 2000) and forearc rotation (Li et al., 2021).

Although the setting of the Bransfield rift is quite different from rifts of continental interiors, water nonetheless plays a pivotal role in some of these settings. One clear example, although by a different mechanism, is found in the magma-poor West Iberia rifted margin, where

fault-controlled hydration leads to serpentinization, thereby weakening the lithosphere (Bayrakci et al., 2016). Beneath Western North America, water released from the dehydration of the Farallon slab during the Laramide Orogeny is inferred to have significantly weakened the lithospheric mantle (Dixon et al., 2004) influencing uplift and volcanism (Humphreys et al., 2010), lithospheric thinning (Li et al., 2008) and potentially styles of extension (Rowe et al., 2015). A mechanism comparable to the Bransfield Rift has been advanced for the Malawi Rift by Njinju et al. (2019) who hypothesize that decoupled extension between the crust and mantle in magma poor portions of the rift is promoted by metasomatic weakening of the lithospheric mantle by fluids released from melting at greater depths.

## 2.7 Conclusions

In this study, we obtained isotropic and anisotropic P-wave tomography models of the subsurface structure of Orca Volcano and surroundings from an active source seismic experiment. We incorporated secondary arrivals (Pmc) into the analysis to obtain improved images of the shallow magma chamber beneath the volcano. The near surface velocity structure suggests that low porosity lavas flow up to 5 km from the volcano while higher porosity extrusives are confined to its flanks. The caldera rim has high velocities consistent with shallow-level intrusions that formed before the caldera, while low velocities on the caldera floor require very high porosities either from fracturing when the caldera formed or infilling by fragmented material. The shallow magma chamber beneath the caldera contains a significant volume of melt and is connected to a low velocity zone that extends to depth below the southwest rift. The isotropic and anisotropic structure of this rift is remarkably similar to an ultra-slow or slow spreading mid-ocean ridge, consistent with the inference that this portion of the rift is close to transitioning to seafloor spreading. There is no evidence that the volcano supports focused extension to the northeast. Here

the seismic structure is consistent with a wide zone of distributed extension that has led to the formation of a deeper, more heavily sedimented basin. Based on a decrease in seismic velocities to the northeast and a change in the composition and vesicularity of samples dredged by a previous study (Keller et al., 2002), we infer that the mantle is more hydrated and weaker to the northeast, leading to a wider zone of deformation (Martinez et al., 2018). This change in hydration can be attributed to a recently discovered slab tear and consequent northeastward decrease in slab depth (Parera-Portell et al., 2023) that places the release of slab fluids beneath the rift to the northeast but trenchward beneath the South Shetland Island to the southwest.

## 2.8 Acknowledgments

We thank all participants and the crew members in the BRAVOSEIS 2018, 2019, and 2020 cruises that made this work possible. We especially thank Emilie Hooft, Douglas Toomey, and Brandon VanderBeek for extensive advice on using the Tomolab tomography code. Luis Vizcaíno provided the magma chamber interfaces from reflection seismic profiles collected as part of the BRAVOSEIS project. Seafloor seismic instruments were provided by the Ocean Bottom Seismic Instrument Center (OBSIC), supported by the U.S. National Science Foundation (NSF), and one instrument by the German Instrument Pool for Amphibian Seismology (DEPAS). OBSIC data used here are archived at the EarthScope Consortium Data Management Center. This work has been funded by the National Science Foundation awards ANT-17744651 and ANT-1744581. Funding for experiment was provided by project BRAVOSEIS (CTM201677315-R) of the Spanish Ministry of Science, the Alfred Wegener Institute and the National Science Foundation. We thank three anonymous reviewers for constructive comments.

## Chapter 3: Insights into the Inflation of Axial Seamount from Horizontal Seafloor Geodesy

**Maleen Kidiwela[1], William S. D. Wilcock[1], Dana Manalang[2] and Erik Frederikson[1,3]**

[1]School of Oceanography, University of Washington, Seattle.

[2]Applied Physics Laboratory, University of Washington, Seattle

[3]University of Texas Institute of Geophysics, University of Texas, Austin

### 3.0 Abstract

Axial Seamount, a hotspot volcano on the Juan de Fuca Ridge, has been monitored through three eruptions with vertical geodesy documenting cycles of inflation and deflation. However, vertical motions alone cannot fully discriminate between distributed volumetric inflation and fault-accommodated uplift. We present three years of horizontal acoustic ranging observations from 2022-2025 across Axial's caldera from seafloor transponders demarcating 1.8-km, 1.6-km, and 3.3-km baselines spanning the western and eastern sides of the caldera and its full width. We observe 30 cm of extension across the caldera that is asymmetric with 24 cm of extension on the eastern baseline. Modeling horizontal and vertical deformation demonstrates that the observed extension is primarily accommodated by volumetric inflation rather than fault motion. The data is consistent with a deeper pressure source coincident with a stacked sill complex under the southern caldera and a smaller shallow source under the northeastern caldera where eruptions originate.

## 3.1 Introduction

Submarine volcanism dominates the Earth's magmatic budget, with approximately 75% of magma emplaced at mid-ocean ridges (Crisp, 1984). Oceanic spreading centers represent a primary manifestation of plate tectonics and are responsible for renewing 60% of the Earth's surface on timescales of ~100 Myr. While eruptions at these sites pose no hazard to human populations, advancing our understanding of volcanic processes and eruption forecasting benefits from studying volcanism across a wide variety of settings (Schmandt et al., 2019). Despite substantial progress in characterizing various volcanic systems globally, fundamental questions persist across all volcano types regarding the mechanics of magma accumulation and migration, the evolution of stress fields throughout eruptive cycles, and the quantitative relationships linking surface deformation to subsurface magmatic and tectonic processes (National Academies of Sciences, Engineering, and Medicine, 2017). Mid-ocean ridge volcanoes may represent some of the most tractable systems for addressing these questions because of their shallow magmatic systems, relatively uniform petrology, and well-constrained crustal thickness (Cabaniss et al., 2020; National Academies of Sciences, Engineering, and Medicine, 2017). Furthermore, the presence of the overlying ocean enables seismic imaging of internal volcanic structure at resolutions unachievable on land. However, the marine setting also hinders efforts to observe deformation and seismicity on timescales spanning full eruptive cycles. Sustained observation of these systems therefore requires concentrating resources at a small number of well-instrumented sites.

Axial Seamount is one of the most extensively studied sites on the global mid-ocean ridge system. Located on the Juan de Fuca Ridge at its intersection with the Cobb hotspot (the Cobb–Eickelberg Seamount chain), Axial is a ridge–hotspot hybrid volcano with elevated magma supplies relative to typical ridge settings. It is characterized by a 3 × 9 $km^2$, 100-m-deep summit caldera (Figure 1). Three eruptions have been observed in 1998, 2011, and 2015, and a near-continuous >20-year record from calibrated seafloor pressure sensors documents repeated cycles of gradual inflation of ~3 m followed by rapid syn-eruptive deflation. These observations are consistent with the hypothesis that eruptions at Axial are inflation-predictable (Chadwick et al., 2006, 2012; Nooner & Chadwick, 2009; Nooner & Chadwick, 2016). Current pressure measurements indicate that the volcano has re-inflated near to the level reached prior to the 2015 eruption, suggesting another eruption may be imminent (Chadwick et al., 2025).

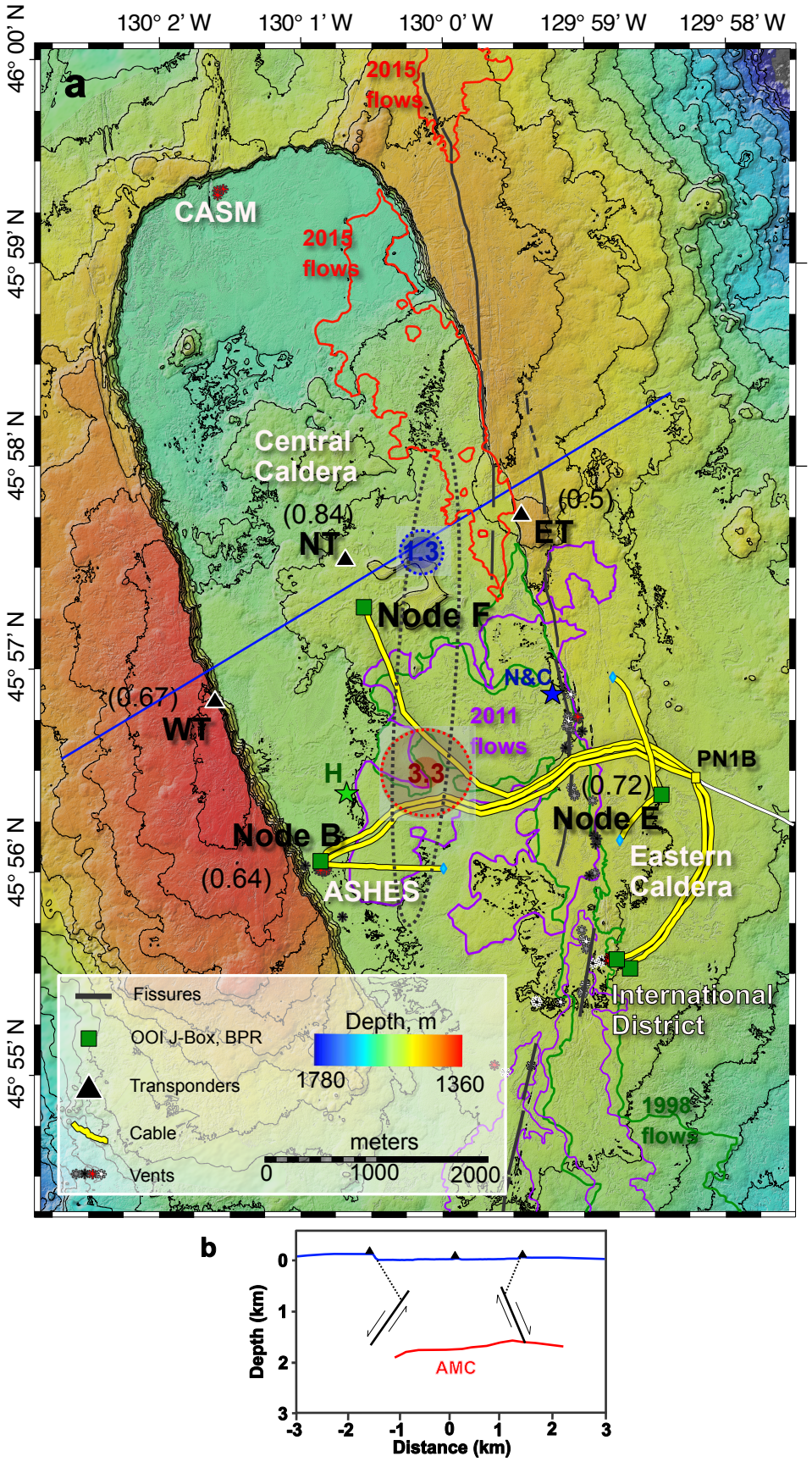
a
130° 2' W
130° 1' W
130° 0' W
129° 59' W
129° 58' W
46° 00' N
45° 59' N
45° 58' N
45° 57' N
45° 56' N
45° 55' N
2015 flows
CASM
2015 flows
Central Caldera
(0.84)
NT
1.3
ET
(0.5)
Node F
N&C
2011 flows
(0.67)
WT
H
3.3
PN1B
(0.72)
Node E
Node B
(0.64)
ASHES
Eastern Caldera
International District
1998 flows
Fissures
OOI J-Box, BPR
Transponders
Cable
Vents
Depth, m
1780
1360
meters
0
1000
2000
b
Depth (km)
0
1
2
3
AMC
-3
-2
-1
0
1
2
3
Distance (km)

**Figure 1.** (a) Map of Axial Seamount showing the bathymetry and lava flows contoured with 20 m intervals, acoustic transponders as labeled triangles (ET - Eastern Transponder; NT- Northern Transponder; WT - Western Transponder), the Ocean Observatory Initiative (OOI) cables as yellow lines with green squares for cabled bottom pressure recorders (BPR) labeled with the corresponding observatory node. Red and black stars indicate black smoker and diffuse vents, respectively, gray stars are vents covered by lava and white stars are snowblower vents. One-meter scale bathymetry was obtained from Caress et al. (2024). The numbers in parenthesis are the uplift observed during the acoustic ranging experiment as a fraction of that at Node F. A dashed black ellipse and red and blue circles mark the outline of the inverted spheroid and dual sphere source models in this study (See text S1). Value within the spheres indicate their depth in kilometers. The center of the Nooner and Chadwick (2016) and Hefner et al. (2020) spheroids are shown as blue and green stars labelled N&C and H. (b) A cross section along the blue line drawn across the caldera in (a) showing the transponders, the approximate location of the buried outward dipping faults as solid black lines, inward dipping faults as dashed black lines and the axial magma chamber.

Earthquake locations since 2015 have revealed long-lived, narrow (<200 m), outward-dipping ring fault with convex, hourglass-shaped geometry along the east and west caldera walls (Figure 1b) (Waldhauser et al., 2020; Wang et al., 2025; Wilcock et al., 2016). Cyclical reactivation of these structures has been proposed to accommodate magma reservoir inflation and deflation before, during, and after eruptions (Levy et al., 2018; Nooner & Chadwick, 2016). During inter-eruptive periods, the outward-dipping ring fault (Figure 1b) undergoes normal-sense motion to accommodate volcanic inflation, with high and increasing rates of seismicity in the lead-up to eruptions (Dziak et al., 2012; Wilcock et al., 2016). During eruptions, fault motion reverses to

accommodate deflation (Levy et al., 2018). It is unclear how much of the deformation is accommodated by fault motion and how much by distributed volumetric expansion/compaction (Hefner et al., 2020; Levy et al., 2018). The caldera walls are the expression of a conjugate inward-dipping ring fault (Arnulf et al., 2018; Baillard et al., 2019b). Any motion on the outer-ring fault appears to be largely aseismic. Evidence for seismic slip on this structure remains ambiguous: two earthquake catalogs contain shallow inward-dipping planes on the east side of the caldera, though in different locations (Arnulf et al., 2018; Baillard et al., 2019b), while the most precise double-difference catalog does not show such features (Waldhauser et al., 2020).

Seismic imaging at Axial Seamount has revealed a complex magmatic system, beginning with the identification of a main magma reservoir beneath the caldera (West et al., 2001) that is 3 km wide, 14 km long, 1 km thick, and contains 8–30 $km^3$ of melt (Arnulf et al., 2018; Arnulf, Harding, Kent, Carbotte, et al., 2014). More recent studies resolve multiple reservoirs, including a flat axial magma lens and a funnel-shaped lithosphere–asthenosphere boundary that channels magma toward the caldera, modulating eruptive and hydrothermal activity (Arnulf et al., 2018; Carbotte et al., 2008; Kent et al., 2025).

Vertical geodetic observations at Axial Seamount are currently obtained from multiple instruments. These comprise four bottom pressure and tilt instruments and a self-calibrating pressure recorder attached to the Ocean Observatories Initiative Regional Cabled Array (OOI RCA) (Smith et al., 2018), 13 standalone seafloor pressure gauges (Chadwick et al., 2022), a network of benchmarks periodically occupied in closed-loop surveys with a mobile pressure recorder (Nooner & Chadwick, 2016), and repeat bathymetric mapping with an autonomous underwater vehicle (AUV) (Caress et al., 2024). Ocean bottom pressure observations have been

used to develop a series of inflation models (Nooner & Chadwick, 2016; Slead et al., 2024). Initial models for the 2015 eruption invoked a steeply southwestward dipping prolate spheroid source (Nooner & Chadwick, 2016), later refined to incorporate surface displacement from outward-dipping caldera ring faults (Hefner et al., 2020). More recent modeling with realistic geometry for the reservoir roof suggests the magma system is compartmentalized (Slead et al., 2024).

However, while the vertical geodetic record at Axial Seamount has provided a remarkable picture of how inflation and deflation are linked to the volcanic cycle, models based on vertical motions alone have inherent limitations (Hefner et al., 2020; Nooner & Chadwick, 2016; Slead et al., 2024).Acoustic ranging between seafloor transponders is an established marine geodetic technique for monitoring horizontal strain. Some of the earliest experiments were performed on the Juan de Fuca Ridge (Chadwell et al., 1999; Chadwell & Spiess, 2008; Chadwick & Stapp, 2002), including at Axial Seamount (Chadwick et al., 1999). The technique has since been applied to subduction zones (Petersen et al., 2019), transform faults (Lange et al., 2019; McGuire & Collins, 2013; Sakic et al., 2016), unstable continental margins (Blum et al., 2010), and the submerged flanks of deforming volcanic edifices (Brooks et al., 2009; Urlaub et al., 2018). The acoustic ranging experiment at Axial Seamount (Chadwick et al., 1999) comprised five transponders in a linear array deployed across the North Rift approximately 3 km north of the caldera from June 1996 to March 1998. Approximately 9 cm of steady extension was observed prior to the January 1998 eruption, followed by 4 cm of rapid contraction during the eruption. The length change during the eruption is consistent with predictions from a point-source Mogi model located 3.8 km below the center of the caldera that fits the subsidence observed on two BPRs (Fox et al., 2001). Chadwick et al. (1999) could not fully rule out an instrumental explanation for the 9

cm of apparent pre-eruptive extension but concluded it was likely real and related to magma migration into the north rift.

In this study, we present three years of horizontal acoustic ranging observations across the caldera at Axial Seamount collected during the latter part of the current pre-eruptive inflation phase (September 2022 to August 2025). Our objective is to constrain the partitioning of strain between distributed inflation and slip on the inward- and outward-dipping ring faults that underlie the caldera (Figure 1b) by combining acoustic ranging measurements of vertical deformation.

### 3.2 Data

In summer 2022, we deployed an acoustic ranging network comprising four Sonardyne FETCH transponders mounted on 3-meter tripods (Figure 1). The Central Transponder (CT) was cabled to the Ocean Observatories Initiative Regional Cabled Array (OOI-RCA) at the central caldera site and controlled via custom software. The remaining three units operate autonomously: the North Transponder (NT) was deployed on the caldera floor north of the cabled unit at 1527 m depth, the West Transponder (WT) was deployed on the western caldera wall at 1401 m depth, and the East Transponder (ET) was deployed on the eastern caldera wall at 1458 m depth. Each FETCH unit houses a thermometer, sound speed sensor, pressure gauge and inclinometer (Figure S1). WT lacked velocimeter data, and NT recorded temperature values with a systematic offset. The cabled central transponder lost the ability to communicate acoustically shortly after deployment, However, each autonomous unit continued to independently obtain and store ranges to the other transponders and sensor data every four hours. Data from the autonomous FETCH units were uploaded to research vessels in September 2023, September 2024, early and late August 2025, accumulating three years of observations. The acoustic baselines between transponders on the

caldera rims and floor (NT-ET, WT-NT) measure the combined effects of inflation and motion on either the east or west buried outward-dipping faults. Motion on the ring fault forming the caldera rim has little effect on ranging times because the fault is near-vertical at the surface. The 3 km baseline across the caldera between the elevated rims (WT-ET) provides a redundant measurement. The baseline within the caldera (CT-NT), sub-parallel to the buried faults, would have provided a measure of the horizontal component of distributed inflation without fault influence and enabled resolution of areal strain.

### 3.3 Methods

In addition to velocimetry data, acoustic velocities for each station were calculated using the Thermodynamic Equation of Seawater 2010 (TEOS-10) (McDougall & Barker, 2011) with onboard temperature and pressure measurements from each FETCH unit and central caldera salinity from the MJ03F-CTDPFB305 station on the OOI RCA. Prior to calculating TEOS-10 velocities, a tidal model for Axial Seamount was subtracted from the pressure data to assess the consistency of the data, and salinity data were corrected using discrete salinity measurements collected at Axial Seamount during JASON ROV operations. Temperature values from the northern station were corrected by determining the offset that minimizes the misfit between observed velocimeter data and TEOS-10 velocities. We calculated the range, $L$ for each baseline using

$$L = \left(\frac{t_m}{2} - t_{\mathrm{lag}}\right)\bar{v} \qquad (1)$$

where $t_{\mathrm{m}}$ is the measured travel time, $t_{\mathrm{lag}}$ is the lag time, and $\bar{v}$ is the harmonic mean acoustic velocity derived from the endpoint velocities at the two transponders.

Once ranges were calculated, we used the heading of each instrument to perform a tilt correction, subtracting the distance range of anomalies caused by the pitch and roll of the tripod (Figure S1).

Noting that the pattern of inflation at Axial Seamount is to first order spatially self-similar (Hefner et al., 2020) and that there is very little pressure gauge drift at Node F (Chadwick, 2022), we estimated the seasonality of each baseline, $L$, fitting a model of the form

$$L(t) = a\,P_F(t) + b\,\sin\omega t + c\,\cos\omega t + d \qquad (2)$$

where $P_F$ is the pressure at Node F, $\omega$ the annual angular frequency and $a$, $b$, $c$ and $d$ are constant coefficients. The seasonally corrected change in each baselines, $L'(t)$ are calculated according to

$$L'(t) = L(t) - b\,\sin\omega t + c\,\cos\omega t - L'_0 \qquad (3)$$

where $L'_0$ is the starting baseline length obtained by averaged over first 30 days of observations.

We estimated the linear drift of each pressure sensor other than Node F by fitting a model of the form

$$\mathrm{P}(t) = f P_{\mathrm{F}}(t) + gt + h \qquad (4)$$

where $f$, $g$ and $h$ are constant coefficients. Since pressure gauges are typically observed to have an exponentially decaying component of drift for a few months after deployment (Polster et al., 2009), we excluded from the fit the first six months of data for the pressure gauges on the transponders. We obtained a drift correct pressure, $P$' according to

$$P'(t) = P(t) - gt \qquad (5)$$

In previous studies, caldera uplift has been modeled using an prolate spheroid pressure source (Nooner & Chadwick, 2016) and by considering the magma reservoir geometry and using spatially

variable pressure source on either a horizontal surface at the mean depth of the magma reservoir roof (Slead model 3a) or on the 3D roof geometry (Slead model 3b) (Slead et al., 2024). We scaled each of these inflation models to match the observed uplift during our experiment at Node F (32.9 cm) and then calculated the predicted vertical uplift at each transponder and cabled pressure gauge and the predicted horizontal baseline change. These calculations were performed with the dMODELS package (Battaglia et al., 2013) for the prolate spheroid and with Slead (2024) for models of Slead et al. (2024).

To consider fault slip, we performed Okada dislocation modeling using the dMODELS package (Battaglia et al., 2013) with a 55°-dipping west fault and a 67°-dipping east fault (Figure 1b) extending from 0.5 to 30 km depth. These large values avoid edge effects and mimic faults that are rooted in the shallow magma reservoir. Fault dips were determined by fitting planes to hypocenters in the catalog of Wang et al. (2024) beneath each wall after iteratively removing outliers greater than 0.6 km from the best-fitting plane. We calculated differential uplift between Node F and the ET and WT for 1 m of slip on each fault, then solved for the slip required on each fault to reproduce the observed differential. These slip values were used to predict changes in horizontal distances between transponders.

### 3.4 Results

We used the TEOS-10 velocities for calculating distance ranges instead of the velocimeter data (Figure S2), because TEOS-10 produces slightly more consistent results. The standard deviation of the misfit relative to a 30-day running mean was 3.90 cm for the TEOS-10 calculation and 3.95 cm for velocimeter data (Figure S3). Additionally, because the western station lacked velocimeter data, adopting TEOS-10 velocities ensures consistency across all transponders. Changing from TEOS-10 to velocimeter velocities has an insignificant impact on the results.

Individual ranges calculated for each baseline exhibit significant scatter (Figure 2). A 30-day moving average (180-point) reduces the scatter and reveals how baseline lengths evolved over time. We calculated the standard deviation within each 30-day bin for a given baseline and used this as a proxy for measurement precision (Petersen et al., 2019). Precision values are, 3.9 cm/km for the NT-ET baseline, 5.2 cm/km for the WT-NT baseline and 4.8 cm/km for the WT-ET baseline. At 4-hour sampling, the RMS pairwise differences (Δd) are 7.46 cm for NT–ET (n=6135), 11.02 cm for WT–NT (n=6462), and 20.03 cm for WT–ET (n=6455), corresponding to single-measurement scatters of 5.3 cm, 7.8 cm, and 14.2 cm (1σ; $\sigma = \mathrm{RMS}/\sqrt{2}$) or equivalently 3.2 cm/km, 4.4 cm/km, and 4.4 cm/km for NT–ET, WT–NT, and WT–ET, respectively. If the measurement errors were uncorrelated, these estimates would be expected to agree with 30-day bin standard deviations. Their close but systematically lower values suggest a modest correlated component of error, with amplitudes of 2.2 cm/km, 2.8 cm/km, and 1.9 cm/km. The large amount of uncorrelated error is consistent with a significant contribution from rapidly varying acoustic path effects such as multipathing (Mourya et al., 2021), or internal-wave-driven fluctuations (Flatté & Rovner, 2000) . The amplitudes of the seasonal signal normalized to baseline length are 1.1

cm/km, 0.9 cm/km and 1.2 cm/km in NT-ET, WT-NT, WT-ET baselines with longer paths in September (Figure S8). Additionally, temporal changes in baseline standard deviation show annual modulation of scatter, with scatter a minimum in September and a maximum in March (Figure S5). We infer that the seasonality in the baselines is likely an oceanographic signal linked to seasonal changes in the pattern of circulation above the seamount.

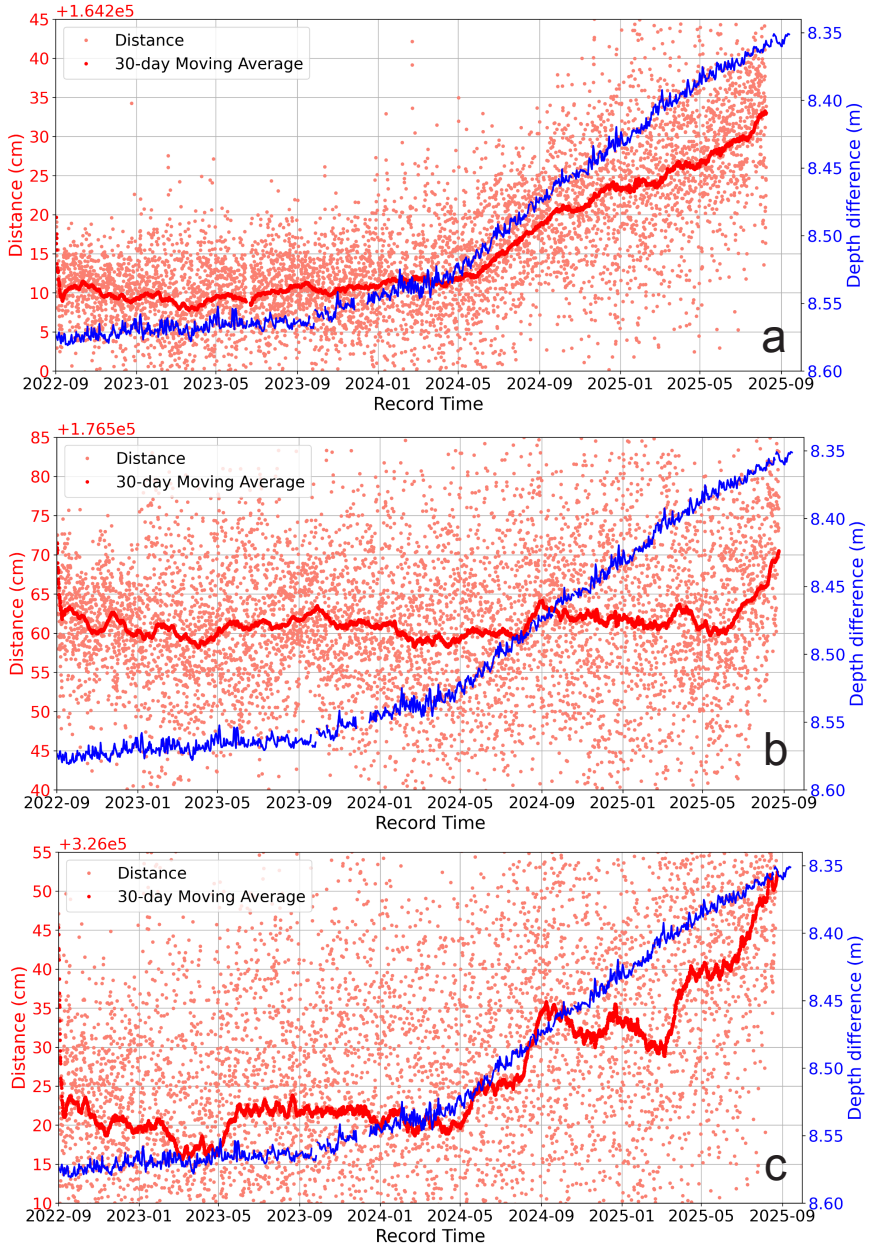

**Figure 2.** Distance baselines for (a) NT-ET, (b) WT-NT, (c) WT-ET (light red dots) along with the 30-day moving average (dark red line) and the depth difference, Node F minus Node E (blue line).

All baselines except for WT-ET and ET-WT shows good agreement between reciprocal solutions (Figure S6). Mismatch between WT-ET and ET-WT occurs only from 2024-09 to 2025-01. We infer that the WT-ET path is more reliable since the anomaly closely matches the sum between NT-ET and WT-NT (Figure S7).

The pattern of extension observed in the ranging data reveals a striking asymmetry between the eastern and western baselines (Figure 2a-b, 3a-b). Until May 2024, both baselines show minimal extension, consistent with the low inflation rate observed in pressure data and cumulative seismic moment during this period (Figure S3). The seasonally corrected NT-ET and WT-ET baselines (Figure S8) starts to lengthen at the same time as the increase in seismicity and differential uplift in November 2023 (Figure 3a). A second inflection point in May 2024 coincides with the accelerated inflation with the eastern baseline then lengthening 24 cm over 16 months (Figure 3a, S9). In contrast, the WT-NT baseline remained relatively stable and did not begin increasing until May 2025, at which point it lengthened by 10 cm within four months. During this last interval, the rate of baseline extension in the west appears higher than the east.

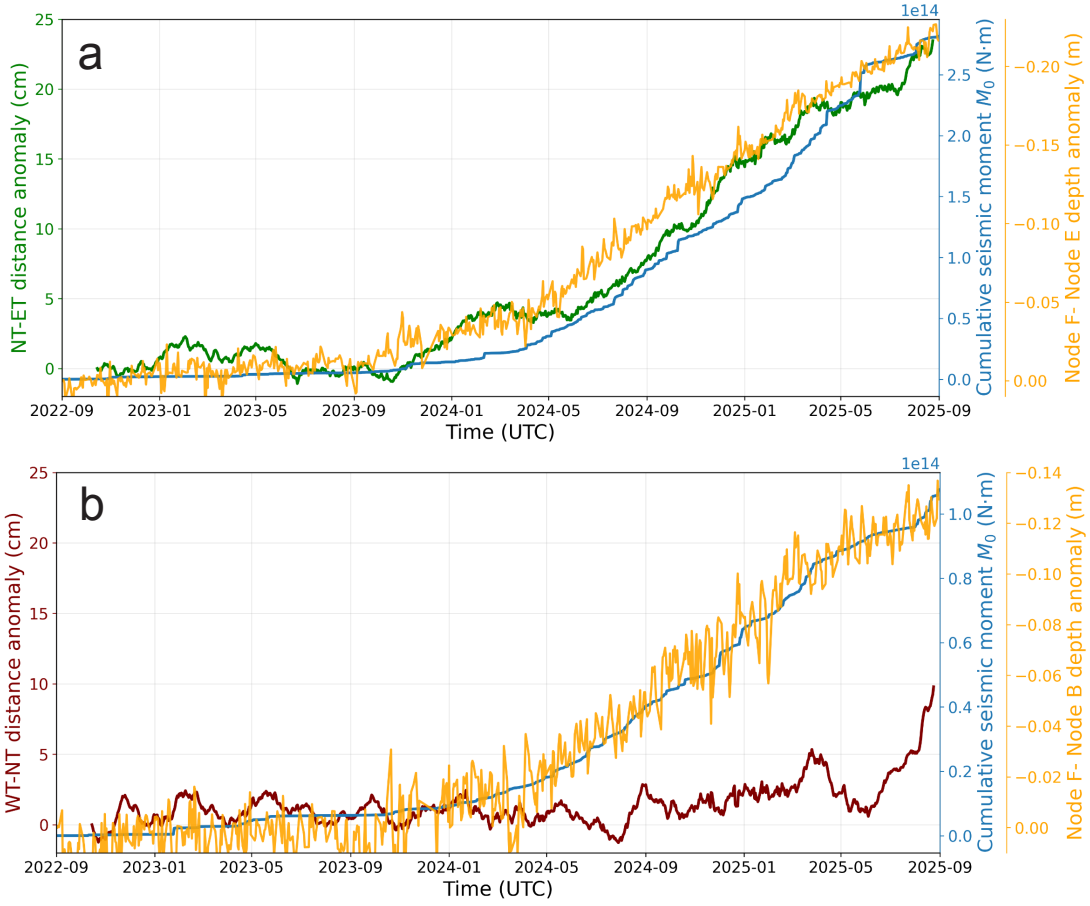


**Figure 3.** Acoustic ranging and pressure geodesy time series. (a) Seasonally corrected NT-ET baseline (green) with differential uplift between Node F and Node E (gold) and cumulative seismic moment for the east fault (blue). Time period from 2025-08-09 to 2025-08-28 in NT-ET baseline was extrapolated to match the end time of WT-NT baseline. (b) Seasonally corrected WT-NT baseline (dark red) with differential uplift between Node F and Node B (gold) and cumulative seismic moment for the west fault (blue).

Combining the three transponders (WT, NT, ET) and three cabled pressure gauges (Node B, Node F, Node E) on the OOI-RCA we examined seafloor pressure variability across the

caldera (Table 1, S1). Drift corrected uplift values based on assuming no drift at Node F show similar inflation at the eastern (ET, Node E) and western (WT, Node B) caldera sites, with the most inflation in the central caldera (NT, Node F) (Table 1). The small RMS misfit values for the modeled drift curves are consistent with a pattern of inflation that is self-similar (Table S1).

**Table 1.** Geodetic observations and model predictions. The observed uplift without and with drift corrections and the observed horizontal extension from 2022-09-02 to 2025-08-09 are compared with the predictions of the prolate spheroid pressure source model of Nooner & Chadwick (2016) models 3A and 3B of Slead et al. (2024) for the observed amount of uplift at Node F, two new pressure source models presented here and the Okada dislocation fault slip only model.

| Pressure Station / Baseline | Observed uplift/ extension (cm) | | Modeled uplift/ extension (cm) | | | | | |
|---|---|---|---|---|---|---|---|---|
| | Uncorrected | Drift Corrected | Nooner and Chadwick | Slead 3a | Slead 3b | New Spheroid | Dual Spheres | Fault only |
| **Node F** | 32.9 | | 32.9 | 32.9 | 32.9 | 33.2 | 32.7 | 32.9 |
| **Node E** | 11.3 | 17.4 | 23.7 | 13.5 | 13.4 | 16.7 | 16.4 | |
| **Node B** | 19.8 | 21.7 | 23.3 | 20.7 | 15.5 | 22.0 | 22.9 | |
| **ET** | 11.5 | 21.2 | 33.5 | 20.9 | 18.6 | 22.4 | 22.9 | 21.2 |
| **NT** | 28.5 | 28.4 | 28.7 | 33.0 | 34.9 | 28.2 | 29.5 | |
| **WT** | 7.1 | 21.1 | 20.1 | 21.0 | 12.9 | 21.4 | 18.8 | 21.1 |

| | | | | | | | |
|---|---|---|---|---|---|---|---|
| **NT-ET** | 22.3 | 18.4 | 9.5 | 10.1 | 21.2 | 21.3 | 2.0 |
| **WT-NT** | 6.1 | 12.1 | 8.0 | 8.9 | 7.3 | 7.2 | 3.6 |
| **WT-ET** | 26.4 | 28.5 | 17.3 | 19.8 | 26.5 | 25.6 | 5.9 |

The existing models of inflation are reasonably consistent with the observed uplift, but they do not predict the observed horizontal extension (Table 1). Both models of Slead et al. (2024) significantly underpredict the observed horizontal extension and do not predict the asymmetry, while the model of Nooner and Chadwick (2016), predicts the magnitude of extension but not the asymmetry. The fault only model explains only 20% of the observed extension.

**3.5 Discussion**

The scatter observed in our acoustic ranging experiment (3.6-5.2 cm/km) is substantially larger than precisions of 0.2–1.2 cm/km reported for studies in non-hydrothermal environments (McGuire & Collins, 2013; Petersen et al., 2019). Modern transponders can provide two-way travel times with an accuracy of 1 μs, equivalent to sub-millimeter ranging precision (McGuire & Collins, 2013; Petersen et al., 2019). In deep-water settings with stable oceanographic conditions, acoustic ranging can achieve repeatability with a standard deviation as low as 1 mm/km (McGuire & Collins, 2013). However, in regions with more complex temperature structure, such as sites of ocean upwelling, the standard deviation of repeated measurements can exceed 1 cm/km (Petersen et al., 2019). Acoustic ranging errors at mid-ocean ridges are typically higher than other settings because of variations in seawater properties induced by hydrothermal venting. At the Cleft segment of the Juan de Fuca Ridge, Chadwell et al. (1999) observed ranging differences between two

summers of 1 cm over approximately 700 m for a path on one side of the spreading axis, but 2 cm over a similar distance for a path crossing it. This difference was attributed to hydrothermally induced temperature variations. A second experiment at the same site showed a scatter of 2 cm for a 1.2-km-long linear transponder array deployed for one year (Chadwick & Stapp, 2002). The extensometer experiment across the northern rift of Axial seamount reported a scatter of 1 cm over a 400 m baseline (Chadwick et al., 1999). Acoustic velocities change by 4.4 m/s per 1°C of temperature change. This suggests an equivalent temperature change 0.012 - 0.017 ° C is required to produce the observed 3.6-5.2 cm/km scatter in the baselines. In a hydrothermal setting like Axial Seamount, temperature fluctuations up to 0.1° C are entirely plausible (Xu et al., 2018) but the scatter we observe likely has an additional contribution from multipathing.

The acoustic ranging array lies north of the International District and ASHES high-temperature vent fields as well as many sites of diffuse venting and south of the CASM vent field (Figure 1a). The depth of these neutrally buoyant plumes are estimated to be between 1340–1470 m (Mattes et al., 2013) and they circulate over the seamount and around the caldera in an anticyclonic toroidal pattern (clockwise) with large vertical flows on the western caldera wall at these depths (Xu & Lavelle, 2017). As a result, two of the three hydrothermal plumes and the diffuse venting will reach the western baseline first. This pattern of circulation is consistent with the observation that the ranging scatter for the WT-NT baseline (5.2 cm/km) is larger than the NT-ET baseline (3.69 cm/km).

There is a pronounced spatial asymmetry in average extension rates across the caldera. Over the study, the NT-ET extended 24 cm while the WT-NT extended 10 cm (Figure 3a-b). The WT-ET baseline closely tracks NT-ET until May 2025, after which they diverge, indicating that

across-caldera deformation was dominated by eastern extension until this month (Figure S7). The asymmetry is consistent with eruptions occurring in proximity to the eastern caldera wall (Chadwick et al., 2022; Wilcock et al., 2018), where higher extension rates in the east may facilitate fissure opening. The eastern caldera likely experiences more extension simultaneously with inflation because of its proximity to the shallow magma reservoir (Kent et al., 2025).

The extension in the western caldera starts later and accelerates more rapidly than the eastern caldera. The onset of extension on the NT-ET baseline coincides with accelerating uplift starting in May 2024 (Figure 2a), whereas WT-NT extension begins approximately one year later at roughly twice the eastern rate (Figure 2b). The rapid western extension is puzzling; the signal lacks accompanying seismicity or increased moment release rates beneath the west wall (Figure 3b) and is not matched by changes in uplift at the western pressure gauge sites. The signal is short lived and several more months of data will be required to confirm the high rates.

To understand the mechanisms of deformation, we considered the total amount of extension on the three baselines and the uplift observed on the transponder and cabled pressure gauges from September 2022 to August 2025. If the differential uplift between sites in the center of the caldera and near the walls is attributed to slip on the outward-dipping ring faults, the resulting horizontal extension is minimal (Table 1). This indicates that the observed horizontal extension is largely accommodated by distributed volumetric inflation. Previous inflation models (Nooner & Chadwick, 2016; Slead et al., 2024) reproduce vertical uplift reasonably well (Table 1) but do not reproduce the asymmetric pattern of extension (Table 1) and only prolate spheroid source of Nooner & Chadwick (2016) predicts sufficient extension. Analysis of how the depth of a Mogi source (Mogi, 1958) affects extension across a symmetric baseline of 3.3 km suggests that a deep

source at a depth of ~2.5 km below the seafloor is required to match the differential uplift and across-caldera extension (Figure S10).

To further constrain source geometry, we inverted the total extension and drift correct uplift using two model configurations: a single prolate spheroid and two spherical sources (Text S1). The use of non-drift-corrected pressures does not significantly alter the models or their interpretation, nor does excluding the duration of rapid western extension. The best-fit single prolate spheroid accommodates asymmetric baseline deformation by orienting its deeper portion beneath the southern caldera and its shallower portion near the northeastern caldera (Figure 1, S11). Although a single spheroidal source is unlikely to represent the true magma reservoir geometry, this elongated configuration suggests the presence of both shallow and deep pressure sources. The dual spherical source inversion supports this interpretation, placing one shallow source near the eastern caldera at 1.3 km depth and a second deeper source near the southern caldera at 3.3 km depth (Figure 1, S11). The deeper source coincides with the depth at which the Nooner and Chadwick (2016) and Hefner et al. (2020) spheroids are centered. This depth and the location is also consistent with the stacked sill complex imaged at 3 to 5 km depth beneath the southern caldera (Carbotte et al., 2020). The shallow source lies near the northeastern edge of the funnel-like magma structure imaged in 3D multichannel seismic data (Kent et al., 2025), where one of the shallowest portion of the axial magma lens is located. This is a collocated with the highest density of pre-eruptive mixed frequency earthquakes (Wang et al., 2024) indicating eruptive dikes may initiate from this shallow source.

## 3.6 Conclusions

Our three-year acoustic ranging experiment provides the first sustained horizontal geodetic observations during a pre-eruptive inflation phase at Axial Seamount. Deployed transponder units ranged at precision of 3.9-5.2 cm/km. Measurements every 4 hours are smoothed with a 30-day running means to achieve precisions of ~1 cm along each baseline. The data reveal asymmetric extension between the eastern and western caldera, with the east extending more than the west. Our source models reveal that the deformation of Axial Seamount is primarily accommodated by distributed volumetric inflation rather than fault motion, with a deeper source near the southern caldera where stacked sills are located and a shallower source near the northeastern caldera where the axial magma lens is shallow and eruptions originate. Continued data collection from the transponder array is needed to confirm the apparent extensional phase across the western caldera. Deployment of the cabled central caldera transponder will enable real-time ranging and support future development of an AUV capable of navigating using the transponder network for high-resolution seafloor surveys.

## 3.7 Acknowledgments

This material is based partially upon work supported by the Ocean Observatories Initiative (OOI), a major facility fully funded by the US National Science Foundation under Cooperative Agreement No. 2244833, and the Woods Hole Oceanographic Institution OOI Program Office. We thank the personnel of OOI RCA who assisted with the deployments and helped with data downloads over three cruises. We thank William Chadwick and Scott Nooner for their constructive comments and suggestions. Maochuan Zhang for the assistance with the cumulative seismic

moment data and David Caress for providing the high-resolution bathymetry data. This work was supported by NSF award number 2439442.

## Chapter 4: Active Protothrusts and Fluid Highways: Seismic Noise Reveals Hidden Subduction Dynamics in Cascadia

**Authors:** Maleen Kidiwela[1]*, Marine A. Denolle[2], William S. D. Wilcock[1], Kuan-Fu Feng[2,3]

**Affiliations:**

[1]School of Oceanography, University of Washington, Seattle, WA, 98105, USA.

[2]Department of Earth and Space Sciences, University of Washington, Seattle, WA, 98105, USA.

[3]University of Utah, Salt Lake City, UT, 84112, USA.

### 4.0 Abstract

Complex interactions between strain accumulation, fault slip, and fluid migration influence shallow subduction zone dynamics. Using a decade of continuous ambient seismic data from Cascadia's seafloor observatories, we identified distinct regional variations in subduction dynamics. Northern Cascadia exhibits a fully locked megathrust with persistent strain accumulation, while central Cascadia displays a slow slip event on protothrusts and rapid fluid migration along fault systems in the overriding plate. Effective fluid transport through the décollement and the Alvin Canyon Fault likely modulates the earthquake behavior but does not cause slow slip events on the megathrust and likely stabilizes large earthquakes, promoting rupture arrest.

### 4.1 Introduction

The mechanical behavior of megathrusts is crucial for understanding and anticipating tsunami generation and earthquake hazards. The shallow subduction faulting structure affects both short-term earthquake rupture (Wirth et al., 2022) and long-term accretionary wedge development (Barnes et al., 2018). Active geophysical surveys (Carbotte et al., 2024) provide precise structural

data, but most geophysical surveys are onshore, preventing direct observation of seismic activity (Ledeczi et al., 2023). Active faults may behave seismically (with earthquakes), quasi-seismically (with slow earthquakes and tremors), or aseismically through creep. The absence of seismicity and lack of frictional data led to the belief that shallow aseismic creep is ubiquitous (Lay, 2012). However, trench-rupturing earthquakes and new geodetic surveys reveal a slip rate deficit, likely due to frictional locking or stress shadowing (Lindsey et al., 2021). Slow slip and tremor downdip of the megathrust are observed worldwide (Behr & Bürgmann, 2021), with mechanisms proposed to enhance this, such as fluid migration from mineral phase transitions (Bürgmann, 2018). Shallow tremors and low-frequency earthquakes sometimes accompany slow slip events, as seen in the Nankai subduction zone, Japan (Nakano et al., 2018), and the Guerrero segment of the Mexican subduction zone (Plata-Martinez et al., 2021). Determining whether the shallow megathrust and upper-plate faults are locked, partially slipping, or creeping is challenging without near-trench seismic and geodetic observations (Woods et al., 2024).

The active Cascadia Subduction Zone (CZS) exhibits unique characteristics: low background seismicity and downdip episodic tremor and slip (ETS) (Walton et al., 2021). However, its history of large and tsunamigenic earthquakes (Goldfinger et al., 2012) suggests complex deformation mechanisms in the shallow megathrust that remain unexplained. Variations in the downdip ETS and modeled megathrust slip-rate deficit (Schmalzle et al., 2014) may indicate that northern Cascadia is fully locked to the deformation front (Fig. 1), while central Cascadia may be partially locked. The central Cascadia megathrust splay faults are seaward-verging and intersected by west-northwest-striking, left-lateral strike-slip faults, such as the Alvin Canyon Fault (ACF, Fig. 1) (Goldfinger et al., 1997). Recent seismic imaging studies have confirmed the ACF as a major structural discontinuity and crustal tear across the margin, which shifts the slab

depth deeper by ~1.5 km along strike (Fig. 1) (Carbotte et al., 2024). Additionally, central Cascadia has thicker underthrusting sediments and a shallower décollement compared to northern Cascadia (Han et al., 2017), likely reducing fault coupling. Fluids play a key role in both ETS and shallow earthquakes (Hyndman et al., 2015), with deep-origin fluids released to the seafloor (Philip et al., 2023; Teichert et al., 2005). These fluids are generated at the mantle wedge and released updip during ETS (Gosselin et al., 2020). Despite extensive research, the migration pathways, whether through hydraulically connected faults or more complex routes in the upper plate, remain uncertain (Gosselin et al., 2020; Han et al., 2017; Tonegawa et al., 2022b). This uncertainty holds significant implications, as it may directly influence the behavior of the next major earthquake in Cascadia.

The lack of continuous geodetic monitoring in the shallow subduction zone has limited our ability to assess the offshore seismic activity. Recent advances in seismic monitoring, particularly the use of temporal changes in seismic velocity (dv/v), provide a powerful proxy for measuring subsurface strains (Okubo et al., 2024). The approximation that volumetric strain $\varepsilon = -(1/\beta)*dv/v$, with $\beta$ typically around ~ $10^3$-$10^4$ across various regions, units, and materials (Clements & Denolle, 2023; Hillers et al., 2015; Sens-Schönfelder & Eulenfeld, 2019; Takano et al., 2019), seismic frequencies, and depth, allows us to estimate strain values from dv/v. Continuous seismometer recording of ambient seismic waves now enables frequent, high-resolution strain measurements (Larose et al., 2015), once thought unattainable. Using this breakthrough method and a decade of data from broadband seafloor seismometers connected by the Ocean Observatory Initiative Regional Cabled Array in central Cascadia and the Ocean Networks Canada NEPTUNE cabled observatory in northern Cascadia, we gain new insights into offshore strain dynamics, opening opportunities to study fault activity in real-time using dv/v.

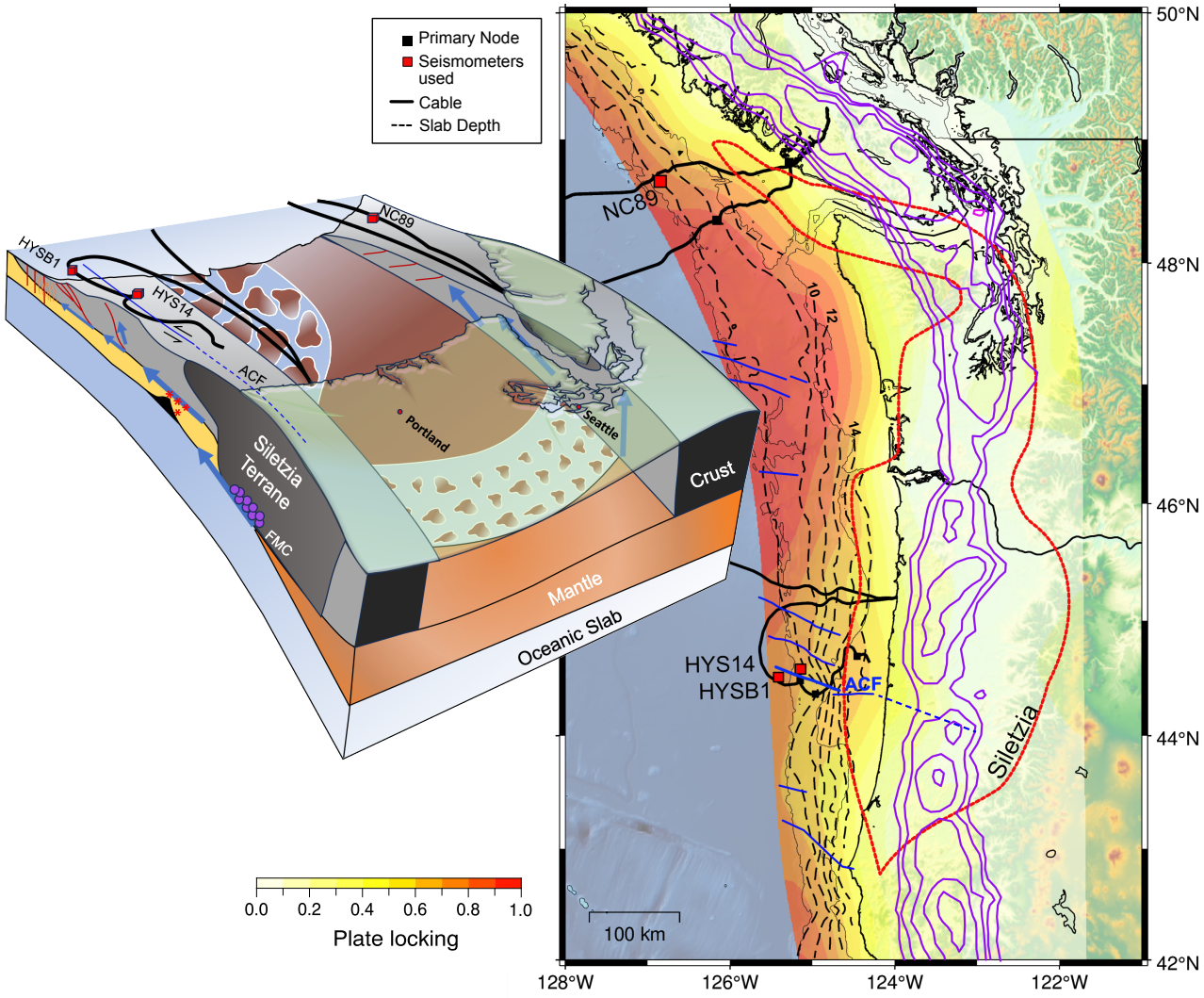


**Figure 1:** Map and schematic of the subduction-zone system in Central and Northern Cascadia. The map shows a locking model for Cascadia (Li et al., 2018), with red contours marking the Siletzia terrane and purple contours representing tremor density (logarithmically spaced 30 to 2,430 per 100 km). Dashed contours indicate plate interface depths (Carbotte et al., 2024), and blue lines show strike-slip faults (Goldfinger et al., 1997). The dashed blue line extends the Alvin Canyon Fault (ACF), where tremor density decreases. Geological units are labeled: the Siletzia Terrane (dark gray), accretionary wedge (light gray), upper mantle (orange), oceanic slab (light blue), forearc crust (light gray), and underthrust sediments in central Cascadia (yellow). The cross-

section shows fluid migration with blue arrows, splay faults and protothrusts in red, and the ACF in blue. The observatory cables and studied stations are shown as black lines and red boxes. Stress barriers are marked in brown, and seismicity related to the black seamount is shown by red stars. Downdip tremor is indicated by purple markers, matching small, locked patches.

## 4.2 Materials and Methods

### 4.2.1 Ambient noise cross-correlation

Ambient Noise interferometric workflows are well-established, and we utilize open-source software in the programming language Julia (SeisNoise.jl (Timothy Clements & Denolle, 2020) and SeisDVV.jl) as well as in Python.

First, station metadata is read from the appropriate StationXML files. These metadata include the instrument response, which is then removed from the raw data to convert the waveforms into physical units of ground motion. Next, the raw time series for each day is detrended, tapered, and initially bandpass-filtered within the frequency range of interest (0.01-10 Hz), ensuring the removal of long-term offsets and out-of-band noise. Amplitude clipping is applied to reduce the effect of high-amplitude transients, and whitening is applied to mitigate the influence of strong narrow-band signals. Finally, the cross-correlation is computed between pairs of channel data streams, with a 1800 s window length and a 100 s lag time, and the results are saved in files. Cross-correlations are stacked daily (or over another specified interval) to improve the signal-to-noise ratio and saved to a file. We perform the dv/v analysis over different frequency bands by applying bandpass filters (0.1-0.3, 0.3-0.6, 0.5-1.0, 1.0-3.0, 3.0-5.0 Hz). We then smooth the cross-correlations using moving average stacks (40-day or 60-day) with a 1-day step to enhance the stability of the correlation function. We further improve the cross-correlation using the denoising

method, which involves combining the singular value decomposition (SVD) of a 2-D NCF with a Wiener filter (Moreau et al., 2017). By applying the Wiener filter to the singular vectors, we maximized the coherency directly in the signal subspace before reconstructing the cross-correlation matrix. This global frequency-domain Wiener deconvolution is not a moving window smoother and does not artificially extend months-long signals. This method is essential for producing stable correlation functions in our ocean-bottom seismometer data, where incoherent signals resulting from non-uniform noise sources are readily present. We created dv/v time series, excluding values with correlation coefficients (CC) less than 0.8. After creating the dv/v time-series *n* for each channel pair, *i*, we performed weighted averaging based on the correlation coefficient (Equation 1-2 obtained from (T. Clements & Denolle, 2023)) to obtain the weighted dv/v time-series. Equation 3 calculates the mean correlation coefficient (*CCmean)*, over a specified number of channels ($N_{ch}$) shown in each dv/v time series (Figure 2 and 3)

$$CC_{sum} = \sum_{i=1}^{n} cc_i^2 \quad (1)$$

$$dv/v = \frac{1}{CC_{sum}} \sum_{i=1}^{n} cc_i^2 \, dv/v_i \quad (2)$$

$$CC_{mean} = \frac{1}{N_{ch}} \sum_{i=1}^{n} cc_i \quad (3)$$

Our investigation revealed that changing the stacking length, window length, and choice of reference cross-correlation significantly control the stability of dv/v observations. We performed a series of experiments to determine which parameters help produce a robust dv/v time series.

60-day stacks are ideal for observing long-term changes, but are not capable of observing transients that are shorter and smaller in magnitude. 40-day stacks are ideal for observing shorter transients. To increase the temporal resolution, the moving average stacking length needs to be changed from

40 days to 3 days. But this alone would not improve the stability of the time series. With the high noise power, the number of singular values must be manually reduced rather than using the Wiener filter. The 2016 asymmetric dv/v (drop + recovery) remains a consistent feature in 3-day stacks, albeit with increased scatter. Therefore, the slow slip is resolved at this frequency.

Separately, dv/v measurements are also affected by parameters such as the stretching window length, stacking length, choice of coda window, choice of reference, and width of the frequency bands. Use of different references other than limiting to a global reference is an important tuning parameter for seismic monitoring (Sens-Schönfelder et al., 2014). The reference is affected by the strongest signals: the 2016 slow slip event is the largest of all signals and obscures the velocity changes of smaller transients that induce a phase shift. This is apparent in the muted visibility of the 2019 velocity drop in Figure 3. In order to emphasize the smaller events, we created a separate reference (2017-2021), excluding the 2016 slow slip event and reducing the correlation function moving average to 40 days (Fig. 4). We chose the stretching window based on the coda decay and the signal-to-noise ratio (SNR) of the correlation function. To achieve this, we computed the squared envelope of the correlation function to determine the coda decay window and its signal-to-noise ratio (SNR). We picked windows where the SNR is higher, and the coda decay rate is higher. This investigation showed that the dv/v time series are more stable when the window lengths are longer in lower frequencies and shorter in higher frequencies.

We experimented with frequency bands, including a 1 Hz bandwidth, in frequencies above 1 Hz. These bands yielded increased variance compared to a 2 Hz bandwidth. However, through an iterative approach, we settled on the hyperparameters listed in Table S1.

### 4.2.2 Depth sensitivity analysis

We used the Ridge2Trench P-wave velocity models (Han et al., 2017) for HYSB1 and HYS14. Based on the Vp/Vs values from the ridge-to-trench study, we calculated an estimated S-wave velocity profile for both locations. We used the open-source software: Disba (Luu, 2024) to solve for the depth sensitivity with depth for single station cross component correlation, which we ran for several frequency bands of interest. The script for running this analysis is available in a Python notebook (src/sensitivity_analysis.ipynb) within our main project repository.

We used a barycentric estimate of the depth sensitivity for each frequency, calculated using

$H_d = \frac{\int Kz\, dz}{\int K\, dz}$, with $K$ the frequency-dependent depth sensitivity shown in Figure S2, to determine the depth of each frequency band. We decided to use this approach because most kernels consist of singular peak. For 0.1 Hz kernel with two peaks, we used the deeper more prominent peak rather than the shallower peak. Table S2 shows each depth estimate corresponding to the frequency. When calculating the distance of fluid migration, we calculated the difference between the lowest and highest depths of the two bands that were compared.

### 4.2.3 Strain calculation

A volumetric strain rate of 0.12 μstrains/year (Davis et al., 2024) was calculated for the northern Cascadia subduction zone using the borehole 1364A. Borehole 1364A is located in proximity to the NC89 seismometer, which we used to assess seismic velocity variability. We used this strain value to optimize the crustal sensitivity β for the CSZ, based on our observed dv/v increase rate of 0.038% per year. This yielded a β value of $3.16 \times 10^3$. In Nankai, a β value of $2.14 \times 10^3$ could be calculated using a volumetric strain rate of 0.14 μstrains/year (Davis et al., 2024)

and a dv/v increase of 0.03% per year (Tonegawa et al., 2022b). Therefore, these β values are consistent with each other even under the presence of large scale geological differences between Nankai and Cascadia.. We used the β value of $3.16 \times 10^3$ for Cascadia to approximate strain values for the central Cascadia strain drop during the inferred slow slip event.

### 4.2.4 Slip calculation

In linear elasticity (shear mode):

$$\Delta\tau = G\,\varepsilon, \tag{3}$$

where, $\Delta\tau$ is the shear stress drop, G is the shear modulus (also denoted μ), ε is the net shear *strain* change ("strain drop") in the region of the fault/crack. In an infinite medium, the standard stress drop of a penny-shaped crack of radius a in an infinite isotropic medium is

$$\Delta\tau = G/\left[\,2\,(1-\nu)\right]\; D_{max} \tag{4}$$

where ν is Poisson's ratio and Dmax is the peak (center) slip. Therefore, $Dmax = 2\,(1-\nu)\,a\,\varepsilon$

If the same circular shear crack of radius a is cut in half by a free surface or boundary, its effective shear stress drop is about half that in the infinite-medium case (the crack is more compliant). Hence, $Dmax = 4\,(1-\nu)\,a\,\varepsilon$

### 4.2.5 Full Waveform Modeling for Seasonal Signals

While the lower frequency bands provide us with important insights into changes in seismic velocity at deep depths, dv/v for frequencies below 1 Hz in ocean environments is influenced by microseismic noise from ocean waves acting on the solid seafloor. Because the cross-correlation is the convolution between the noise source and the path, the microseismic noise in oceans heavily

impinges upon frequencies below 1 Hz. Thus, the seasonal variability of noise sources impacts the correlation functions and, ultimately, dv/v observations. The temporal variability of noise frequency content causes apparent velocity changes due to changes in both amplitude and phase spectra resulting from waveform stretching (Zhan et al., 2013). In stations HYSB1 and NC89, we see an annual and seasonal pattern for the dv/v time series at frequencies below 1 Hz. These observations are similar to the dv/v signals observed in frequency bands between 0.1 and 1 Hz at Axial Seamount (Lee, 2024) and the Greenland ice sheet (Luo et al., 2023).

While oceanographic noise source effects typically affect inter-station cross-correlations, we investigate their impact on the single-station correlation here, anticipating fewer artifacts. We utilize the open-source package Wave Model Sources of Ambient Noise (WMSAN) (Tomasetto et al., 2024) to develop synthetic correlation functions for the HYSB1 station, specifically between the radial and vertical components. In particular, we selected the northern and southern Pacific Ocean basins. The notebook for the analysis is available in the CascadiaDVV project repository (src/synthetic_CC.ipynb). This workflow utilizes oceanic hindcast WAVEWATCH III data (Gaffet et al., 2024) (spectral density of the pressure field) at the ocean surface to calculate temporal variations in the source force amplitude across the Pacific Ocean's ocean bathymetry, with a spatial resolution of 0.5° x 0.5 °. By convolving these as microseism sources with the 3-D synthetic Green's function from a radially symmetric Earth, solved using AXISEM3D in ak135f model (Krischer et al., 2017), and available at the Earthscope Consortium Syngine service. We generated synthetic seismograms for the vertical and radial components of HYSB1. Synthetic seismograms were then used to produce daily correlation functions. The correlation functions were processed using the same processing as in the data examples for the frequency band 0.1-0.3 Hz (e.g., same window length, filtering, FFT, cross-correlation, denoising, dv/v). We observe the same seasonality

pattern within our synthetic DV/V time series (Fig. S3). This suggests that the noise source variability itself is likely responsible for the seasonality observed in the DV/V for frequencies less than 1 Hz.

### 4.2.6 Hierarchical clustering of deep ETS events

We spatially selected tremor locations based on latitude bounds to focus on the region of interest, ensuring that our subsequent analysis only includes events located between 44.4°N and 44.6°N directly downdip of the RCA stations. After sorting and binning the filtered data by time to identify peaks (i.e., intervals that exceed a threshold of 200 events in a seven-day window, shown in Fig. S7), we generate 2D images of their spatial density distribution. We then extract features from these two-dimensional density maps, such as mean density, local maxima counts, and spatial moments. We normalized the feature using standard scaling to homogenize their contribution. Then, we compute a matrix with Euclidean distances between features and each event. We next apply hierarchical clustering, wherein a Ward linkage algorithm iteratively merges the two most similar clusters until all peaks coalesce into a single cluster, producing a dendrogram. Each leaf in this dendrogram represents an individual peak, and clusters merge at higher branches according to greater dissimilarity. We determine where to "cut" the dendrogram by examining silhouette scores across multiple cluster counts, selecting the threshold that yields the most coherent grouping of peaks.

We identify four clusters, defined as cluster 1 (orange), cluster 2 (green), cluster 3 (red), and cluster 4 (blue), in Figures S8 and S9. We find that cluster 3 (in green). Our investigation also revealed that the Tremor episodes in cluster 2 also has the highest cumulative radiative energy and the highest number of recorded tremors among other events.

### 4.2.7 Diffusivity calculation for vertical fluid migration in shallow accretionary wedge

To estimate hydraulic diffusivity for observed fluid migration along the subduction interface, we apply the classic error function solution to the diffusion equation:

$$\frac{(dv/v)}{(dv/v_0)} = erf\left(\frac{z}{2\sqrt{Dt}}\right), \quad (5)$$

where $z$ is the migration depth, $t$ is the lag time between the two depths, and $\frac{(dv/v)}{(dv/v_0)}$ is the ratio of peak dv/v values taken at the shallow over the deep values. Lag time is calculated at the lowest point in each triangular function, and as each timeseries has undergone the same processing, this will not impact the calculation of migration speeds or width comparisons between the frequencies.

From this equation, we can solve for hydraulic diffusivity $D$ as:

$$D = \frac{1}{t}\left(\frac{z}{2 \cdot erf^{-1}((dv/v)/(dv/v_0))}\right)^2. \quad (6)$$

At Slope Base, where the fluid pulse migrated $z$ = 200 m over $t$ = 69 days, the calculated diffusivity is approximately $D = 1.4\times10^{-4}$ m$^2$/s. At Hydrate Ridge, $z$ = 300 m and $t$ = 57 days, the diffusivity is $D = 3.8\times10^{-4}$ m$^2$/s. These values are consistent with hydraulic diffusivity values in Nankai and Costa-Rica subduction zones, ranging from $10^{-6}$ and $10^{-4}$ m$^2$/s (Hammerschmidt et al., 2013; LaBonte et al., 2009; Tanikawa et al., 2014).

### 4.2.8 Fluid Flow on the Décollement or the ACF

For the **horizontal flow**, which we assume occurs along the décollement between Hydrate Ridge and Slope Base, the migration is thought to be an efficient process in a conduit. We use equation (4) of (Saffer, 2014)

$$(dv/v)/(dv/v_0) = \left(\frac{1}{1+4tD/h^2}\right)^{1/2} \quad (7)$$

Given the ratio in $(dv/v)/(dv/v_0)$, assuming that channel width can range from a fault (h = 10 m) to thick underthrusted sediment (1000 m), the décollement or ACF fault width at the two stations and the lag time of 34 days, we find hydraulic diffusivity to range from 8.86 x $10^{-6}$ to 8.86 x $10^{-2}$ $m^2/s$.

We could calculate hydraulic diffusivity using the hydrogeological definition and known parameters for subduction zone shallow sediments:

$$D=k/\mu\,(\alpha+ne\,\beta) \quad (8)$$

where the intrinsic permeability is $k=1\times10^{-14}$ $m^2$, the effective porosity is $n_e$= 0.15 (Philip et al., 2023), the matrix compressibility is $\alpha = 1\times10^{-10}$ $Pa^{-1}$(Dugan & Sheahan, 2012), fluid compressibility thermodynamic equation of state (TEOS-10) $\beta=4.0\times10^{-10}$ $Pa^{-1}$, and fluid viscosity $\mu=1\times10^{-3}$ Pa·s (Philip et al., 2023). Substituting these gives $D \approx 6.3\times10^{-2}$ $m^2/s$. This value is in the same order of magnitude as the hydraulic diffusivity calculated above for a conduit as wide as 1 km.

**4.3 Results**

We analyzed single-station cross-component ambient noise interferometry at the northern Cascadia Clayoquot Canyon station (NC89) and at the central Cascadia stations Hydrate Ridge (HYS14) and Slope Base (HYSB1) (Figure 1). In central Cascadia, we also conducted interstation ambient noise interferometry between these stations.

Northern Cascadia shows a persistent, quasi-linear increase in seismic velocity, with a dv/v trend of +0.038% per year over 13 years in the 1-3 Hz band (Fig. 2). Assuming $\beta = 10^3$-$10^4$, we

calculated a volumetric strain rate of approximately 0.04-0.4 μstrains/year. This is consistent with borehole pressure data from Hole 1364A in proximity to NC89 at Clayoquot Canyon, which shows compressional volumetric strain rate of 0.12 μstrains/year (Davis et al., 2024), and with the linear geodetic strain rate of 0.4 μstrains/year from a 4.1 cm/year convergence rate over 100 km; although linear convergence represents only part of the total volumetric strain. This aligns well with the full locking inferred from onshore geodetic data in northern Cascadia, where megathrust locking causes compaction of the shallow accretionary wedge sediments, increasing seismic velocities in the subsurface.

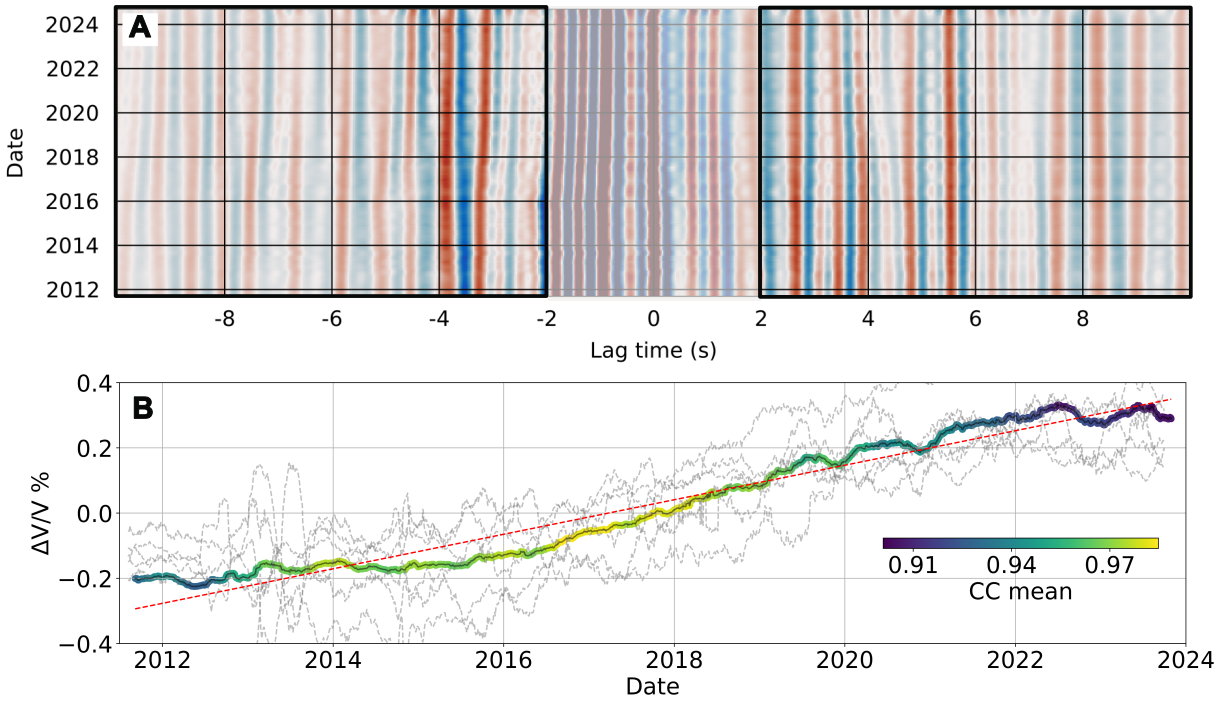


**Figure 2:** Long-term dv/v in northern Cascadia. (A) Single-station cross-correlation between HHZ and HHE components at NC89, bandpass filtered from 1-3 Hz and smoothed with a 60-day running mean, with the coda window for dv/v measurements highlighted. (**B**) dv/v measurements, showing individual causal and anticausal time series for ZE, NE, ZN cross-components in gray, with the

weighted average represented by a color-coded line and the average correlation coefficient. The absence of sudden changes in (A) and the steady increase in dv/v in (B) indicate continuous strain accumulation.

The velocity changes in central Cascadia differ significantly from those in northern Cascadia, with two key events. First, a drop in seismic velocity occurred on 17 July 2016, lasting about two months (Fig. 3). Temporal changes in dv/v are typically observed during earthquakes (Okubo et al., 2024). Still, in this case, the changes are not instantaneous (Fig. S1), and do not follow standard earthquake relaxation models (Snieder et al., 2017). Since this event was not observed at Hydrate Ridge, we rule out the possibility of a slow earthquake on the megathrust or the ACF. Submarine landslides are also unlikely, as they typically increase seismic velocity (positive dv/v) due to the added load of sediments sliding down to the slope base. Instead, reflection surveys (Han et al., 2017) show 45-degree dipping protothrusts beneath the station, with approximately $a$ = 3 km fault widths. A dv/v drop of 0.2% yields a maximum volumetric strain drop of $\varepsilon$ = 2 μstrains. The maximum displacement of a half-crack on a traction-free boundary $Dmax = 4(1-\nu)a\varepsilon \sim 1$ cm *(50),* where the Poisson ratio $\nu$ = 0.5 is consistent with elevated pore pressure in shallow sediments (Han et al., 2017). The resulting displacement is consistent with those of known slow slip events (Araki et al., 2017).

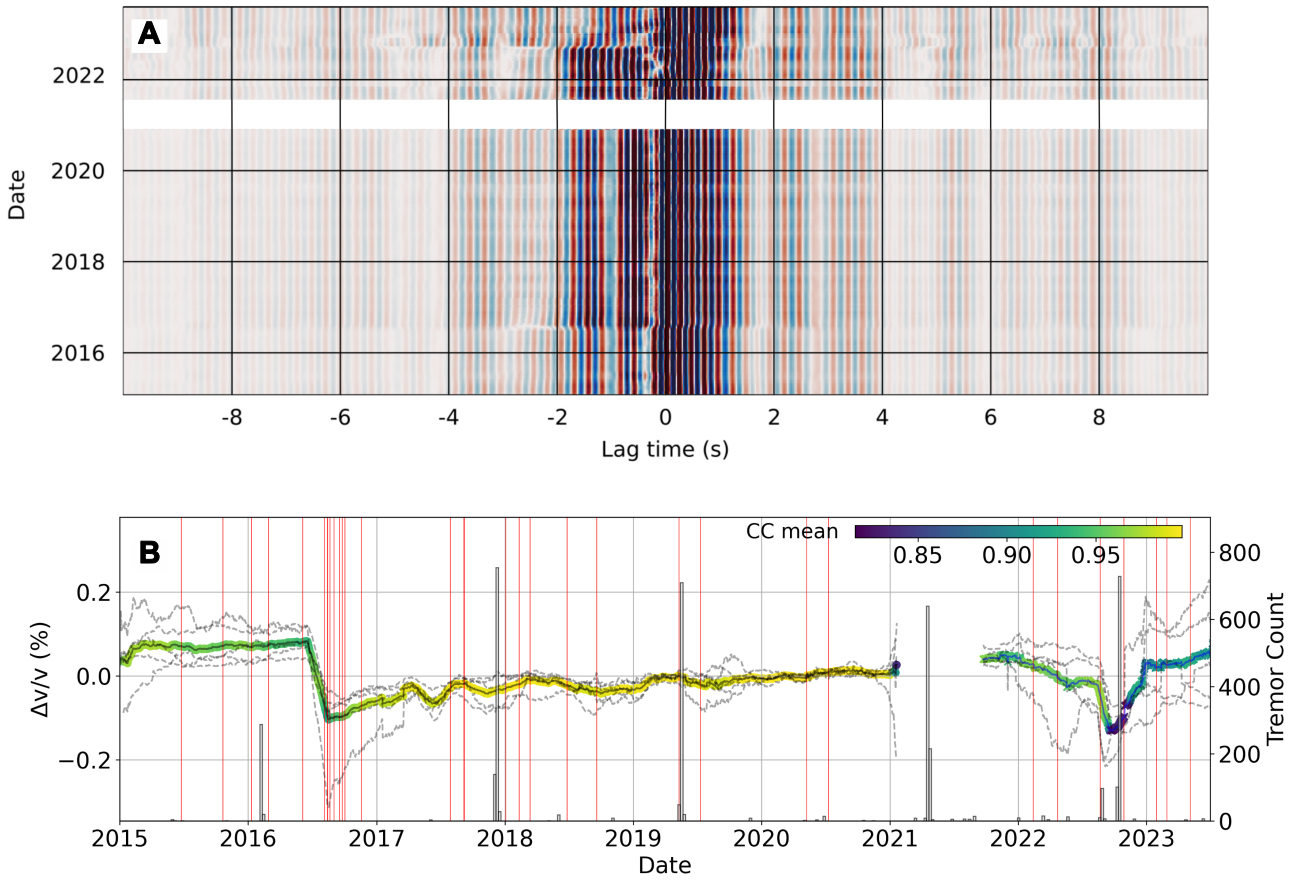


**Figure 3:** dv/v suggests a slow slip and episodic fluid expulsion in central Cascadia protothrusts. (A) Cross-correlation function between BHZ and BHE components at HYSB1. (B) dv/v at HYSB1 in the 3-5 Hz range, averaged over causal and anti-causal windows of ZE, ZN components and causal window of NE cross-components in dashed grey lines. Red lines mark shallow tectonic tremor timing (Krauss et al., 2024), and black histograms show deep tectonic tremor timing at 44.4˚N-44.6˚N (PNSN, binned at 7 days, (Wech, 2010). Unlike northern Cascadia, where strain builds monotonically, the Juan de Fuca Plate shows an asymmetric 2-month dv/v drop with partial recovery, interpreted as slow slip on the protothrust. Several transient pulses in 2019 and 2022 suggest slip-free strain changes, likely due to fluid migration.

A second event type was observed in 2022 on the Slope Base, marked by a gradual decrease in seismic velocity followed by a slow recovery over several months (Fig. 3). Although only the HYSB1 station was operational in 2022, similar events were detected in 2019 at both HYS14 and HYSB1 by focusing on the period from 2017 to 2021. Unlike earthquake-induced changes, this gradual drop and recovery does not indicate strain released through fast fault slip. During these transients, the wavefield correlation coefficient (CC) decreases (Fig. S7), suggesting a temporary change in scattering properties (Tonegawa et al., 2022b). We propose that these events are pulses of elevated pore pressure, likely driven by fluids. Similar dv/v and CC transients have also been documented during fluid-injection operations (Hillers et al., 2015). The most notable results are the lag times between the peaks of these pulses at different sites and frequencies. In the 1-3 Hz, a 34-day lag is observed between HYS14 (megathrust side) and HYSB1 (protothrust side), implying a horizontal propagation velocity of 0.58 km/day. The inter-station correlations show that the phenomenon occurs both at and between the stations (Fig. S5). At higher frequencies, which are more sensitive to shallower depths, the lag times between 1-3 Hz and 3-5 Hz are longer–69 days at Slope Base and 57 days at Hydrate Ridge. These differences imply upward fluid migration velocities of 4 m/day at Slope Base (HYSB1) and 9 m/day at Hydrate Ridge (HYS14). Another key feature is that the pulse narrows below HYS14 (lasting 4 months) at greater depths but broadens as it moves past the deformation front at Slope Base (6 months) and into shallow sediments. The broadening suggests diffusion. The primary fluid migration pathways between Hydrate Ridge and Slope Base are the décollement (Han et al., 2017) and ACF (Philip et al., 2023), while splay faults, ACF and the proto-thrusts (Han et al., 2017) play a crucial role in upward fluid transport. Further evidence for fluid migration is shown by the drop in the lagged correlation

coefficient and temporal variations, indicating scattering changes likely induced by fluids (Fig. S9).

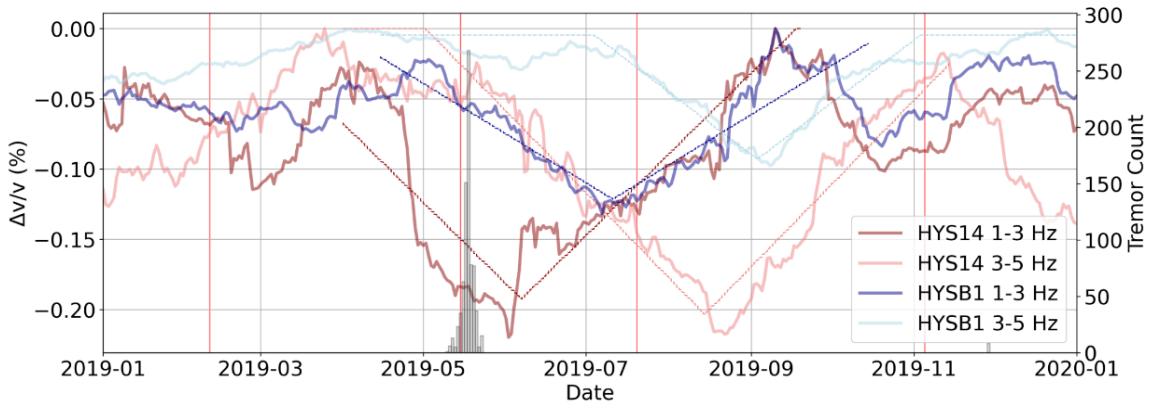


**Figure 4:** Multi-component weighted dv/v observations associated with fluid pulse migration during the 2019 ETS event. dv/v for Hydrate Ridge (HYS14) and Slope Base (HYSB1) stations in 2019 at 1-3 Hz and 3-5 Hz frequency bands, with deeper and shallower sensitivity *(50)*. Red represents the downdip site at Hydrate Ridge (HYS14), one on the upper plate, and blue represents the updip site at Slope Base (HYS1B), past the deformation front on the downgoing plate. Dashed lines are triangle functions fitted to velocity drops. Lag times are intervals between the lowest points of these functions.

Finally, another key finding is the timing of downdip tremor with the onset of the 2019 and 2022 events (Figs. 3 and 4). Hydromechanical models predict that solitary pore pressure waves, without fluid transport, could propagate updip at approximately 90 km/hr (Cruz-Atienza et al., 2018) along the décollement and are consistent with speeds of rapid tremor streaking in Cascadia (Ghosh et al., 2010). This may explain the synchronization between deep ETS and fluid pulses at Hydrate Ridge (Fig. 4) in our data. While downdip ETS occurs regularly, the shallow response is

more erratic with no dv/v drop was detected during the 2016, 2018, and 2021 ETS events. Hierarchical clustering of tremor spatial density *(50)* shows that only the highest radiative energy released, spatially connected tremor episodes with large tremor counts coincided with dv/v drops (Figs. S8-S10). These results provide the first in situ measurements of shallow fluid release during ETS events in Cascadia, offering new insights into the interaction between fluid migration and seismogenic processes.

**4.4 Discussion**

The long-term trends dv/v between northern and central Cascadia align with variations in geodetic models of slip-rate deficit and underlying mechanisms at play. In northern Cascadia, the consistent increase in seismic velocity and its magnitude suggests a high locking ratio at the megathrust, consistent with observations of a fully locked margin up to the deformation front. This interpretation is supported by relatively low offshore seismicity (Stone et al., 2018), a steady increase in borehole pore pressure (Davis et al., 2024), and higher offshore locking ratios derived from onshore geodetic data (Li et al., 2018). In contrast, central Cascadia shows both lower strain accumulation and the presence of transient phenomena, suggesting a lower locking ratio. These differences are also apparent in the lowest frequency band (0.1-0.3 Hz), with dv/v rates of 0.006%/year in northern Cascadia and 0.003% in central Cascadia (Fig. S4). When interpreted in terms of locking rate, the locking ratio in central Cascadia is approximately half that of northern Cascadia. This observation is consistent with models of slip-rate deficit inferred from lower coastal uplift rates (Burgette et al., 2009) and onshore geodetic data (Li et al., 2018; Schmalzle et al., 2014). The difference in locking ratios may also be influenced by factors such as the subduction of a seamount (Carbotte et al., 2024), the underthrusting of fluid-rich sediments (Han et al., 2017),

higher seismicity rates compared to other parts of Cascadia (Stone et al., 2018), and the presence of very low-frequency earthquakes (Chaudhuri & Ghosh, 2022).

ETS events in subduction zones are suspected to trigger the upward migration of deep fluids (Nakajima & Uchida, 2018). At 30–40 km depth, near the forearc mantle corner, the dehydration of subducted metabasalt releases fluids that accumulate and build up pore pressure beneath an impermeable seal, as indicated by low-velocity, high Poisson's ratio anomalies in the oceanic crust (Audet et al., 2009; Calvert et al., 2020; Hyndman et al., 2015; Rubinstein et al., 2008, 2009). A "fault-valve" mechanism, which couples fault slip, the evolution of near-fault permeability, and fluid flow driven by pressure gradient (Gosselin et al., 2020; Ozawa et al., 2024), may explain the temporal variations in seismic properties observed in the ETS zone (Herath & Audet, 2024). We propose that synchronizing deep ETS with fluid-related transients in dv/v points to the episodic release of deep fluids through the seafloor, as also hypothesized in other subduction zones like Nankai (Nakajima & Uchida, 2018; Tonegawa et al., 2022b). Our hierarchical clustering of the deep ETS events in Cascadia between latitudes 44.4˚N and 44.7˚N reveals that ETS clusters occurring concurrently with dv/v drops in 2019 (Fig. 4) and 2022 (Fig. 3) are tightly grouped (Figs. S8-S10). The tremor density analysis shows that these clusters are denser and interconnected, with many ETS events (Fig. S10). This suggests that specific characteristics of ETS may be modulating a pore pressure wave that propagates from the ETS zone to the seafloor and along the décollement.

The permeability structure of the upper plate plays a crucial role in the propagation of solitary pore-pressure waves or in the migration of fluids themselves during ETS and co-seismic ruptures (Viesca & Garagash, 2015). When pore pressure reaches a critical level, trapped fluids are often released during slow slip events due to dilatancy (Cruz-Atienza et al., 2018; Warren-Smith et al.,

2019), typically coinciding with low-frequency earthquakes. These fluids begin to migrate upward, either through the overriding plate if it is permeable or along a megathrust channel (Herath & Audet, 2024; Kita et al., 2021; Nakajima & Uchida, 2018). The more permeable upper plate in northern Cascadia allows fluids to migrate through the upper plate itself, as observed in Hikurangi, New Zealand. In contrast, in central Cascadia, where the upper plate is less permeable due to the presence of Siletzia terrane (Egbert et al., 2022), we propose that fluids migrate along the décollement, similar to those in the Nankai Trough (Nakajima & Uchida, 2018). The fluids that migrate may be stored in shallow regions up-dip edge of Siletzia (Egbert et al., 2022). The solitary pore-pressure waves may or may not be related to these longer-term fluid migrations (43) as described in (29).

The Alvin Canyon Fault (ACF) is a crustal tear across the margin (Carbotte et al., 2024) that serves as another potential conduit for the observed fluid pulses during deep ETS events, as it is known to transport fluids from the décollement to the surface (Philip et al., 2023). Similar to the ACF, the Wecoma fault is another strike-slip fault north of the ACF that has been shown to be a high-angle fluid escape conduit, dewatering the megathrust décollement (Tobin et al., 1993). Whether fluids move upward along the ACF or the décollement, both pathways indicate effective fluid transport, preventing the buildup of high pore pressure during coseismic events and thereby mitigating dynamic weakening effects such as thermal pressurization. The stabilization effect may explain why Hydrate Ridge has been a location where many partial margin ruptures have terminated (Goldfinger et al., 2012). Additionally, the presence of ACF, Daisy Banks, and Wecoma strike-slip faults in this region likely locally inverts thrusting to seaward vergence (Tobin et al., 1993) by facilitating the escape of highly overpressured fluids from the megathrust décollement.

In Northern Cascadia, magnetotelluric (Egbert et al., 2022) and seismic imaging (Delph et al., 2018) studies reveal that the forearc crust is relatively conductive, exhibiting lower seismic velocities and a high Vp-Vs ratio, which indicates fluid-rich conditions. These characteristics suggest that fluids, potentially at lithostatic pressure, can migrate vertically within the overriding plate (Audet et al., 2009; Calvert et al., 2020). Additionally, seismic velocity drops followed by rapid recovery during deep ETS events have indicated a temporal reduction in pore pressure and the breaching of a low-permeability material near the megathrust during slow slip events (Gosselin et al., 2020). The regular expulsion of fluids from the deep ETS zone into the upper plate likely prevents pore pressure buildup along the megathrust, thereby enhancing the fault clamping and locking (Saffer, 2014). Furthermore, borehole pressure data from U1364A show no transient pressure change during slow slip events (Davis et al., 2023), which aligns with our observations of stable dv/v measurements in northern Cascadia.

The upper plate structure of Central Cascadia is dominated by the thicker, impermeable Siletzia Terrane, which contacts the plate interfaces and extends offshore into central Oregon. The ACF plays a key role in the shallow subduction system, acting as a barrier to the along-strike propagation of both fast and slow earthquakes (Carbotte et al., 2024). Fluids generated at depth become trapped up-dip and stored on the up-dip edge of Siletzia Terrane (Egbert et al., 2022). The geological structure between the downdip ETS zone and the deformation front is complex, including a subducted seamount, land-vergence splay faults thought to be seismically active (Ledeczi et al., 2023), and protothrusts interpreted as being fluid-saturated past the deformation front (Moore et al., 1995). Geochemical evidence shows that fluids from the frontal protothrust zone and Hydrate Ridge contain significant amounts of fluids originating from the décollement (Teichert et al., 2005). We propose that hydraulic connectivity between the updip ETS zone and

the frontal thrust, where pore pressure waves propagating from the ETS zone drive the flow of shallow stored fluids (Egbert et al., 2022) up to the protothrusts along the decollement or ACF. Numerical models suggest that fault-valve instability, driven by cyclic permeability changes during slow slip events, triggers the propagation of pore-pressure waves (Cruz-Atienza et al., 2018). The décollement and the ACF are the primary fluid pathways, as indicated by negative polarity reflections at the base of the protothrusts (Cochrane et al., 1994; Han et al., 2017; Moore et al., 1995). Although these pulses occur at a greater depth than the dv/v sensitivity shown in Fig. 4, our depth-integrated measurements, which have enhanced sensitivity at lower frequencies of dv/v, also contain transient dv/v drops, confirming that the source of these perturbations lies in the deeper crust (Fig. S6).

As the elevated pore pressure wave arrives in the shallow subduction zone, we propose that the high fluid pressure gradient induces flow along hydraulically connected pathways, such as décollement, splay faults, protothrusts, and cross-cutting strike-slip faults. The vertical migration is well explained by diffusion through narrow faults distributed across complex networks, including splay faults and protothrusts. We find a vertical diffusivity of $\sim 3.8\times10^{-4}$ $m^2/s$, consistent with hydraulic diffusivity values in Nankai and Costa-Rica *(50)*. Horizontal migration is similarly well explained by a flow in a 1 km-thick conduit with a hydraulic diffusivity of $\sim 6.3x10^{-2}$ (Saffer, 2014), which aligns with expectations based on hydrogeological parameters and the role of underthrusted sediments below the plate interface in fluid transport (Han et al., 2017). Over time, the pore pressure in the seaward décollement may lower the effective normal stress within the proto-thrusts and leading to slow slip.

An alternative explanation for the delayed dv/v drops is potentially a strain wave occurring along the decollement. While there is no substantial evidence for this claim exists from tremor and seafloor geodesy, it has been shown that a strain wave migrating along the decollement could potentially causes pore pressure transients in the wedge above it without a permanent change in strain (Edgington et al., 2025). Whether this may a possibility in Cascadia needs to be investigated through future geophysical experiments in the region.

Our transient dv/v signatures provide the first *in-situ* evidence of the dynamics and timescales associated with fluid transport in shallow subduction zones. Our observations are consistent with the possibility of a rapid pressure wave migrating from the ETS zone, which transitions into a slower fluid migration accommodated by flow in the primary conduits such as the décollement and the ACF and diffusion vertically to the seafloor through more distributed fault networks along protothrusts, splay faults, and cross-cutting ACF. We hypothesize that elevated pore pressure buildup at the base of protothrusts drains through intermittent slow slip and fluid diffusion. Over the past few decades, fluid transport has not been accompanied by slow slip on the shallow megathrust, nor has it altered the strain accumulation rate on the central Cascadia megathrust. The current locking ratio at 50% (Li et al., 2018) (Fig. 1) implies that partial creep has proceeded uninterrupted by fluid transport phenomena during the instrumental record. We cannot infer that fluids are pressurized enough to trigger earthquakes on the splay faults or the ACF at this location. While this does not negate the possibility of their activation during large megathrust earthquakes (Ledeczi et al., 2023), their role as fluid pathways likely reduces fluid-induced dynamic frictional weakening effects, stabilizes large ruptures, and acts as barriers to megathrust earthquakes in Cascadia. The upcoming expansion of the seafloor observatory will provide new

opportunities to validate our interpretation further and enhance our ability to detect micro-seismicity that may otherwise be overlooked by the current network of two stations.

### 4.5 Acknowledgments:

We thank Demian Saffer and Harold Tobin for their discussion about permeability structure in a shallow subduction zone, Zoe Krauss for providing the offshore shallow tremor catalog for HYSB1, and Lisa Tomasetto for providing the WMSAN codebase used to create synthetic correlation functions. This material is based upon work supported by the Ocean Observatories Initiative (OOI), a major facility fully funded by the US National Science Foundation under Cooperative Agreement No.2244833, and the Woods Hole Oceanographic Institution OOI Program Office. The facilities of EarthScope Consortium were used for access to waveforms, related metadata, and/or derived products used in this study. These services are funded through the National Science Foundation's Seismological Facility for the Advancement of Geoscience (SAGE) Award under Cooperative Agreement EAR-1724509 to William Wilcock. This work is supported by the Seismic Computational Platform for Empowering Discovery (SCOPED) project under the National Science Foundation (Award no. OAC-2103701 to Marine Denolle), and by the Jerome M. Paros Endowed Chair in Sensor Networks at the University of Washington (William Wilcock).

## Chapter 5: Conclusions

This thesis investigates three distinct modes of oceanic crustal deformation, progressing from continental rifting through oceanic crustal formation to subduction. Each chapter employs a different geophysical method (tomography, geodesy, and ambient noise interferometry) and advances its application to seafloor settings. Chapter 2 examines back-arc rifting in the Bransfield Basin, demonstrating that subducting plate architecture exerts a first-order control on basin evolution and crustal thinning. We introduce a new tomographic workflow that exploits secondary arrivals traversing a magma chamber to improve P-wave imaging of the melt reservoir. Chapter 3 characterizes inter-eruptive extensional processes at Axial Seamount, a mid-ocean ridge volcano strongly influenced by the Cobb hotspot. We combine vertical uplift from pressure gauges with horizontal distance changes measured along one of the longest acoustic ray paths to model the sources contributing to the volcanic deformation field. Chapter 4 investigates shallow megathrust dynamics in the Cascadia subduction zone, with respect to strain accumulation, fluid flow, strike-slip faulting, protothrust development, and upper plate permeability structure. We apply novel denoising methods to improve single-station cross-component ambient noise interferometry for ocean settings.

Two themes unify the thesis. First theme showcases how fluids play a critical role in crustal deformation at all three settings. In Chapter 2, fluids released from the deep subducting slab control deformational patterns in the back-arc basin. In Chapter 3, magmatic fluid migration into different reservoirs beneath the volcano produces asymmetric caldera deformation. In Chapter 4, deep fluids migrating from the forearc mantle corner to the shallow megathrust may influence earthquake rupture dynamics. Second theme addresses how slab tears at different depths along the subducting

plate influence crustal deformation in distinct ways. In Chapter 2, a deep slab tear governs the formation of a large volcano and modify the slab depth, increasing the water supply to the back arc and altering the rates of slab rollback. In Chapter 4, a shallower crustal tear manifests as a strike-slip fault across the megathrust, accommodating fluid flow across the forearc.

**Chapter 6: Future work**

The three-dimensional tomography model from Chapter 2 provides the foundation for relocating earthquakes at Orca Volcano to better understand the processes that led to the 2020 seismic crisis (over 85,000 earthquakes). Incorporating this velocity model into gravity and magnetic inversions would further constrain subsurface rheology.

Chapter 3 represents only the first three years of a 10-year acoustic ranging experiment at Axial Seamount. A continuous dataset spanning pre-eruptive, eruptive, and post-eruptive periods would clarify the eruption dynamics shaping this volcano. Redeploying the central caldera cabled acoustic transponder would enable real-time ranging capability. These transponders could also support experiments controlling an Autonomous Underwater Vehicle (AUV) from shore, with the objective of enabling remote AUV response to eruptions detected by the OOI-RCA.

The geodynamic analysis in Chapter 4 provides a starting point for monitoring continuous strain evolution in Cascadia. New seismometer deployments associated with the central Cascadia OOI-RCA expansion will enable long-term ambient noise workflows that can be cross-validated against complementary instruments, including pressure gauges, optical strain meters, and distributed acoustic sensing networks.

**References**

Ágústsdóttir, T., Winder, T., Woods, J., White, R. S., Greenfield, T., & Brandsdóttir, B. (2019). Intense Seismicity During the 2014–2015 Bárðarbunga-Holuhraun Rifting Event, Iceland, Reveals the Nature of Dike-Induced Earthquakes and Caldera Collapse Mechanisms. *Journal of Geophysical Research: Solid Earth*, *124*(8), 8331–8357. https://doi.org/10.1029/2018JB016010

Almendros, J., Wilcock, W., Soule, D., Teixidó, T., Vizcaíno, L., Ardanaz, O., et al. (2020). BRAVOSEIS: Geophysical investigation of rifting and volcanism in the Bransfield strait, Antarctica. *Journal of South American Earth Sciences*, *104*, 102834. https://doi.org/10.1016/j.jsames.2020.102834

Anderson, M. O., Chadwick Jr., W. W., Hannington, M. D., Merle, S. G., Resing, J. A., Baker, E. T., et al. (2017). Geological interpretation of volcanism and segmentation of the Mariana back-arc spreading center between 12.7°N and 18.3°N. *Geochemistry, Geophysics, Geosystems*, *18*(6), 2240–2274. https://doi.org/10.1002/2017GC006813

Arai, R., & Dunn, R. A. (2014). Seismological study of Lau back arc crust: Mantle water, magmatic differentiation, and a compositionally zoned basin. *Earth and Planetary Science Letters*, *390*, 304–317. https://doi.org/10.1016/j.epsl.2014.01.014

Araki, E., Saffer, D. M., Kopf, A. J., Wallace, L. M., Kimura, T., Machida, Y., et al. (2017). Recurring and triggered slow-slip events near the trench at the Nankai Trough subduction megathrust. *Science*, *356*(6343), 1157–1160. https://doi.org/10.1126/science.aan3120

Arnoux, G. M., Toomey, D. R., Hooft, E. E. E., & Wilcock, W. S. D. (2019). Seismic Imaging and Physical Properties of the Endeavour Segment: Evidence that Skew Between Mantle

and Crustal Magmatic Systems Governs Spreading Center Processes. *Geochemistry, Geophysics, Geosystems*, *20*(3), 1319–1339. https://doi.org/10.1029/2018GC007978

Arnulf, A. F., Harding, A. J., Kent, G. M., Carbotte, S. M., Canales, J. P., & Nedimović, M. R. (2014). Anatomy of an active submarine volcano. *Geology*, *42*(8), 655–658. https://doi.org/10.1130/G35629.1

Arnulf, A. F., Harding, A. J., Kent, G. M., Singh, S. C., & Crawford, W. C. (2014). Constraints on the shallow velocity structure of the Lucky Strike Volcano, Mid-Atlantic Ridge, from downward continued multichannel streamer data. *Journal of Geophysical Research: Solid Earth*, *119*(2), 1119–1144. https://doi.org/10.1002/2013JB010500

Arnulf, A. F., Harding, A. J., Kent, G. M., & Wilcock, W. S. D. (2018a). Structure, Seismicity, and Accretionary Processes at the Hot Spot-Influenced Axial Seamount on the Juan de Fuca Ridge. *Journal of Geophysical Research: Solid Earth*, *123*(6), 4618–4646. https://doi.org/10.1029/2017JB015131

Arnulf, A. F., Harding, A. J., Kent, G. M., & Wilcock, W. S. D. (2018b). Structure, Seismicity, and Accretionary Processes at the Hot Spot-Influenced Axial Seamount on the Juan de Fuca Ridge. *Journal of Geophysical Research: Solid Earth*, *123*(6), 4618–4646. https://doi.org/10.1029/2017JB015131

Artemieva, I. M. (2023). Back-arc basins: A global view from geophysical synthesis and analysis. *Earth-Science Reviews*, *236*, 104242. https://doi.org/10.1016/j.earscirev.2022.104242

Aster, R., Thurber, C., & Borchers, B. (2012). Parameter Estimation and Inverse Problems. In *Parameter Estimation and Inverse Problems*.

Audet, P., Bostock, M. G., Christensen, N. I., & Peacock, S. M. (2009). Seismic evidence for overpressured subducted oceanic crust and megathrust fault sealing. *Nature*, *457*(7225), 76–78. https://doi.org/10.1038/nature07650

Avouac, J.-P. (2015). From Geodetic Imaging of Seismic and Aseismic Fault Slip to Dynamic Modeling of the Seismic Cycle. *Annual Review of Earth and Planetary Sciences*, *43*(Volume 43, 2015), 233–271. https://doi.org/10.1146/annurev-earth-060614-105302

Baillard, C., Wilcock, W. S. D., Arnulf, A. F., Tolstoy, M., & Waldhauser, F. (2019a). A Joint Inversion for Three-dimensional P and S Wave Velocity Structure and Earthquake Locations Beneath Axial Seamount. *Journal of Geophysical Research: Solid Earth*, *124*(12), 12997–13020. https://doi.org/10.1029/2019JB017970

Baillard, C., Wilcock, W. S. D., Arnulf, A. F., Tolstoy, M., & Waldhauser, F. (2019b). A Joint Inversion for Three-dimensional P and S Wave Velocity Structure and Earthquake Locations Beneath Axial Seamount. *Journal of Geophysical Research: Solid Earth*, *124*(12), 12997–13020. https://doi.org/10.1029/2019JB017970

Bajgain, S. K., Ashley, A. W., Mookherjee, M., Ghosh, D. B., & Karki, B. B. (2022). Insights into magma ocean dynamics from the transport properties of basaltic melt. *Nature Communications*, *13*(1), 7590. https://doi.org/10.1038/s41467-022-35171-y

Barclay, A. H., Toomey, D. R., & Solomon, S. C. (1998). Seismic structure and crustal magmatism at the Mid-Atlantic Ridge, 35°N. *Journal of Geophysical Research: Solid Earth*, *103*(B8), 17827–17844. https://doi.org/10.1029/98JB01275

Barker, D. H. N., & Austin, J. A. (1998). Rift propagation, detachment faulting, and associated magmatism in Bransfield Strait, Antarctic Peninsula. *Journal of Geophysical Research: Solid Earth*, *103*(B10), 24017–24043. https://doi.org/10.1029/98JB01117

Barker, P. F. (1982). The Cenozoic subduction history of the Pacific margin of the Antarctic Peninsula: ridge crest–trench interactions. *Journal of the Geological Society*, *139*(6), 787–801. https://doi.org/10.1144/gsjgs.139.6.0787

Barker, P. F., Dalziel, I. W. D., & Storey, B. C. (1988). *Tectonic development of the Scotia Arc region* (Antarctic geology). Oxford: Clarendon Press.

Barnes, P. M., Ghisetti, F. C., Ellis, S., & Morgan, J. K. (2018). The role of protothrusts in frontal accretion and accommodation of plate convergence, Hikurangi subduction margin, New Zealand. *Geosphere*, *14*(2), 440–468. https://doi.org/10.1130/GES01552.1

Battaglia, M., Cervelli, P. F., & Murray, J. R. (2013). *Modeling crustal deformation near active faults and volcanic centers: a catalog of deformation models and modeling approaches* (No. 13-B1). *Techniques and Methods*. U.S. Geological Survey. https://doi.org/10.3133/tm13B1

Bayrakci, G., Minshull, T. A., Sawyer, D. S., Reston, T. J., Klaeschen, D., Papenberg, C., et al. (2016). Fault-controlled hydration of the upper mantle during continental rifting. *Nature Geoscience*, *9*(5), 384–388. https://doi.org/10.1038/ngeo2671

Beachly, M. W., Hooft, E. E. E., Toomey, D. R., & Waite, G. P. (2012). Upper crustal structure of Newberry Volcano from P-wave tomography and finite difference waveform modeling. *Journal of Geophysical Research: Solid Earth*, *117*(B10). https://doi.org/10.1029/2012JB009458

Behr, W. M., & Bürgmann, R. (2021). What's down there? The structures, materials and environment of deep-seated slow slip and tremor. *Philosophical Transactions of the Royal Society A*. https://doi.org/10.1098/rsta.2020.0218

Ben-Zvi, T., Wilcock, W. S. D., Barclay, A. H., Zandomeneghi, D., Ibáñez, J. M., & Almendros, J. (2009). The P-wave velocity structure of Deception Island, Antarctica, from two-dimensional seismic tomography. *Journal of Volcanology and Geothermal Research*, *180*(1), 67–80. https://doi.org/10.1016/j.jvolgeores.2008.11.020

Berrocoso, M., Fernández-Ros, A., Prates, G., García, A., & Kraus, S. (2016). Geodetic implications on block formation and geodynamic domains in the South Shetland Islands, Antarctic Peninsula. *Tectonophysics*, *666*, 211–219. https://doi.org/10.1016/j.tecto.2015.10.023

Berryman, J. G. (1980). Long-wavelength propagation in composite elastic media II. Ellipsoidal inclusions. *The Journal of the Acoustical Society of America*, *68*(6), 1820–1831. https://doi.org/10.1121/1.385172

Birkenmajer, K., Guterch, A., Grad, M., Janik, T., & Perchuc, E. (1990). Lithospheric transect antarctic Peninsula-South shetland islands, west Antarctica. *Pol. Polar Res.*, *11*, 241–258.

Blum, J. A., Chadwell, C. D., Driscoll, N., & Zumberge, M. A. (2010). Assessing slope stability in the Santa Barbara Basin, California, using seafloor geodesy and CHIRP seismic data. *Geophysical Research Letters*, *37*(13). https://doi.org/10.1029/2010GL043293

Bosworth, W., & Stockli, D. F. (2016). Early magmatism in the greater Red Sea rift: timing and significance. *Canadian Journal of Earth Sciences*, *53*(11), 1158–1176. https://doi.org/10.1139/cjes-2016-0019

Bosworth, W., Burke, K., & Strecker, M. (2000). Magma chamber elongation as an indicator of intraplate stress field orientation: “borehole breakout mechanism” and examples from the Late Pleistocene to Recent Kenya Rift Valley. *Journal of The Virtual Explorer*, *02*. https://doi.org/10.3809/jvirtex.2000.00008

Brooks, B. A., Foster, J. H., McGuire, J. J., & Behn, M. (2009). Submarine Landslides and Slow Earthquakes: Monitoring Motion with GPS and Seafloor Geodesy. In *Encyclopedia of Complexity and Systems Science* (pp. 8850–8869). Springer, New York, NY. https://doi.org/10.1007/978-0-387-30440-3_529

Brune, S., Kolawole, F., Olive, J.-A., Stamps, D. S., Buck, W. R., Buiter, S. J. H., et al. (2023). Geodynamics of continental rift initiation and evolution. *Nature Reviews Earth & Environment*, *4*(4), 235–253. https://doi.org/10.1038/s43017-023-00391-3

Buck, W. R. (1991). Modes of continental lithospheric extension. *Journal of Geophysical Research: Solid Earth*, *96*(B12), 20161–20178. https://doi.org/10.1029/91JB01485

Burgette, R. J., Weldon II, R. J., & Schmidt, D. A. (2009). Interseismic uplift rates for western Oregon and along-strike variation in locking on the Cascadia subduction zone. *Journal of Geophysical Research: Solid Earth*, *114*(B1). https://doi.org/10.1029/2008JB005679

Bürgmann, R. (2018). The geophysics, geology and mechanics of slow fault slip. *Earth and Planetary Science Letters*, *495*, 112–134. https://doi.org/10.1016/j.epsl.2018.04.062

Bürgmann, R., & Chadwell, D. (2014). Seafloor Geodesy. *Annual Review of Earth and Planetary Sciences*, *42*(Volume 42, 2014), 509–534. https://doi.org/10.1146/annurev-earth-060313-054953

Bürgmann, R., & Thatcher, W. (2013). Space geodesy: A revolution in crustal deformation measurements of tectonic processes. In M. E. Bickford (Ed.), *The Web of Geological Sciences: Advances, Impacts, and Interactions* (p. 0). Geological Society of America. https://doi.org/10.1130/2013.2500(12)

Bushenkova, N., Koulakov, I., Senyukov, S., Gordeev, E. I., Huang, H.-H., El Khrepy, S., & Al Arifi, N. (2019). Tomographic Images of Magma Chambers Beneath the Avacha and

Koryaksky Volcanoes in Kamchatka. *Journal of Geophysical Research: Solid Earth*, *124*(9), 9694–9713. https://doi.org/10.1029/2019JB017952

Cabaniss, H. E., Gregg, P. M., Nooner, S. L., & Chadwick, W. W. (2020). Triggering of eruptions at Axial Seamount, Juan de Fuca Ridge. *Scientific Reports*, *10*(1), 10219. https://doi.org/10.1038/s41598-020-67043-0

Calvert, A. J., Bostock, M. G., Savard, G., & Unsworth, M. J. (2020). Cascadia low frequency earthquakes at the base of an overpressured subduction shear zone. *Nature Communications*, *11*(1), 3874. https://doi.org/10.1038/s41467-020-17609-3

Cameselle, A. L., Ranero, C. R., & Barckhausen, U. (2020). Understanding the 3D Formation of a Wide Rift: The Central South China Sea Rift System. *Tectonics*, *39*(12), e2019TC006040. https://doi.org/10.1029/2019TC006040

Canales, J. P., Detrick, R. S., Lin, J., Collins, J. A., & Toomey, D. R. (2000a). Crustal and upper mantle seismic structure beneath the rift mountains and across a nontransform offset at the Mid-Atlantic Ridge (35°N). *Journal of Geophysical Research: Solid Earth*, *105*(B2), 2699–2719. https://doi.org/10.1029/1999JB900379

Canales, J. P., Collins, J. A., Escartín, J., & Detrick, R. S. (2000b). Seismic structure across the rift valley of the Mid-Atlantic Ridge at 23°20′ (MARK area): Implications for crustal accretion processes at slow spreading ridges. *Journal of Geophysical Research: Solid Earth*, *105*(B12), 28411–28425. https://doi.org/10.1029/2000JB900301

Cannat, M., Sauter, D., Lavier, L. L., Bickert, M., Momoh, E., & Leroy, S. (2019). On spreading modes and magma supply at slow and ultraslow mid-ocean ridges. *Earth and Planetary Science Letters*, *519*, 223–233. https://doi.org/10.1016/j.epsl.2019.05.012

Carbotte, S. M., Nedimović, M. R., Canales, J. P., Kent, G. M., Harding, A. J., & Marjanović, M. (2008). Variable crustal structure along the Juan de Fuca Ridge: Influence of on-axis hot spots and absolute plate motions. *Geochemistry, Geophysics, Geosystems*, *9*(8). https://doi.org/10.1029/2007GC001922

Carbotte, S. M., Arnulf, A., Spiegelman, M., Lee, M., Harding, A., Kent, G., et al. (2020). Stacked sills forming a deep melt-mush feeder conduit beneath Axial Seamount. *Geology*, *48*(7), 693–697. https://doi.org/10.1130/G47223.1

Carbotte, S. M., Boston, B., Han, S., Shuck, B., Beeson, J., Canales, J. P., et al. (2024). Subducting plate structure and megathrust morphology from deep seismic imaging linked to earthquake rupture segmentation at Cascadia. *Science Advances*, *10*(23), eadl3198. https://doi.org/10.1126/sciadv.adl3198

Caress, D. W., Clague, D. A., Paduan, J. B., Martin, J. F., Dreyer, B. M., Chadwick, W. W., et al. (2012). Repeat bathymetric surveys at 1-metre resolution of lava flows erupted at Axial Seamount in April 2011. *Nature Geoscience*, *5*(7), 483–488. https://doi.org/10.1038/ngeo1496

Caress, D. W., Paduan, J. B., Clague, D. A., Chadwick, W. W., Nooner, S. L., Beeson, J. W., & Headley, K. L. (2024). Updated 1-m-scale Topography Model for Axial Seamount and Vertical deformation of Axial Seamount summit from AUV Surveys. Presented at the AGU Annual Meeting, Washington DC: AGU. Retrieved from https://agu.confex.com/agu/agu24/meetingapp.cgi/Paper/1706958

Caristan, Y. (1982). The transition from high temperature creep to fracture in Maryland diabase. *Journal of Geophysical Research: Solid Earth*, *87*(B8), 6781–6790. https://doi.org/10.1029/JB087iB08p06781

Carlson, R. L. (2014). The effects of alteration and porosity on seismic velocities in oceanic basalts and diabases. *Geochemistry, Geophysics, Geosystems*, *15*(12), 4589–4598. https://doi.org/10.1002/2014GC005537

Castellano, M., Augusti, V., De Cesare, W., Favali, P., Frugoni, F., Montuori, C., et al. (2008). Seismic Tomography Experiment at Italy's Stromboli Volcano. *Eos, Transactions American Geophysical Union*, *89*(30), 269–270. https://doi.org/10.1029/2008EO300001

Catalán, M., Galindo-Zaldivar, J., Davila, J. M., Martos, Y. M., Maldonado, A., Gambôa, L., & Schreider, A. A. (2013). Initial stages of oceanic spreading in the Bransfield Rift from magnetic and gravity data analysis. *Tectonophysics*, *585*, 102–112. https://doi.org/10.1016/j.tecto.2012.09.016

Cesca, S., Sugan, M., Rudzinski, Ł., Vajedian, S., Niemz, P., Plank, S., et al. (2022). Massive earthquake swarm driven by magmatic intrusion at the Bransfield Strait, Antarctica. *Communications Earth & Environment*, *3*(1), 89. https://doi.org/10.1038/s43247-022-00418-5

Chadwell, C. D., & Spiess, F. N. (2008). Plate motion at the ridge-transform boundary of the south Cleft segment of the Juan de Fuca Ridge from GPS-Acoustic data. *Journal of Geophysical Research: Solid Earth*, *113*(B4). https://doi.org/10.1029/2007JB004936

Chadwell, C. D., & Sweeney, A. D. (2010). Acoustic Ray-Trace Equations for Seafloor Geodesy. *Marine Geodesy*, *33*(2–3), 164–186. https://doi.org/10.1080/01490419.2010.492283

Chadwell, C. D., Hildebrand, J. A., Spiess, F. N., Morton, J. L., Normark, W. R., & Reiss, C. A. (1999). No spreading across the Southern Juan de Fuca Ridge axial cleft during 1994–

1996. *Geophysical Research Letters*, *26*(16), 2525–2528. https://doi.org/10.1029/1999GL900570

Chadwick Jr, W. W., Paduan, J. B., Clague, D. A., Dreyer, B. M., Merle, S. G., Bobbitt, A. M., et al. (2016). Voluminous eruption from a zoned magma body after an increase in supply rate at Axial Seamount. *Geophysical Research Letters*, *43*(23), 12,063-12,070. https://doi.org/10.1002/2016GL071327

Chadwick Jr., William W., Embley, R. W., Milburn, H. B., Meinig, C., & Stapp, M. (1999). Evidence for deformation associated with the 1998 eruption of Axial Volcano, Juan de Fuca Ridge, from acoustic extensometer measurements. *Geophysical Research Letters*, *26*(23), 3441–3444. https://doi.org/10.1029/1999GL900498

Chadwick Jr., William W., Wilcock, W. S. D., Nooner, S. L., Beeson, J. W., Sawyer, A. M., & Lau, T.-K. (2022). Geodetic Monitoring at Axial Seamount Since Its 2015 Eruption Reveals a Waning Magma Supply and Tightly Linked Rates of Deformation and Seismicity. *Geochemistry, Geophysics, Geosystems*, *23*(1), e2021GC010153. https://doi.org/10.1029/2021GC010153

Chadwick Jr, W.W., & Stapp, M. (2002). A deep-sea observatory experiment using acoustic extensometers: precise horizontal distance measurements across a mid-ocean ridge. *IEEE Journal of Oceanic Engineering*, *27*(2), 193–201. https://doi.org/10.1109/JOE.2002.1002473

Chadwick, W. (2022). *Cruise TN404 on RV Thomas G. Thompson* (Version 1). University of Washington. https://doi.org/10.7284/909745

Chadwick, W. W., Nooner, S. L., Zumberge, M. A., Embley, R. W., & Fox, C. G. (2006). Vertical deformation monitoring at Axial Seamount since its 1998 eruption using deep-

sea pressure sensors. *Journal of Volcanology and Geothermal Research*, *150*(1), 313–327. https://doi.org/10.1016/j.jvolgeores.2005.07.006

Chadwick, W. W., Nooner, S. L., Butterfield, D. A., & Lilley, M. D. (2012). Seafloor deformation and forecasts of the April 2011 eruption at Axial Seamount. *Nature Geoscience*, *5*(7), 474–477. https://doi.org/10.1038/ngeo1464

Chadwick, W. W., Merle, S. G., Baker, E. T., Walker, S. L., Resing, J. A., Butterfield, D. A., et al. (2018). A Recent Volcanic Eruption Discovered on the Central Mariana Back-Arc Spreading Center. *Frontiers in Earth Science*, *6*. Retrieved from https://www.frontiersin.org/articles/10.3389/feart.2018.00172

Chadwick, W. W., Wilcock, W. S. D., Nooner, S. L., Beeson, J. W., Sawyer, A. M., & Lau, T. - K. (2022). Geodetic Monitoring at Axial Seamount Since Its 2015 Eruption Reveals a Waning Magma Supply and Tightly Linked Rates of Deformation and Seismicity. *Geochemistry, Geophysics, Geosystems*, *23*(1), e2021GC010153. https://doi.org/10.1029/2021GC010153

Chadwick, W. W., Wilcock, W. S. D., Nooner, S. L., Beeson, J. W., & Zhang, M. (2025). A Comparison of Inflation and Seismicity Rates Before and Since the 2015 Eruption at Axial Seamount and Implications for Eruption Forecasting. Presented at the AGU25, AGU. Retrieved from https://agu.confex.com/agu/agu25/meetingapp.cgi/Paper/1897367

Chaudhuri, K., & Ghosh, A. (2022). Widespread Very Low Frequency Earthquakes (VLFEs) Activity Offshore Cascadia. *Geophysical Research Letters*, *49*(13), e2022GL097962. https://doi.org/10.1029/2022GL097962

Chrapkiewicz, K., Paulatto, M., Heath, B. A., Hooft, E. E. E., Nomikou, P., Papazachos, C. B., et al. (2022). Magma Chamber Detected Beneath an Arc Volcano With Full-Waveform

Inversion of Active-Source Seismic Data. *Geochemistry, Geophysics, Geosystems*, *23*(11), e2022GC010475. https://doi.org/10.1029/2022GC010475

Christensen, N. I. (1979). Compressional wave velocities in rocks at high temperatures and pressures, critical thermal gradients, and crustal low-velocity zones. *Journal of Geophysical Research: Solid Earth*, *84*(B12), 6849–6857. https://doi.org/10.1029/JB084iB12p06849

Christensen, N. I. (1996). Poisson's ratio and crustal seismology. *Journal of Geophysical Research: Solid Earth*, *101*(B2), 3139–3156. https://doi.org/10.1029/95JB03446

Christeson, G. L., Barker, D. H. N., Austin, J. A., & Dalziel, I. W. D. (2003). Deep crustal structure of Bransfield Strait: Initiation of a back arc basin by rift reactivation and propagation. *Journal of Geophysical Research: Solid Earth*, *108*(B10). https://doi.org/10.1029/2003JB002468

Clements, T., & Denolle, M. A. (2023). The Seismic Signature of California's Earthquakes, Droughts, and Floods. *Journal of Geophysical Research: Solid Earth*, *128*(1), e2022JB025553. https://doi.org/10.1029/2022JB025553

Clements, Timothy, & Denolle, M. A. (2020). SeisNoise.jl: Ambient Seismic Noise Cross Correlation on the CPU and GPU in Julia. *Seismological Research Letters*, *92*(1), 517–527. https://doi.org/10.1785/0220200192

Cochran, J. R. (2005). Northern Red Sea: Nucleation of an oceanic spreading center within a continental rift. *Geochemistry, Geophysics, Geosystems*, *6*(3). https://doi.org/10.1029/2004GC000826

Cochrane, G. R., Moore, J. C., MacKay, M. E., & Moore, G. F. (1994). Velocity and inferred porosity model of the Oregon accretionary prism from multichannel seismic reflection

data: Implications on sediment dewatering and overpressure. *Journal of Geophysical Research: Solid Earth*, *99*(B4), 7033–7043. https://doi.org/10.1029/93JB03206

Conder, J. A. (2022). Oceanic isostasy as a trigger for the rift-to-drift transition. *Geology*, *50*(7), 843–847. https://doi.org/10.1130/G49914.1

Corti, G. (2012). Evolution and characteristics of continental rifting: Analog modeling-inspired view and comparison with examples from the East African Rift System. *Tectonophysics*, *522–523*, 1–33. https://doi.org/10.1016/j.tecto.2011.06.010

Creager, K. C., & Dorman, L. M. (1982). Location of instruments on the seafloor by joint adjustment of instrument and ship positions. *Journal of Geophysical Research*, *87*(B10), 8379. https://doi.org/10.1029/JB087iB10p08379

Crisp, J. A. (1984). Rates of magma emplacement and volcanic output. *Journal of Volcanology and Geothermal Research*, *20*(3), 177–211. https://doi.org/10.1016/0377-0273(84)90039-8

Cruz-Atienza, V. M., Villafuerte, C., & Bhat, H. S. (2018). Rapid tremor migration and pore-pressure waves in subduction zones. *Nature Communications*, *9*(1), 2900. https://doi.org/10.1038/s41467-018-05150-3

Dannowski, A., Grevemeyer, I., Phipps Morgan, J., Ranero, C. R., Maia, M., & Klein, G. (2011). Crustal structure of the propagating TAMMAR ridge segment on the Mid-Atlantic Ridge, 21.5°N. *Geochemistry, Geophysics, Geosystems*, *12*(7). https://doi.org/10.1029/2011GC003534

Davis, E. E., Sun, T., Heesemann, M., Becker, K., & Schlesinger, A. (2023). Long-Term Offshore Borehole Fluid-Pressure Monitoring at the Northern Cascadia Subduction Zone

and Inferences Regarding the State of Megathrust Locking. *Geochemistry, Geophysics, Geosystems*, *24*(6), e2023GC010910. https://doi.org/10.1029/2023GC010910

Davis, E. E., Sun, T., Becker, K., Heesemann, M., Villinger, H., & Wang, K. (2024). Deep-sea borehole fluid pressure and temperature observations at subduction zones and their geodynamic implications. *Canadian Journal of Earth Sciences*. https://doi.org/10.1139/cjes-2024-0093

Delph, J. R., Levander, A., & Niu, F. (2018). Fluid Controls on the Heterogeneous Seismic Characteristics of the Cascadia Margin. *Geophysical Research Letters*, *45*(20), 11,021-11,029. https://doi.org/10.1029/2018GL079518

Deng, H., Ren, J., Pang, X., Rey, P. F., McClay, K. R., Watkinson, I. M., et al. (2020). South China Sea documents the transition from wide continental rift to continental break up. *Nature Communications*, *11*(1), 4583. https://doi.org/10.1038/s41467-020-18448-y

DeSanto, J. B., Schmidt, D. A., Chadwell, C. D., Zumberge, M. A., & Sasagawa, G. S. (2022). Horizontal deformation rates near the Cascadia subduction zone trench revealed by offshore GNSS-Acoustic time series, *2022*, T56A-05. Presented at the AGU Fall Meeting Abstracts.

Dewey, J. F. (1980). Episodicity, sequence, and style at convergent plate boundaries. In D. W. Strangway (Ed.), The continental crust and its mineral deposits. *Waterloo, Ontario: Geological Association of Canada*, 554–573.

Dietrich, R., Rülke, A., Ihde, J., Lindner, K., Miller, H., Niemeier, W., et al. (2004). Plate kinematics and deformation status of the Antarctic Peninsula based on GPS. *Global and Planetary Change*, *42*(1), 313–321. https://doi.org/10.1016/j.gloplacha.2003.12.003

Dixon, J. E., Dixon, T. H., Bell, D. R., & Malservisi, R. (2004). Lateral variation in upper mantle viscosity: role of water. *Earth and Planetary Science Letters*, *222*(2), 451–467. https://doi.org/10.1016/j.epsl.2004.03.022

Dobashi, Y., & Inazu, D. (2021). Improving Detectability of Seafloor Deformation From Bottom Pressure Observations Using Numerical Ocean Models. *Frontiers in Earth Science*, *8*. https://doi.org/10.3389/feart.2020.598270

Dugan, B., & Sheahan, T. C. (2012). Offshore sediment overpressures of passive margins: Mechanisms, measurement, and models. *Reviews of Geophysics*, *50*(3). https://doi.org/10.1029/2011RG000379

Dunn, R. A., & Martinez, F. (2011). Contrasting crustal production and rapid mantle transitions beneath back-arc ridges. *Nature*, *469*(7329), 198–202. https://doi.org/10.1038/nature09690

Dunn, R. A., & Toomey, D. R. (2001). Crack-induced seismic anisotropy in the oceanic crust across the East Paci¢c Rise (9$^3$30PN). *Earth and Planetary Science Letters*, *189*(1–2), 9–17.

Dunn, R. A., Toomey, D. R., & Solomon, S. C. (2000). Three-dimensional seismic structure and physical properties of the crust and shallow mantle beneath the East Pacific Rise at 9°30'N. *Journal of Geophysical Research: Solid Earth*, *105*(B10), 23537–23555. https://doi.org/10.1029/2000JB900210

Dunn, R. A., Lekić, V., Detrick, R. S., & Toomey, D. R. (2005). Three-dimensional seismic structure of the Mid-Atlantic Ridge (35°N): Evidence for focused melt supply and lower crustal dike injection: MID-ATLANTIC RIDGE IN THREE DIMENSIONS. *Journal of Geophysical Research: Solid Earth*, *110*(B9). https://doi.org/10.1029/2004JB003473

Dunn, R. A., Martinez, F., & Conder, J. (2013). Crustal construction and magma chamber properties along the Eastern Lau Spreading Center. *Earth and Planetary Science Letters*, *s 371–372*, 112–124. https://doi.org/10.1016/j.epsl.2013.04.008

Dunn, R. A., Arai, R., Eason, D. E., Canales, J. P., & Sohn, R. A. (2017). Three-Dimensional Seismic Structure of the Mid-Atlantic Ridge: An Investigation of Tectonic, Magmatic, and Hydrothermal Processes in the Rainbow Area. *Journal of Geophysical Research: Solid Earth*, *122*(12), 9580–9602. https://doi.org/10.1002/2017JB015051

Dushaw, B. (2009). Worldwide Sound Speed, Temperature, Salinity, and Buoyancy from the NOAA World Ocean Atlas. Retrieved July 29, 2024, from https://staff.washington.edu/dushaw/WOA/

Dziak, R. P., Haxel, J. H., Bohnenstiehl, D. R., Chadwick, W. W., Nooner, S. L., Fowler, M. J., et al. (2012). Seismic precursors and magma ascent before the April 2011 eruption at Axial Seamount. *Nature Geoscience*, *5*(7), 478–482. https://doi.org/10.1038/ngeo1490

Dziak, Robert P., & Fox, C. G. (1999). The January 1998 Earthquake swarm at Axial Volcano, Juan de Fuca Ridge: Hydroacoustic evidence of seafloor volcanic activity. *Geophysical Research Letters*, *26*(23), 3429–3432. https://doi.org/10.1029/1999GL002332

Dziak, Robert P., Park, M., Lee, W. S., Matsumoto, H., Bohnenstiehl, D. R., & Haxel, J. H. (2010). Tectonomagmatic activity and ice dynamics in the Bransfield Strait back-arc basin, Antarctica. *Journal of Geophysical Research*, *115*(B1), B01102. https://doi.org/10.1029/2009JB006295

Eagles, G., & Jokat, W. (2014). Tectonic reconstructions for paleobathymetry in Drake Passage. *Tectonophysics*, *611*, 28–50. https://doi.org/10.1016/j.tecto.2013.11.021

Eason, D. E., & Dunn, R. A. (2015). Petrogenesis and structure of oceanic crust in the Lau back-arc basin. *Earth and Planetary Science Letters*, *429*, 128–138. https://doi.org/10.1016/j.epsl.2015.07.065

Ebinger, C.J., & Casey, M. (2001). Continental breakup in magmatic provinces: An Ethiopian example. *Geology*, *29*(6), 527. https://doi.org/10.1130/0091-7613(2001)029%3C0527:CBIMPA%3E2.0.CO;2

Ebinger, Cynthia J., Van Wijk, J., & Keir, D. (2013). The time scales of continental rifting: Implications for global processes. In M. E. Bickford, *The Web of Geological Sciences: Advances, Impacts, and Interactions*. Geological Society of America. https://doi.org/10.1130/2013.2500(11)

Edgington, J. R., Saffer, D. M., & Williams, C. A. (2025). Migrating shallow slow slip on the Nankai Trough megathrust captured by borehole observatories. *Science*, *388*(6754), 1396–1400. https://doi.org/10.1126/science.ads9715

Egbert, G. D., Yang, B., Bedrosian, P. A., Key, K., Livelybrooks, D. W., Schultz, A., et al. (2022). Fluid transport and storage in the Cascadia forearc influenced by overriding plate lithology. *Nature Geoscience*, *15*(8), 677–682. https://doi.org/10.1038/s41561-022-00981-8

El Khrepy, S., Koulakov, I., Gerya, T., Al-Arifi, N., Alajmi, M. S., & Qadrouh, A. N. (2021). Transition from continental rifting to oceanic spreading in the northern Red Sea area. *Scientific Reports*, *11*(1), 5594. https://doi.org/10.1038/s41598-021-84952-w

Embley, R. W., & Rubin, K. H. (2018). Extensive young silicic volcanism produces large deep submarine lava flows in the NE Lau Basin. *Bulletin of Volcanology*, *80*(4), 36. https://doi.org/10.1007/s00445-018-1211-7

Escartín, J., Soule, S. A., Cannat, M., Fornari, D. J., Düşünür, D., & Garcia, R. (2014). Lucky Strike seamount: Implications for the emplacement and rifting of segment-centered volcanoes at slow spreading mid-ocean ridges. *Geochemistry, Geophysics, Geosystems*, *15*(11), 4157–4179. https://doi.org/10.1002/2014GC005477

Flatté, S. M., & Rovner, G. (2000). Calculations of internal-wave-induced fluctuations in ocean-acoustic propagation. *The Journal of the Acoustical Society of America*, *108*(2), 526–534. https://doi.org/10.1121/1.429583

Fox, C. G., Chadwick, W. W., & Embley, R. W. (2001). Direct observation of a submarine volcanic eruption from a sea-floor instrument caught in a lava flow. *Nature*, *412*(6848), 727–729. https://doi.org/10.1038/35089066

Fredrickson, E. K., Wilcock, W. S. D., Schmidt, D. A., MacCready, P., Roland, E., Kurapov, A. L., et al. (2019). Optimizing Sensor Configurations for the Detection of Slow-Slip Earthquakes in Seafloor Pressure Records, Using the Cascadia Subduction Zone as a Case Study. *Journal of Geophysical Research: Solid Earth*, *124*(12), 13504–13531. https://doi.org/10.1029/2019JB018053

Fretzdorff, S., Worthington, T. J., Haase, K. M., Hékinian, R., Franz, L., Keller, R. A., & Stoffers, P. (2004). Magmatism in the Bransfield Basin: Rifting of the South Shetland Arc? *Journal of Geophysical Research*, *109*(B12), B12208. https://doi.org/10.1029/2004JB003046

Frizon de Lamotte, D., Fourdan, B., Leleu, S., Leparmentier, F., & de Clarens, P. (2015). Style of rifting and the stages of Pangea breakup. *Tectonics*, *34*(5), 1009–1029. https://doi.org/10.1002/2014TC003760

Gaffet, A., Bertin, X., Sous, D., Michaud, H., & Roland, A. (2024). A new global high resolution model for the tropical ocean using WAVEWATCH III version 7.14 - WaveWatchIII codebase. Retrieved from https://zenodo.org/records/14011562

Gagnon, K., Chadwell, C. D., & Norabuena, E. (2005). Measuring the onset of locking in the Peru–Chile trench with GPS and acoustic measurements. *Nature*, *434*(7030), 205–208. https://doi.org/10.1038/nature03412

Galindo-Zaldívar, J., Gamboa, L., Maldonado, A., Nakao, S., & Bochu, Y. (2006). Bransfield Basin Tectonic Evolution. In D. K. Fütterer, D. Damaske, G. Kleinschmidt, H. Miller, & F. Tessensohn (Eds.), *Antarctica: Contributions to Global Earth Sciences* (pp. 243–248). Berlin, Heidelberg: Springer. https://doi.org/10.1007/3-540-32934-X_29

García, M., Ercilla, G., & Alonso, B. (2009). Morphology and sedimentary systems in the Central Bransfield Basin, Antarctic Peninsula: sedimentary dynamics from shelf to basin. *Basin Research*, *21*(3), 295–314. https://doi.org/10.1111/j.1365-2117.2008.00386.x

García, M., Ercilla, G., Alonso, B., Casas, D., & Dowdeswell, J. A. (2011). Sediment lithofacies, processes and sedimentary models in the Central Bransfield Basin, Antarctic Peninsula, since the Last Glacial Maximum. *Marine Geology*, *290*(1), 1–16. https://doi.org/10.1016/j.margeo.2011.10.006

Geoffroy, L. (2005). Volcanic passive margins. *Comptes Rendus Geoscience*, *337*(16), 1395–1408. https://doi.org/10.1016/j.crte.2005.10.006

Georgatou, A. A., de Ronde, C. E. J., Kouzmanov, K., Charlier, B. L. A., & Adams, D. (2024). Metals, Volatiles, and Lithostratigraphy of Brothers Submarine Volcano. *Geochemistry, Geophysics, Geosystems*, *25*(9), e2024GC011716. https://doi.org/10.1029/2024GC011716

Geshi, N., Oikawa, T., Weller, D. J., & Conway, C. E. (2022). Evolution of the magma plumbing system of Miyakejima volcano with periodic recharge of basaltic magmas. *Earth, Planets and Space*, *74*(1), 20. https://doi.org/10.1186/s40623-022-01577-7

Ghosh, A., Vidale, J. E., Sweet, J. R., Creager, K. C., Wech, A. G., Houston, H., & Brodsky, E. E. (2010). Rapid, continuous streaking of tremor in Cascadia. *Geochemistry, Geophysics, Geosystems*, *11*(12). https://doi.org/10.1029/2010GC003305

Gianni, G. M., Navarrete, C., & Spagnotto, S. (2019). Surface and mantle records reveal an ancient slab tear beneath Gondwana. *Scientific Reports*, *9*(1), 19774. https://doi.org/10.1038/s41598-019-56335-9

Gini, C., Escartín, J., Cannat, M., & Barreyre, T. (2021). Extrusive upper crust formation at slow-spreading ridges: Fault steering of lava flows. *Earth and Planetary Science Letters*, *576*, 117202. https://doi.org/10.1016/j.epsl.2021.117202

Goldfinger, C., Kulm, L. D., Yeats, R. S., McNeill, L., & Hummon, C. (1997). Oblique strike-slip faulting of the central Cascadia submarine forearc. *Journal of Geophysical Research: Solid Earth*, *102*(B4), 8217–8243. https://doi.org/10.1029/96JB02655

Goldfinger, C., Nelson, C. H., Morey, A. E., Johnson, J. E., Patton, J. R., Karabanov, E. B., et al. (2012). *Turbidite event history—Methods and implications for Holocene paleoseismicity of the Cascadia subduction zone* (No. 1661- F). *Professional Paper*. U.S. Geological Survey. https://doi.org/10.3133/pp1661F

González-Casado, J. M., Giner Robles, J. L., & López-Martínez, J. (2000). Bransfield Basin, Antarctic Peninsula: Not a normal backarc basin. *Geology*, *28*(11), 1043. https://doi.org/10.1130/0091-7613(2000)28%3C1043:BBAPNA%3E2.0.CO;2

González-Ferrán, O. (1991). The Bransfield rift and its active volcanism. In *Geological evolution of Antarctica* (pp. 505–509). Cambridge, UK: Cambridge University Press.

Gosselin, J. M., Audet, P., Estève, C., McLellan, M., Mosher, S. G., & Schaeffer, A. J. (2020). Seismic evidence for megathrust fault-valve behavior during episodic tremor and slip. *Science Advances*, *6*(4), eaay5174. https://doi.org/10.1126/sciadv.aay5174

Gràcia, E., Canals, M., Lí Farràn, M., José Prieto, M., Sorribas, J., & Team, G. (1996). Morphostructure and evolution of the central and Eastern Bransfield Basins (NW Antarctic Peninsula). *Marine Geophysical Researches*, *18*(2–4), 429–448. https://doi.org/10.1007/BF00286088

Grad, M., Guterch, A., & Środa, P. (1992). Upper crustal structure of Deception Island area, Bransfield Strait, West Antarctica. *Antarctic Science*, *4*(4), 469–476. https://doi.org/10.1017/S0954102092000683

Gregg, T. K. P., & Fornari, D. J. (1998). Long submarine lava flows: Observations and results from numerical modeling. *Journal of Geophysical Research: Solid Earth*, *103*(B11), 27517–27531. https://doi.org/10.1029/98JB02465

Gudmundsson, O., Brandsdóttir, B., Menke, W., & Sigvaldason, G. (1994). The crustal magma chamber of the Katla volcano in south Iceland revealed by 2-D undershooting. *Geophysical Journal International*, *119*, 277–296. https://doi.org/10.1111/j.1365-246X.1994.tb00928.x

Hammerschmidt, S. B., Davis, E. E., Hüpers, A., & Kopf, A. (2013). Limitation of fluid flow at the Nankai Trough megasplay fault zone. *Geo-Marine Letters*, *33*(5), 405–418. https://doi.org/10.1007/s00367-013-0337-z

Han, S., Bangs, N. L., Carbotte, S. M., Saffer, D. M., & Gibson, J. C. (2017). Links between sediment consolidation and Cascadia megathrust slip behaviour. *Nature Geoscience*, *10*(12), 954–959. https://doi.org/10.1038/s41561-017-0007-2

Hannemann, K., Lange, D., Kopp, H., Petersen, F., & Contreras-Reyes, E. (2017). Deformation offshore Northern Chile monitored by a seafloor geodetic network (GeoSEA).

Harding, J. L., Van Avendonk, H. J. A., Hayman, N. W., Grevemeyer, I., Peirce, C., & Dannowski, A. (2017). Magmatic-tectonic conditions for hydrothermal venting on an ultraslow-spread oceanic core complex. *Geology*, *45*(9), 839–842. https://doi.org/10.1130/G39045.1

Harmon, N., & Blackman, D. K. (2010). Effects of plate boundary geometry and kinematics on mantle melting beneath the back-arc spreading centers along the Lau Basin. *Earth and Planetary Science Letters*, *298*(3), 334–346. https://doi.org/10.1016/j.epsl.2010.08.004

Hawkins, J. W., & Melchior, J. T. (1985). Petrology of Mariana Trough and Lau Basin basalts. *Journal of Geophysical Research: Solid Earth*, *90*(B13), 11431–11468. https://doi.org/10.1029/JB090iB13p11431

Heath, B. A., Hooft, E. E. E., Toomey, D. R., Papazachos, C. B., Nomikou, P., Paulatto, M., et al. (2019). Tectonism and Its Relation to Magmatism Around Santorini Volcano From Upper Crustal *P* Wave Velocity. *Journal of Geophysical Research: Solid Earth*, *124*(10), 10610–10629. https://doi.org/10.1029/2019JB017699

Heath, Benjamin A., Hooft, E. E. E., Toomey, D. R., & Bezada, M. J. (2015). Imaging the magmatic system of Newberry Volcano using joint active source and teleseismic tomography. *Geochemistry, Geophysics, Geosystems*, *16*(12), 4433–4448. https://doi.org/10.1002/2015GC006129

Hefner, W. L., Nooner, S. L., Chadwick Jr, W. W., & Bohnenstiehl, D. R. (2020). Revised Magmatic Source Models for the 2015 Eruption at Axial Seamount Including Estimates of Fault-Induced Deformation. *Journal of Geophysical Research: Solid Earth*, *125*(4), e2020JB019356. https://doi.org/10.1029/2020JB019356

Henriet, J. P., Meissner, R., Miller, H., & The Grape Team. (1992). Active margin processes along the Antarctic Peninsula. *Tectonophysics*, *201*(3), 229–253. https://doi.org/10.1016/0040-1951(92)90235-X

Herath, P., & Audet, P. (2024). Fluid upwelling across the Hikurangi subduction thrust during deep slow-slip earthquakes. *Communications Earth & Environment*, *5*(1), 1–8. https://doi.org/10.1038/s43247-024-01864-z

Hillers, G., Retailleau, L., Campillo, M., Inbal, A., Ampuero, J.-P., & Nishimura, T. (2015). In situ observations of velocity changes in response to tidal deformation from analysis of the high-frequency ambient wavefield. *Journal of Geophysical Research: Solid Earth*, *120*(1), 210–225. https://doi.org/10.1002/2014JB011318

Hillers, Gregor, Husen, S., Obermann, A., Planès, T., Larose, E., & Campillo, M. (2015). Noise-based monitoring and imaging of aseismic transient deformation induced by the 2006 Basel reservoir stimulation. *Geophysics*, *80*(4), KS51–KS68. https://doi.org/10.1190/geo2014-0455.1

Hirth, G., & Kohlstedt, D. L. (1996). Water in the oceanic upper mantle: implications for rheology, melt extraction and the evolution of the lithosphere. *Earth and Planetary Science Letters*, *144*(1), 93–108. https://doi.org/10.1016/0012-821X(96)00154-9

Hollingsworth, J., Leprince, S., Ayoub, F., & Avouac, J.-P. (2012). Deformation during the 1975–1984 Krafla rifting crisis, NE Iceland, measured from historical optical imagery.

*Journal of Geophysical Research: Solid Earth*, *117*(B11). https://doi.org/10.1029/2012JB009140

Hooft, E. E. E., Detrick, R. S., Toomey, D. R., Collins, J. A., & Lin, J. (2000). Crustal thickness and structure along three contrasting spreading segments of the Mid-Atlantic Ridge, 33.5°–35°N. *Journal of Geophysical Research: Solid Earth*, *105*(B4), 8205–8226. https://doi.org/10.1029/1999JB900442

Hooft, E. E. E., Heath, B. A., Toomey, D. R., Paulatto, M., Papazachos, C. B., Nomikou, P., et al. (2019). Seismic imaging of Santorini: Subsurface constraints on caldera collapse and present-day magma recharge. *Earth and Planetary Science Letters*, *514*, 48–61. https://doi.org/10.1016/j.epsl.2019.02.033

Huismans, R., & Beaumont, C. (2011). Depth-dependent extension, two-stage breakup and cratonic underplating at rifted margins. *Nature*, *473*(7345), 74–78. https://doi.org/10.1038/nature09988

Humphreys, E., Hessler, E., Dueker, K., Farmer, G. L., Erslev, E., & Atwater, T. (2010). How Laramide-Age Hydration of North American Lithosphere by the Farallon Slab Controlled Subsequent Activity in the Western United States. *International Geology Review*, *45*(7), 575–595. https://doi.org/10.2747/0020-6814.45.7.575

Hyndman, R. D., McCrory, P. A., Wech, A., Kao, H., & Ague, J. (2015). Cascadia subducting plate fluids channelled to fore-arc mantle corner: ETS and silica deposition. *Journal of Geophysical Research: Solid Earth*, *120*(6), 4344–4358. https://doi.org/10.1002/2015JB011920

Ikeda, T., & Tsuji, T. (2018). Temporal change in seismic velocity associated with an offshore MW 5.9 Off-Mie earthquake in the Nankai subduction zone from ambient noise cross-

correlation. *Progress in Earth and Planetary Science*, *5*(1), 62. https://doi.org/10.1186/s40645-018-0211-8

Ikegami, F., McPhie, J., Carey, R., Mundana, R., Soule, A., & Jutzeler, M. (2018). The Eruption of Submarine Rhyolite Lavas and Domes in the Deep Ocean – Havre 2012, Kermadec Arc. *Frontiers in Earth Science*, *6*. Retrieved from https://www.frontiersin.org/articles/10.3389/feart.2018.00147

Jacoby, W. R. (1973). Model Experiment of Plate Movements. *Nature Physical Science*, *242*(122), 130–134. https://doi.org/10.1038/physci242130a0

Kaminuma, K. (2001). A Possibility of Earthquake Swarms around ORCA Sea Mount in the Bransfield Strait, the Antarctic. *Proceedings of the Joint International Seminar: Recent Interests on Antarctic Earth Sciences of Korea and Japan*, 23–34.

Kanamori, H. (1977). Seismic and Aseismic Slip Along Subduction Zones and their Tectonic Implications. In *Island Arcs, Deep Sea Trenches and Back-Arc Basins* (pp. 163–174). American Geophysical Union (AGU). https://doi.org/10.1029/ME001p0163

Karato, S. (1993). Importance of anelasticity in the interpretation of seismic tomography. *Geophysical Research Letters*, *20*(15), 1623–1626. https://doi.org/10.1029/93GL01767

van Keken, P. E., Hacker, B. R., Syracuse, E. M., & Abers, G. A. (2011). Subduction factory: 4. Depth-dependent flux of H2O from subducting slabs worldwide. *Journal of Geophysical Research: Solid Earth*, *116*(B1). https://doi.org/10.1029/2010JB007922

Keller, R. A., Strelin, J. A., Lawver, L. A., & Fisk, M. R. (1994). Dredging young volcanic rocks in Bransfield Strait, Antarct. J. U. S., 2. *Antarctic Journal*, *29*, 100–102.

Keller, Randall A., Fisk, M. R., White, W. M., & Birkenmajer, K. (1992). Isotopic and trace element constraints on mixing and melting models of marginal basin volcanism,

Bransfield Strait, Antarctica. *Earth and Planetary Science Letters*, *111*(2), 287–303. https://doi.org/10.1016/0012-821X(92)90185-X

Keller, Randall A., Fisk, M. R., Smellie, J. L., Strelin, J. A., & Lawver, L. A. (2002). Geochemistry of back arc basin volcanism in Bransfield Strait, Antarctica: Subducted contributions and along-axis variations. *Journal of Geophysical Research*, *107*(B8), 2171. https://doi.org/10.1029/2001JB000444

Kent, G. M., Arnulf, A. F., Singh, S. C., Carton, H., Harding, A. J., & Saustrup, S. (2025). Melt focusing along lithosphere–asthenosphere boundary below Axial volcano. *Nature*, *641*(8062), 380–387. https://doi.org/10.1038/s41586-025-08865-8

Key, K., & Constable, S. (2002). Broadband marine MT exploration of the East Pacific Rise at 9°50′N. *Geophysical Research Letters*, *29*(22). https://doi.org/10.1029/2002GL016035

Kidiwela, M., Denolle, M. A., Wilcock, W. S. D., & Feng, K.-F. (2026b). Active protothrusts and fluid highways: Seismic noise reveals hidden subduction dynamics in Cascadia. *Science Advances*, *12*(9), eaea3684. https://doi.org/10.1126/sciadv.aea3684

Kidiwela, M., Wilcock, W. S. D., Soule, D. C., & Almendros, J. (2026a). Late-Stage Rift Evolution at Back Arc Basins: Insights From a Tomography Experiment at Orca Volcano, Bransfield Basin. *Geochemistry, Geophysics, Geosystems*, *27*(2), e2025GC012224. https://doi.org/10.1029/2025GC012224

Kirby, S., Engdahl, R. E., & Denlinger, R. (1996). Intermediate-Depth Intraslab Earthquakes and Arc Volcanism as Physical Expressions of Crustal and Uppermost Mantle Metamorphism in Subducting Slabs. In *Subduction* (pp. 195–214). American Geophysical Union (AGU). https://doi.org/10.1029/GM096p0195

Kita, S., Houston, H., Yabe, S., Tanaka, S., Asano, Y., Shibutani, T., & Suda, N. (2021). Effects of episodic slow slip on seismicity and stress near a subduction-zone megathrust. *Nature Communications*, *12*(1), 7253. https://doi.org/10.1038/s41467-021-27453-8

Klepeis, K. A., & Lawver, L. A. (1996). Tectonics of the Antarctic-Scotia plate boundary near Elephant and Clarence Islands, West Antarctica. *Journal of Geophysical Research: Solid Earth*, *101*(B9), 20211–20231. https://doi.org/10.1029/96JB01510

Klingelhöfer, F., Géli, L., Matias, L., Steinsland, N., & Mohr, J. (2000). Crustal structure of a super-slow spreading centre:a seismic refraction study of Mohns Ridge, 72° N. *Geophysical Journal International*, *141*(2), 509–526. https://doi.org/10.1046/j.1365-246x.2000.00098.x

Kolawole, F., & Evenick, J. C. (2023). Global distribution of geothermal gradients in sedimentary basins. *Geoscience Frontiers*, *14*(6), 101685. https://doi.org/10.1016/j.gsf.2023.101685

Krauss, Z., Wilcock, W. S. D., & Creager, K. C. (2024). Potential Shallow Tectonic Tremor Signals Near the Deformation Front in Central Cascadia. https://doi.org/10.22541/au.173498202.28863970/v1

Krischer, L., Hutko, A. R., van Driel, M., Stähler, S., Bahavar, M., Trabant, C., & Nissen-Meyer, T. (2017). On-Demand Custom Broadband Synthetic Seismograms. *Seismological Research Letters*, *88*(4), 1127–1140. https://doi.org/10.1785/0220160210

LaBonte, A. L., Brown, K. M., & Fialko, Y. (2009). Hydrologic detection and finite element modeling of a slow slip event in the Costa Rica prism toe. *Journal of Geophysical Research: Solid Earth*, *114*(B4). https://doi.org/10.1029/2008JB005806

Lange, D., Kopp, H., Royer, J.-Y., Henry, P., Çakir, Z., Petersen, F., et al. (2019). Interseismic strain build-up on the submarine North Anatolian Fault offshore Istanbul. *Nature Communications*, *10*(1), 3006. https://doi.org/10.1038/s41467-019-11016-z

Larose, E., Carrière, S., Voisin, C., Bottelin, P., Baillet, L., Guéguen, P., et al. (2015). Environmental seismology: What can we learn on earth surface processes with ambient noise? *Journal of Applied Geophysics*, *116*, 62–74. https://doi.org/10.1016/j.jappgeo.2015.02.001

Larter, R. D., & Barker, P. F. (1991). Effects of ridge crest-trench interaction on Antarctic-Phoenix Spreading: Forces on a young subducting plate. *Journal of Geophysical Research: Solid Earth*, *96*(B12), 19583–19607. https://doi.org/10.1029/91JB02053

Lawver, L. A., Keller, R. A., Fisk, M. R., & Strelin, J. A. (1995). Bransfield Strait, Antarctic Peninsula Active Extension behind a Dead Arc. In B. Taylor (Ed.), *Backarc Basins: Tectonics and Magmatism* (pp. 315–342). Boston, MA: Springer US. https://doi.org/10.1007/978-1-4615-1843-3_8

Lawver, L. A., Sloan, B. J., Barker, D. H. N., Keller, R. A., Klinkhammer, G. P., & Chin, C. S. (1996). Distributed, Active Extension in Bransfield Basin, Antarctic Peninsula: Evidence from Multibeam Bathymetry. *GSA TODAY*, 6.

Lay, T. (2012). Why giant earthquakes keep catching us out. *Nature*, *483*(7388), 149–150. https://doi.org/10.1038/483149a

Ledeczi, A., Lucas, M., Tobin, H., Watt, J., & Miller, N. (2023). Late Quaternary Surface Displacements on Accretionary Wedge Splay Faults in the Cascadia Subduction Zone: Implications for Megathrust Rupture. *Seismica*, *2*(4). https://doi.org/10.26443/seismica.v2i4.1158

Lee, Michelle K., Tan, Y. J., Russell, J. B., Tolstoy, M., & Waldhauser, F. (2024). Relative Seismic Velocity Variations at Axial Seamount Observed With Ambient Seismic Noise Capture Transition Point in Volcanic Inflation. *Geophysical Research Letters*, *51*(10), e2024GL108883. https://doi.org/10.1029/2024GL108883

Lee, Michelle Khuu. (2024). *Imaging and characterizing subseafloor structures associated with active magmatic and hydrothermal processes at and near seamounts on the Juan de Fuca plate from ridge to trench*. Columbia University. https://doi.org/10.7916/ytyg-ee71

Lesage, P., Heap, M., & Kushnir, A. (2018). A generic model for the shallow velocity structure of volcanoes. *Journal of Volcanology and Geothermal Research*. https://doi.org/10.1016/j.jvolgeores.2018.03.003

Levy, S., Bohnenstiehl, D. R., Sprinkle, P., Boettcher, M. S., Wilcock, W. S. D., Tolstoy, M., & Waldhauser, F. (2018). Mechanics of fault reactivation before, during, and after the 2015 eruption of Axial Seamount. *Geology*, *46*(5), 447–450. https://doi.org/10.1130/G39978.1

Li, S., Wang, K., Wang, Y., Jiang, Y., & Dosso, S. E. (2018a). Geodetically Inferred Locking State of the Cascadia Megathrust Based on a Viscoelastic Earth Model. *Journal of Geophysical Research: Solid Earth*, *123*(9), 8056–8072. https://doi.org/10.1029/2018JB015620

Li, S., Wang, K., Wang, Y., Jiang, Y., & Dosso, S. E. (2018b). Geodetically Inferred Locking State of the Cascadia Megathrust Based on a Viscoelastic Earth Model. *Journal of Geophysical Research: Solid Earth*, *123*(9), 8056–8072. https://doi.org/10.1029/2018JB015620

Li, W., Yuan, X., Heit, B., Schmidt-Aursch, M. C., Almendros, J., Geissler, W. H., & Chen, Y. (2021). Back-Arc Extension of the Central Bransfield Basin Induced by Ridge–Trench

Collision: Implications From Ambient Noise Tomography and Stress Field Inversion. *Geophysical Research Letters*, *48*(21). https://doi.org/10.1029/2021GL095032

Li, Z.-X. A., Lee, C.-T. A., Peslier, A. H., Lenardic, A., & Mackwell, S. J. (2008). Water contents in mantle xenoliths from the Colorado Plateau and vicinity: Implications for the mantle rheology and hydration-induced thinning of continental lithosphere. *Journal of Geophysical Research: Solid Earth*, *113*(B9). https://doi.org/10.1029/2007JB005540

Liao, J., & Gerya, T. (2015). From continental rifting to seafloor spreading: Insight from 3D thermo-mechanical modeling. *Gondwana Research*, *28*(4), 1329–1343. https://doi.org/10.1016/j.gr.2014.11.004

Lindsey, E. O., Mallick, R., Hubbard, J. A., Bradley, K. E., Almeida, R. V., Moore, J. D. P., et al. (2021). Slip rate deficit and earthquake potential on shallow megathrusts. *Nature Geoscience*, *14*(5), 321–326. https://doi.org/10.1038/s41561-021-00736-x

Livermore, R., Cunningham, A., Vanneste, L., & Larter, R. (1997). Subduction influence on magma supply at the East Scotia Ridge. *Earth and Planetary Science Letters*, *150*(3), 261–275. https://doi.org/10.1016/S0012-821X(97)00074-5

Loureiro Olivet, J., Sánchez Bettucci, L., Castro-Artola, O. A., Castro, H., Rodríguez, M., & Latorres, E. (2021). A seismic swarm at the Bransfield Rift, Antarctica. *Journal of South American Earth Sciences*, *111*, 103412. https://doi.org/10.1016/j.jsames.2021.103412

Luo, B., Zhang, S., & Zhu, H. (2023). Monitoring Seasonal Fluctuation and Long-Term Trends for the Greenland Ice Sheet Using Seismic Noise Auto-Correlations. *Geophysical Research Letters*, *50*(7), e2022GL102146. https://doi.org/10.1029/2022GL102146

Luu, K. (2024, December 20). disba: Numba-accelerated computation of surface wave dispersion (Version v0.7.0). Zenodo. https://doi.org/10.5281/zenodo.14534395

Maestrelli, D., Corti, G., Bonini, M., Montanari, D., & Sani, F. (2021). Caldera collapse and tectonics along the Main Ethiopian Rift: Reviewing possible relationships. *Comptes Rendus Geosciences*, *353*, 1–19. https://doi.org/10.5802/crgeos.63

Martinez, F., Stern, R. J., Kelley, K. A., Ohara, Y., Sleeper, J. D., Ribeiro, J. M., & Brounce, M. (2018). Diffuse Extension of the Southern Mariana Margin. *Journal of Geophysical Research: Solid Earth*, *123*(1), 892–916. https://doi.org/10.1002/2017JB014684

Mattes, T. E., Nunn, B. L., Marshall, K. T., Proskurowski, G., Kelley, D. S., Kawka, O. E., et al. (2013). Sulfur oxidizers dominate carbon fixation at a biogeochemical hot spot in the dark ocean. *The ISME Journal*, *7*(12), 2349–2360. https://doi.org/10.1038/ismej.2013.113

McDougall, T., & Barker, P. M. (2011). *Getting started with TEOS-10 and the Gibbs Seawater (GSW)Oceanographic Toolbox* (Vol. 127). SCOR/IAPSO WG127.

McGuire, J. J., & Collins, J. A. (2013). Millimeter-level precision in a seafloor geodesy experiment at the Discovery transform fault, East Pacific Rise. *Geochemistry, Geophysics, Geosystems*, *14*(10), 4392–4402. https://doi.org/10.1002/ggge.20225

McNutt, S. R. (2002). 25 - Volcano Seismology and Monitoring for Eruptions. In W. H. K. Lee, H. Kanamori, P. C. Jennings, & C. Kisslinger (Eds.), *International Geophysics* (Vol. 81, pp. 383-cp1). Academic Press. https://doi.org/10.1016/S0074-6142(02)80228-5

McVey, B. G., Hooft, E. E. E., Heath, B. A., Toomey, D. R., Paulatto, M., Morgan, J. V., et al. (2020). Magma accumulation beneath Santorini volcano, Greece, from P-wave tomography. *Geology*, *48*(3), 231–235. https://doi.org/10.1130/G47127.1

Meier, M., Schlindwein, V., & Schmid, F. (2022). Magmatic Activity and Dynamics of Melt Supply of Volcanic Centers of Ultraslow Spreading Ridges: Hints From Local

Earthquake Tomography at the Knipovich Ridge. *Geochemistry, Geophysics, Geosystems*, *23*(10), e2021GC010210. https://doi.org/10.1029/2021GC010210

Michael, P. J., Langmuir, C. H., Dick, H. J. B., Snow, J. E., Goldstein, S. L., Graham, D. W., et al. (2003). Magmatic and amagmatic seafloor generation at the ultraslow-spreading Gakkel ridge, Arctic Ocean. *Nature*, *423*(6943), 956–961. https://doi.org/10.1038/nature01704

Minshull, T. A., Bruguier, N. J., & Brozena, J. M. (2003). Seismic structure of the Mid-Atlantic Ridge, 8–9°S. *Journal of Geophysical Research: Solid Earth*, *108*(B11). https://doi.org/10.1029/2002JB002360

Minshull, T. A., Muller, M. R., & White, R. S. (2006). Crustal structure of the Southwest Indian Ridge at 66°E: seismic constraints. *Geophysical Journal International*, *166*(1), 135–147. https://doi.org/10.1111/j.1365-246X.2006.03001.x

Mogi, K. (1958). Relations between the Eruptions of Various Volcanoes and the Deformations of the Ground Surfaces around them. Retrieved from https://www.semanticscholar.org/paper/Relations-between-the-Eruptions-of-Various-and-the-Mogi/b7c310b9f1459599952a57b31f6827e3756eea95

Molnar, P., & Atwater, T. (1978). Interarc spreading and Cordilleran tectonics as alternates related to the age of subducted oceanic lithosphere. *Earth and Planetary Science Letters*, *41*(3), 330–340. https://doi.org/10.1016/0012-821X(78)90187-5

Momoh, E., Cannat, M., & Leroy, S. (2020). Internal Structure of the Oceanic Lithosphere at a Melt-Starved Ultraslow-Spreading Mid-Ocean Ridge: Insights From 2-D Seismic Data. *Geochemistry, Geophysics, Geosystems*, *21*(2), e2019GC008540. https://doi.org/10.1029/2019GC008540

Moore, J. C., Moore, G. F., Cochrane, G. R., & Tobin, H. J. (1995). Negative-polarity seismic reflections along faults of the Oregon accretionary prism: Indicators of overpressuring. *Journal of Geophysical Research: Solid Earth*, *100*(B7), 12895–12906. https://doi.org/10.1029/94JB02049

Moreau, L., Stehly, L., Boué, P., Lu, Y., Larose, E., & Campillo, M. (2017). Improving ambient noise correlation functions with an SVD-based Wiener filter. *Geophysical Journal International*, *211*(1), 418–426. https://doi.org/10.1093/gji/ggx306

Morton, E. A., Bilek, S. L., & Rowe, C. A. (2018). Newly detected earthquakes in the Cascadia subduction zone linked to seamount subduction and deformed upper plate. *Geology*, *46*(11), 943–946. https://doi.org/10.1130/G45354.1

Moser, T. J. (1991). Shortest path calculation of seismic rays. *Geophysics*, (56), 59–67. https://doi.org/10.1190/1.1442958

Mourya, R., Dragone, M., & Petillot, Y. (2021). Robust Silent Localization of Underwater Acoustic Sensor Network Using Mobile Anchor(s). *Sensors (Basel, Switzerland)*, *21*(3), 727. https://doi.org/10.3390/s21030727

Nakajima, J., & Uchida, N. (2018). Repeated drainage from megathrusts during episodic slow slip. *Nature Geoscience*, *11*(5), 351–356. https://doi.org/10.1038/s41561-018-0090-z

Nakano, M., Hori, T., Araki, E., Kodaira, S., & Ide, S. (2018). Shallow very-low-frequency earthquakes accompany slow slip events in the Nankai subduction zone. *Nature Communications*, *9*(1), 984. https://doi.org/10.1038/s41467-018-03431-5

National Academies of Sciences, Engineering, and Medicine. (2017). *Volcanic Eruptions and Their Repose, Unrest, Precursors, and Timing* (p. 24650). Washington, D.C.: National Academies Press. https://doi.org/10.17226/24650

Niu, X., Ruan, A., Li, J., Minshull, T. A., Sauter, D., Wu, Z., et al. (2015). Along-axis variation in crustal thickness at the ultraslow spreading Southwest Indian Ridge (50°E) from a wide-angle seismic experiment. *Geochemistry, Geophysics, Geosystems*, *16*(2), 468–485. https://doi.org/10.1002/2014GC005645

Njinju, E. A., Atekwana, E. A., Stamps, D. S., Abdelsalam, M. G., Atekwana, E. A., Mickus, K. L., et al. (2019). Lithospheric Structure of the Malawi Rift: Implications for Magma-Poor Rifting Processes. *Tectonics*, *38*(11), 3835–3853. https://doi.org/10.1029/2019TC005549

Nooner, S. L., & Chadwick Jr., W. W. (2009). Volcanic inflation measured in the caldera of Axial Seamount: Implications for magma supply and future eruptions. *Geochemistry, Geophysics, Geosystems*, *10*(2). https://doi.org/10.1029/2008GC002315

Nooner, S. L., & Chadwick, W. W. (2016). Inflation-predictable behavior and co-eruption deformation at Axial Seamount. *Science*, *354*(6318), 1399–1403. https://doi.org/10.1126/science.aah4666

Nowacki, A., Wilks, M., Kendall, J.-M., Biggs, J., & Ayele, A. (2018). Characterising hydrothermal fluid pathways beneath Aluto volcano, Main Ethiopian Rift, using shear wave splitting. *Journal of Volcanology and Geothermal Research*, *356*, 331–341. https://doi.org/10.1016/j.jvolgeores.2018.03.023

Obana, K., & Kodaira, S. (2009). Low-frequency tremors associated with reverse faults in a shallow accretionary prism. *Earth and Planetary Science Letters*, *287*(1), 168–174. https://doi.org/10.1016/j.epsl.2009.08.005

Okubo, K., Delbridge, B. G., & Denolle, M. A. (2024). Monitoring Velocity Change Over 20 Years at Parkfield. *Journal of Geophysical Research: Solid Earth*, *129*(4), e2023JB028084. https://doi.org/10.1029/2023JB028084

Ozawa, S., Yang, Y., & Dunham, E. M. (2024). Fault-Valve Instability: A Mechanism for Slow Slip Events. *Journal of Geophysical Research: Solid Earth*, *129*(10), e2024JB029165. https://doi.org/10.1029/2024JB029165

Pagli, C., Mazzarini, F., Keir, D., Rivalta, E., & Rooney, T. O. (2015). Introduction: Anatomy of rifting: Tectonics and magmatism in continental rifts, oceanic spreading centers, and transforms. *Geosphere*, *11*(5), 1256–1261. https://doi.org/10.1130/GES01082.1

Parera-Portell, J. A., Mancilla, F. D. L., Almendros, J., Morales, J., & Stich, D. (2023). Slab Tearing Underneath the Bransfield Strait, Antarctica. *Geophysical Research Letters*, *50*(13), e2023GL103813. https://doi.org/10.1029/2023GL103813

Paulatto, M., Annen, C., Henstock, T. J., Kiddle, E., Minshull, T. A., Sparks, R. S. J., & Voight, B. (2012). Magma chamber properties from integrated seismic tomography and thermal modeling at Montserrat. *Geochemistry, Geophysics, Geosystems*, *13*(1). https://doi.org/10.1029/2011GC003892

Paulatto, Michele, Moorkamp, M., Hautmann, S., Hooft, E., Morgan, J. V., & Sparks, R. S. J. (2019). Vertically Extensive Magma Reservoir Revealed From Joint Inversion and Quantitative Interpretation of Seismic and Gravity Data. *Journal of Geophysical Research: Solid Earth*, *124*(11), 11170–11191. https://doi.org/10.1029/2019JB018476

Paulatto, Michele, Hooft, E. E. E., Chrapkiewicz, K., Heath, B., Toomey, D. R., & Morgan, J. V. (2022). Advances in seismic imaging of magma and crystal mush. *Frontiers in Earth Science*, *10*. Retrieved from https://www.frontiersin.org/articles/10.3389/feart.2022.970131

Pearce, J., & Stern, B. (2006). Origin of Back-Arc Basin Magmas: Trace Element and Isotope Perspectives. *Monograph Series American Geophysical Union*, *166*, 63–86. https://doi.org/10.1029/166GM06

Petersen, F., Kopp, H., Lange, D., Hannemann, K., & Urlaub, M. (2019). Measuring tectonic seafloor deformation and strain-build up with acoustic direct-path ranging. *Journal of Geodynamics*, *124*, 14–24. https://doi.org/10.1016/j.jog.2019.01.002

Philip, B. T., Solomon, E. A., Kelley, D. S., Tréhu, A. M., Whorley, T. L., Roland, E., et al. (2023). Fluid sources and overpressures within the central Cascadia Subduction Zone revealed by a warm, high-flux seafloor seep. *Science Advances*, *9*(4), eadd6688. https://doi.org/10.1126/sciadv.add6688

Planert, L., Flueh, E. R., & Reston, T. J. (2009). Along- and across-axis variations in crustal thickness and structure at the Mid-Atlantic Ridge at 5°S obtained from wide-angle seismic tomography: Implications for ridge segmentation. *Journal of Geophysical Research: Solid Earth*, *114*(B9). https://doi.org/10.1029/2008JB006103

Plata-Martinez, R., Ide, S., Shinohara, M., Garcia, E. S., Mizuno, N., Dominguez, L. A., et al. (2021). Shallow slow earthquakes to decipher future catastrophic earthquakes in the Guerrero seismic gap. *Nature Communications*, *12*(1), 3976. https://doi.org/10.1038/s41467-021-24210-9

Polster, A., Fabian, M., & Villinger, H. (2009). Effective resolution and drift of Paroscientific pressure sensors derived from long-term seafloor measurements. *Geochemistry, Geophysics, Geosystems*, *10*(8). https://doi.org/10.1029/2009GC002532

Prieto, M. J., Canals, M., Ercilla, G., & de Batist, M. (1998). Structure and geodynamic evolution of the Central Bransfield Basin (NW Antarctica) from seismic reflection data. *Marine Geology*, *149*(1–4), 17–38. https://doi.org/10.1016/S0025-3227(98)00038-3

Prieto, M. J., Ercilla, G., Canals, M., & de Batist, M. (1999). Seismic stratigraphy of the Central Bransfield Basin (NW Antarctic Peninsula): interpretation of deposits and sedimentary processes in a glacio-marine environment. *Marine Geology*, *157*(1), 47–68. https://doi.org/10.1016/S0025-3227(98)00149-2

Prôno, E., Battaglia, J., Monteiller, V., Got, J.-L., & Ferrazzini, V. (2009). P-wave velocity structure of Piton de la Fournaise volcano deduced from seismic data recorded between 1996 and 1999. *Journal of Volcanology and Geothermal Research*, *184*(1), 49–62. https://doi.org/10.1016/j.jvolgeores.2008.12.009

Purdy, G. M., & Detrick, R. S. (1986). Crustal structure of the Mid-Atlantic Ridge at 23°N from seismic refraction studies. *Journal of Geophysical Research: Solid Earth*, *91*(B3), 3739–3762. https://doi.org/10.1029/JB091iB03p03739

Robertson Maurice, S. D., Wiens, D. A., Shore, P. J., Vera, E., & Dorman, L. M. (2003). Seismicity and tectonics of the South Shetland Islands and Bransfield Strait from a regional broadband seismograph deployment: SOUTH SHETLAND ISLANDS SEISMICITY. *Journal of Geophysical Research: Solid Earth*, *108*(B10). https://doi.org/10.1029/2003JB002416

Rodrigo, C., Blamey, J. M., Huhn, O., & Provost, C. (2018). Is there an active hydrothermal flux from the Orca seamount in the Bransfield Strait, Antarctica? *Andean Geology*, *45*(3), 344–356.

Roger Buck, W., Carbotte, S. M., & Mutter, C. (1997). Controls on extrusion at mid-ocean ridges. *Geology*, *25*(10), 935–938. https://doi.org/10.1130/0091-7613(1997)025%3C0935:COEAMO%3E2.3.CO;2

Romanowicz, B., Dreger, D., Pasyanos, M., & Uhrhammer, R. (1993). Monitoring of strain release in central and northern California using broadband data. *Geophysical Research Letters*, *20*(15), 1643–1646. https://doi.org/10.1029/93GL01540

Romer, R. H. W., Beier, C., Haase, K. M., Eberts, A., & Hübscher, C. (2021). The Evolution of Central Volcanoes in Ultraslow Rift Systems: Constraints From D. João de Castro Seamount, Azores. *Tectonics*, *40*(7), e2020TC006663. https://doi.org/10.1029/2020TC006663

Rowe, M. C., Lassiter, J. C., & Goff, K. (2015). Basalt volatile fluctuations during continental rifting: An example from the Rio Grande Rift, USA. *Geochemistry, Geophysics, Geosystems*, *16*(5), 1254–1273. https://doi.org/10.1002/2014GC005649

Rubinstein, J. L., La Rocca, M., Vidale, J. E., Creager, K. C., & Wech, A. G. (2008). Tidal Modulation of Nonvolcanic Tremor. *Science*, *319*(5860), 186–189. https://doi.org/10.1126/science.1150558

Rubinstein, J. L., Gomberg, J., Vidale, J. E., Wech, A. G., Kao, H., Creager, K. C., & Rogers, G. (2009). Seismic wave triggering of nonvolcanic tremor, episodic tremor and slip, and earthquakes on Vancouver Island. *Journal of Geophysical Research: Solid Earth*, *114*(B2). https://doi.org/10.1029/2008JB005875

Ruppel, C. (1995). Extensional processes in continental lithosphere. *Journal of Geophysical Research: Solid Earth*, *100*(B12), 24187–24215. https://doi.org/10.1029/95JB02955

Russell, J. B., Eilon, Z., & Mosher, S. G. (2019). OBSrange: A New Tool for the Precise Remote Location of Ocean-Bottom Seismometers. *Seismological Research Letters*, *90*(4), 1627–1641. https://doi.org/10.1785/0220180336

Saffer, D. M. (2014). The permeability of active subduction plate boundary faults. *Geofluids*, *15*(1–2), 193–215. https://doi.org/10.1111/gfl.12103

Sakic, P., Piété, H., Ballu, V., Royer, J.-Y., Kopp, H., Lange, D., et al. (2016). No significant steady state surface creep along the North Anatolian Fault offshore Istanbul: Results of 6 months of seafloor acoustic ranging. *Geophysical Research Letters*, *43*(13), 6817–6825. https://doi.org/10.1002/2016GL069600

Satake, K., & Atwater, B. F. (2007). Long-Term Perspectives on Giant Earthquakes and Tsunamis at Subduction Zones*. *Annual Review of Earth and Planetary Sciences*, *35*(Volume 35, 2007), 349–374. https://doi.org/10.1146/annurev.earth.35.031306.140302

Sato, T., Mizuno, M., Takata, H., Yamada, T., Isse, T., Mochizuki, K., et al. (2015). Seismic Structure and Seismicity in the Southern Mariana Trough and Their Relation to Hydrothermal Activity. In J. Ishibashi, K. Okino, & M. Sunamura (Eds.), *Subseafloor Biosphere Linked to Hydrothermal Systems: TAIGA Concept* (pp. 229–240). Tokyo: Springer Japan. https://doi.org/10.1007/978-4-431-54865-2_18

Schmalzle, G. M., McCaffrey, R., & Creager, K. C. (2014). Central Cascadia subduction zone creep. *Geochemistry, Geophysics, Geosystems*, *15*(4), 1515–1532. https://doi.org/10.1002/2013GC005172

Schmandt, B., Jiang, C., & Farrell, J. (2019). Seismic perspectives from the western U.S. on magma reservoirs underlying large silicic calderas. *Journal of Volcanology and Geothermal Research*, *384*, 158–178. https://doi.org/10.1016/j.jvolgeores.2019.07.015

Schmid, F., Schlindwein, V., Koulakov, I., Plötz, A., & Scholz, J.-R. (2017). Magma plumbing system and seismicity of an active mid-ocean ridge volcano. *Scientific Reports*, *7*(1), 42949. https://doi.org/10.1038/srep42949

Schmidt-Aursch, M. C., & Haberland, C. (2017). DEPAS (Deutscher Geräte-Pool für amphibische Seismologie): German Instrument Pool for Amphibian Seismology. *Journal of Large-Scale Research Facilities JLSRF*, *3*, A122. https://doi.org/10.17815/jlsrf-3-165

Searle, R. C., Murton, B. J., Achenbach, K., LeBas, T., Tivey, M., Yeo, I., et al. (2010). Structure and development of an axial volcanic ridge: Mid-Atlantic Ridge, 45°N. *Earth and Planetary Science Letters*, *299*(1), 228–241. https://doi.org/10.1016/j.epsl.2010.09.003

Seccia, D., Chiarabba, C., De Gori, P., Bianchi, I., & Hill, D. P. (2011). Evidence for the contemporary magmatic system beneath Long Valley Caldera from local earthquake tomography and receiver function analysis. *Journal of Geophysical Research: Solid Earth*, *116*(B12). https://doi.org/10.1029/2011JB008471

Sens-Schönfelder, C., & Eulenfeld, T. (2019). Probing the in situ Elastic Nonlinearity of Rocks with Earth Tides and Seismic Noise. *Physical Review Letters*, *122*(13), 138501. https://doi.org/10.1103/PhysRevLett.122.138501

Sens-Schönfelder, C., Pomponi, E., & Peltier, A. (2014). Dynamics of Piton de la Fournaise volcano observed by passive image interferometry with multiple references. *Journal of Volcanology and Geothermal Research*, *276*, 32–45. https://doi.org/10.1016/j.jvolgeores.2014.02.012

Shaw, P. R., & Orcutt, J. A. (1985). Waveform inversion of seismic refraction data and applications to young Pacific crust. *Geophysical Journal International*, *82*(3), 375–414. https://doi.org/10.1111/j.1365-246X.1985.tb05143.x

Shillington, D. J., Scott, C. L., Minshull, T. A., Edwards, R. A., Brown, P. J., & White, N. (2009). Abrupt transition from magma-starved to magma-rich rifting in the eastern Black Sea. *Geology*, *37*(1), 7–10. https://doi.org/10.1130/G25302A.1

Sinton, J. M., & Detrick, R. S. (1992). Mid-ocean ridge magma chambers. *Journal of Geophysical Research: Solid Earth*, *97*(B1), 197–216. https://doi.org/10.1029/91JB02508

Slead, S. (2024). Data and Code for Modeling Axial Seamount. https://doi.org/10.5281/zenodo.10785669

Slead, S. R., Wei, M., Nooner, S. L., Chadwick Jr., W. W., Caress, D. W., & Beeson, J. (2024). Compartmentalization of Axial Seamount's Magma Reservoir Inferred by Analytical and Numerical Deformation Modeling With Realistic Geometry. *Journal of Geophysical Research: Solid Earth*, *129*(5), e2023JB028414. https://doi.org/10.1029/2023JB028414

Sleeper, J. D., Martinez, F., Fryer, P., Stern, R. J., Kelley, K. A., & Ohara, Y. (2021). Diffuse spreading, a newly recognized mode of crustal accretion in the southern Mariana Trough backarc basin. *Geosphere*, *17*(5), 1382–1404. https://doi.org/10.1130/GES02360.1

Smith, L., Cowles, T., Vaillancourt, R., & Yelisetti, S. (2018). Introduction to the Special Issue on the Ocean Observatories Initiative. *Oceanography*, *31*(1), 12–15. https://doi.org/10.5670/oceanog.2018.104

Snieder, R., Sens-Schönfelder, C., & Wu, R. (2017). The time dependence of rock healing as a universal relaxation process, a tutorial. *Geophysical Journal International*, *208*(1), 1–9. https://doi.org/10.1093/gji/ggw377

Soule, D., Granja-Bruña, J., Tinto, K., Almendros, J., Vizcaino, L., & Wilcock, W. (2025). Geophysical characterization of the crustal structure of the Central Bransfield Basin around Orca Volcano: Evidence for a rapidly evolving back-arc rift. *Geophysical Research Letters*.

Stockli, D., & Bosworth, W. (2019). Timing of Extensional Faulting Along the Magma-Poor Central and Northern Red Sea Rift Margin—Transition from Regional Extension to Necking Along a Hyperextended Rifted Margin (pp. 81–111). https://doi.org/10.1007/978-3-319-99408-6_5

Stone, I., Vidale, J. E., Han, S., & Roland, E. (2018). Catalog of Offshore Seismicity in Cascadia: Insights Into the Regional Distribution of Microseismicity and its Relation to Subduction Processes. *Journal of Geophysical Research: Solid Earth*, *123*(1), 641–652. https://doi.org/10.1002/2017JB014966

Strak, V., Xue, K., & Schellart, W. P. (2024). Mantle upwelling induced by slab rollover subduction could explain widespread intraplate volcanism in Tibet. *Communications Earth & Environment*, *5*(1), 1–13. https://doi.org/10.1038/s43247-024-01581-7

Sun, Q., Jackson, C. A.-L., Magee, C., Mitchell, S. J., & Xie, X. (2019). Extrusion dynamics of deepwater volcanoes revealed by 3-D seismic data. *Solid Earth*, *10*(4), 1269–1282. https://doi.org/10.5194/se-10-1269-2019

Sun, T., Wang, K., Iinuma, T., Hino, R., He, J., Fujimoto, H., et al. (2014). Prevalence of viscoelastic relaxation after the 2011 Tohoku-oki earthquake. *Nature*, *514*(7520), 84–87. https://doi.org/10.1038/nature13778

Sutherland, F. H. (2006). *Continental rifting across the Southern Gulf of California*. UC San Diego. Retrieved from https://escholarship.org/uc/item/0179n31h

Syracuse, E. M., Thurber, C. H., & Power, J. A. (2011). The Augustine magmatic system as revealed by seismic tomography and relocated earthquake hypocenters from 1994 through 2009. *Journal of Geophysical Research: Solid Earth*, *116*(B9). https://doi.org/10.1029/2010JB008129

Taira, T., Brenguier, F., & Kong, Q. (2015). Ambient noise-based monitoring of seismic velocity changes associated with the 2014 $M_w$ 6.0 South Napa earthquake. *Geophysical Research Letters*, *42*(17), 6997–7004. https://doi.org/10.1002/2015GL065308

Takano, T., Nishimura, T., Nakahara, H., Ueda, H., & Fujita, E. (2019). Sensitivity of Seismic Velocity Changes to the Tidal Strain at Different Lapse Times: Data Analyses of a Small Seismic Array at Izu-Oshima Volcano. *Journal of Geophysical Research: Solid Earth*, *124*(3), 3011–3023. https://doi.org/10.1029/2018JB016235

Tanikawa, W., Mukoyoshi, H., Lin, W., Hirose, T., & Tsutsumi, A. (2014). Pressure dependence of fluid transport properties of shallow fault systems in the Nankai subduction zone. *Earth, Planets and Space*, *66*(1), 90. https://doi.org/10.1186/1880-5981-66-90

Taylor, B., & Martinez, F. (2003). Back-arc basin basalt systematics. *Earth and Planetary Science Letters*, *210*(3), 481–497. https://doi.org/10.1016/S0012-821X(03)00167-5

Taylor, F. W., Bevis, M. G., Dalziel, I. W. D., Smalley Jr., R., Frohlich, C., Kendrick, E., et al. (2008). Kinematics and segmentation of the South Shetland Islands-Bransfield basin system, northern Antarctic Peninsula. *Geochemistry, Geophysics, Geosystems*, *9*(4). https://doi.org/10.1029/2007GC001873

Taylor, M. A. J., & Singh, S. C. (2002). Composition and microstructure of magma bodies from effective medium theory. *Geophysical Journal International*, *149*(1), 15–21. https://doi.org/10.1046/j.1365-246X.2002.01577.x

Teichert, B. M. A., Torres, M. E., Bohrmann, G., & Eisenhauer, A. (2005). Fluid sources, fluid pathways and diagenetic reactions across an accretionary prism revealed by Sr and B geochemistry. *Earth and Planetary Science Letters*, *239*(1), 106–121. https://doi.org/10.1016/j.epsl.2005.08.002

Thatcher, W. (2009). How the Continents Deform: The Evidence From Tectonic Geodesy*. *Annual Review of Earth and Planetary Sciences*, *37*(Volume 37, 2009), 237–262. https://doi.org/10.1146/annurev.earth.031208.100035

Tobin, H., Moore, J. C., MacKay, M. E., Orange, D. L., & Kulm, L. (1993). Fluid flow along a strike-slip fault at the toe of the Oregon accretionary prism: Implications for the geometry of frontal accretion. *GSA Bulletin*, *105*(5), 569–582. https://doi.org/10.1130/0016-7606(1993)105%3C0569:FFAASS%3E2.3.CO;2

Tolstoy, M., Waldhauser, F., Bohnenstiehl, D. R., Weekly, R. T., & Kim, W.-Y. (2008). Seismic identification of along-axis hydrothermal flow on the East Pacific Rise. *Nature*, *451*(7175), 181–184. https://doi.org/10.1038/nature06424

Tolstoy, Maya, Vernon, F. L., Orcutt, J. A., & Wyatt, F. K. (2002). Breathing of the seafloor: Tidal correlations of seismicity at Axial volcano. *Geology*, *30*(6), 503–506. https://doi.org/10.1130/0091-7613(2002)030%3C0503:BOTSTC%3E2.0.CO;2

Tomasetto, L., Boué, P., Ardhuin, F., Stutzman, E., Xu, Z., de Plaen, R., et al. (2024). WMSAN Python Package: From Oceanic Forcing to Synthetic Cross-correlations of Microseismic Noise. *EathArXiv*. https://doi.org/10.31223/X5CB08

Tonegawa, T., Takemura, S., Yabe, S., & Yomogida, K. (2022a). Fluid Migration Before and During Slow Earthquakes in the Shallow Nankai Subduction Zone. *Journal of*

*Geophysical Research: Solid Earth*, *127*(3), e2021JB023583. https://doi.org/10.1029/2021JB023583

Tonegawa, T., Takemura, S., Yabe, S., & Yomogida, K. (2022b). Fluid Migration Before and During Slow Earthquakes in the Shallow Nankai Subduction Zone. *Journal of Geophysical Research: Solid Earth*, *127*(3), e2021JB023583. https://doi.org/10.1029/2021JB023583

Toomey, D. R., Solomon, S. C., & Purdy, G. M. (1994). Tomographic imaging of the shallow crustal structure of the East Pacific Rise at 9°30′N. *Journal of Geophysical Research: Solid Earth*, *99*(B12), 24135–24157. https://doi.org/10.1029/94JB01942

Turner, I. M., Peirce, C., & Sinha, M. C. (1999). Seismic imaging of the axial region of the Valu Fa Ridge, Lau Basin—the accretionary processes of an intermediate back-arc spreading ridge. *Geophysical Journal International*, *138*(2), 495–519. https://doi.org/10.1046/j.1365-246X.1999.00883.x

Uemura, M., Ito, Y., Ohta, K., Hino, R., & Shinohara, M. (2018). Spatio-temporal changes in the seismic velocity induced by the 2011 Tohoku-Oki earthquake and slow slip event revealed from seismic interferometry, using ocean bottom seismometer's records. *Progress in Earth and Planetary Science*, *5*(1), 87. https://doi.org/10.1186/s40645-018-0240-3

Urlaub, M., Petersen, F., Gross, F., Bonforte, A., Puglisi, G., Guglielmino, F., et al. (2018). Gravitational collapse of Mount Etna's southeastern flank. *Science Advances*, *4*(10), eaat9700. https://doi.org/10.1126/sciadv.aat9700

Uyeda, S., & Kanamori, H. (1979). Back-arc opening and the mode of subduction. *Journal of Geophysical Research*, *84*(B3), 1049. https://doi.org/10.1029/JB084iB03p01049

VanderBeek, B. P., & Faccenda, M. (2021). Imaging upper mantle anisotropy with teleseismic P-wave delays: insights from tomographic reconstructions of subduction simulations. *Geophysical Journal International*, *225*(3), 2097–2119. https://doi.org/10.1093/gji/ggab081

Viesca, R. C., & Garagash, D. I. (2015). Ubiquitous weakening of faults due to thermal pressurization. *Nature Geoscience*, *8*(11), 875–879. https://doi.org/10.1038/ngeo2554

Wada, I., & Wang, K. (2009). Common depth of slab-mantle decoupling: Reconciling diversity and uniformity of subduction zones. *Geochemistry, Geophysics, Geosystems*, *10*(10). https://doi.org/10.1029/2009GC002570

Waldhauser, F., Wilcock, W. S. D., Tolstoy, M., Baillard, C., Tan, Y. J., & Schaff, D. P. (2020). Precision Seismic Monitoring and Analysis at Axial Seamount Using a Real-Time Double-Difference System. *Journal of Geophysical Research: Solid Earth*, *125*(5), e2019JB018796. https://doi.org/10.1029/2019JB018796

Walton, M. A. L., Staisch, L. M., Dura, T., Pearl, J. K., Sherrod, B., Gomberg, J., et al. (2021). Toward an Integrative Geological and Geophysical View of Cascadia Subduction Zone Earthquakes. *Annual Review of Earth and Planetary Sciences*, *49*(Volume 49, 2021), 367–398. https://doi.org/10.1146/annurev-earth-071620-065605

Wang, H., Huismans, R. S., & Rondenay, S. (2019). Water Migration in the Subduction Mantle Wedge: A Two-Phase Flow Approach. *Journal of Geophysical Research: Solid Earth*, *124*(8), 9208–9225. https://doi.org/10.1029/2018JB017097

Wang, J., Gleeson, M., Smith, W. D., Ma, L., Lei, Z., Shi, G., & Chen, L. (2022). Frontiers | The factors controlling along-arc and across-arc variations of primitive arc magma compositions: A global perspective. https://doi.org/10.3389/feart.2022.1055255

Wang, Kaiwen, Waldhauser, F., Schaff, D., Tolstoy, M., Wilcock, W. S. D., & Tan, Y. J. (2024). Real-Time Detection of Volcanic Unrest and Eruption at Axial Seamount Using Machine Learning. *Seismological Research Letters*, *95*(5), 2651–2662. https://doi.org/10.1785/0220240086

Wang, Kaiwen, Waldhauser, F., Tolstoy, M., Schaff, D., Sawi, T., Wilcock, W. S. D., & Tan, Y. J. (2024). Volcanic Precursor Revealed by Machine Learning Offers New Eruption Forecasting Capability. *Geophysical Research Letters*, *51*(19), e2024GL108631. https://doi.org/10.1029/2024GL108631

Wang, Kelin, & Tréhu, A. M. (2016). Invited review paper: Some outstanding issues in the study of great megathrust earthquakes—The Cascadia example. *Journal of Geodynamics*, *98*, 1–18. https://doi.org/10.1016/j.jog.2016.03.010

Wang, L., Wang, Q., & Ruan, Y. (2025). Monitoring Dynamic Magma Movement in the Lower Crust During the 2015 Eruption of Axial Seamount. *Journal of Geophysical Research: Solid Earth*, *130*(7), e2024JB030481. https://doi.org/10.1029/2024JB030481

Wang, W., Savage, M. K., Yates, A., Zal, H. J., Webb, S., Boulton, C., et al. (2022). Temporal velocity variations in the northern Hikurangi margin and the relation to slow slip. *Earth and Planetary Science Letters*, *584*, 117443. https://doi.org/10.1016/j.epsl.2022.117443

Warren-Smith, E., Fry, B., Wallace, L., Chon, E., Henrys, S., Sheehan, A., et al. (2019). Episodic stress and fluid pressure cycling in subducting oceanic crust during slow slip. *Nature Geoscience*, *12*(6), 475–481. https://doi.org/10.1038/s41561-019-0367-x

Watanabe, M., Okino, K., & Kodera, T. (2010). Rifting to spreading in the southern Lau Basin: Variations within the transition zone. *Tectonophysics*, *494*(3), 226–234. https://doi.org/10.1016/j.tecto.2010.09.001

Weaver, S. D., Saunders, A. D., Pankhurst, R. J., & Tarney, J. (1979). A geochemical study of magmatism associated with the initial stages of back-arc spreading. *Contributions to Mineralogy and Petrology*, *68*(2), 151–169. https://doi.org/10.1007/BF00371897

Wech, A. G. (2010). Interactive Tremor Monitoring. *Seismological Research Letters*, *81*(4), 664–669. https://doi.org/10.1785/gssrl.81.4.664

Weekly, R. T., Wilcock, W. S. D., Toomey, D. R., Hooft, E. E. E., & Kim, E. (2014). Upper crustal seismic structure of the Endeavour segment, Juan de Fuca Ridge from traveltime tomography: Implications for oceanic crustal accretion. *Geochemistry, Geophysics, Geosystems*, *15*(4), 1296–1315. https://doi.org/10.1002/2013GC005159

Weir, N. R. W., White, R. S., Brandsdóttir, B., Einarsson, P., Shimamura, H., & Shiobara, H. (2001). Crustal structure of the northern Reykjanes Ridge and Reykjanes Peninsula, southwest Iceland. *Journal of Geophysical Research: Solid Earth*, *106*(B4), 6347–6368. https://doi.org/10.1029/2000JB900358

Wernicke, B. (1985). Uniform-sense normal simple shear of the continental lithosphere. *Canadian Journal of Earth Sciences*, *22*(1), 108–125. https://doi.org/10.1139/e85-009

West, M., Menke, W., Tolstoy, M., Webb, S., & Sohn, R. (2001). Magma storage beneath Axial volcano on the Juan de Fuca mid-ocean ridge. *Nature*, *413*(6858), 833–836. https://doi.org/10.1038/35101581

Wilcock, W. S. D., Tolstoy, M., Waldhauser, F., Garcia, C., Tan, Y. J., Bohnenstiehl, D. R., et al. (2016). Seismic constraints on caldera dynamics from the 2015 Axial Seamount eruption. *Science*, *354*(6318), 1395–1399. https://doi.org/10.1126/science.aah5563

Wilcock, W. S. D., Dziak, R. P., Tolstoy, M., Jr, W. W. C., & Nooner, S. L. (2018). The Recent Volcanic History of Axial Seamount: Geophysical Insights into Past Eruption Dynamics

with an Eye Toward Enhanced Observations of Future…. *Oceanography*, *31*(1), 114–123. https://doi.org/10.5670/oceanog.2018.117

Wilson, R. C. L., Manatschal, G., & Wise, S. (2001). Rifting along non-volcanic passive margins: stratigraphic and seismic evidence from the Mesozoic successions of the Alps and western Iberia. *Geological Society, London, Special Publications*, *187*(1), 429–452. https://doi.org/10.1144/GSL.SP.2001.187.01.21

Wilson, R. W., Houseman, G. A., Buiter, S. J. H., McCaffrey, K. J. W., & Doré, A. G. (2019). Fifty years of the Wilson Cycle concept in plate tectonics: an overview. *Geological Society, London, Special Publications*, *470*(1), 1–17. https://doi.org/10.1144/SP470-2019-58

Wirth, E. A., Sahakian, V. J., Wallace, L. M., & Melnick, D. (2022). The occurrence and hazards of great subduction zone earthquakes. *Nature Reviews Earth & Environment*, *3*(2), 125–140. https://doi.org/10.1038/s43017-021-00245-w

Woods, K., Wallace, L. M., Williams, C. A., Hamling, I. J., Webb, S. C., Ito, Y., et al. (2024). Spatiotemporal Evolution of Slow Slip Events at the Offshore Hikurangi Subduction Zone in 2019 Using GNSS, InSAR, and Seafloor Geodetic Data. *Journal of Geophysical Research: Solid Earth*, *129*(8), e2024JB029068. https://doi.org/10.1029/2024JB029068

Xu, G., & Lavelle, J. W. (2017). Circulation, hydrography, and transport over the summit of Axial Seamount, a deep volcano in the Northeast Pacific. *Journal of Geophysical Research: Oceans*, *122*(7), 5404–5422. https://doi.org/10.1002/2016JC012464

Xu, Guangyu, Chadwick Jr., W. W., Wilcock, W. S. D., Bemis, K. G., & Delaney, J. (2018). Observation and Modeling of Hydrothermal Response to the 2015 Eruption at Axial

Seamount, Northeast Pacific. *Geochemistry, Geophysics, Geosystems*, *19*(8), 2780–2797. https://doi.org/10.1029/2018GC007607

Yamaoka, K., Kawamura, M., Kimata, F., Fujii, N., & Kudo, T. (2005). Dike intrusion associated with the 2000 eruption of Miyakejima Volcano, Japan. *Bulletin of Volcanology*, *67*(3), 231–242. https://doi.org/10.1007/s00445-004-0406-2

Yang, J., Zhu, H., Zhao, Z., Huang, J., Lumley, D., Stern, R. J., et al. (2024). Asymmetric magma plumbing system beneath Axial Seamount based on full waveform inversion of seismic data. *Nature Communications*, *15*(1), 4767. https://doi.org/10.1038/s41467-024-49188-y

Yokota, Y., Ishikawa, T., Watanabe, S., Tashiro, T., & Asada, A. (2016). Seafloor geodetic constraints on interplate coupling of the Nankai Trough megathrust zone. *Nature*, *534*(7607), 374–377. https://doi.org/10.1038/nature17632

Yousefi, M., Milne, G., Li, S., Wang, K., & Bartholet, A. (2020). Constraining Interseismic Deformation of the Cascadia Subduction Zone: New Insights From Estimates of Vertical Land Motion Over Different Timescales. *Journal of Geophysical Research: Solid Earth*, *125*(3), e2019JB018248. https://doi.org/10.1029/2019JB018248

Zandomeneghi, D., Barclay, A., Almendros, J., Ibañez Godoy, J. M., Wilcock, W. S. D., & Ben-Zvi, T. (2009). Crustal structure of Deception Island volcano from *P* wave seismic tomography: Tectonic and volcanic implications. *Journal of Geophysical Research*, *114*(B6), B06310. https://doi.org/10.1029/2008JB006119

Zhan, Z., Tsai, V. C., & Clayton, R. W. (2013). Spurious velocity changes caused by temporal variations in ambient noise frequency content. *Geophysical Journal International*, *194*(3), 1574–1581. https://doi.org/10.1093/gji/ggt170

Zhao, D., & Hua, Y. (2021). Anisotropic tomography of the Cascadia subduction zone. *Physics of the Earth and Planetary Interiors*, *318*, 106767. https://doi.org/10.1016/j.pepi.2021.106767

Zhao, M., Canales, J. P., & Sohn, R. A. (2012). Three-dimensional seismic structure of a Mid-Atlantic Ridge segment characterized by active detachment faulting (Trans-Atlantic Geotraverse, 25°55′N-26°20′N). *Geochemistry, Geophysics, Geosystems*, *13*(11). https://doi.org/10.1029/2012GC004454

Zollo, A., Judenherc, S., Auger, E., D'Auria, L., Virieux, J., Capuano, P., et al. (2003). Evidence for the buried rim of Campi Flegrei caldera from 3-d active seismic imaging. *Geophysical Research Letters*, *30*(19). https://doi.org/10.1029/2003GL018173

## Appendix A: Supplementary Information for chapter 2

### Introduction

Within the Supporting Information, we detail the methods for ocean bottom seismometer (OBS) relocation, the optimization of smoothing and damping parameters for the velocity inversions, the optimization of the magma chamber volume used to separate the paths of modeled Pg and Pmc arrivals, and the calculations of melt fractions. Additional figures are included showing water column velocities, the shadow zones with Pmc arrivals, Pmc ray paths, record sections with picks of the 1$^{st}$, 2$^{nd}$, and 3$^{rd}$ cycles of Pmc arrival, L curves for parameter selection, magma chamber geometry tests, a variety of checkerboard tests and synthetic inversions to understand the resolution of the tomographic inversions.

### Text S1. OBS Relocation and Station BRA05 Time Correction

OBS station locations were determined by inverting 8394 acoustic water wave arrival times (Creager & Dorman, 1982) that were manually picked on the hydrophone or vertical channel for all shots within 5 km of each station (Table S1).

The three eXpendable BathyThermographs (XBT) profiles collected during the BRAVOISEIS experiment (Figure 2a) show significant variability in the water column velocity structure (Figure S1), possibly because of the effects of melting icebergs. However, the average velocity down to 1300 m depth for the three XBTs (1454.2 m/s) is quite similar to the average of water column velocity profiles obtained at the same locations (1455.8 m/s) for the month of January obtained from the World Ocean Atlas 2009 (Figure S1) (Matlab datasets obtained from Dushaw, 2009). For simplicity, we chose to locate the OBSs using a constant water velocity and by trying different values, found that the RMS travel time residual was minimized to 4.45 ms for a velocity of 1456 m/s.

During the location process, we discovered that station BRA05 had a significant timing error. We addressed this by solving for a timing offset in the inverse problem and found an offset

of +0.167 s (OBS clock running fast). We inspected the residuals as a function of shot time and found no evidence of significant clock drift.

The mean formal location uncertainties based on residual are 0.6 m, 0.5 m, and 0.7 m for x, y, and z, respectively (Table S1), but these errors do not include biases from the simplified water column structure assumed. The mean and standard deviation of the difference between the inverted depths and depth obtained from the bathymetric map (Almendros et al., 2020) created during the experiment (inverted minus bathymetric) is -8.3 ± 20 m. Because the inverted depths are likely biased by the choice of a uniform water column velocity, we assume the bathymetric depth for the station location. The horizontal coordinates of the inverted locations will be more accurate than the vertical coordinate because the shots surround the OBS. Horizontal uncertainties are likely accurate to ~10 m (Russell et al., 2019).

**Text S2. Smoothing and Damping Parameter Optimization**

We performed a series of isotropic and anisotropic inversions using the spatially smoothed isotropic starting model in which we systematically varied the damping and smoothing weights $\lambda_{p,}$ $\lambda_{H,}$ $\lambda_{V,}$ $\lambda_{Ap}$,$\lambda_{AH}$, and $\lambda_{AV.}$ We then selected the preferred smoothing and damping parameters by inspecting of the L-curves in which the residual variance (define in Equation 2) is plotted against the squared model norm (Aster et al., 2012; VanderBeek & Faccenda, 2021).

$$\|\partial s\| = \sum_{i=1}^{M} \left(\frac{\partial s_i}{s_{0i}}\right)^2 \quad \text{(S1)}$$

The model norm is the sum of the squared fractional slowness perturbations (slowness perturbation $\delta s,$ weighted by starting model value $s_0$) (Equation S1). The preferred solution lies in the corner of the L-curve where further decreases in regularization does not substantially improve the fit of the data (VanderBeek & Faccenda, 2021). We visually determined the knee of the L-curve based on the inversions performed.

In our exploration of the isotropic Pg inversion, we kept the $l_H$ and $l_V$ the same, at a value, $l_S = l_H = l_V$. We started out at the same level of smoothing and damping used in Weekly et al., (2014). We selected the preferred parameters for the isotropic inversion before exploring the

anisotropic parameters. We systematically explored damping values, $l_p$, for different fixed ratios of $l_S/l_p$ (1,2,5,10,25,50,100,200,500,1000) to determine the L-curve with the lowest *c2* where the optimum $l_p$ is located (Figure S5). For the anisotropic inversion, we started at $l_{Ap} = 1$ and explored different values for $l_{AS} = l_{AH} = l_{AV}$ that minimize the $c^2$. Then, we explored damping values $l_{Ap}$ for different fixed ratios of $l_{AS}/l_{Ap}$ (1000, 2000, 3000, 4000) that would produce an L curve with lower $c^2$ values where the optimum $l_{AS}$ is located (Figure S4). Using this approach, we selected preferred values of $l_p = 1.6$, $l_V = l_H = 80$ for the isotropic inversions and $l_{Ap} = 1$, $l_{AV} = l_{AH} = 3000$ for the anisotropic inversion. The preferred anisotropic inversion achieved a $c^2$ value of 1.01 (Figure 2) indicating that the Pg data is fit to its uncertainty.

**Text S3. Optimizing the Magma Chamber Volume for Guiding Ray Paths**

Modeling the Pg and Pmc arrivals for their joint inversion requires that we define a volume for the magma chamber beneath Orca volcano and then force Pmc ray paths to pass through it and Pg ray paths to avoid it. The absence of Pg arrivals for ray paths passing beneath the volcano (Figures 3b-c, S3) can be explained by the shadow zone from a cylindrical body with a radius of ~3 km (Figure S2). There is no evidence that Pg arrivals pass beneath this so this body must extend to >3.8 km depth, the depth of the deepest Pg ray paths in the isotropic Pg inversion. The top of the magma chamber volume is constrained by the presence of magma chamber reflections at 0.6 - 1 km depth on several reflection profiles that cross the volcano(Soule et al., 2025). All of these reflectors can be enclosed within a 0.6 km radius circle centered on the caldera (x=2, y=0) (Figure S2a). Based on these constraints we chose to model the magma chamber volume by an elliptical conical frustum on top of an elliptical cylinder with the geometry defined by an azimuth of the major axis, $\theta$, half dimensions of the major and minor axes at the base and top of the frustum of $R_1$ and $R_2$, and $r_1$ and $r_2$, respectively (Figure 4), the top of the frustum at $d$ km depth, and the base of the frustum at a depth, $D$, with the underlying elliptical cylinder extending to the base of the model.

To force Pmc arrivals through the magma chamber volume when forward modeling (Figure S3), a 0.6 km wide blocking curtain with slowness of 100000 s/km was placed above and to the sides of the magma chamber, centered on a plane that passes through the axis of the magma

chamber volume and that is perpendicular to a horizontal line connecting the OBS to the center of the magma chamber volume. To force Pg arrival to avoid the magma chamber volume, its slowness was set to 100000 s/km for the forward modeling.

The dimensions and position of the magma chamber volume were determined iteratively, by exploring a range of values for each parameter and seeking the solution that minimized the squared data residual norm (equation S1) using the same smoothing and damping weights used in the isotropic inversion. Specifically, we considered:

- $R_1$ : 2, 3, 4, 5 km
- $r_1$ : 0.4, 0.6, 0.8, 1, 1.2, 1.4, 1.6, 1.8, 2.0 km
- $R_2/R_1 = r_2/r_1$ : 0.4, 0.6, 0.8, 0.83, 0.9, 1.0
- d : 0.6, 1 km
- $D$ : 2, 3, 4, 5 km
- $q$ : 0°, 45°, 90°, 135° and directions parallel to the axes of the rotated geometry (i.e., 36° and 126°)
- $X$ and $Y$ coordinates that deviated by up to 1 km from the $X = 2$ km, $Y = 0$ km in increments of 0.4 km in each of $X$ and $Y$.

We did not consider every combination of parameters but instead considered enough to ensure that we converged on the best choice (Figure S5). The parameters selected were $\theta = 36°$, $R_1 = 3$ km, $R_2 = 2.5$ km, $r_1 = 0.6$ km, $r_2 = 0.5$ km, $D = 4$ km, $d = 1$ km, $X = 2$ km and $Y = 0$ km .

**Text S4. Melt and Water Calculations**

For our melt and, in the shallow crust above the magma chamber, water calculations we followed closely the method described in Paulatto et al., (2019). The choice of parameters is summarized in Table S2. We obtain vertical P-wave velocity profiles for the caldera, the southwest ridge, and a reference background region by averaging velocities for the Pg-Pmc isotropic inversion within the regions shown by the purple box in Figure 6f, red, and tan boxes in Figure 6b, respectively. We assumed a background geothermal gradient of 100°C/km based on geothermal

gradients for regions with similar crustal thickness (Kolawole & Evenick, 2023) and assuming a crustal thickness of 10 km (Christeson et al., 2003). We determined the temperature required to change from the reference P wave velocity profile to that in the caldera and southwest ridge profiles, accounting for both anharmonic and anelastic effects with no frequency dependence (equation (4) in Karato, 1993). Following, previous studies (Dunn et al., 2000, Hooft et al., 2019, McVey et al., 2020), we used a $Q$ value of 100 (Hooft et al., 2019), an activation enthalpy of 276 kJ/mol, and an anharmonic $d\ln V_P/dT$ of -8.1e-5 $K^{-1}$ (Christensen, 1979). Dredge samples from Orca volcano have MORB-like compositions (Keller et al., 2002), so we assume a solidus temperature of 1000 °C (Sinton, 1992). We assigned any velocity difference between the reference and caldera or southwest ridge profile that cannot be explained by this maximum temperature to the effects of melt.

The effect of fluid on seismic properties depends upon the composition and microstructure of fluid pockets and crystals (Taylor & Singh, 2002). Following the approach of Paulatto et al., (2019) we used a self-consistent effective medium theory (Berryman, 1980; Paulatto et al., 2019; Taylor & Singh, 2002) to estimate the melt fraction for randomly oriented ellipsoidal melt inclusions for endmember aspect ratios of 0.5 and 0.05. For the solid matrix, we used a density of 2900 kg $m^{-3}$ (Buck et al., 1997) and Poisson's ratio of 0.3 for the oceanic crust (Christensen, 1996) and the maximum velocity at 3 km depth (6.8 km/s) to obtain a bulk modulus of 101.7 GPa and a Shear Modulus of 24.3 GPa. We assumed a density of 2800 kg $m^{-3}$ (Buck et al., 1997), and a bulk modulus of 20 GPa (Bajgain et al., 2022) for the basaltic melt. We estimated the water content in the upper 0.8 km above the caldera considering both cold seawater with a density of 1030 kg $m^{-3}$ and a bulk modulus of 2.0 GPa and hot hydrothermal fluid with a density of 700 kg $m^{-3}$ and a bulk modulus of 0.2 GPa. We obtain the water fraction for shallow crustal depths above 0.8 km using these two end-member values for aspect ratios 0.5 and 0.05.

We estimated the volume for the magma chamber and the volume of melt beneath Orca Volcano by integrating over the region with a melt content exceeding 3.5%. The total volume of the magma chamber is 11.5 $km^3$ and the melt content is 0.83 $km^3$ and 2.25 $km^3$ for melt aspect ratios of 0.5 and 0.05, respectively.

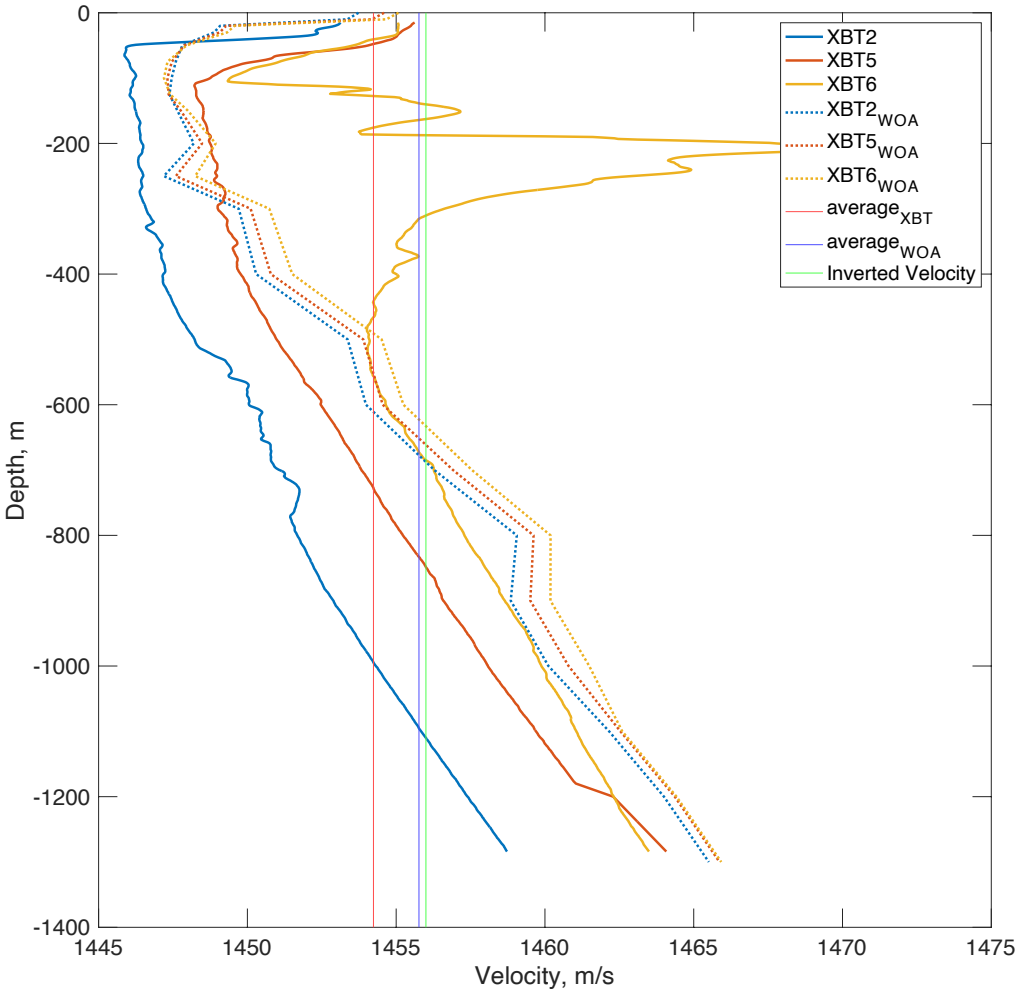


**Figure S1.** Water column velocity profiles for three Expendable Bathythermographs (XBTs) collected during the BRAVOSEIS experiment (locations shown in Figure 2b) and extracted from the World Ocean Atlas 2009 (WOA) for January at the same sites. Vertical red and blue Lines show the mean value of the XBT and WOA profiles respectively. Vertical green line shows the constant velocity used in the inversion.

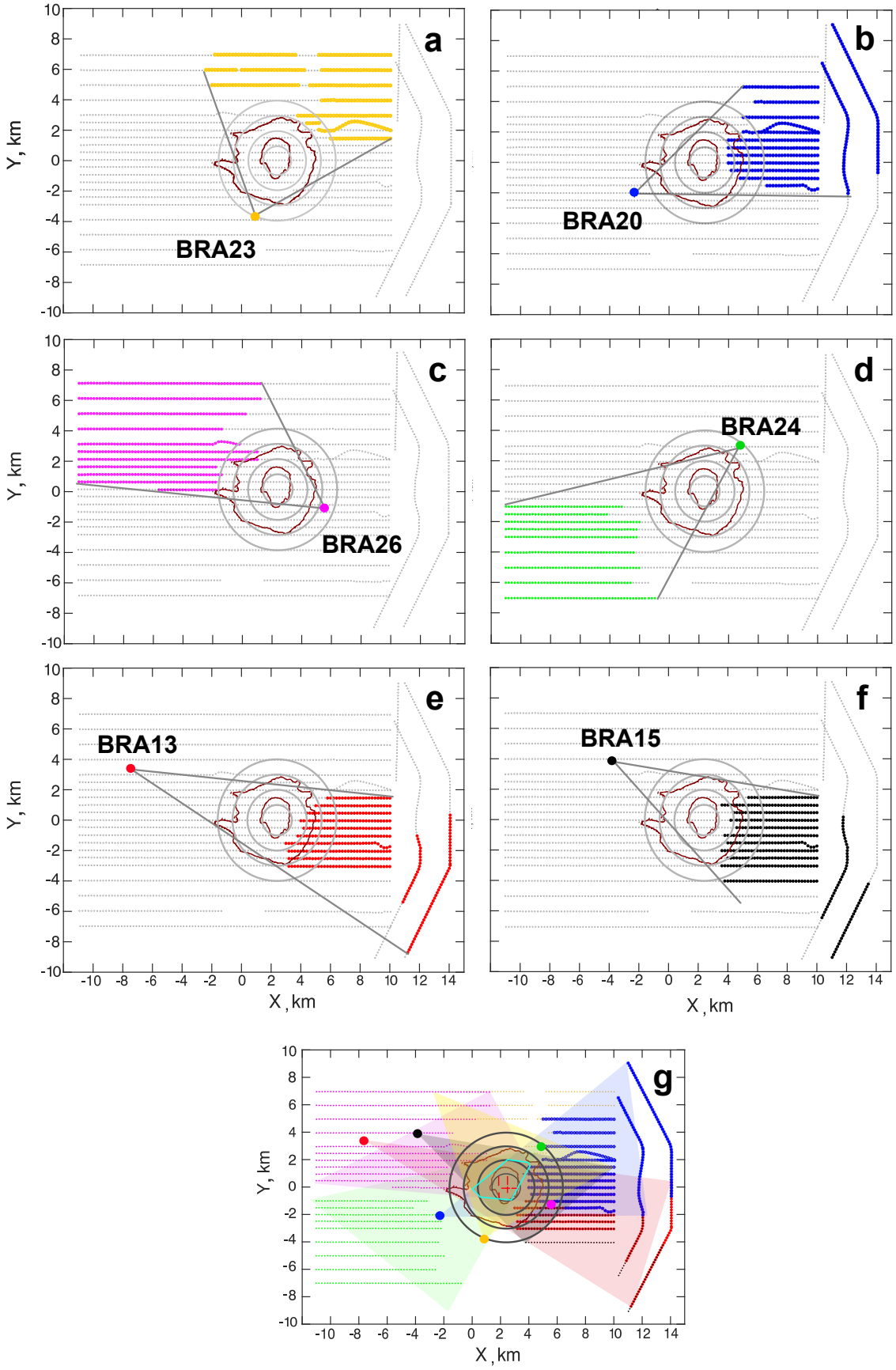
a
BRA23
b
BRA20
c
BRA26
d
BRA24
e
BRA13
f
BRA15
g
Y, km
X, km

**Figure S2.** Map view for the inversion geometry showing the limits of shadow zones (grey lines) that enclose all the shot locations with Pmc arrivals in the Pg shadow zone (dots), with the station marked as a big circle and shot locations for (a) BRA23, (b) BRA20, (c) BRA26, (d) BRA24, (e) BRA13, (f) BRA15. Brown contours are at 1000 m depth on the flanks of the volcano and on caldera rim to show the location of the volcano, grey circles of radius 0.6 km , 2 km , 3 km (bold) and 4 km centered on the volcano. (g) Combined map view of panels (a-f) with large circles colored red for station BRA13, black for BRA15, blue for BRA20, pink for BRA26, yellow for BRA23, green for BRA24. The red lines inside the inner most 0.6 km circle represent the top of the magma chamber reflections inferred from reflection seismic images. Colored shading of emphasize the intersection of the shadow zones in a region centered beneath the volcano. The cyan polygon shows where all angular ranges illuminated by the Pmc arrivals intersect.

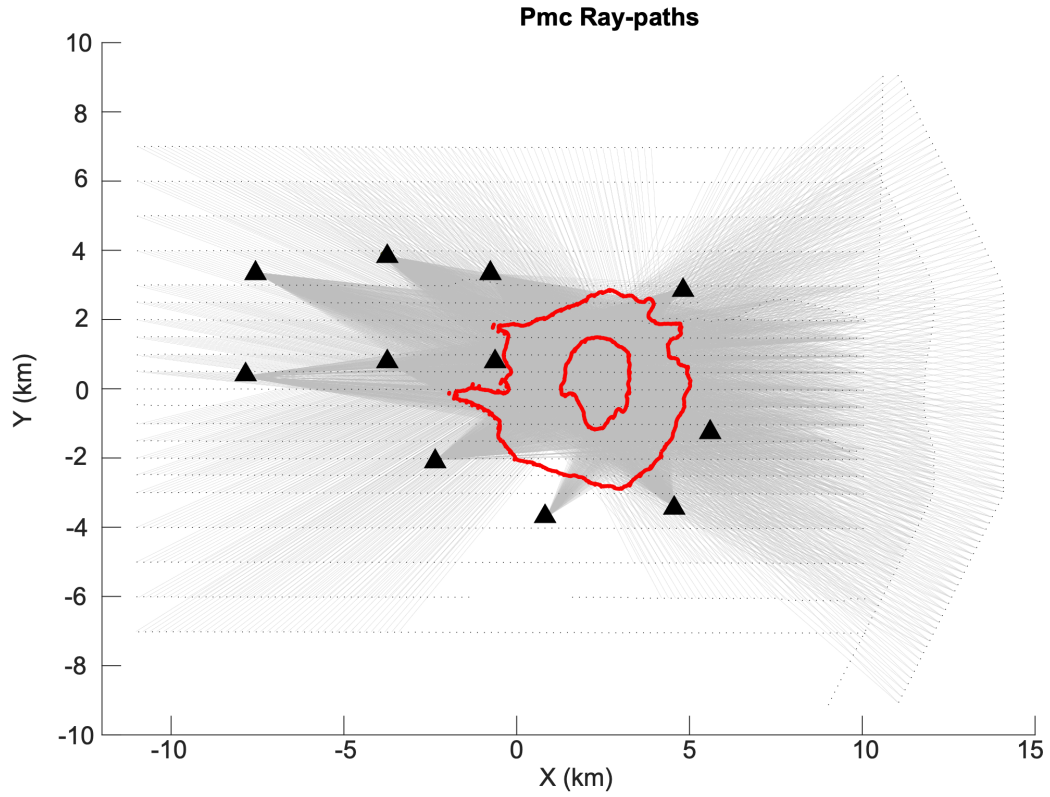


**Figure S3.** Pmc ray-paths traveling through the magma chamber (gray lines) with black triangles marking the stations where each ray-path is recorded and red lines the volcano contoured at 1000 m.

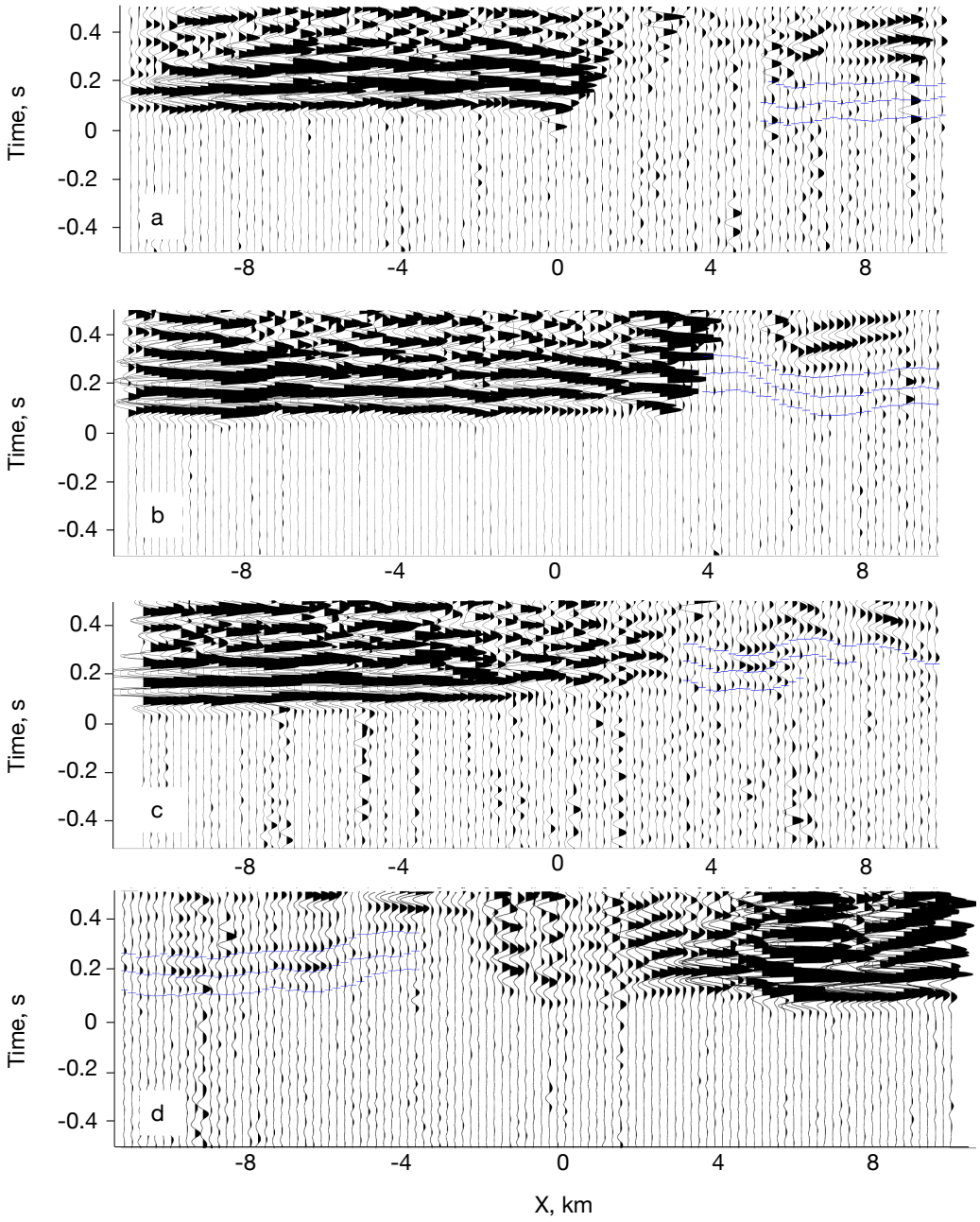


**Figure S4.** Example record sections for (a) station BRA15 and Line 13 (b) BRA18 and Line 15, (c) BRA13 and Line 9 and (d) BRA24 and Line 9 with picked onset of the 1st, 2nd and 3rd cycles of Pmc (thin blue ticks). The onset of 1st and 2nd cycles are not always visible but are consistently offset from the 3rd cycle allowing for a good estimate of the Pmc onset for all picks.

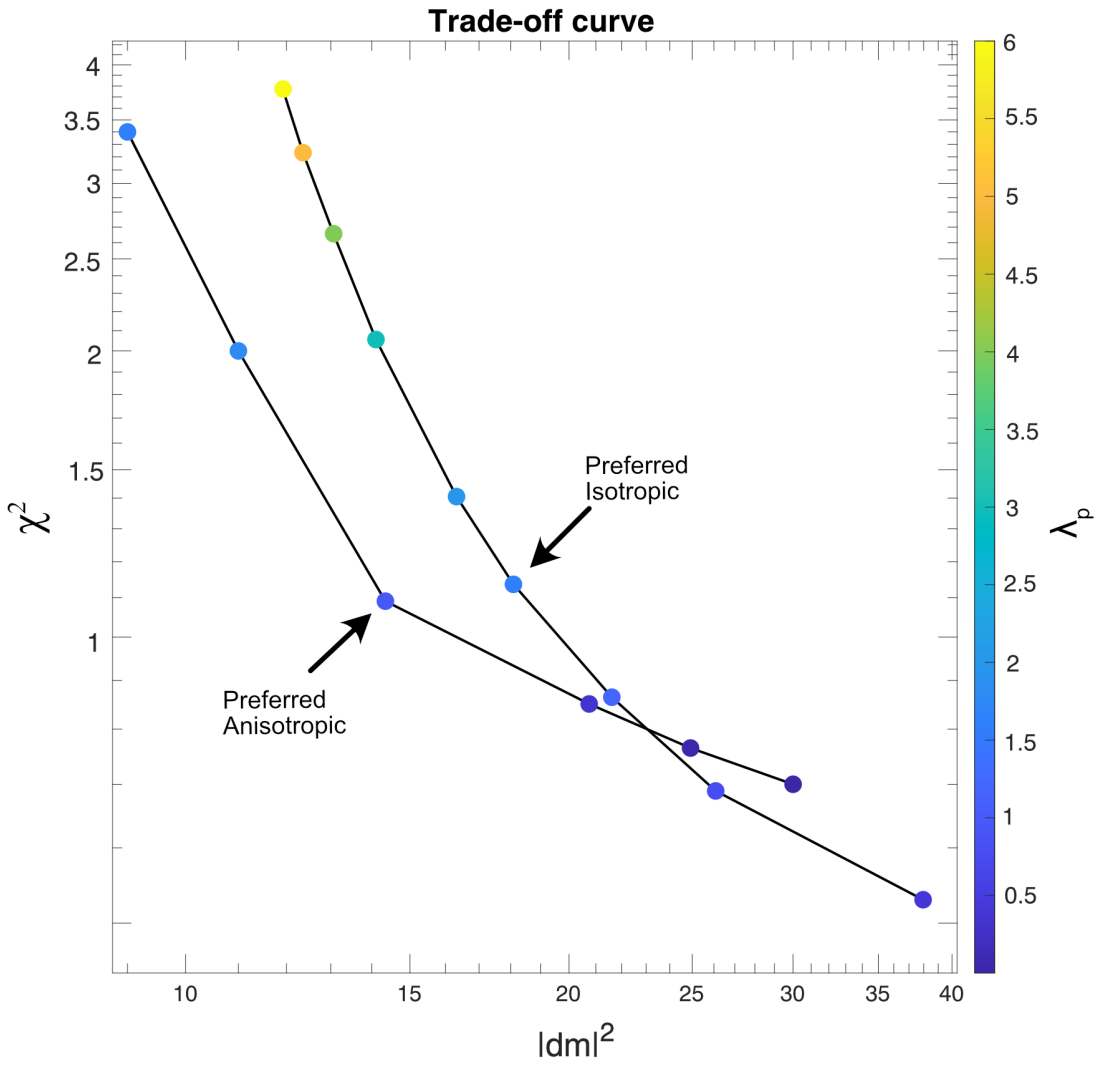


**Figure S5.** Examples of L-curves for parameter selection. The residual variance ($\chi^2$) is plotted as a function of the squared model norm (|dm|) for different values of $\lambda_p$ (color scale) in log scale. Both trade-off curves have $\lambda_S/\lambda_p$ = 50 with $\lambda_{AS}/\lambda_{Ap}$ = 3000 for the anisotropic curve.

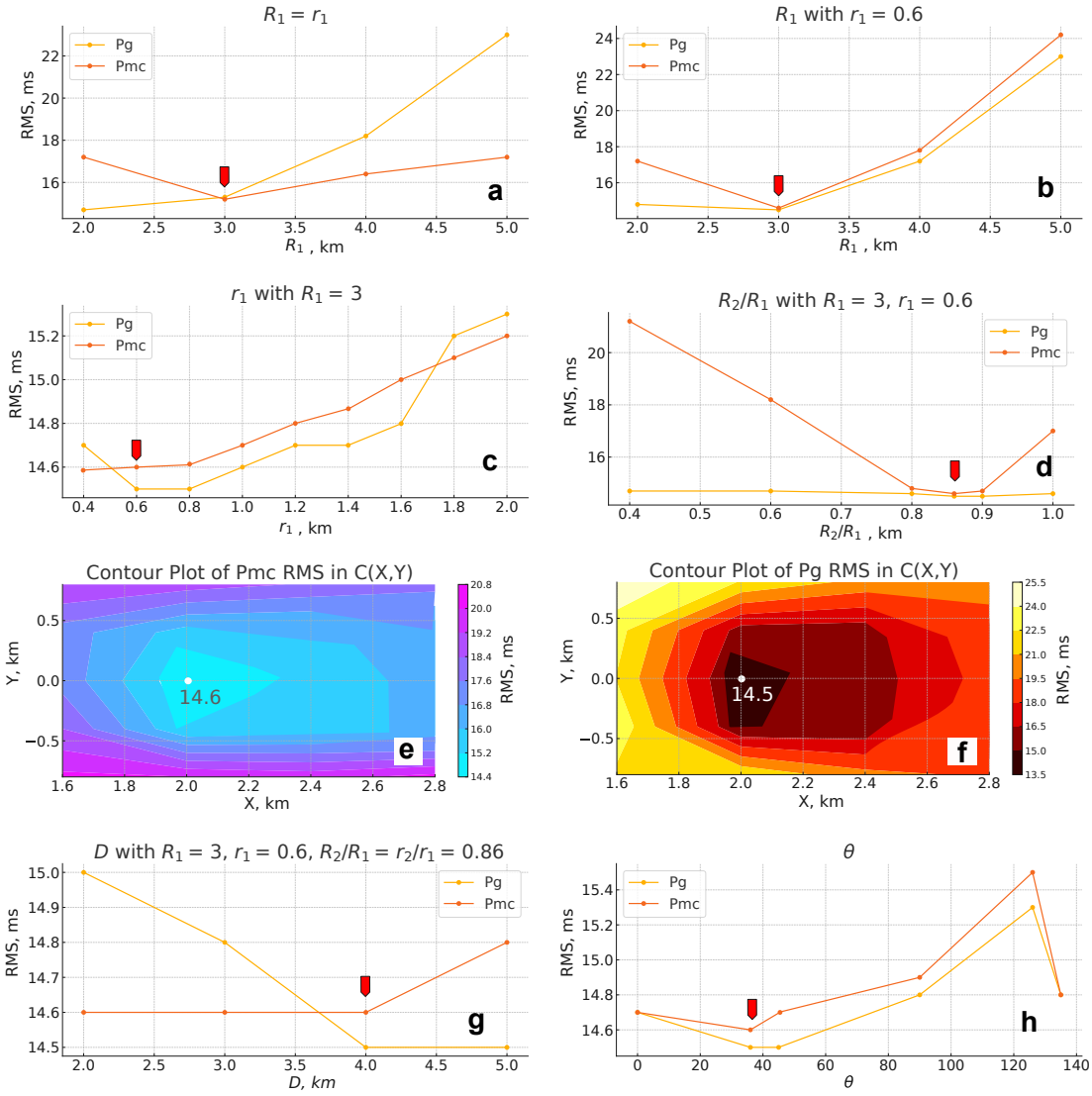


**Figure S6.** Dependence of RMS travel time residuals for Pg and Pmc arrivals on the parameters defining the magma chamber volume. (a) RMS residuals for a cylindrical body for different choices of $R_1 = R_2 = r_1 = r_2$. (b) RMS residuals for a conical frustrum on top of a cylinder for different choices of $R_1 = R_2$ while holding $r_1 = r_2 = 0.6$ km. (c) RMS residuals for a conical frustrum on top of a cylinder for different values of $r_1 = r_2$ while holding $R_1 = R_2 = 3$ km. (d) RMS residuals for an elongated conical frustum on top of a cylinder for different values of elongation $R_2/R_1 = r_2/r_1$ while holding $R_1 = 3$ km, $r_1 = 0.6$ km and $\theta = 36°$. (e) Pmc and (f) Pg residuals for conical frustum on top of a cylinder for different center coordinate $C$ for $r_1 = r_2 = 0.6$ km and $R_1 = R_2 = 3$ km. The minimum RMS value is marked and labelled. (g) RMS residuals for an elongated conical frustum on top of a cylinder for different depths of the bottom of frustum, $D$, with $R_1 = 3$ km, $r_1 = 0.6$ km, $R_2/R_1 = 0.86$, $r_2/r_1 = 0.86$ and $\theta = 36°$. (h) RMS residuals for different values of $\theta$ with $D$

= 4 km and other parameters as in (g). The optimum value for each variable is marked by red arrows.

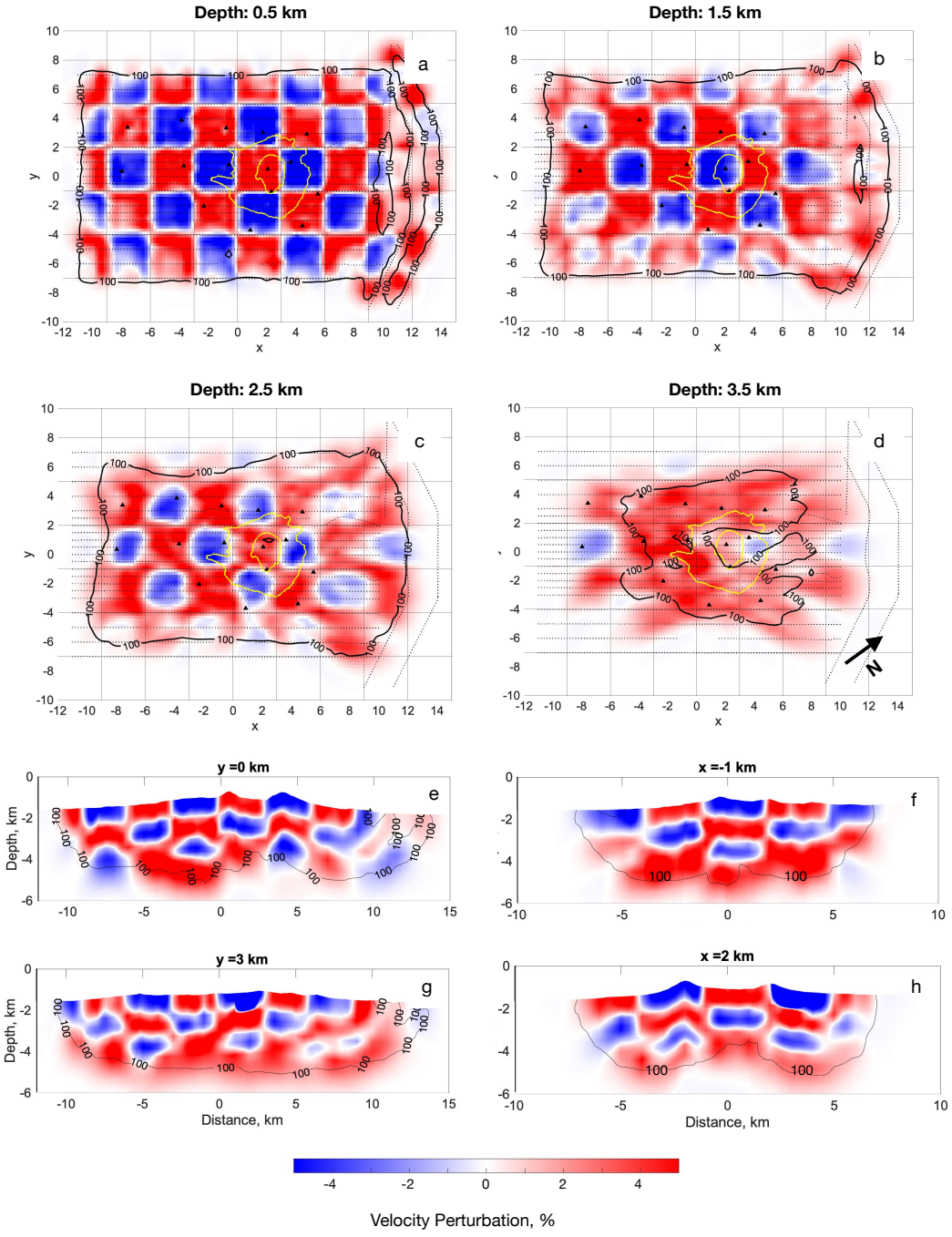


**Figure S7.** Isotropic Checkerboard Tests for checkers with velocity perturbations of ±5% and measuring 3 km x 3 km x 1 km in the X, Y, and Z directions. The starting model was generated by adding checker perturbations to the preferred isotropic Pg model. Travel times

were inverted for the velocity model with six iterations by adding the same uncertainties of the Pg travel time used for the Pg inversion.

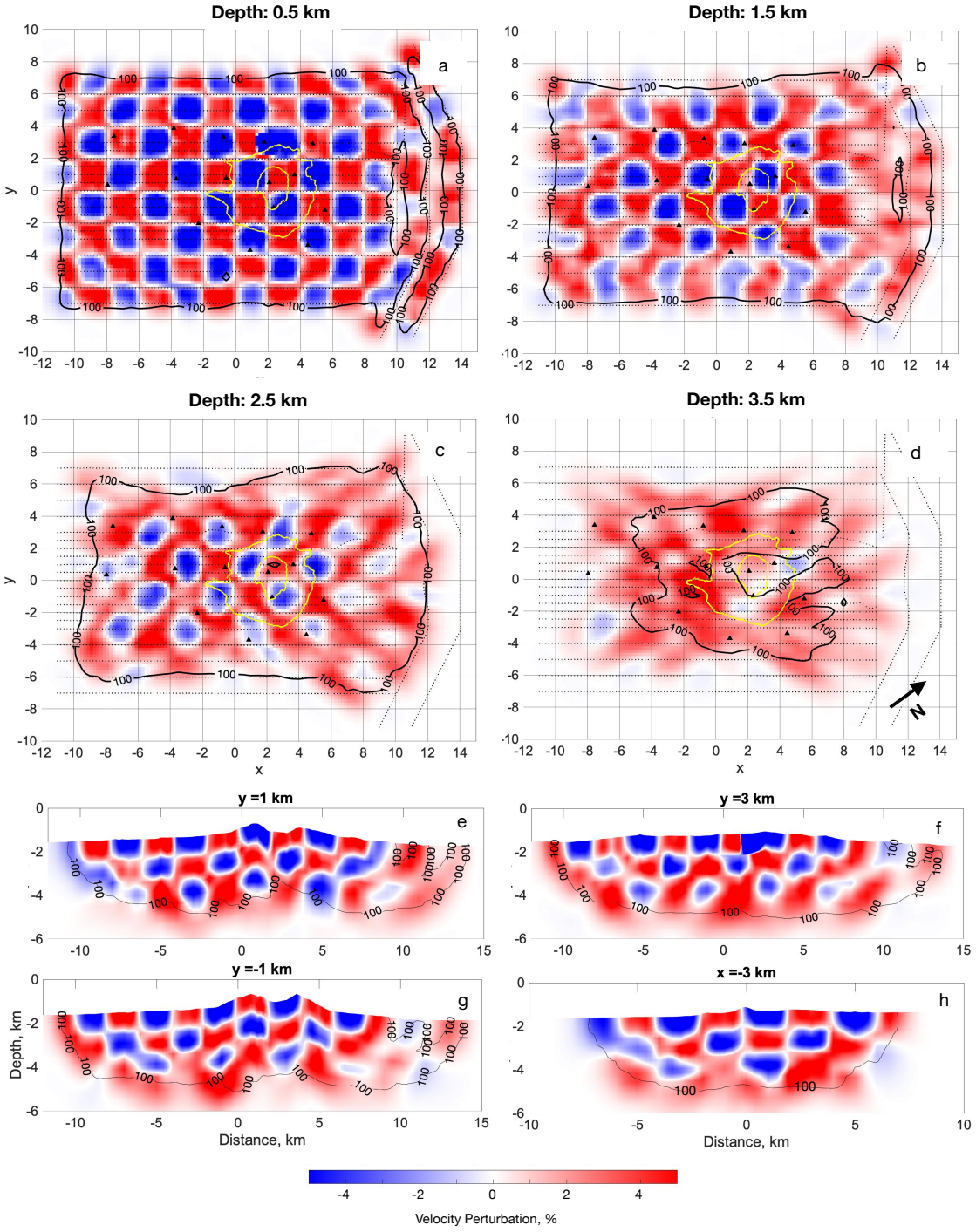

**Figure S8.** Isotropic Checkerboard Tests for checkers with slowness perturbations of ±5% and measuring 2 km x 2 km x 1 km in the X, Y, Z directions. The starting model was generated by adding checker perturbations to the preferred isotropic Pg model. Travel times were inverted for the velocity model with six iterations by adding the same uncertainties of the Pg travel times used for the Pg inversion.

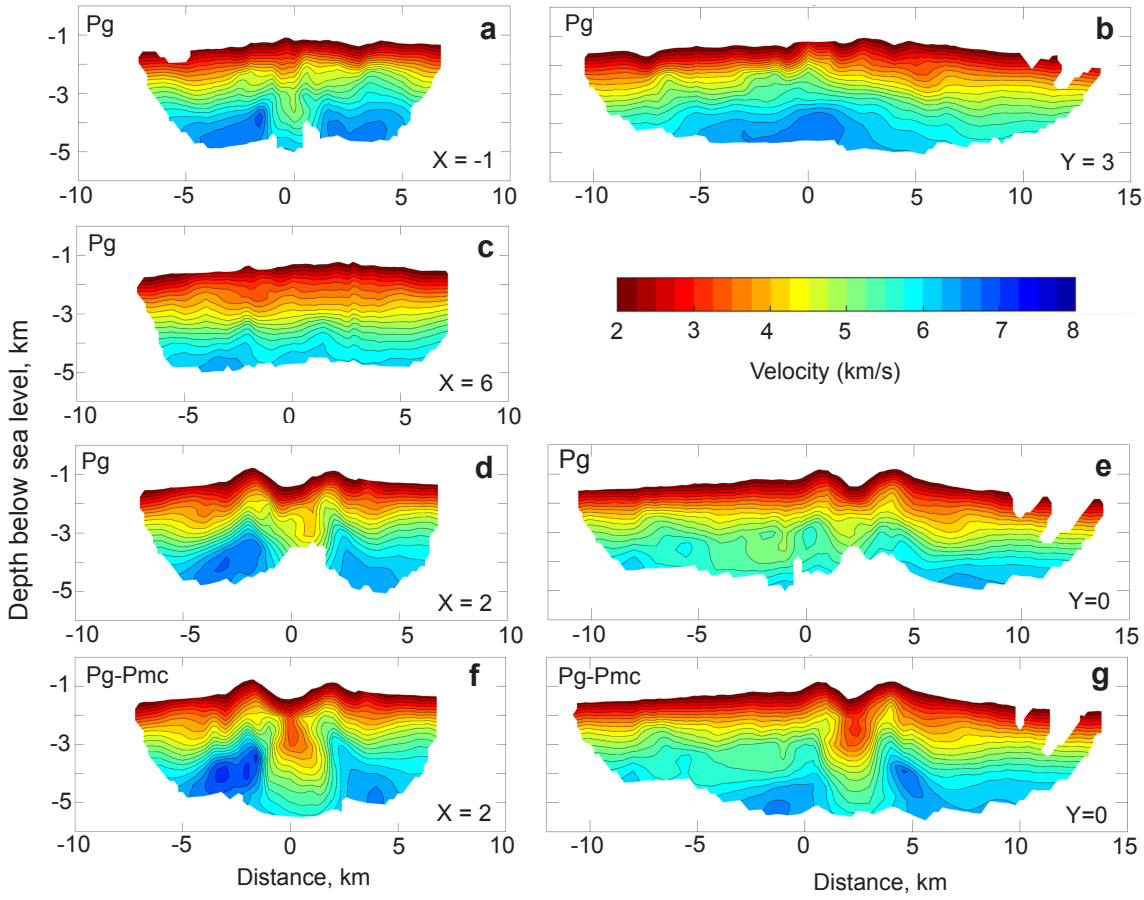


**Figure S9.** Vertical cross-sections of velocity for the Pg isotropic tomography model at (a) $X$ = -1 km, (b) $Y$ = 3 km, (c) $X$ = 6 km, and (d) $X$ = 2 km (e) $Y$ = 0 km and for the Pg-Pmc isotropic tomography model at (f) $X$ = 2 km, and (g) $Y$ = 0 km plotted as depth below the sea surface. The velocity perturbations are cropped for DWS < 100. The locations of these cross-sections are shown in Figures 6a and 6f. The models are masked to show regions with a DWS ≥100.

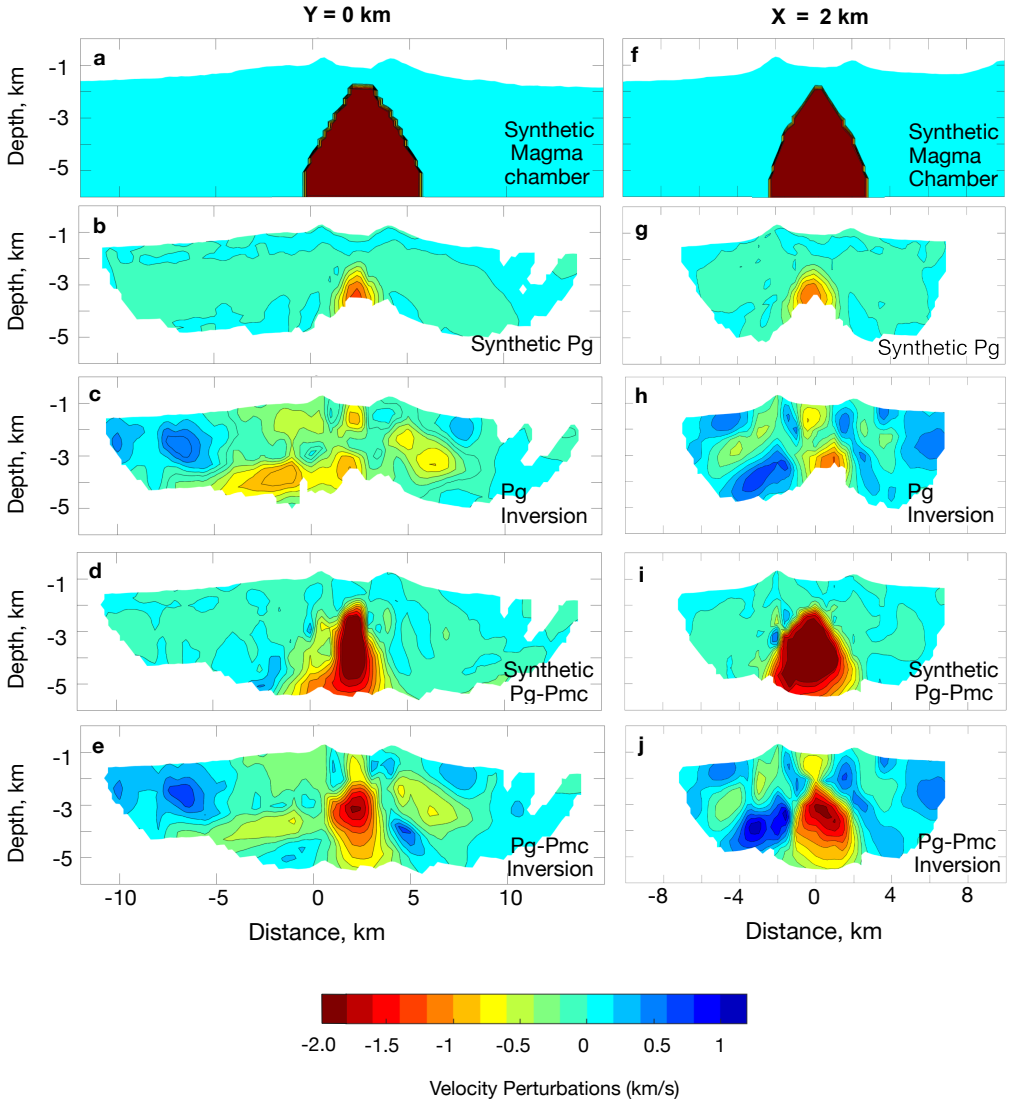


**Figure S10.** Results of isotropic synthetic inversions for a magma chamber, with the same volume as used for guiding rays in our preferred Pg-Pmc inversion and a velocity anomaly of -2.0 km/s added to a 3-D model filled with the smooth 1-D model obtained by inverting Pg times (purple line in Figure 5). Travel times were obtained by forward modeling through the synthetic low-velocity body and the synthetic inversions performed with the same setup and parameters as the preferred isotropic Pg and Pg-Pmc isotropic inversions and adding the same travel time uncertainties of Pg and Pmc picks used to generate the Pg-Pmc model. (a-e) Cross sections at Y = 0 km showing (a) the synthetic model, (b) the synthetic Pg inversion, (c) the actual Pg inversion, (d) the synthetic Pg-Pmc inversion and (e) the actual Pg-Pmc inversion. (f-k) As for (a-e), except for cross sections at X = 2 km.

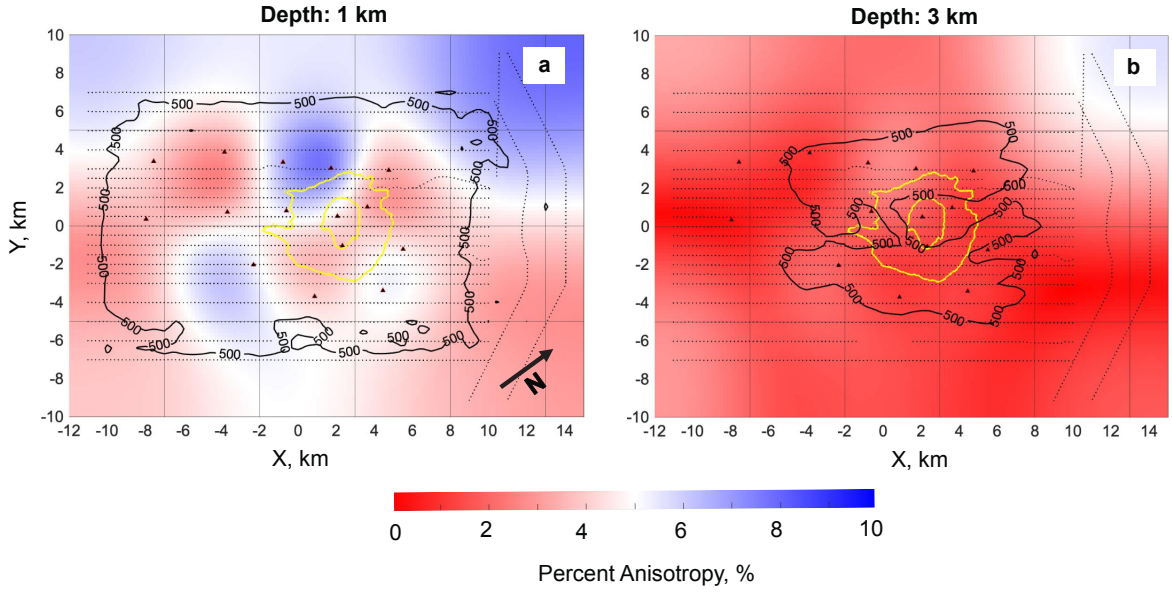


**Figure S11.** Anisotropic checkerboard test in which checkers (grid lines) measuring 5 km x 5 km x 2 km in X, Y, Z directions, respectively, alternate between 10% anisotropy with the fast direction parallel to the x-axis and isotropic velocities. The starting model was generated by adding anisotropic checkers to the preferred isotropic Pg model. Travel times were inverted for the velocity model with six iterations. In the upper layer, the checker pattern is recovered within a 15 km x 10 km area with a significant loss of amplitude but the inversion does not resolve the vertical change in the pattern of the checkers below 2 km depth.

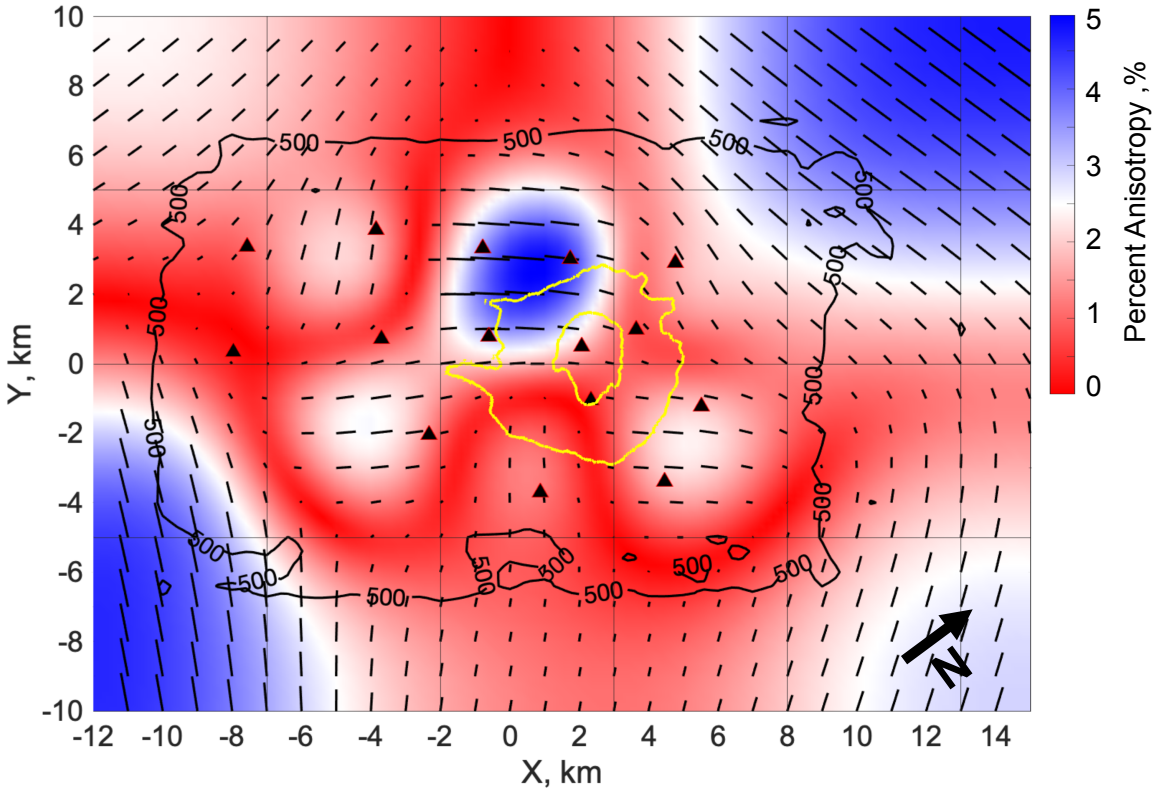


**Figure S12.** Anisotropic checkerboard test in which 2-D checkers (grid lines) measuring 5 km x 5 km with 5% anisotropy have a fast direction that alternates 90° between the direction of the X and Y axes. The starting model was generated by adding anisotropic checkers to the preferred isotropic Pg model. Travel times were inverted for the velocity model with six iterations. Ticks indicate the scale and amplitude of the recovered anisotropy, with shading also showing the recovered amplitude.

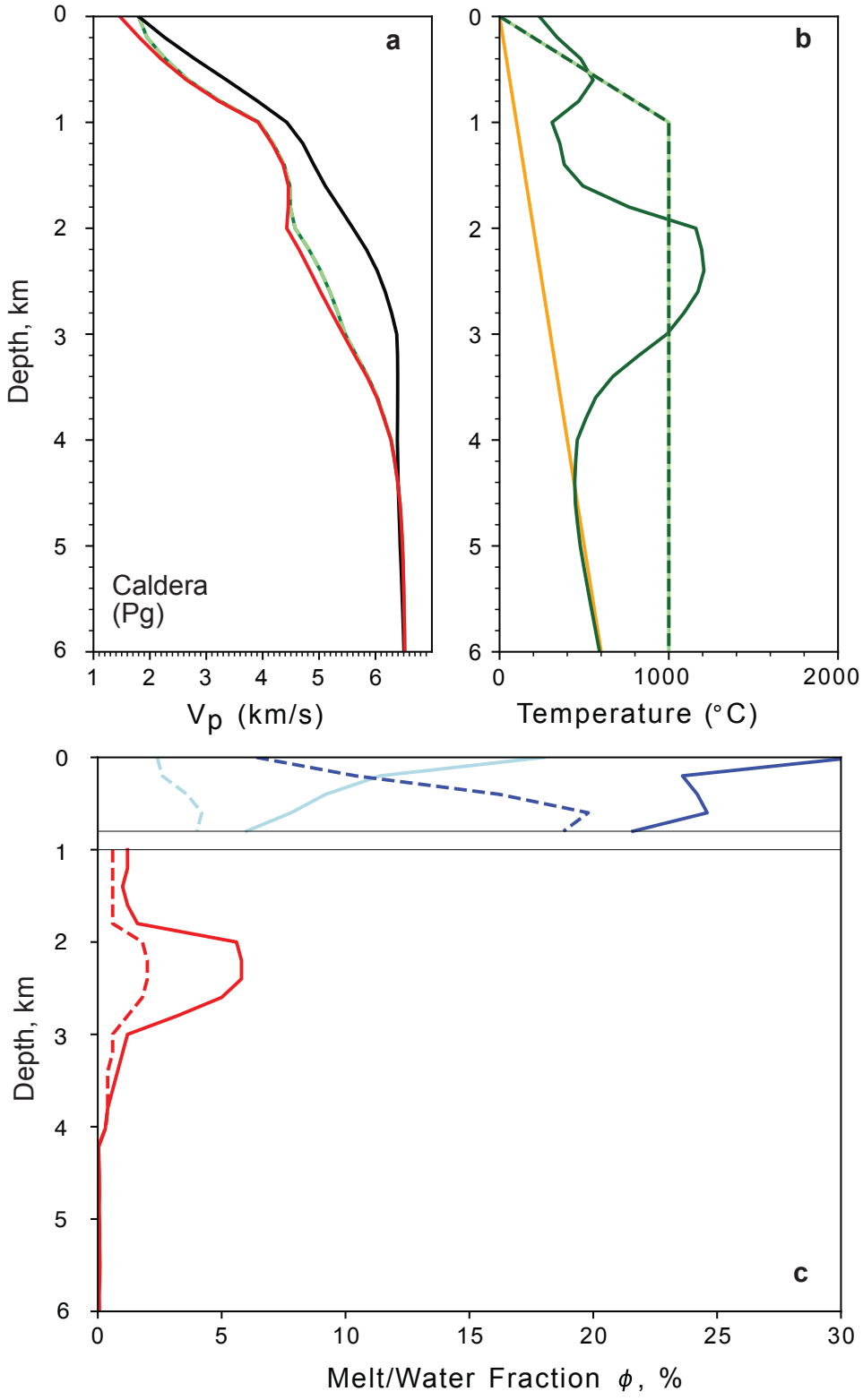
a
b
c
Caldera
(Pg)
Depth, km
$V_P$ (km/s)
Temperature (°C)
Melt/Water Fraction $\phi$, %
0
1
2
3
4
5
6
1
2
3
4
5
6
0
1000
2000
0
5
10
15
20
25
30

**Figure S13.** Physical property calculations beneath the caldera as for Figure 11a-c, except that velocity profiles are obtained from the Pg isotropic inversion. (a) Background (black) and caldera (red) vertical velocity models obtained by averaging velocities in the regions shown by tan in Figure 6b and purple box in Figure 6f, respectively. The green dashed line shows the background velocity profile adjusted to 1000°C, the assumed solidus temperature. (b) Temperature profile obtained by assuming the difference between the background and caldera velocity profiles is explained by temperature (green) assuming at geothermal gradient of 100°C / km (orange). The dashed line shows the assumed solidus temperature of 1000°C for the melt calculations. (c) Estimated fluid content for pore aspect ratios of 0.05 (dashed lines) and 0.5 (solid lines) for melt at ≥1 km depth (red) and water at ≤0.8 km depth assuming cold water (dark blue) and hot hydrothermal fluid (light blue).

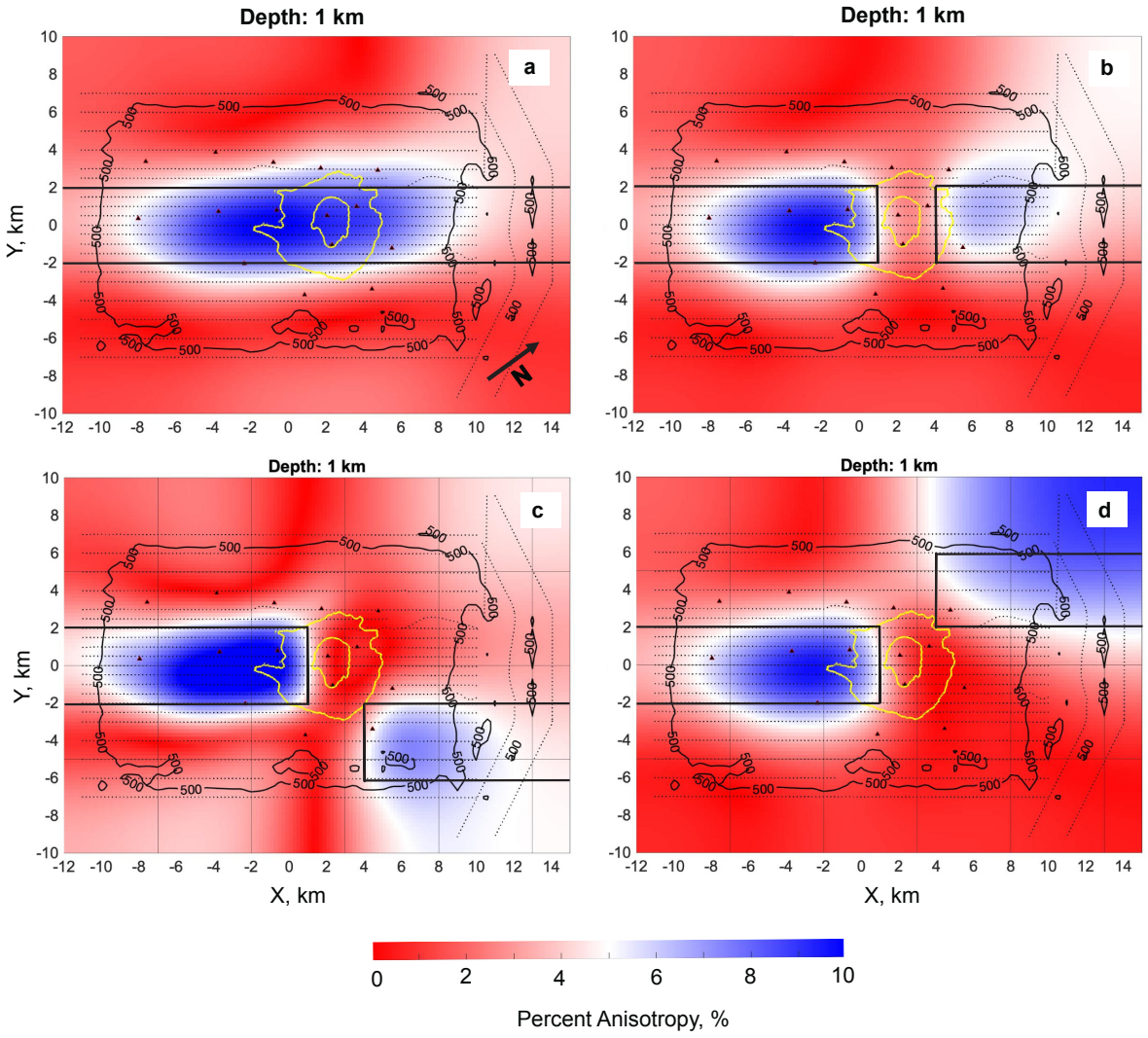


**Figure S14.** Synthetic inversions to understand the recovery of anisotropic features paralleling the inferred rift axis (a) Synthetic inversion based on forward modeling travel times through the preferred Pg isotropic model in which there is band of of 10% anisotropy with the fast axis parallel to the X-axis for -2 km < Y < 2 km and for Z ≤ 2 km (delineated bold black lines) and 0% anisotropy elsewhere. (b) Introducing 0% anisotropy between km 1 km < X < 4 km along the 10% anisotropy band (c) Shifting the 10% anisotropy block in the northeast to -6 km < Y < -2 km. (d) shifting the the 10% anisotropy block in the northeast to 2 km < Y < 6 km. Black contours show the limits of a derivative weight sum (DWS). Black triangles are the OBS stations and black dots the tomography shot locations. Yellow contours at 1000 m show the location of Orca Volcano

**Table S1.** Station relocation summary table showing the difference between inverted location and drop location and the formal location uncertainties

| Station ID | Drop Location | | | | | Inverted Location | | | | | | | | | | |
|---|---|---|---|---|---|---|---|---|---|---|---|---|---|---|---|---|
| | Lon (deg) | Lat (deg) | z (km) | x (km) | y (km) | Lon (deg) | Lat (deg) | z (km) | x (km) | y (km) | Bathymetric Depth (km) | Inverted Depth Minus Bathymetric Depth (km) | RMS Residual (s) | Formal Uncertainty (km) x | Formal Uncertainty (km) y | Formal Uncertainty (km) z |
| BRA 13 | -58.59940 | -62.45600 | 1.460 | -7.625 | 3.502 | -58.59685 | -62.45666 | 1.425 | -7.562 | 3.365 | 1.447 | -0.023 | 0.0034 | 0.0006 | 0.0005 | 0.0007 |
| BRA 14 | -58.56990 | -62.47970 | 1.495 | -7.939 | 0.470 | -58.56904 | -62.48072 | 1.509 | -7.970 | 0.352 | 1.499 | 0.010 | 0.0049 | 0.0005 | 0.0005 | 0.0006 |
| BRA 15 | -58.54850 | -62.43330 | 1.349 | -4.013 | 4.012 | -58.54442 | -62.43361 | 1.327 | -3.862 | 3.860 | 1.323 | 0.004 | 0.0047 | 0.0005 | 0.0005 | 0.0008 |
| BRA 16 | -58.50890 | -62.45500 | 1.335 | -3.776 | 0.854 | -58.50607 | -62.45566 | 1.295 | -3.700 | 0.708 | 1.333 | -0.039 | 0.0042 | 0.0004 | 0.0005 | 0.0006 |
| BRA 18 | -58.49420 | -62.42220 | 1.254 | -1.015 | 3.367 | -58.48997 | -62.42123 | 1.250 | -0.775 | 3.326 | 1.245 | 0.006 | 0.0031 | 0.0005 | 0.0005 | 0.0008 |
| BRA 19 | -58.46030 | -62.43920 | 1.103 | -0.711 | 0.805 | -58.45841 | -62.43880 | 1.090 | -0.605 | 0.784 | 1.084 | 0.006 | 0.0043 | 0.0004 | 0.0005 | 0.0007 |
| BRA 20 | -58.45490 | -62.46850 | 1.374 | -2.404 | -2.001 | -58.45315 | -62.46845 | 1.361 | -2.328 | -2.050 | 1.363 | -0.002 | 0.0035 | 0.0005 | 0.0005 | 0.0007 |
| BRA 21 | -58.41400 | -62.42750 | 1.092 | 1.991 | 0.455 | -58.41302 | -62.42670 | 1.111 | 2.084 | 0.497 | 1.093 | 0.018 | 0.0051 | 0.0004 | 0.0005 | 0.0007 |
| BRA 22 | -58.39080 | -62.43640 | 1.019 | 2.376 | -1.053 | -58.39121 | -62.43655 | 0.995 | 2.349 | -1.054 | 1.023 | -0.028 | 0.0039 | 0.0004 | 0.0006 | 0.0008 |
| BRA 23 | -58.38670 | -62.46370 | 1.365 | 0.757 | -3.637 | -58.38415 | -62.46350 | 1.341 | 0.877 | -3.696 | 1.356 | -0.015 | 0.0039 | 0.0005 | 0.0005 | 0.0008 |
| BRA 24 | -58.40070 | -62.39650 | 1.161 | 4.579 | 2.844 | -58.39849 | -62.39504 | 1.119 | 4.767 | 2.909 | 1.160 | -0.041 | 0.0061 | 0.0005 | 0.0005 | 0.0008 |
| BRA 25 | -58.39000 | -62.41430 | 1.326 | 3.859 | 0.915 | -58.39411 | -62.41485 | 0.857 | 3.651 | 0.990 | 0.896 | -0.040 | 0.0032 | 0.0005 | 0.0005 | 0.001 |
| BRA 26 | -58.33790 | -62.42130 | 1.431 | 5.576 | -1.301 | -58.33942 | -62.42110 | 1.416 | 5.525 | -1.237 | 1.411 | 0.006 | 0.0047 | 0.0005 | 0.0005 | 0.0006 |
| BRA 27 | -58.33130 | -62.44360 | 1.467 | 4.387 | -3.510 | -58.33115 | -62.44238 | 1.472 | 4.474 | -3.405 | 1.460 | 0.012 | 0.0074 | 0.0005 | 0.0006 | 0.0007 |
| BRA 05 | -58.44830 | -62.41060 | 1.146 | 1.664 | 3.020 | -58.44720 | -62.41020 | 1.147 | 1.735 | 3.024 | 1.146 | 0.001 | 0.0044 | 0.0005 | 0.0005 | 0.0009 |

**Table S2.** Parameters used for melt calculation described in Text S4

| **Parameter** | **Value** | **Description** |
|---|---|---|
| H * | 276 kJ/mol | Activation enthalpy (Caristan, 1982) |
| R | 8.315 | Gas constant |
| Q | 100 | Attenuation quality factor |
| $d\ln V_P/dT$ | -8.1e-5 $K^{-1}$ | Temperature derivative of seismic velocity (Christensen, 1979) |
| n | 0.3 | Poisson's ratio for oceanic crust (Christensen, 1996) |
| K solidmatrix | 73.66 GPa | Calculated bulk modulus of solid rock matrix |
| K interstitial melt | 20 GPa | Bulk modulus of melt (Bajgain et al., 2022) |
| K interstitial water | 2.0 / 0.2 GPa | Bulk modulus of cold / hot water |
| Solidus | 1000° C | Solidus for mid oceanic ridge basalt (Sinton & Detrick, 1992) |
| G solidmatrix | 3.8 GPa | Calculated shear modulus of solid rock matrix |
| G interstitial melt | 0 GPa | Shear modulus of melt and water |
| p_solidmatrix | 2900 $kg/m^3$ | Density of solid rock matrix (Buck et al., 1997) |
| p_interstitial melt | 2800 $kg/m^3$ | Density of melt (Buck et al., 1997) |
| p_interstitial water | 700 / 1000 $kg/m^3$ | Density of cold / hot water |
| a water | 0.5 & 0.05 | Aspect ratio of inclusions for water |
| a melt | 0.5 & 0.05 | Aspect ratio of inclusion for melt |
| a solidmatrix | 1 | Aspect ratio of solid grains |

## Appendix B: Supplementary Information for chapter 3

### Text S1: Inverting for a source model without fault slip

We estimated the geometry and location of a pressurized magma reservoir by jointly inverting for vertical uplift at six seafloor sites (Node F, Node E, Node B, ET, NT, WT) and horizontal baseline increases for three station pairs (NT-ET, WT-NT, WT-ET), with all displacement observations expressed in centimeters. Station coordinates were transformed from geographic coordinates (latitude/longitude/depth) to a local Cartesian reference frame ($x,y$) in kilometers (x east, y north) with a fixed geographic origin at 130.1°W, 45.9°N. Model predictions were evaluated on the seafloor plane ($z$=0) in meters to ensure consistent comparison between observed and modeled displacements at a uniform reference surface.

We tested two elastic inflation-source geometries: (1) a Yang prolate spheroid and (2) a McTigue finite spherical source. Source code for forward modeling both inflation models (*yangdisp, mctigue3d*) are available through the dMODELS package (Battaglia et al., 2013). The forward deformation model employed a Yang spheroid inflation source parameterized by

$$\boldsymbol{P}_{spheroid} = \{x_0, y_0, z_0, h, i, \theta, \phi, P\} \quad \text{(S1)}$$

where ($x_0$, $y_0$) represents the spheroid center location in km, $z_0 > 0$ is the depth to the spheroid center in km (positive downward), $h$ and $i$ are the spheroid semi-axes in km, $\theta$ is the tilt angle and $\phi$ is the azimuth describing spheroid orientation (degrees), and $P$ is the uniform overpressure (GPa). For each parameter set $\boldsymbol{P}_{spheroid}$, predicted displacements at station i located at ($x_i$, $y_i$, $z = 0$) were computed by converting geometric parameters from kilometers to meters, angles to radians, and pressure from GPa to Pa, then evaluating

$$\left(u_{x,i}, u_{y,i}, u_{z,i}\right) = yangdisp(x_0, y_0, z_0, a, b, \lambda, \mu, v, P, \theta, \phi;\ x_i, y_i, 0) \quad \text{(S2)}$$

with elastic constants $\mu$ = 1 GPa and $v$ = 0.25, and Lamé parameter λ computed as

$$\lambda = 2v\mu/(1 - 2v) \quad \text{(S3)}$$

and converted internally to Pa.

The forward deformation model employed a Mctigue sphere inflation source parameterized by

$$\boldsymbol{P}_{sphere} = \{x_0, y_0, z_0, R, P\} \quad \text{(S4)}$$

where $R$ is the sphere radius (km). For each $\boldsymbol{P}_{\text{sphere}}$, predicted displacements were computed with the same unit conversions and elastic constants, evaluating

$$(u_{x,i}, u_{y,i}, u_{z,i}) = mctigue3d(x_0, y_0, z_0, R, \lambda, \mu, v, P, x_i, y_i, 0) \quad \text{(S5)}$$

To evaluate whether multiple reservoirs improved the fit, we also considered a **two-sphere** model in which displacements are the linear superposition of two McTigue sources, with parameter vector

$$\mathbf{p}_{2\text{sphere}} = \{x_1, y_1, z_1, R_1, P_1,\ x_2, y_2, z_2, R_2, P_2\}, \quad \text{(S6)}$$

and $\boldsymbol{u}^{pred} = \boldsymbol{u}^{(1)} + \boldsymbol{u}^{(2)}$, where each $\boldsymbol{u}^{(j)}$is computed with equation S5**.**

Predicted vertical uplift at station $i$ was then $U_i^{pred} = 100 \cdot u_{z,i}$ (cm). Predicted baseline extension between endpoints A and B was computed using the exact change in endpoint separation after applying modeled horizontal displacements to both endpoints rather than a linearized strain approximation. Defining $r = (x,y)$ in meters and $u = (u_x, u_y)$ in meters, the predicted baseline change in cm was

$$\Delta R_{A-B\ Pred} = 100[|(\boldsymbol{r}B + \boldsymbol{u}B) - (\boldsymbol{r}A + \boldsymbol{u}A)| - |\boldsymbol{r}B - \boldsymbol{r}A|)] \quad \text{(S7)}$$

This formulation explicitly accounts for both endpoint motions and thus, corresponds to the baseline-length observables measured by acoustic ranging.

The inversion solved a bounded, constrained nonlinear least-squares problem by minimizing a weighted sum-of-squares objective function augmented by soft regularization terms:

$$J(\boldsymbol{p}) = \sum_{i=1}^{6} w_u^2 (U_i^{obs} - U_i^{pred}(\boldsymbol{p}))^2 + \\ + \sum_{i=1}^{6} w_b^2 \left(\Delta R_k^{obs} - \Delta R_k^{pred}(\boldsymbol{p})\right)^2 + w_{\text{shape}} \max\left(0, \frac{a}{b} - 10\right)^2 \quad \text{(S8)}$$

where $w_u$, *and* $w_b$ weight the uplift and baseline residuals and were set to 1. Shape regularization penalizes extreme aspect ratios by activating only when $a/b > 10$ (weight $w_{\text{shape}} = 5$). This stabilizes the inversion against highly elongated geometries that can fit the data but lack physical interpretability.

Optimization was subjected to explicit parameter bounds that reflect the assumed physical and geometric search space. Bounds restricted the source location ($x_0$, $y_0$) to 6 km from the center of the caldera (130.1°W, 45.9°N), constrained depth $z_0$ between 1 and 8 km, limited semi-axes a and $b$ to physically plausible ranges (0.2-5.0 km and 0.1-2.0 km respectively), restricted tilt angle $\theta \in [0°, 90°]$ and azimuth $\phi \in [180°, 180°]$, and required positive overpressure $P$ between 0.0001-0.1 GPa. We enforced a nonlinear burial constraint requiring the entire spheroid to remain below a minimum depth ($z_{\text{min}}$) of 1 km which approximates the shallowest reaches of magma of 1.1 km seen by Kent et al. (Kent et al., 2025). This constraint was expressed as

$$z_0 - z_{\text{extent}}(a, b, \theta) \geq z_{\text{min}} \quad \text{(S9)}$$

where $z_{\text{extent}}$ represents the maximum upward half-extent of the spheroid or sphere measured vertically. This burial constraint prevents shallow solutions where the spheroid surface would approach or breach the minimum allowable depth, ensuring geological feasibility of the inferred magma reservoir geometry.

Because the objective function J(**p**) (Equation S8) is nonconvex due to the nonlinear forward model and complex parameter interactions, we implemented a robust multi-start

optimization strategy to avoid local minima. We generated 100 randomized initial models by perturbing a plausible seed model (the prolate spheroid model of Chadwick and Nooner (2016)) while respecting all parameter bounds. Each randomized starting point was refined using by MATLAB's SQP algorithm with convergence tolerances set at Step Tolerance of $10^{-10}$ and Optimality Tolerance of $10^{-8}$, allowing up to 1500 iterations and 50,000 function evaluations per start. We retained the solution with minimum final objective value as the best-fitting model.

**Text S2: Dimensions of inverted spheroid and spheres**

The best fit spheroid model has parameters:

$x_0$ : 7.56 km

$y_0$ : 5.41 km

$z_0$ : 2.94 km

$a$ : 2.93 km

$b$ : 0.29 km

$\theta$ : 40.0°

$\phi$ : -176.5°

$P$ : 0.0142 GPa

The misfits are

RMS error for uplifts : 1.10 cm

RMS error for horizontal baselines : 1.90 cm

The best fit dual spheres model has parameters:

Sphere 1

$x_0$ : 7.57 km

$y_0$ : 4.55 km

$z_0$ : 3.33 km

$R$ : 0.43 km

$P$: 0.0500 GPa

Sphere 2

$x_0$ : 7.53 km

$y_0$ : 6.60 km

$z_0$ : 1.25 km

$R$ : 0.20 km

$P$: 0.0500 Gpa

The misfits are

RMS error for uplifts : 1.40 cm

RMS error for horizontal baselines: 0.90 cm

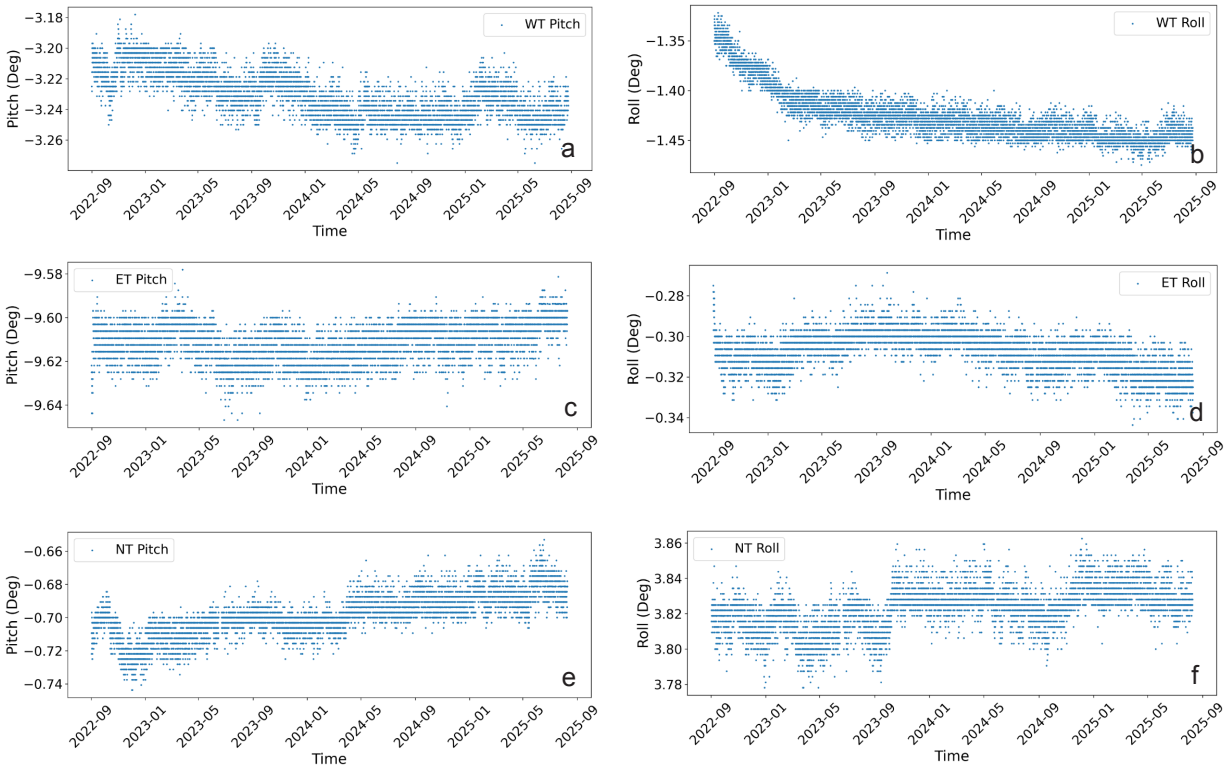


**Figure S1.** Pitch and roll measuring instrument tilt of the three transponders (a-b) WT at 1400.9 m depth with a heading of 195°, (c-d) ET at 1458.2 m depth with a heading of 120°, and (e-f) NT at 1527.4 m depth with a heading of 127°.

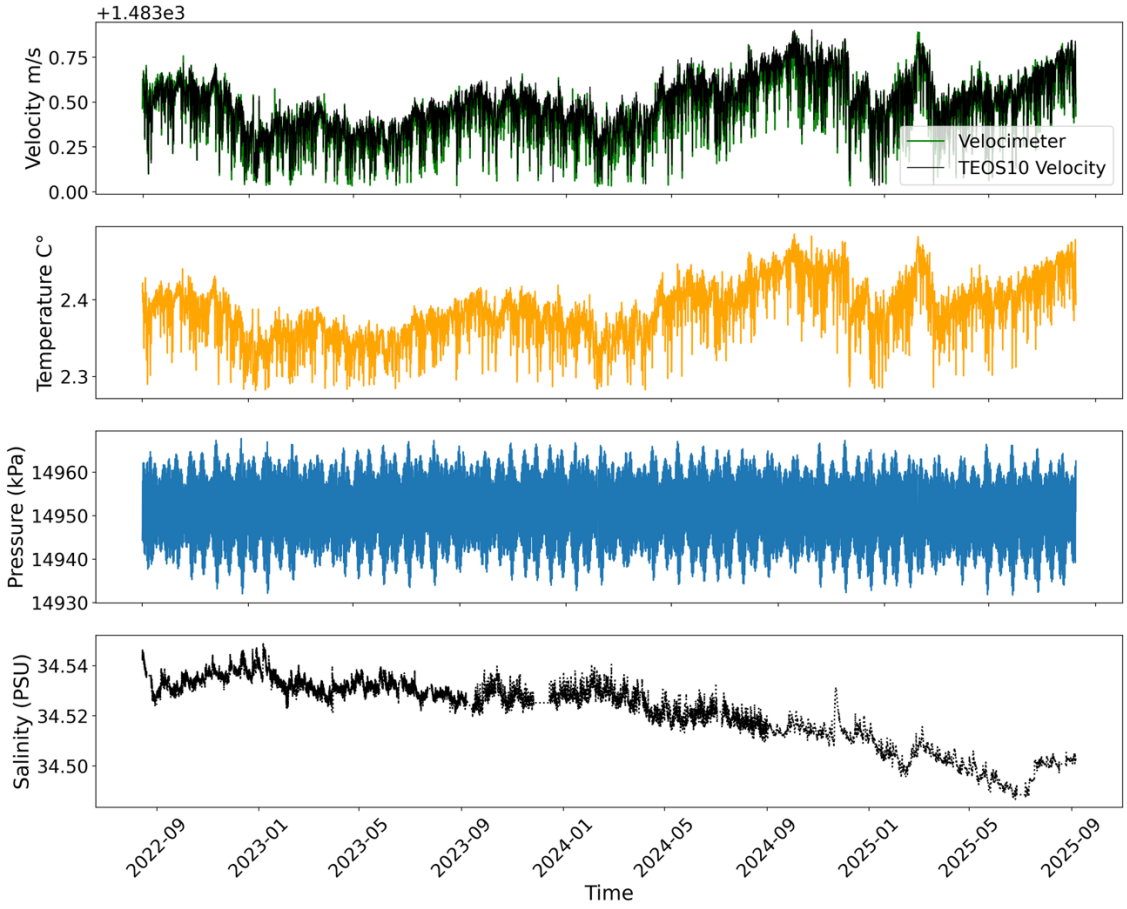


**Figure S2.** Examples of sensor data used to calculate the TEOS-10 (McDougall & Barker, 2011) velocity at the eastern transponder. (a) Velocity calculated through TEOS-10 in black and velocimeter data in green, (b) temperature and (c) pressure from ET, and (d) corrected salinity from Central Caldera Node F.

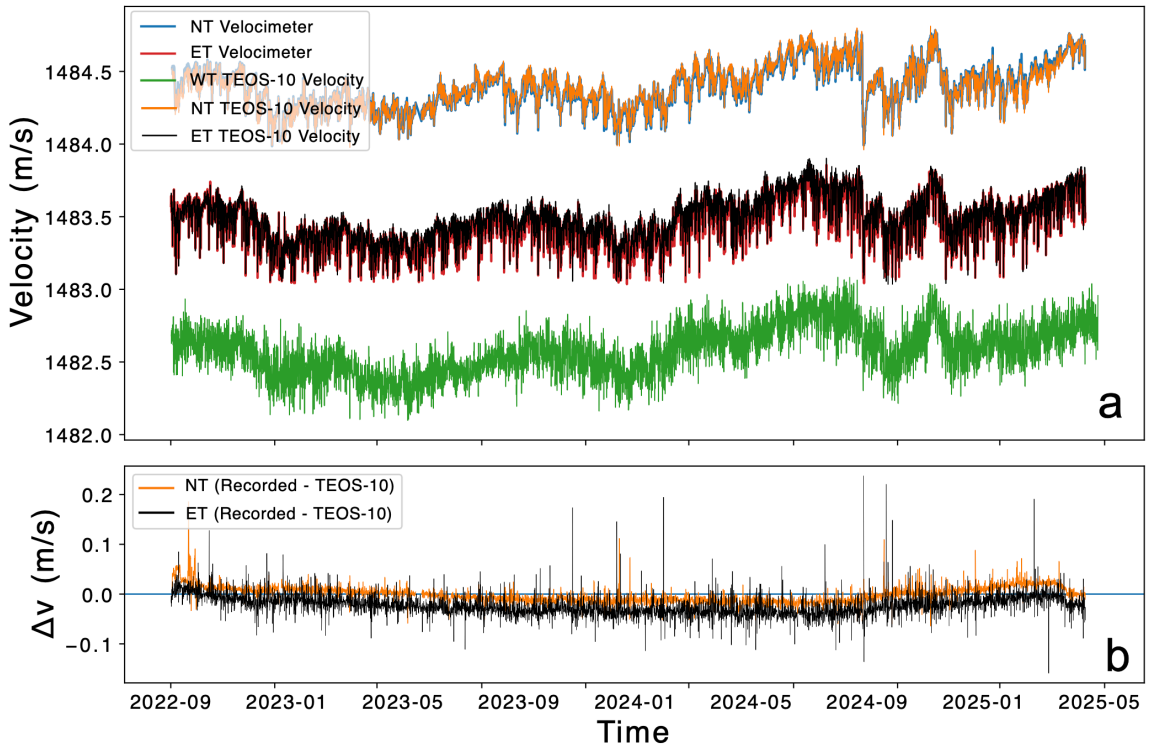


**Figure S3.** (a) Calculated TEOS-10 velocity (McDougall & Barker, 2011) and observed velocimeter data for each FETCH unit. NT timeseries are in orange and blue, ET timeseries in red and black and the WT timeseries in green (there is no velocimeter data). (b) Difference between velocimeter and TEOS-10 velocity for NT and ET stations.

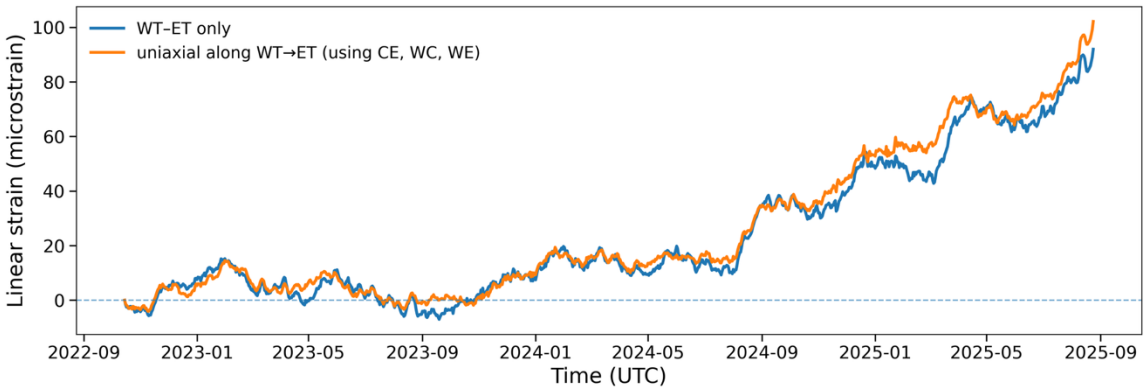


**Figure S4.** Across-caldera linear strain from acoustic ranging at Axial Seamount. Time series show horizontal extension expressed as linear strain (microstrain, $\mu\varepsilon$) derived from the seasonality-removed acoustic-ranging baseline products between the caldera benchmarks WT, ET, and NT. Baseline anomalies $\Delta L(t)$(cm) are referenced to the first common timestamp of each record (so the curves begin at zero) and converted to strain using $\varepsilon(t) = \Delta L(t)/L_0$, where $L_0$is the geodesic distance between transponder coordinates. One curve represents the direct fractional extension of the WT–ET baseline (i.e., extension measured along the line spanning the caldera between WT and ET). The second curve represents an "across-caldera" strain component constrained to the WT→ET direction, estimated by combining all available baselines (WT–ET, NT–ET, NT–WT) according to their directional sensitivity (baselines contribute in proportion to the square of their directional cosine with the WT–ET axis).

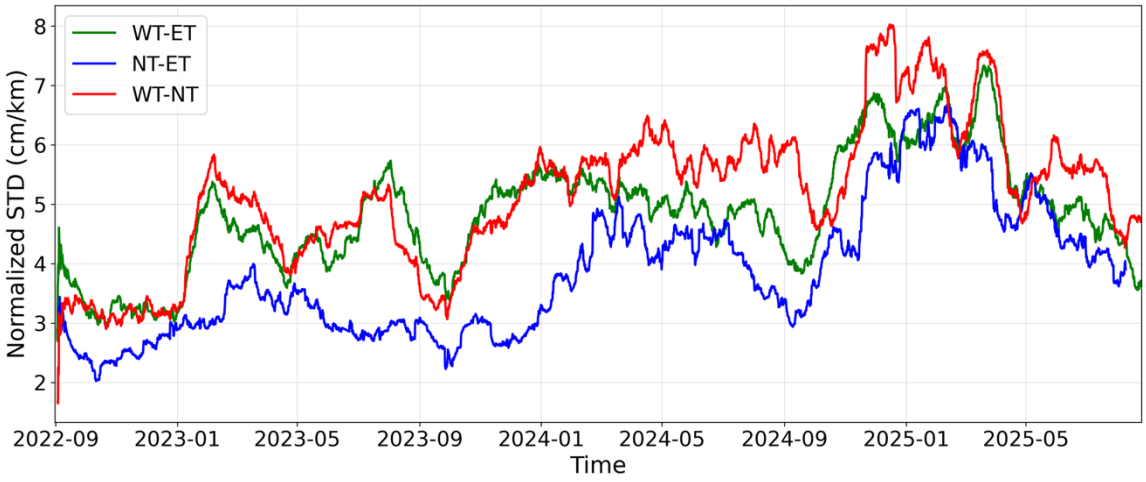


**Figure S5**. Smoothed standard deviation of ranging measurements, normalized by baseline length. The standard deviation was calculated relative to a 30-day moving average of the ranging measurements and then smoothed using a 30-day moving average.

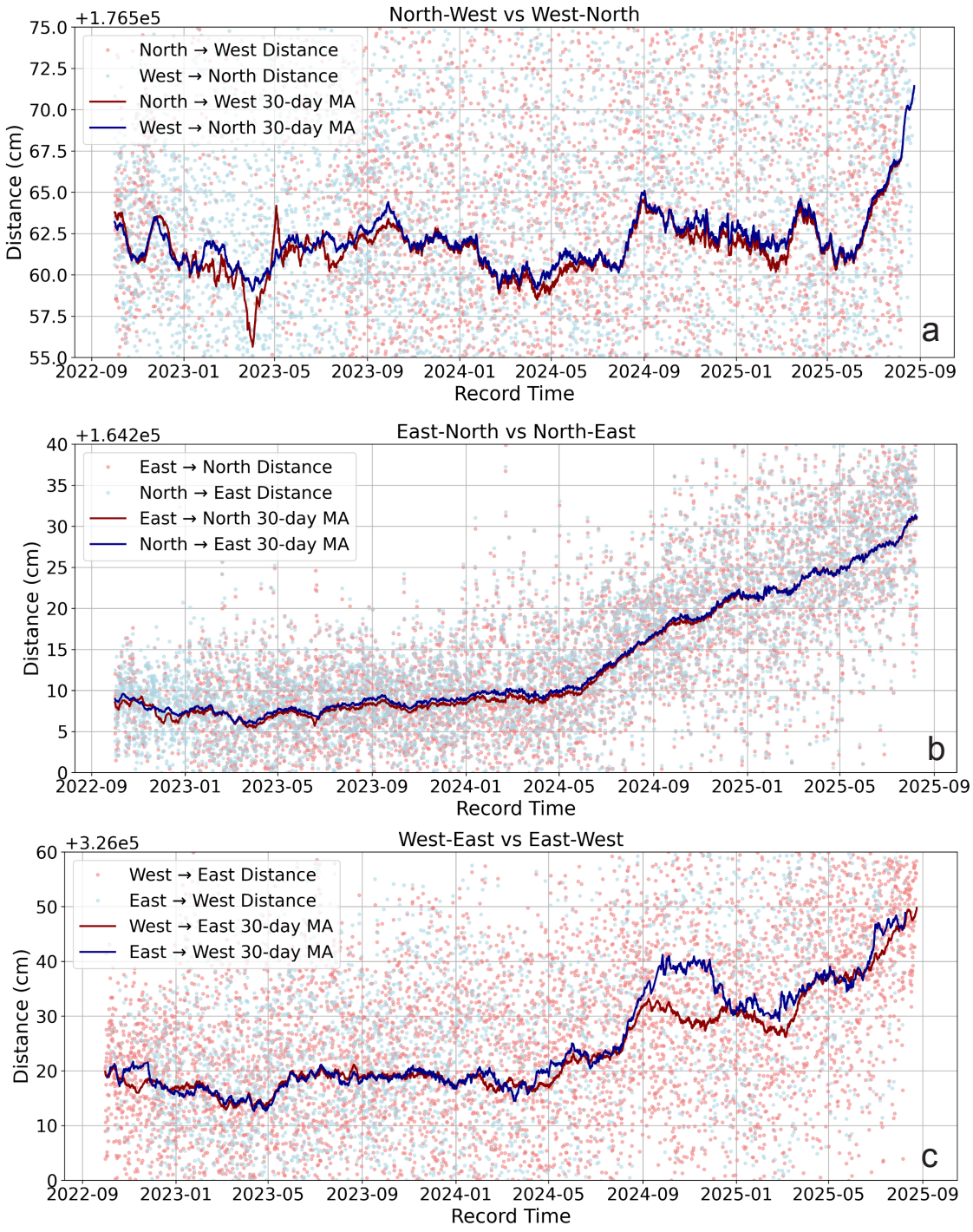


**Figure S6.** Reciprocal baseline distances and their 30-day moving average for (a) NT-WT and WT-NT, (b) NT-ET and ET-NT, (c) WT-ET and ET-WT

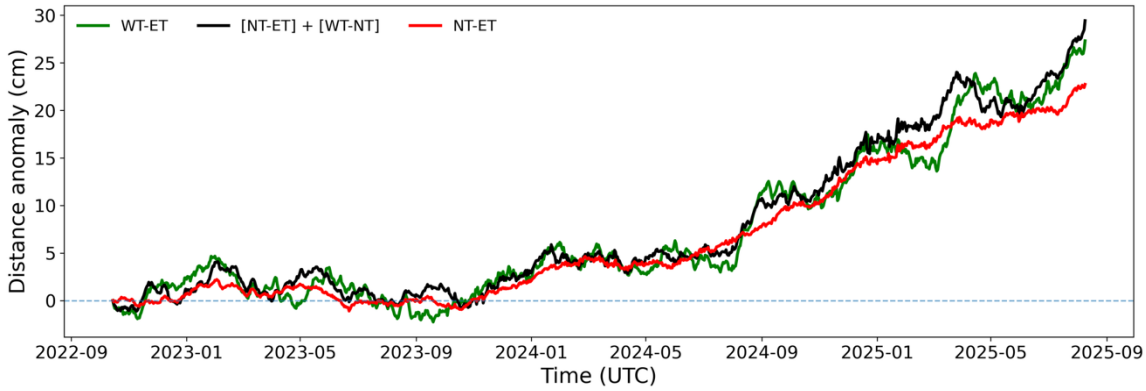


**Figure S7.** Seasonally corrected WT-ET and NT-ET baseline with the addition between NT-ET and WT-NT.

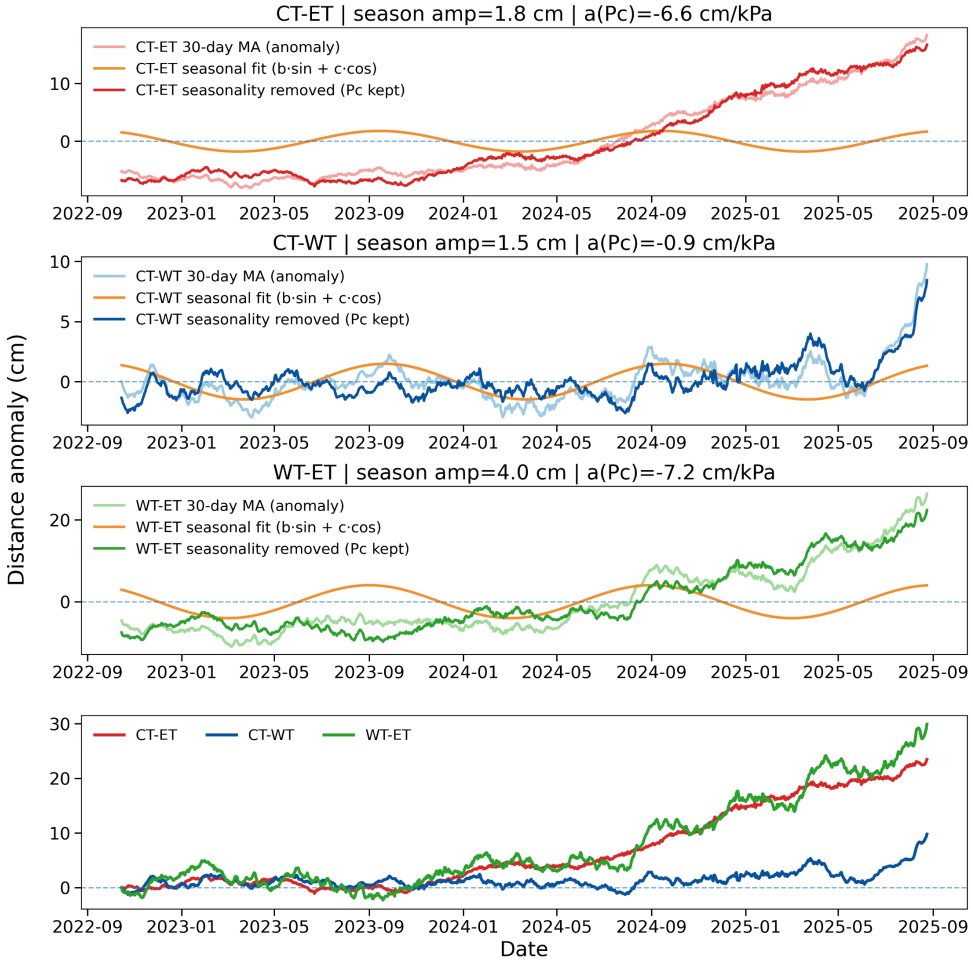


**Figure S8.** Seasonality within each baseline (a) NT-ET in red, (b) WT-NT in blue, (c) WT-ET in green, each showing the lighter red, blue and green timeseries of 30-day moving average of distance across different baselines. Darker red, blue and green showing the seasonality removed timeseries. Seasonal components of the fit is shown in orange. (d) Distance anomaly across each baseline with seasonality removed.

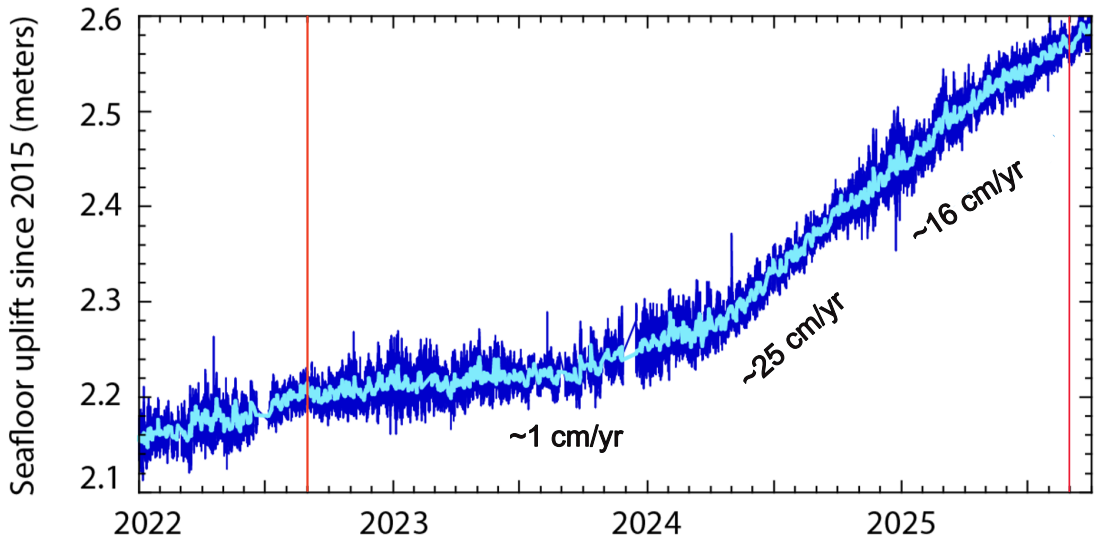


**Figure S9.** The seafloor uplift rates since 2015 derived from differential bottom pressure (corrected x1.67) (Chadwick et al., 2022) between node F and node E in dark blue and the 1 day means in light blue. Red lines mark the start and end of our acoustic ranging observation.

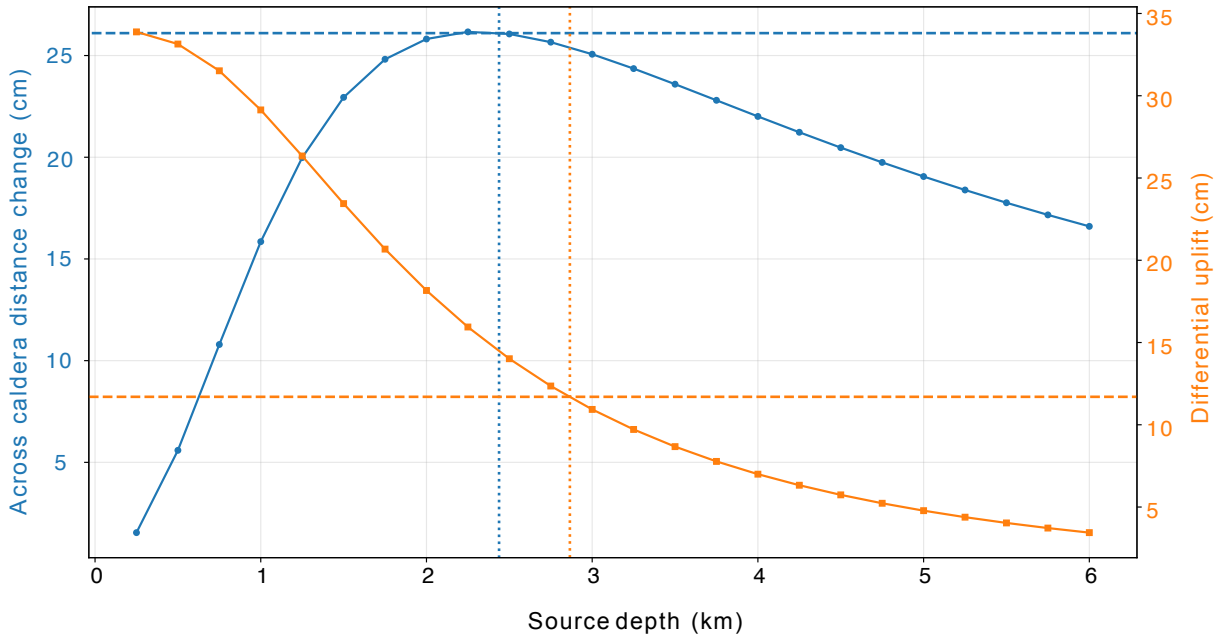


**Figure S10.** Depth dependence of surface deformation for a symmetric Mogi point source (Mogi, 1958) beneath a 3.26-km east-west baseline. A Mogi point source is positioned directly beneath the baseline midpoint, with endpoints at x = ±1.63 km. For each trial depth (0.25 to 6.0 km in 0.25-km increments), the source volume change ($\Delta V$) is adjusted to maintain constant vertical uplift of 33 cm at the center station directly above the source ($u_z$(center) = 33 cm). The blue curve (left axis) shows the predicted east-west baseline extension, computed as $\Delta L_{EW} = u_x(\text{east}) - u_x(\text{west}) = 2u_r(r,d)$ for the symmetric endpoints. The orange curve (right axis) shows the differential uplift between center and eastern endpoint, $\Delta u_z$(center−east) = $u_z$(center) − $u_z$(east). Dashed horizontal lines show approximate observed values: 26 cm for east-west extension (blue) and 12 cm for center-east drift corrected differential uplift (orange). Dotted vertical lines indicate depths where model predictions match these observations. The extension constraint is non-unique, intersecting the observed value at two depths (shallow and deep branches) because extension first increases with depth to a maximum then decreases. In contrast, the differential uplift constraint yields a single intersection within this depth range. The combination of both observables narrows the plausible source depth by identifying where baseline extension and center-east uplift contrast simultaneously match observations.

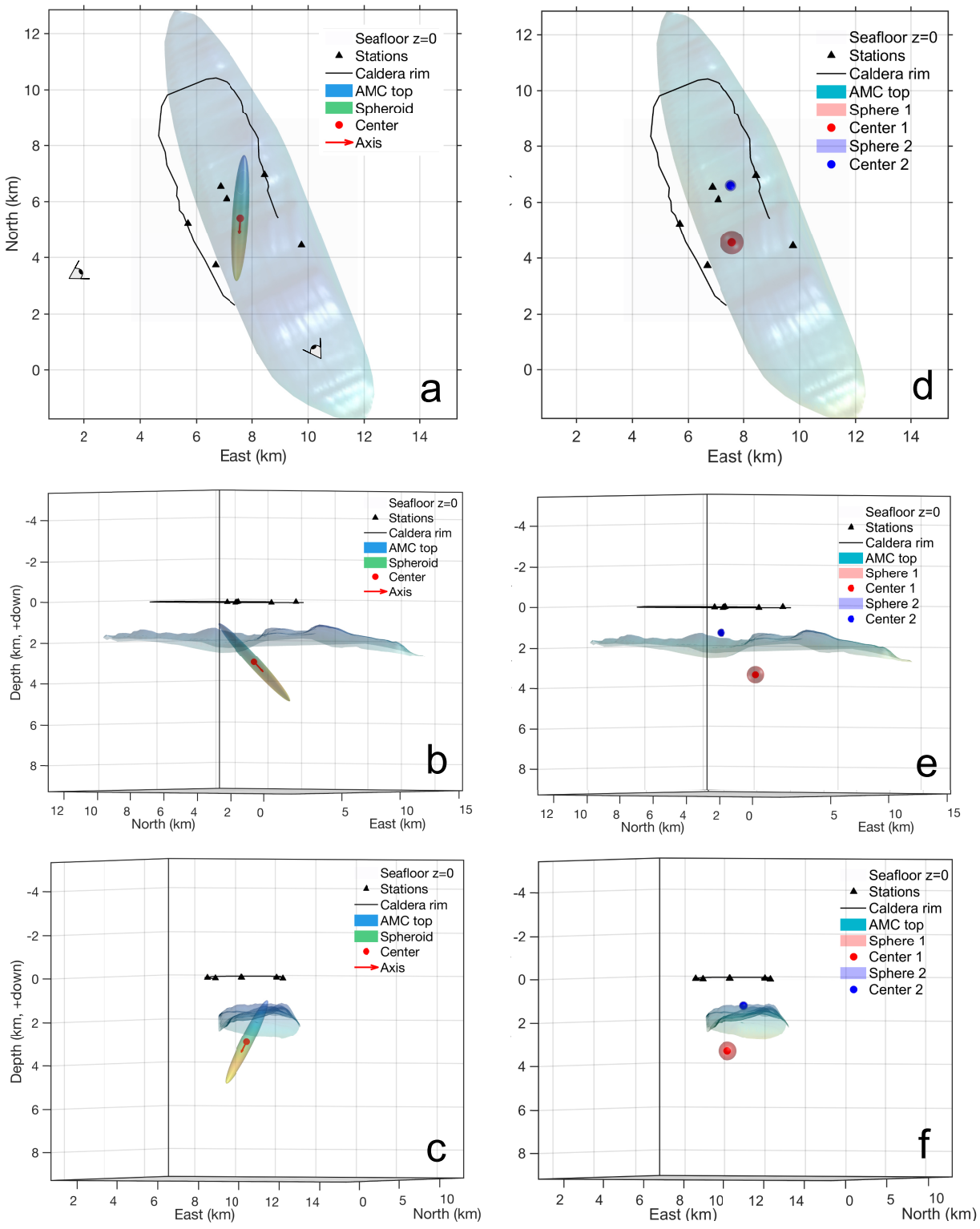
Seafloor z=0
Stations
Caldera rim
AMC top
Spheroid
Center
Axis
Sphere 1
Center 1
Sphere 2
Center 2
North (km)
East (km)
Depth (km, +down)
a
b
c
d
e
f

**Figure S11.** Inverted inflation models showing two different source geometries obtained by fitting observed uplift and extension from 2022-09-02 to 2025-08-09. Sources modeled as (a-c) a single prolate spheroid source and (d-f) two spherical sources. View of source from different angles (a,d) map view, (b,e) northwest-southeast profile viewing from southwest, (c,f) northeast-southwest profile viewing from southeast. The main magma reservoir surface from Arnulf et al. (2014) is plotted in light blue.

**Table S1.** Resulting drift and Fraction of $P_F$ from Equation (4) fitted with and without the drift term along with their rms values.

| | **Modeled with drift term** | | | **Modeled without drift term** | |
|---|---|---|---|---|---|
| | **Fraction of $P_F$ (*b*)** | **Drift kPa/yr (*c*)** | **RMS (cm)** | **Fraction of $P_F$ (*b*)** | **RMS (cm)** |
| $P_E(P_F)$ | 0.50 | 0.213 | 0.97 | 0.35 | 1.22 |
| $P_B(P_F)$ | 0.64 | 0.066 | 0.53 | 0.60 | 0.58 |
| $P_{ET}(P_F)$ | 0.72 | 0.334 | 0.39 | 0.51 | 0.93 |
| $P_{NT}(P_F)$ | 0.84 | -0.004 | 0.33 | 0.85 | 0.33 |
| $P_{WT}(P_F)$ | 0.67 | 0.482 | 0.54 | 0.37 | 1.33 |

**Appendix C: Supplementary Information for chapter 4**

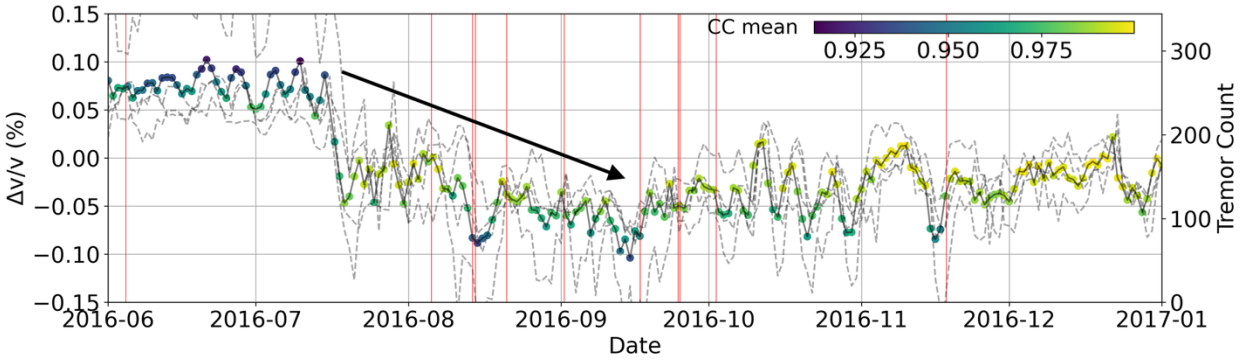


**Figure S1: dv/v of HYSB1 at 3-5 Hz under a 3-day stacked 2016 slow slip event, weighted averaging ZE and ZN positive/negative components.** The arrow indicates the slowly declining dv/v over two months to its lowest dv/v value.

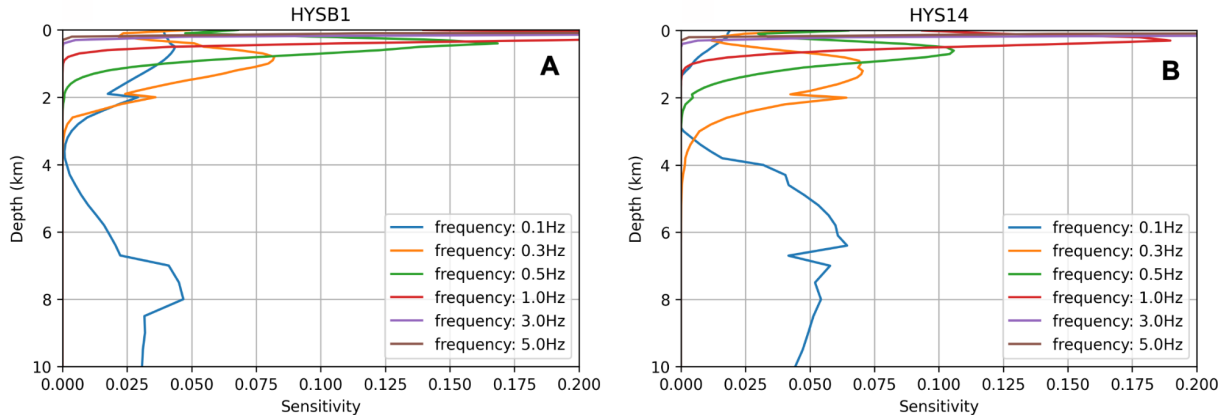


**Figure S2: Depth sensitivity of the dv/v measurements** (assuming Rayleigh waves dominated) as a function of frequency and depth for HYSB1 in (**A**) and HYS14 in (**B**).

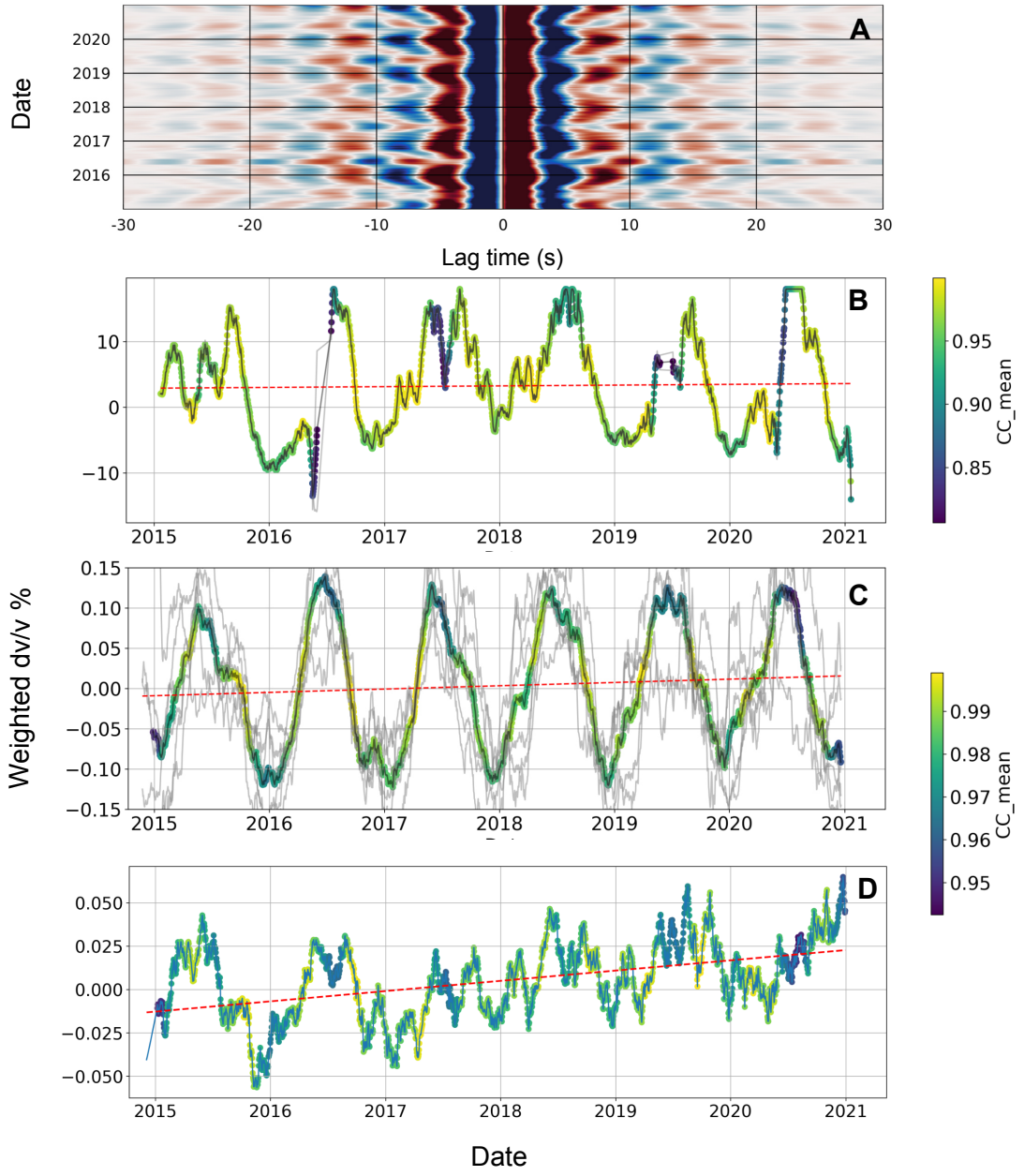


**Figure S3: Low frequency observed and synthetic cross-correlation and dv/v.** (**A**) Synthetic cross-correlation modeled at HYSB1, filtered 0.1-0.3 Hz, using microseismic signals from wavewatch data and WMSAN to compute. (**B**) synthetic dv/v obtained from (A). (**C**) Observed dv/v at HYSB in the 0.1-0.3 Hz range, largely dominated by seasonal spurious signals. (**D**) Notched-filter time series of (C) to remove the 200-400 day period and explore the residual and the remaining positive trend illustrating a compression.

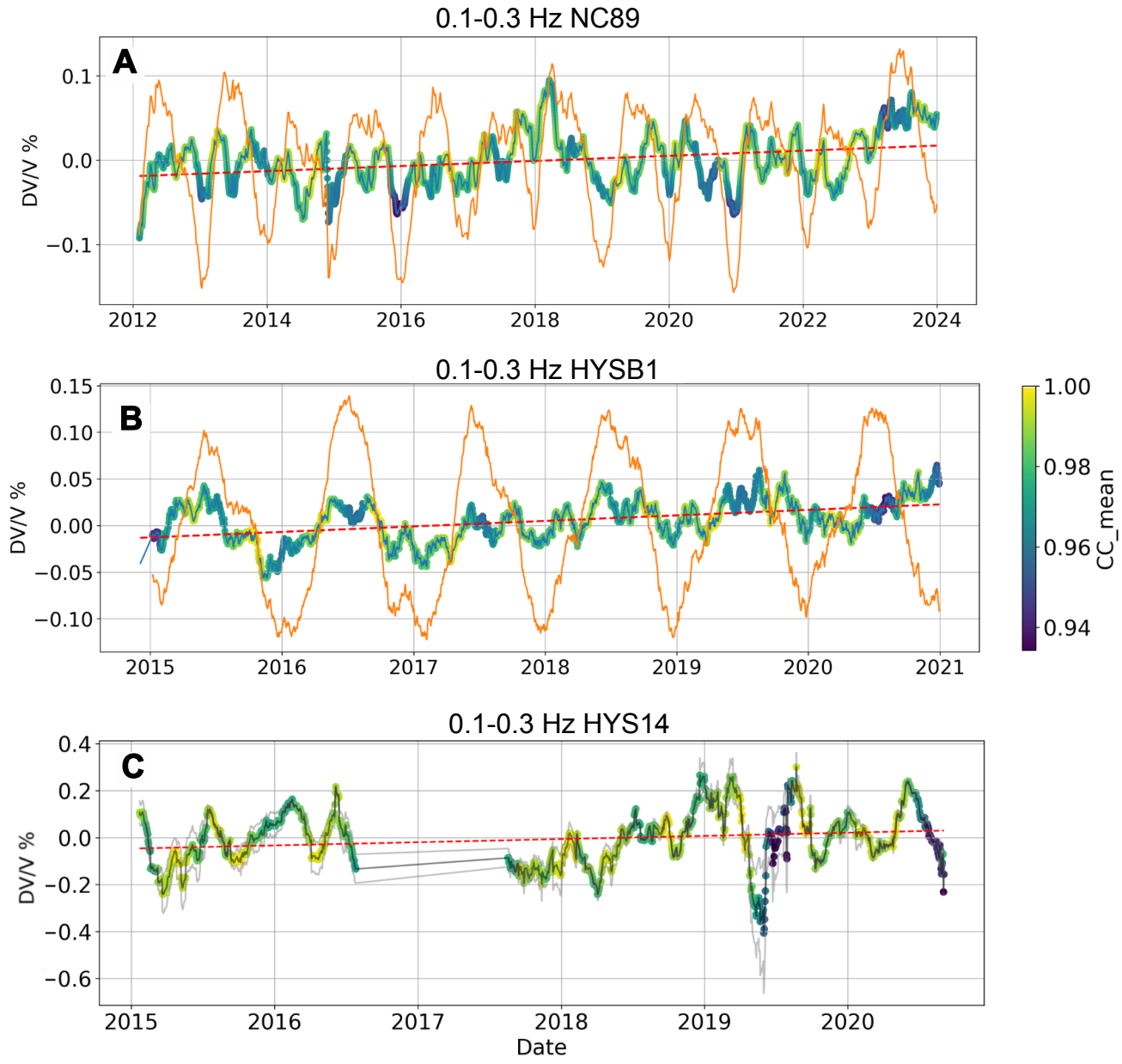


**Figure S4: Removing seasonality from low-frequency dv/v.** We removed seasonal signals using a Gaussian notch filter in the 0.1-0.3 Hz dv/v in (**A**) NC89, (**B**) HYSB1, and (**C**) HYS14. Color-coded values have the cumulative correlation coefficient after stretching.

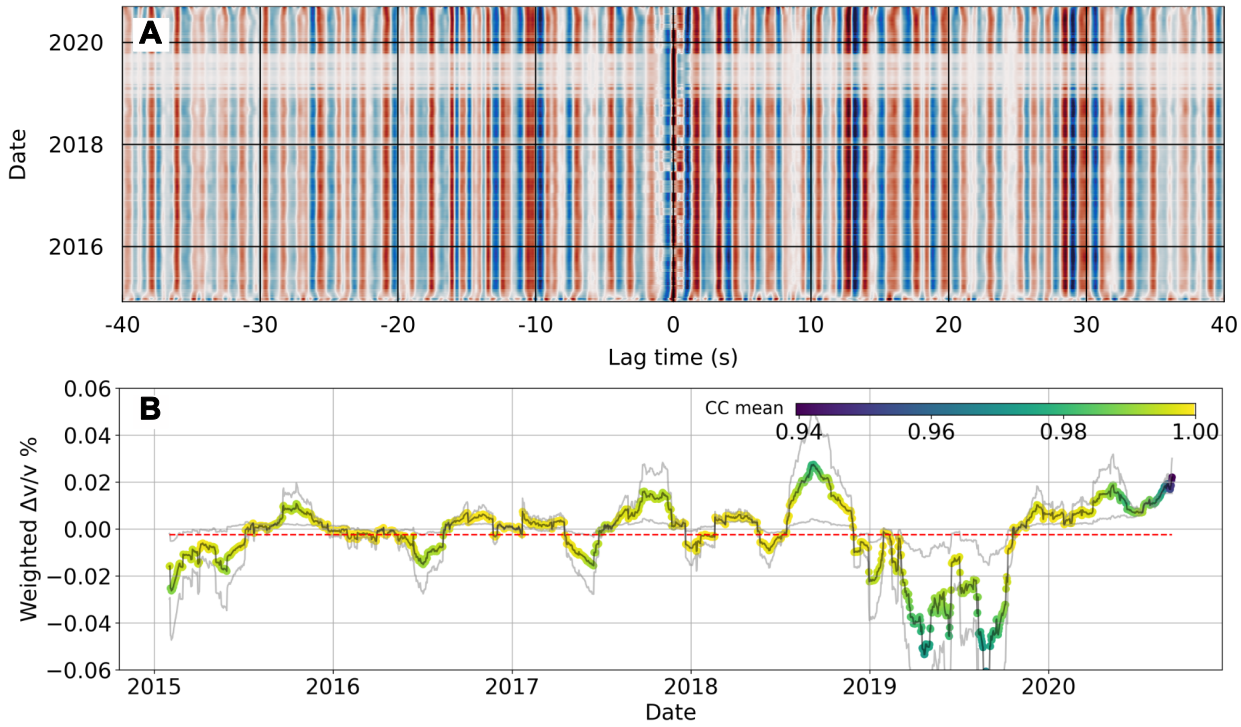


**Figure S5**: **Interstation dv/v between HYS14 and HYSB1** in the 0.5-2 Hz frequency band, with (**A**) the vertical-to-vertical cross-correlation, and (**B**) the resulting dv/v, color-coded by the cumulative correlation coefficient. The dv/v values are 10 times lower than the single-station measurements, which is expected from the decreased sensitivity between the stations. Nevertheless, this dv/v time series coincides well with the average of the two single-station dv/v time series, demonstrating that the transient is located at and between the two stations.

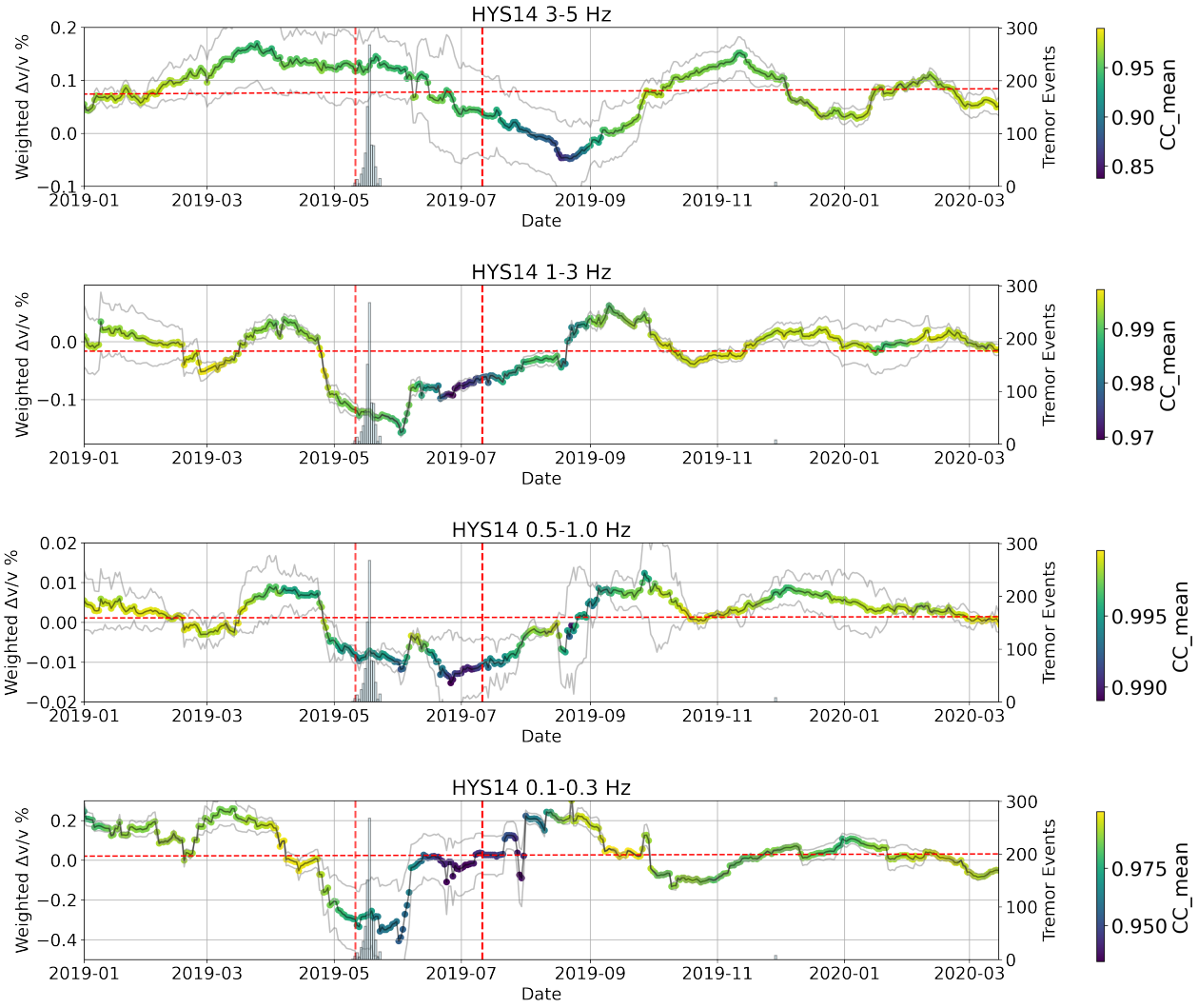


**Figure S6**: **Multi-frequency weighted dv/v at HYS14 for the 2019 transient event**. From high frequency (3-5 Hz, top panel) to low frequency (0.1-0.3 Hz, bottom panel), sorted by depth sensitivity. The cross-correlations have been averaged over 40 days. dv/v is color-coded by the cumulative correlation coefficient after stretching. We observe a shift from deep dv/v to be early, and shallow dv/v to be later. Note that Krauss' shallow tremors (Krauss et al., 2024) also appear during the transient.

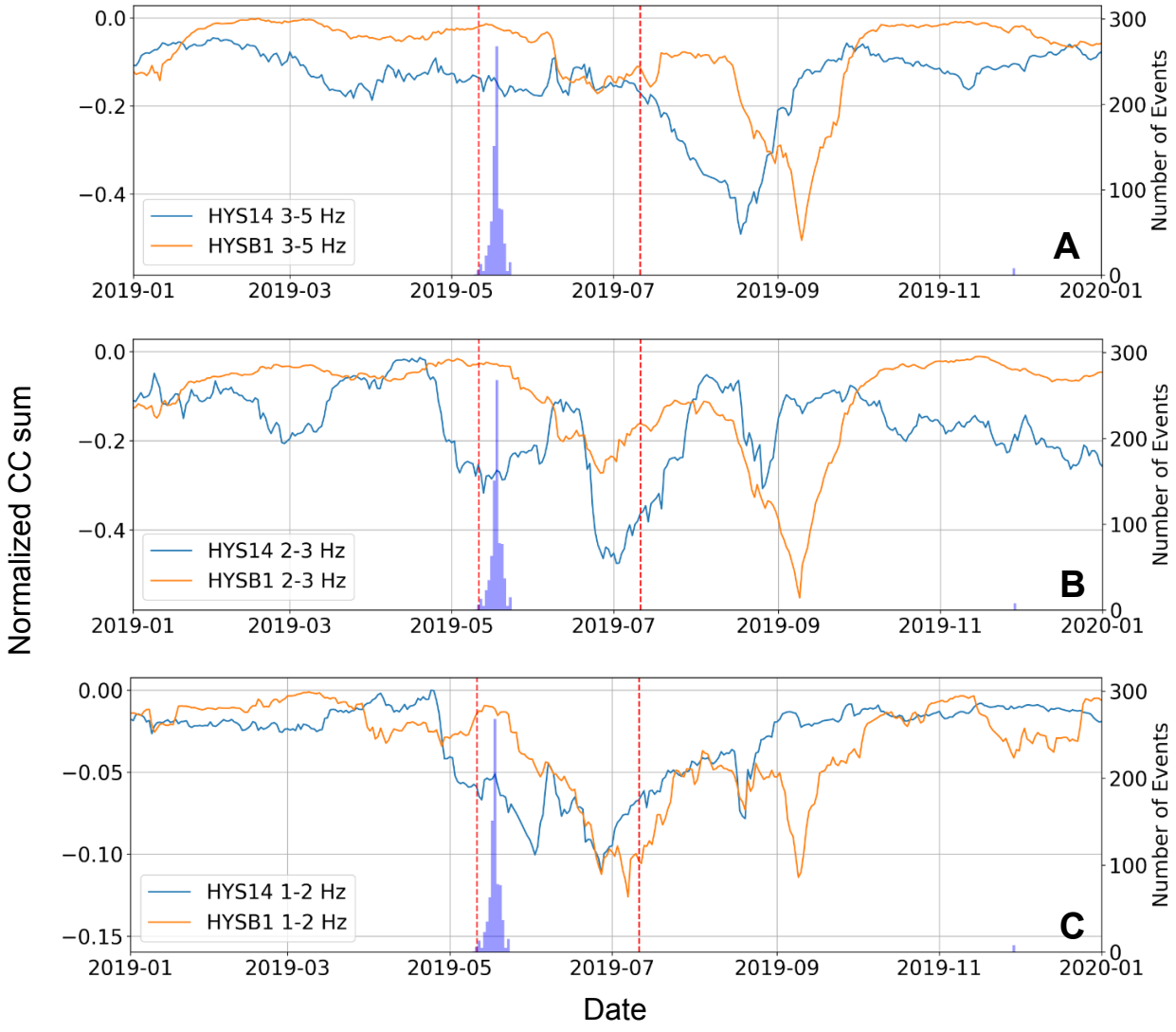


**Figure S7**: **Normalized sum of squared correlation coefficients of each time series** for (**A**) 3-5 Hz (**B**) 2-3 Hz (**C**) 1-2 Hz in HYS14 and HYSB1 stations during the 2019 ETS event. The squared sum of correlation coefficients of each time series are normalized to their maximum value and shifted to align the maximum values with zero for improved visualization.

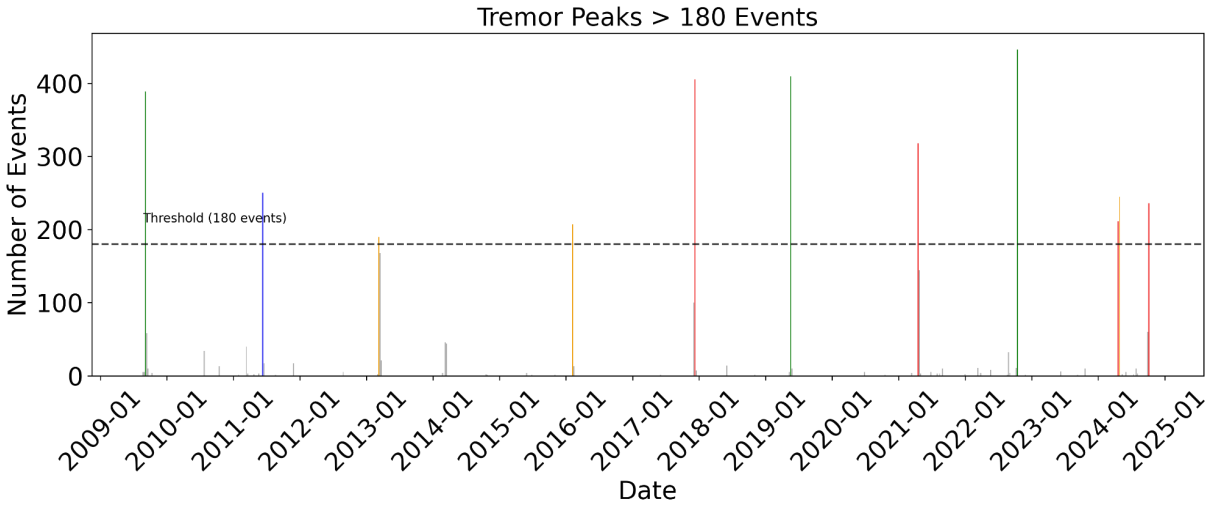


**Figure S8: 7-day binned tremor counts for 44.4°N-44.6°N latitude range.** Colored events refer to those exceeding 180 event counts per episode and correspond to the dendrogram shown in Figure S9.

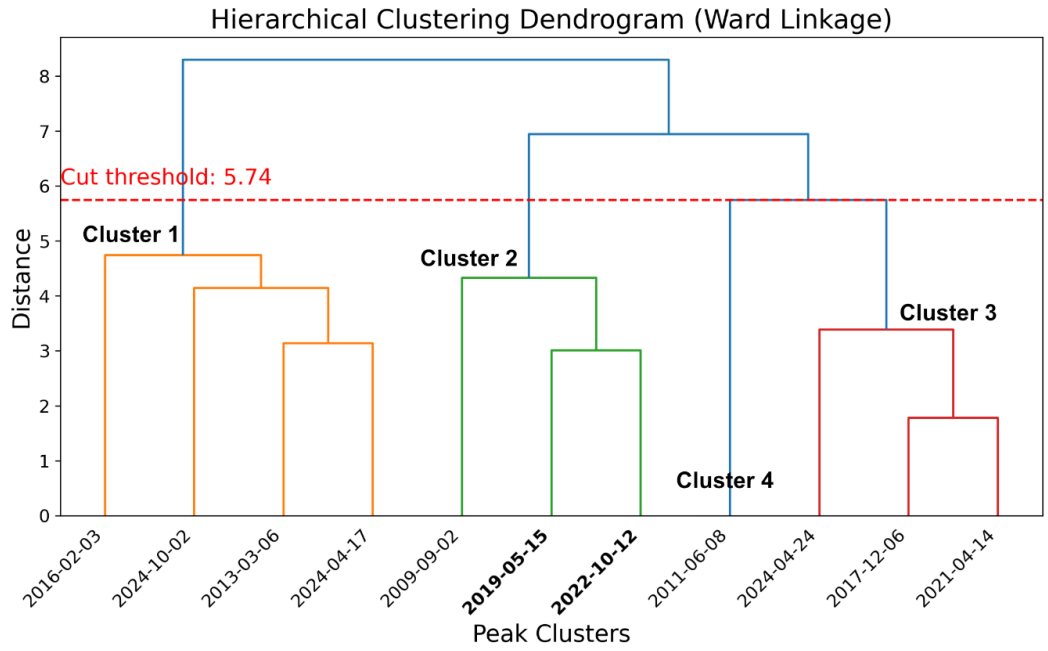


**Figure S9: Ward linkage dendrogram of clustered tremor events.** Bolded events are the two events with dv/v drops in HYSB1.

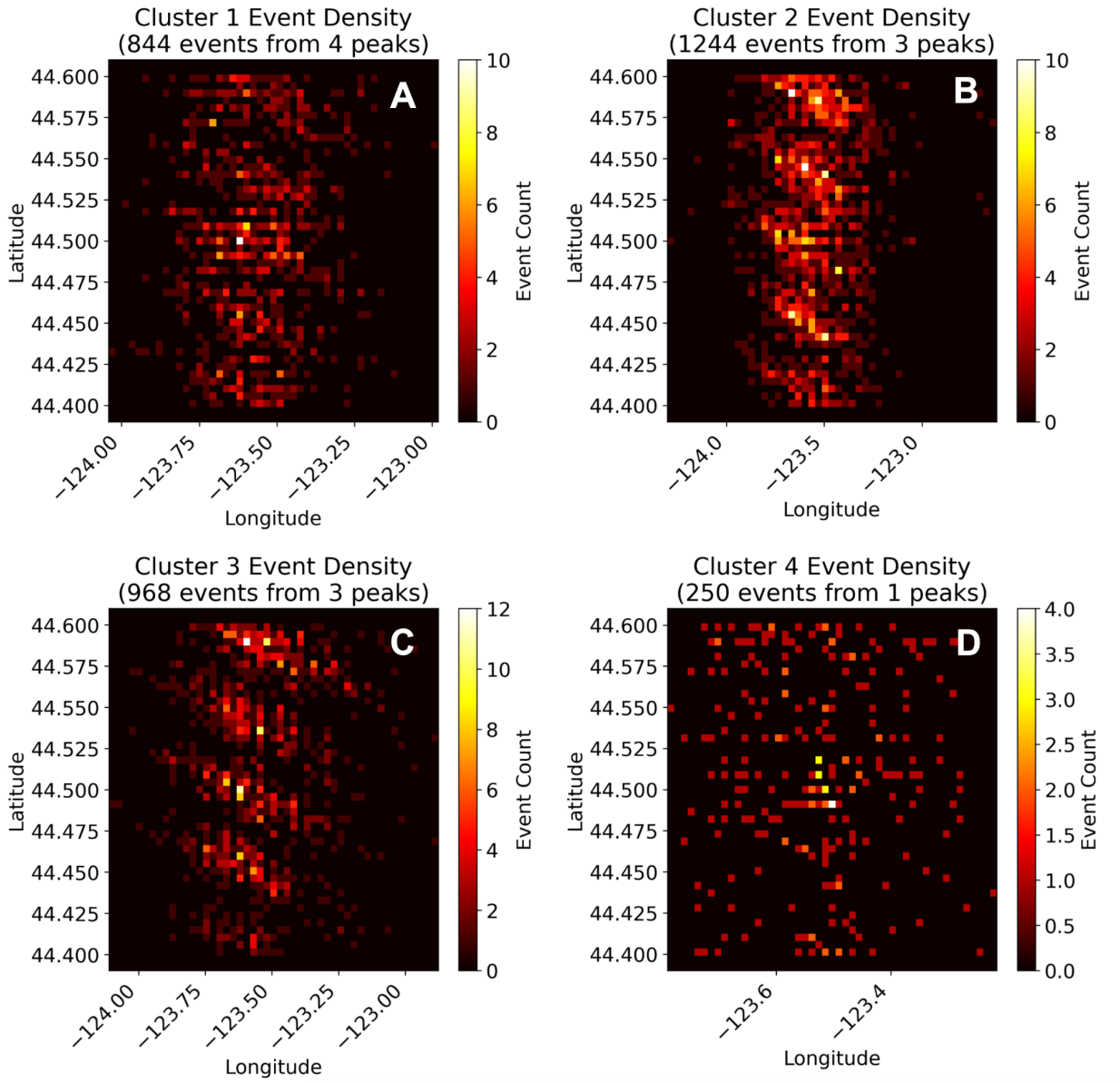


**Figure S10: Density map for each cluster of events in the dendrogram of ward linkage by summing all events within the same cluster.** The cluster density plots correspond to the clusters shown in Figure S9, specifically (**A**) the orange cluster, (**B**) the green cluster, (**C**) the red cluster, and (**D**) the blue cluster in the dendrogram. Cluster B is associated with the dv/v drops observed.

| Freq band (Hz) | 0.1-0.3 | 0.3-0.6 | 0.5-1 | 1-3 | 3-5 |
|---|---|---|---|---|---|
| Coda window: start and end times in seconds. | 10-60 | 10-30 | 10-20 | 2-10 | 2-10 |

**Table S1: Choice of frequency band and coda window.**

| **Frequency** | **$H_d$ at HYSB1 (km)** | **$H_d$ at HYS14 (km)** |
|---|---|---|
| **5 Hz** | 0.03 km | 0.04 km |
| **3 Hz** | 0.1 km | 0.1 km |
| **1 Hz** | 0.2 km | 0.3 km |
| **0.5 Hz** | 0.5 km | 0.75 km |
| **0.3 Hz** | 1 km | 1.5 km |
| **0.1 Hz** | 8 km | 8 km |

**Table S2: Frequency-dependent depth sensitivity of HYSB1 and HYS14**.